Lagrangian Simulation of Transverse Jets with a Distribution-based Diffusion Scheme

by

Daehyun Wee

S.B., Seoul National University (1996)
S.M., Massachusetts Institute of Technology (2002)

Submitted to the Department of Mechanical Engineering
in partial fulfillment of the requirements for the degree of

Doctor of Science in Mechanical Engineering

at the

MASSACHUSETTS INSTITUTE OF TECHNOLOGY

May 2007

Author .....
Department of Mechanical Engineering
May 8, 2007

Certified by .....
Ahmed F. Ghoniem
Ronald C. Crane (1972) Professor
Thesis Supervisor

Accepted by .....
Lallit Anand
Chairman, Department Committee on Graduate Students

Lagrangian Simulation of Transverse Jets with a Distribution-based Diffusion Scheme

by

Daehyun Wee

Submitted to the Department of Mechanical Engineering
on May 8, 2007, in partial fulfillment of the
requirements for the degree of
Doctor of Science in Mechanical Engineering

Abstract

Transverse jets form a dominant group of flow fields arising in many applications of modern energy utilization, including propulsion and effluent dispersion. Furthermore, they form canonical examples where the flow field is dominated by large-scale and small-scale vortical structures, whose inter-related dynamics is a challenging subject in modern fluid mechanics. This study seeks a mechanistic understanding of the vortical structures of the transverse jet and their evolution.

A set of massively parallel three-dimensional vortex simulations of high-momentum transverse jets at intermediate Reynolds number, utilizing a discrete filament representation of the vorticity field to capture stretching and tilting of vorticity, is performed. A diffusion scheme to treat viscosity at intermediate Reynolds number is formulated and analyzed in a distribution-based description. The implementation of the diffusion scheme is achieved by performing interpolation, which is a process that has been widely used to regularize particle distributions in vortex simulations, with a new set of interpolation kernels. These kernels provide an accurate and efficient way to simulate vorticity diffusion in transverse jets.

An improved formulation of the vorticity flux boundary conditions is rigorously derived. This formulation includes separation of the wall boundary layer and feedback from the jet to the wall boundary layer, and describes detailed near-field jet structures.

The results present the underlying mechanisms by which vortical structures evolve. Transformation of the jet shear layer emanating from the nozzle starts with jet-streamwise lift-up of its lee side to form sections of counter-rotating vorticity aligned with the jet trajectory. Periodic rollup of the shear layer, which is similar to the Kelvin-Helmholtz instability in free shear layers, accompanies this deformation. A sudden breakdown of these coherent structures into dense vortical structures of smaller scales is observed. This breakdown to small-scale structures is due to the interaction of counter-rotating vortices and rolled-up shear layer. With a separated wall boundary layer, strong near-wall counter-rotating vortices are observed. This observation substantiates the importance of including the full interaction between the wall boundary layer and the jet shear layer in the investigation of transverse jet dynamics.

Thesis Supervisor: Ahmed F. Ghoniem
Title: Ronald C. Crane (1972) Professor

Acknowledgments

First, I would like to thank Prof. Ghoniem for his guidance through the years of my study. His advice has been invaluable resources to carry out my research. Prof. John Bush, Prof. Nicholas Hadjiconstantinou, and Prof. George Haller have provided critical comments during the entire length of my study, from which I have learned a lot. I also thank Prof. Sigurdur Helgason and Prof. Jeff Viaclovsky, who taught me basic analysis, on which all my mathematical skills build up. The guidance provided by Prof. Suk-Ho Chung, Prof. Sung-Tack Ro, and Prof. Jung-Yul Yoo during my years in Seoul National University has remained as concrete and essential basis for all my research.

I owe great deals to my colleagues. Dr. Youssef Marzouk provided his valuable time for discussion on physics of transverse jets. With great care, Raymond Speth has administered local workstations, on which my data have been post-processed. Fabrice Schlegel's programming skill was also helpful: his improvement of the adaptive tree-code has been essential to perform many of my latest calculations. Many interesting ideas, which were raised by Hurem Murat Altay, Duane Hudgins, and Dr. Jean-Christophe Nave, helped my progress. Careful administrative assistance was provided by Ms. Lorraine Rabb during the last several years of my study.

I greatly enjoyed the period during which Wonyong Lee was preparing his qualifying exam. I must confess that I learned much by discussing many subjects including fluid mechanics and thermodynamics with him.

I am very grateful to my family: my parents, Youngin Wee and Hearyan Koh, and my brother, Soohyun Wee, provided support and guidance. Special thanks to my wife, Jiheyon Kim, for her support during the past years. Three of my grand parents passed away during my stay in the United States. I owe a great deal to them, which I cannot repay any more.

I also want to thank Ms. Leslie Regan. There were many occasions where I could not meet official deadlines. Without her efforts, the process of submitting this dissertation would be impossible.

Finally, I remember Johan Huizinga, whose words enabled me to start writing. Indeed, I feel more or less the same way as the great historian did about seventy years ago [29]. To fill in all the gaps in my knowledge beforehand is out of question to me. I have to write now, or not at all. And I have decided to write.

The research was supported by the Mathematical, Information, and Computational Sciences (MICS) program of the Office of Science in the U.S. Department of Energy under the grant number DE-FG02-98ER25355. Computational support for large-scale scientific simulations was provided by the National Energy Research Scientific Computing Center (NERSC).

Contents

List of Figures

List of Tables

Chapter 1

Introduction

Combustion is one of the most widely used technologies in the modern, post industrial revolution world, and currently the dominant technology in energy conversion, propulsion, heating and industrial production. Since its prehistoric discovery [26], combustion has been an essential part of human civilization, and it likely continues to be so for the foreseeable future. Currently, more than 85% of our energy comes from burning fossil fuels, and the absolute majority of transportation systems rely on combustion engines [55]. Even with gradual introduction of alternative energy sources and conversion processes, combustion will certainly remain an essential part of energy conversion and propulsion systems.

Despite its significance, combustion of fossil fuels is not without challenges, related mostly to performance, safety, health, and environmental concerns. Rising fuel prices and worries over supplies, and alarms over increasing carbon dioxide concentration in the atmosphere are putting more pressure on thermochemical and thermomechanical conversion efficiency. Emission of carbon monoxide, nitrogen oxides and sulphur oxides from uncontrolled combustion processes cause health problems and environmental damage. Fires and explosions remain a major safety concern in many systems and installations. As a natural consequence, tremendous amounts of current research efforts have been concentrated on the improvement of combustion processes of fossil fuels.

The mixing properties of a jet issuing normally into a uniform crossflow are par-

ticularly important in this context: these transverse jets are used as sources of fuel in industrial furnaces, or as diluent jets for blade cooling or exhaust gas cooling in industrial or airborne gas turbines. Pipe-tee mixers, which are extensively used for various industrial applications, form another group of examples. The study of transverse jets are even relevant to environmental problems such as pollutant dispersion from chimneys and the discharge of effluents into the ocean. Such close relationship between this particular flow and our life of energy utilization may be best symbolized in Figure 1-1, where a transverse jet is used to discharge steam and smokes from a steam locomotive into the atmosphere. A modern equivalent may be a fighter jet using thrust vectoring, as illustrated in Figure 1-2.

In many of these examples, complex flow dynamics may offer an opportunity for the control of the mixing rate between the jet and the crossflow, and hence improvements in performance. For instance, gas turbines may benefit from the enhancement of the mixing rate between fuel and air, by achieving smaller size, higher efficiency, lower noise, over a wider range of operating conditions. There are also more fundamental interests in these transverse jets, since they are canonical examples of a flow exhibiting a complex net of coherent vortical structures. Understanding the underlying vorticity dynamics of transverse jets may extend our knowledge on the formation and interaction of different forms of vortical structures.

The objective of this work is to develop better understanding of the dynamics of the transverse jet that control the mixing rate between the jet fluid and the crossflow. Such understanding is essential to develop actuation strategies for transverse jets that optimally manipulate the mixing rate between the jet fluid and the crossflow.

The focus of this thesis is placed on mechanistic understanding of vorticity dynamics of transverse jets. A reliable computational tool is developed to capture the fundamental processes responsible for entrainment and mixing of fluid from the crossflow into the jet. We employ Lagrangian vortex methods as our methodology to simulate transverse jets. Vortex methods provide an attractive framework for dealing Lagrangian vorticity dynamics by providing a direct link between computational elements and vortical structures inherent in such flows. The present simulations are

based on a previous computational study [51], where an invisicd vortex method is used to investigate transient jets at high Reynolds numbers. The present simulations, however, have a layer of complexity added on top of the previous simulations, i.e., diffusion. In this thesis, we investigate transverse jets at moderate Reynolds number, where both convection and diffusion should be simultaneously considered. To implement diffusion, we adapt the vorticity redistribution method [64] in our three-dimensional context. New interpretation and analysis of the method is provided, by using the theory of distributions [22, 68], to investigate the convergence characteristics of the method.

The formulation of vorticity flux boundary conditions provided in [51] is also generalized to investigate the interaction between the jet and the wall boundary layer. The simulation results reveal many interesting near-wall vortical structures, which in turn affect the behavior of the jet.

The thesis also contains the development of adaptive tree-code for a high-order algebraic kernel and the comparison of convergence characteristics of the Rosenhead-Moore kernel and the high-order algebraic kernel as appendices.

1.1 Physics of transverse jets

There have been many studies on transverse jets during past years. Some of the relevant results are reviewed in the following sections to provide contexts for the thesis.

1.1.1 Flow parameters and coherent structures

The structure of the flow field is governed by three major dimensionless parameters: the Reynolds number, $Re_\infty \equiv U_\infty d/\nu$, the jet-to-crossflow momentum ratio, $r \equiv \left(\rho_j V_j^2/\rho_\infty U_\infty^2\right)^{1/2}$, and the relative boundary layer thickness of the wall boundary layer, δ/d. Here, ρ_j and V_j are the density and mean velocity of the jet, while ρ_∞ and U_∞ are the density and velocity of the crossflow. In this thesis, we assume the same fluid for the jet and the crossflow, and $\rho_j = \rho_\infty$. d is the jet diameter, ν is the

kinematic viscosity, and δ is the wall boundary layer thickness. We also define the Reynolds number based on the jet velocity as $Re_j \equiv V_j d/\nu = rRe_\infty$.

The flow field near a transverse jet is primarily dominated by various coherent structures. Experimental observations in [33] identify number of coherent structures, shown schematically in Figure 1-3. The jet shear layer is the result of the advected in-pipe boundary layer. The shear layer, especially on its windward side, develops the Kelvin-Helmholtz instability to generate distinct bands of vortices around the jet column at a sufficiently large Reynolds number. The roll-up phenomena also show certain degree of dependency on the Reynolds number. It was reported by Kelso *et al.* [33] that the shear layer roll-up was limited to the windward side of the jet for the cases with small Reynolds numbers, while large-scale roll-up occurs along the entire perimeter for $Re_\infty > 1000$.

Sometimes, downstream of the orifice, upright wake vortices occur. Although these upright wake vortices show apparent similarity to the vortices shedding from a solid cylinder, in the sense that they show an alternating pattern convected downstream, the origin of upright wake vortices is fundamentally different. Instead of being formed from the vortex sheet on the boundary of the solid cylinder, they are most likely the separated portion of the wall boundary layer [21]. Since these upright wake vortices are due to separation, Re_∞ and r strongly control the behavior of these vortices. It is not expected to have upright wake vortices when $Re_\infty \ll 500$ [33]. The most orderly upright wake vortices are reported around $r = 4$ [21, 33].

Horseshoe vortices, which are developed close to the wall upstream of the jet column, are believed to be resulted in by an adverse pressure gradient and associated separation [21]. They are initially formed from the wall boundary layer, whose circulation per unit length is $1/r$ of that of the jet shear layer. For those horseshoe vortices that have opposite sense of rotation when realigned to the jet streamwise direction, they do not experience major events of entrainment and stretching [33]. As the result, a horseshoe vortex system is initiated as a weak structure, and stays as it is. Kelso *et al.* [33] assert that "the horseshoe vortex system seems to play only a minor role in the overall structure." However, for very low r, i.e., for $r < 1$, the horseshoe vortices

may interact with the reoriented jet shear layer vortices, as suggested in [3].

A counter-rotating vortex pair (CVP) is practically the most important vortical structure observed in a transverse jet. It is a robust feature of the flow over large parameter ranges and has been a focus of the numerous studies [33, 44, 12]. According to Broadwell and Breidenthal [7], the impulse of the jet normal to the crossflow results in a streamwise counter-rotating vortex pair. Such a view is quite effective for explaining jet trajectories in the far field, but provides an only limited explanation on how vorticity is transformed mechanistically to *create* such counter-rotating vortices in the near field. Also, the counter-rotating vortex pair is present in the mean flow, its unsteadiness is also significantly important to examine the overall mixing rate, which cannot be effectively studied by balancing momentum only.

1.1.2 Trajectories and similarity

The trajectory of the transverse jet has long been the subject of experimental measurements and analytical predictions. Many experimental correlations can be collapsed to power-law form [28]:

$$\frac{y}{rd} = A\left(\frac{x}{rd}\right)^{B}. \tag{1.1}$$

For instance, one of the most widely referred correlations is that reported in [49]:

$$\frac{y}{rd} = 4^{1/3}\left(\frac{x}{rd}\right)^{1/3}. \tag{1.2}$$

However, as briefly discussed in [30], reported trajectories show large variations. Thus, naturally, reported values of constants also vary in a wide range, which amounts to a few 10%. Such variation in the coefficients A and B may be due to several causes. There is no unique definition of the jet trajectory, and many different definitions have been used by various authors. The determination of r has some ambiguity as well, since the jet velocity is not perfectly uniform at the jet exit. Finally, the trajectory shows sensitivity to conditions near the jet nozzle exit. The in-pipe jet profile and the crossflow boundary layer thickness show some control over the penetration of the jet

near the nozzle exit, and impact the overall trajectories [54]. Analytical predictions of the jet trajectory have also been pursued. Many analytical results predicted $B = 1/3$ with significant variation over the value of A [7, 31].

We note that many of the previous studies on trajectories are valid only in the far field of the jet. The recent similarity analysis made by Hasselbrink and Mungal [28] is particularly notable in the sense that an attempt to provide a more precise delineation of 'far field' and 'near field' was made. In the far field, for $y/rd \gg 1$, the centerline trajectory follows a 1/3 power law:

$$\frac{y}{rd} = \left(\frac{3}{c_{ew}} \frac{x}{rd} \right)^{1/3}, \tag{1.3}$$

where c_{ew} is a far field entrainment coefficient. For a jet-exit centre streamline trajectory, it is recommended that $(3/c_{ew})^{1/3} = 2.1$. In the near field, for $y/d \gg 1$ and $y/rd \ll 1$, the centerline trajectory obeys a 1/2 power law:

$$\frac{y}{rd} = \left(\frac{2}{c_{ej}} \frac{x}{rd} \right)^{1/2}, \tag{1.4}$$

where c_{ej} denotes a near-field entrainment coefficient. For a jet-exit centre streamline trajectory, a rough estimate is given by $c_{ej} = 0.32$. Unfortunately, these equations are not universally valid. Especially, by neglecting pressure forces on the jet during the derivation, the near-field equation (1.4) turns out to be only useful for very high r, that is, $r \geq 20$.

From the discussion so far, it is clear that the far-field trajectory most likely follows a 1/3 power law, i.e., $B = 1/3$, while the behavior at the near field remains still controversial. Even for far-field correlations, ambiguity over the constant A exists. Bearing such uncertainty in mind, we use jet trajectories only as a secondary measure to check the validity of the calculated results. Comparison of our jet trajectories against a few previously reported ones is made to show that our trajectories are within a reasonable range.

1.1.3 Vorticity introduction and evolution

The flow field of a transverse jet presents subtle physical issues to be resolved. The origin of the counter-rotating vortex pair has been one of the most central issues. Differing accounts of the mechanism by which the counter-rotating vortices form still persist. Recent experimental works [33, 44] suggest that the counter-rotating vortex pair is initiated just above the jet exit as jet shear layer vorticity folds onto itself and Kelvin-Helmholtz instability leads to a simultaneous roll-up. A water-tunnel dye visualization of the folding shear layer is shown in Figure 1-4. The resulting flow pattern can be interpreted as the tilting and folding of vortex rings as they are ejected from the nozzle, where the downstream side of each vortex ring is approximately aligned with the jet trajectory. A slightly different mechanism in [76] points to quasi-steady 'hanging vortices' formed in the skewed mixing layers on lateral edges of the jet; the authors suggest that an adverse pressure gradient causes these vortices to break down into a weak counter-rotating vortex pair.

It should be noted that some researchers have also emphasized the formation of counter-rotating vortices is not purely due to the vorticity from the jet shear layer only. With their water-tunnel flow visualizations, Kelso *et al.* [33] suggest that the counter-rotating vortex pair also contains vorticity generated in the channel wall boundary layer. Since the circulation per unit length of the wall boundary layer is apparently small, that is, $1/r$ times that of the jet shear layer, the evolution of vorticity from the wall boundary layer was neglected in most recent investigations [12], while there was an attempt to partially include the effect by a reduced model [51]. These questions will be addressed in the present work through reconstructing vorticity flux boundary conditions.

1.2 Lagrangian vortex methods

We employ Lagrangian vortex methods to investigate transverse jets computationally. In this section, we briefly discuss how Lagrangian vortex methods fit in the context of our interest.

1.2.1 Advantages of vortex methods

Lagrangian vortex methods [14, 48] have been tools for computing complex fluid flows. Several of the computational advantages of these methods are:

1. While Eulerian methods introduce extra dispersion or dissipation, even in flows with zero velocity gradient, such errors are minimized during advection in Lagrangian vortex methods.

2. The condition of numerical stability is not restricted by the CFL condition.

3. The support of particle distribution remains a small fraction of the total volume of the flow field, determined by where vorticity is confined. The method is endowed with natural 'grid adaptivity', and hence the computational elements are utilized more efficiently.

4. The method provides a natural way to represent small vortical structures that arise at high Reynolds numbers.

The first two items are general advantages of Lagrangian schemes, including smoothed particle hydrodynamics. The others are specific to vortex methods. These advantages make Lagrangian vortex methods an attractive framework for dealing Lagrangian vorticity dynamics and hence physics of transverse jets. Vortex methods are well-suited for a flow with a relatively high Reynolds number for their ability to simulate convection without numerical diffusion. The inherent stability of vortex methods is also a great advantage in such demanding simulations of jets, where one needs to push the computational capability to its limit. In summary, a Lagrangian vortex method is practically one of the best solutions for the mechanistic study of transverse jets.

1.2.2 Theoretical implications

The previous discussion clearly shows how a vortex method practically fit for the study of transverse jets. On the other hand, we can also find theoretical implications on general strategies of numerical analysis: a Lagrangian vortex method serves

as a canonical example where a partial differential equation is converted into an integro-differential equation whose solution can be described by *measures* or even by *distributions*.

This viewpoint has been developed for decades by several researchers. Among them, the most notable one would be Cottet, who explicitly stated [13]:

> Starting from this remark, since the method is based on the explicit solution of the equation satisfied by the vorticity, it seems natural to look for estimates of the vorticity rather than the velocity. Therefore, we have to work in *distribution spaces* whose choice is made to:
>
> 1. give back a satisfactory control of the velocity in order to ensure stability in the nonlinear terms;
> 2. express properties of optimal accuracy for the approximation of continuous functions by *Dirac measures*.

Since this point has motivated one of the main these of the thesis, i.e., diffusion treated in distribution spaces, we shall expand it in the following. To make the discussion brief, we present vortex methods for the Euler equation in $\mathbf{R}^3$ only. The governing equations are given as follows:

$$\frac{D\boldsymbol{\omega}}{Dt} = \boldsymbol{\omega} \cdot \nabla \mathbf{u}, \tag{1.5}$$

and

$$\nabla \cdot \mathbf{u} = 0, \tag{1.6}$$

where $\boldsymbol{\omega} = \nabla \times \mathbf{u}$. For a sufficiently fast-decaying velocity field, $\mathbf{u}$ can be recovered from $\boldsymbol{\omega}$ by the Biot-Savart law:

$$\mathbf{u}(\mathbf{x}) = -\frac{1}{4\pi} \int_{\mathbf{R}^3} \frac{(\mathbf{x}-\mathbf{y}) \times \boldsymbol{\omega}(\mathbf{y})}{|\mathbf{x}-\mathbf{y}|^3} d\mathbf{y} = (\mathbf{K} \star \boldsymbol{\omega})(\mathbf{x}), \tag{1.7}$$

where the following notation is used:

$$(\mathbf{F} \star \mathbf{G})(\mathbf{x}) \equiv \int_{\mathbf{R}^3} \mathbf{F}(\mathbf{x}, \mathbf{y}) \times \mathbf{G}(\mathbf{y}) d\mathbf{y}, \tag{1.8}$$

and

$$\mathbf{K}(\mathbf{x},\mathbf{y}) = -\frac{1}{4\pi}\frac{\mathbf{x}-\mathbf{y}}{|\mathbf{x}-\mathbf{y}|^3}. \tag{1.9}$$

Since (1.9) is singular at $\mathbf{x} = \mathbf{y}$, essential steps of approximation in a vortex method include the following two successive approximations.

1. Desingularization:

   Rewrite (1.5) as

   $$\frac{D\boldsymbol{\omega}_\sigma}{Dt} = \boldsymbol{\omega}_\sigma \cdot \nabla \mathbf{u}_\sigma, \tag{1.10}$$

   where

   $$\mathbf{u}_\sigma(\mathbf{x}) = (\mathbf{K}_\sigma \star \boldsymbol{\omega}_\sigma)(\mathbf{x}). \tag{1.11}$$

   $\mathbf{K}_\sigma$ represents a desingularized version of (1.9), which is smooth.

2. Discretization:

   Discretize the initial vorticity field $\boldsymbol{\omega}(\cdot, 0)$ into δ distributions, i.e., Dirac measures.

Especially, it should be noted that the first step changes the Euler equation into an integro-differential equation with a smooth kernel $\mathbf{K}_\sigma$, allowing $\boldsymbol{\omega}_\sigma$ to be a measure only, which in turn enables the next step of discretization. Once this crucial transformation happens, it is irrelevant to take a function space as the basic space for analysis. Rather, more intuitive descriptions can be given in distribution spaces, where the computational elements are described by Dirac measures, i.e., δ distributions.

Such an idea has motivated the work given in this thesis: it is apparent that, just as in the treatment of convection, diffusion in Lagrangian vortex methods, should be treated in the same way, i.e., in distribution spaces. To this end, a diffusion scheme previously developed for vortex methods [64] is adopted in Chapter 2 and analyzed in Appendix A, as a distribution-based diffusion scheme. The success of the combination of distribution-based convection and diffusion in transverse jet simulations suggests that the same idea can be utilized in various applications.

1.3 Overview of the thesis

The present modeling efforts focus on coherent vortical structures present in the main flow. The present work accompanies the previous investigation of transverse jets in [51], where the impact of the jet shear layer on the formation of the counter-rotating vortex pair at high Reynolds number was primarily considered. The present work still differentiates itself from [51]: we are more interested in the vorticity dynamics at intermediate Reynolds number, where the wall boundary layer may be important as well as the jet shear layer. What we pursue is a mechanistic description of vorticity dynamics in the near field. For simplicity, we focus on incompressible flow, and for relevance to mixing in engineered systems, we consider $r \gg 1$. Our approach is based on Lagrangian vortex simulations, since vorticity dynamics is best described in the Lagrangian sense.

Chapter 2 describes a distribution-based approach to simulate diffusion in Lagrangian vortex methods. The redistribution method [64] is reinterpreted, and new interpolation kernels are constructed to incorporate diffusion. Numerical examples are also provided for validation of the scheme.

Chapter 3 begins with a discussion of vorticity transport in inviscid, incompressible flows, presenting three-dimensional vortex particle methods and details of our filament construction. Vorticity flux boundary conditions are formulated for the transverse jet. Our new vorticity flux boundary conditions generalize the previous reduced formulation provided in [51] to incorporate the full no-slip boundary condition on the wall.

Chapter 4 presents simulation results revealing mechanisms of vorticity transformation in the transverse jet. We describe the formation and eventual breakdown of vortical structures, discussing our results in the context of earlier experimental, theoretical, and computational studies. We also describe the interaction between the wall boundary layer and the jet.

Conclusions and a sketch of future work are given in Chapter 5.

Appendix A provides supplementary materials for Chapter 2, including a detailed

discussion of the convergence analysis of the redistribution method based on the theory of distributions.

Appendices B and C are attached to report achievements made in partially related topics, i.e., the development of an adaptive tree-code for a high-order algebraic kernel and the investigation on convergence issues of algebraic kernels in the context of vortex simulations.

Figure 1-1: Union Pacific train, engine number 7006, engine type 4-8-2. Photographed near Denver, Colorado on November 30, 1929. This image (OP-18695) is from the collection of the photographs of the late Otto Perry (1894–1970) held at the Western History Department of the Denver Public Library, and is copyrighted. The department actively encourages fair use of its images for educational, scholarly purposes and private study, for which the inclusion of the picture in this thesis is qualified.

Figure 1-2: An artist's conception of the Advanced Tactical Fighter (ATF) aircraft proposed by Boeing Military Airplane Company (National Archive Number: NN33300514 2005-06-30). This image is a work of a U.S. military or Department of Defense employee, taken or made during the course of the employee's official duties. As a work of the U.S. federal government, the image is in the public domain.

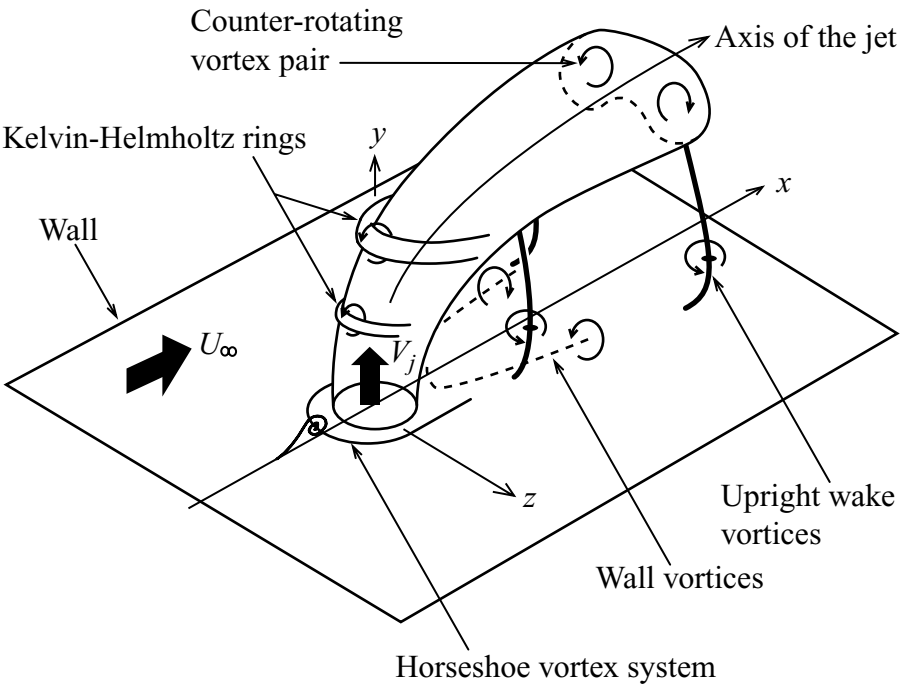

Figure 1-3: Schematic diagram showing vortical structures of a transverse jet. Based on the diagram in [33], major modification is made to show the Kelvin-Helmholtz rings on the windward side explicitly. Upright wake vortices are not expected at conditions considered here. Reprinted with the permission of Cambridge University Press (invoice number: P03J 13028).

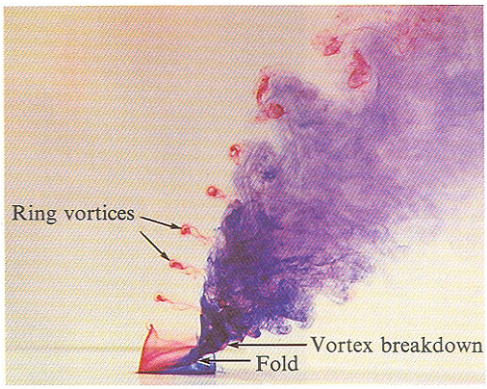

Figure 1-4: Behavior of the jet shear layer for $r = 4.0$ at $Re_\infty = 1600$ and $\delta/d = 0.61$. Reproduced from [33]. Blue dye is injected from the circumferential slot in the pipe and red dye is released from the dye injection port. Reprinted with the permission of Cambridge University Press (invoice number: P03J 13028).

Chapter 2

Distribution-based Diffusion Scheme

2.1 Background

While Lagrangian vortex methods were originally formulated for inviscid flows, successful approaches for viscous flows have been proposed [11, 16, 17, 19, 59, 61]. In some methods, such as random walk [11] and diffusion velocity methods [19], particles are transported while their strength remains fixed. In other methods, the strength assigned to each particle is allowed to change without displacing the particles. In many cases, more particles are introduced to capture the expanding region where vorticity is confined.

One popular algorithm is the PSE (particle strength exchange) scheme [17], in which the diffusion equation is converted into integro-differential equations, which are discretized in space by approximating the integral using a quadrature rule. The semi-discrete equations are again discretized in time in various different ways–implicitly or explicitly–up to whatever order of accuracy is desired. This method has been successfully applied to several complex flows [39, 56, 70, 74], and has been extended to the case of anisotropic diffusion [18], and to the case with spatially variable radius of the core function [15].

The use of a quadrature rule in PSE requires relatively uniform particle distri-

bution, and this naturally necessitates frequent remeshing. Remeshing is also implemented in other methods, even in inviscid simulations to satisfy other conditions. For instance, it has been observed that long-time accuracy of convection computation deteriorates severely due to the distortion of the particle distribution [14, 24]. Several local regridding schemes have been devised to solve this problem, by inserting new particles where inter-particle distance becomes too large [36, 37, 74]. These schemes are limited to geometrically simple flows, and tend to grow the number of particles rapidly, unless careful clustering and merging is also implemented. For these reasons, global remeshing is now considered necessary in most Lagrangian particle methods, and the design and verification of various remeshing schemes have become an active research area [4, 9].

Here, we design a scheme that treats diffusion and remeshing simultaneously and without additional ambiguity or computational overhead. The scheme, 'redistribution onto a grid,' will be formulated as an extension of the vorticity redistribution method [64], and cast in the form of interpolation kernels, which resemble those used in inviscid remeshing [14, 38]. The construction of the method is based on the discretization of the vorticity field into δ distributions, and the analysis of the method is performed in distribution spaces accordingly, which is separately presented in Appendix A for clarity of exposition.

The chapter is organized as follows. In Section 2.2, the vorticity redistribution method is introduced. Next, we develop the modified interpolation kernels in Section 2.3. The error characteristics and the stability properties of these kernels are investigated in Section 2.4. We finally provide numerical examples in Section 2.5.

2.2 A distribution-based diffusion scheme – the redistribution method

The vorticity redistribution method, or simply the redistribution method, developed in [64] is a deterministic approach to solve the constant-diffusivity diffusion equation.

In this method, the fundamental solution of the diffusion equation for each particle vorticity is approximated by a new set of particles within a ball of a finite radius, whose locations and strengths are determined by satisfying a number of 'predictive moment matching conditions.' The latter enforce the requirement that the vorticity assigned to the new particles have approximately the same moments, up to a certain order, as the moments of the fundamental solution generated by the source particle. The new particle vorticity is obtained by redistributing the source particle strength onto the target particles, i.e., by transferring fractions of the source particle strength to the target particles nearby. The spatial resolution of the method is naturally defined by the redistribution radius, that is, the radius of the ball in which the target particles for each source particle lie.

How to obtain a redistribution formula that determines the correct redistribution fractions that satisfy the predictive moment matching conditions depends on the specific problem of interest. When the fundamental solution of the diffusion equation is known explicitly, the moments of the fundamental solution can be exactly determined, and the corresponding redistribution formula can be easily constructed [64]. However, for spatially varying or anisotropic diffusion, the explicit form of the fundamental solution is often not available. To address this difficulty, a more general method to design redistribution formulae satisfying the moment matching conditions was proposed [23, 63], in which the evolution equations for the moments of the fundamental solution of each source particle were discretized by explicit integration schemes, such as the forward Euler scheme. The redistribution formulae were obtained by applying the particle approximation to evaluate the resulting integrals. This method, referred as the Galerkin formulation [41], is more general, and hence we briefly describe it in this section.

Consider the one-dimensional heat equation with spatially dependent conductivity, $\nu(x)$, as in [63]:

$$\mathcal{L}u \equiv \frac{\partial u}{\partial t} - \frac{\partial}{\partial x}\left(\nu(x)\frac{\partial u}{\partial x}\right) = 0, \tag{2.1}$$

where u is the temperature, and the spatial variable is x. We assume that $\nu(x)$ is

positive and its pointwise value and derivatives up to the 2nd order are uniformly bounded. $\mathcal{L}$ has a fundamental solution $Z(x, \xi, t, \tau)$ that satisfies the equation

$$\mathcal{L}(x, t, \partial_x, \partial_t) Z(x, \xi, t, \tau) = \delta(x - \xi)\delta(t - \tau). \tag{2.2}$$

The particle approximation consists of the discrete sum of δ distributions, i.e.,

$$\underline{u}^n = \sum_{i=1}^{N} \Gamma_i^n \delta(x - x_i^n), \tag{2.3}$$

where x_i^n denotes the location of the ith particle at the nth time step, and Γ_i^n is its strength. At $t = 0$, $\Gamma_i^0 = u(x_i^0)\Delta x$, where x_i^0 is the initial location of the ith particle. The initial locations of the particles are assumed to be distributed over the support of the initial temperature field with an equal spacing Δx. In $\mathbf{R}^d$, at each time step, for each source particle, we define the $\mathbf{k}$th moment of the fundamental solution, $G_{\mathbf{k},i}^n$, and its approximation, $\underline{G}_{\mathbf{k},i}^n$, as follows.

$$G_{\mathbf{k},i}^n = \int_{\mathbf{R}^d} (\mathbf{x} - \mathbf{x}_i^{n-1})^{\mathbf{k}} Z(\mathbf{x}, \mathbf{x}_i^{n-1}, \Delta t_d, 0) dx, \tag{2.4}$$

and

$$\underline{G}_{\mathbf{k},i}^n = \int_{\mathbf{R}^d} \left(\sum_{j=1}^{N} f_{ij}^n \delta(\mathbf{x} - \mathbf{x}_j^n) \right) (\mathbf{x} - \mathbf{x}_i^{n-1})^{\mathbf{k}} dx = \sum_{j=1}^{N} f_{ij}^n (\mathbf{x}_j^n - \mathbf{x}_i^{n-1})^{\mathbf{k}}. \tag{2.5}$$

f_{ij}^n is the redistribution fraction, that is, the fraction of the strength of the ith particle transferred to the jth particle at the nth time step. We use standard notations, i.e., $\mathbf{x}^{\mathbf{k}} = x_1^{k_1} x_2^{k_2} x_3^{k_3} \cdots x_d^{k_d}$, and $|\mathbf{k}| = k_1 + k_2 + k_3 + \cdots + k_d$, where d is the dimension of the space. In this one-dimensional problem, $d = 1$, and hence, $\mathbf{x}^{\mathbf{k}} = x^k$, and $|\mathbf{k}| = k$. Δt_d is the time step. (2.4) and (2.5) are given as follows in $\mathbf{R}$:

$$G_{k,i}^n = \int_{\mathbf{R}} (x - x_i^{n-1})^k Z(x, x_i^{n-1}, \Delta t_d, 0) dx, \tag{2.6}$$

and

$$\underline{G}^n_{k,i} = \int_{\mathbf{R}} \left(\sum_{j=1}^{N} f^n_{ij} \delta(x - x^n_j) \right) (x - x^{n-1}_i)^k dx = \sum_{j=1}^{N} f^n_{ij} (x^n_j - x^{n-1}_i)^k. \tag{2.7}$$

Next, multiplying (2.1) by $(x - x_i^{n-1})^k$ and integrating by parts, the evolution equations for $G^n_{k,i}$, where $0 \leq k \leq 2$, can be obtained:

$$\begin{aligned}
\frac{dG^n_{0,i}}{dt} &= \frac{d}{dt} \int_{\mathbf{R}} Z(x, x_i^{n-1}, t, 0) dx \\
&= \int_{\mathbf{R}} \frac{\partial Z}{\partial t} dx = \int_{\mathbf{R}} \frac{\partial}{\partial x} \left(\nu(x) \frac{\partial Z}{\partial x} \right) dx = 0, \\
\frac{dG^n_{1,i}}{dt} &= \frac{d}{dt} \int_{\mathbf{R}} Z(x, x_i^{n-1}, t, 0)(x - x_i^{n-1}) dx \\
&= \int_{\mathbf{R}} \frac{\partial Z}{\partial t} (x - x_i^{n-1}) dx = \int_{\mathbf{R}} \frac{\partial}{\partial x} \left(\nu(x) \frac{\partial Z}{\partial x} \right) (x - x_i^{n-1}) dx \\
&= \int_{\mathbf{R}} Z(x, x_i^{n-1}, t, 0) \frac{d\nu}{dx} dx, \\
\frac{dG^n_{2,i}}{dt} &= \frac{d}{dt} \int_{\mathbf{R}} Z(x, x_i^{n-1}, t, 0)(x - x_i^{n-1})^2 dx \\
&= \int_{\mathbf{R}} \frac{\partial Z}{\partial t} (x - x_i^{n-1})^2 dx = \int_{\mathbf{R}} \frac{\partial}{\partial x} \left(\nu(x) \frac{\partial Z}{\partial x} \right) (x - x_i^{n-1})^2 dx \\
&= 2 \int_{\mathbf{R}} Z(x, x_i^{n-1}, t, 0) \left(\nu(x) + (x - x_i^{n-1}) \frac{d\nu}{dx} \right) dx.
\end{aligned} \tag{2.8}$$

The redistribution formulae are designed by discretizing these equations using the forward Euler scheme and utilizing the following expression for particle distribution:

$$\begin{aligned}
\underline{u}^{n-1} &= \sum_{i=1}^{N} \Gamma^{n-1}_i \delta(x - x^{n-1}_i), \\
\underline{u}^{n} &= \sum_{i=1}^{N} \Gamma^{n}_i \delta(x - x^{n}_i) = \sum_{i=1}^{N} \Gamma^{n-1}_i \left(\sum_{j=1}^{N} f^n_{ij} \delta(x - x^n_j) \right).
\end{aligned} \tag{2.9}$$

The outcomes are the discrete equations describing the evolution of $\underline{G}^n_{k,i}$ expressed in terms of f^n_{ij}:

$$
\begin{aligned}
\frac{\underline{G}^n_{0,i} - \underline{G}^{n-1}_{0,i}}{\Delta t_d} &= \frac{1}{\Delta t_d}\left(\sum_j f^n_{ij} - 1\right) = 0, \\
\frac{\underline{G}^n_{1,i} - \underline{G}^{n-1}_{1,i}}{\Delta t_d} &= \frac{1}{\Delta t_d}\sum_j f^n_{ij}(x^n_j - x^{n-1}_i) \\
&= \int_{\mathbf{R}} Z(x, x^{n-1}_i, 0, 0)\frac{d\nu}{dx}dx = \left(\frac{d\nu}{dx}\right)_{x=x^{n-1}_i}, \\
\frac{\underline{G}^n_{2,i} - \underline{G}^{n-1}_{2,i}}{\Delta t_d} &= \frac{1}{\Delta t_d}\sum_j f^n_{ij}(x^n_j - x^{n-1}_i)^2 \\
&= 2\int_{\mathbf{R}} Z(x, x^{n-1}_i, 0, 0)\left(\nu(x) + (x - x^{n-1}_i)\frac{d\nu}{dx}\right)dx \\
&= 2\nu(x^{n-1}_i).
\end{aligned}
\tag{2.10}
$$

Therefore, the corresponding redistribution formulae for f^n_{ij} are:

$$
\begin{aligned}
\sum_j f^n_{ij} &= 1, \\
\sum_j f^n_{ij}(x^n_j - x^{n-1}_i) &= \left(\frac{d\nu}{dx}\right)_{x=x^{n-1}_i}\Delta t_d, \\
\sum_j f^n_{ij}(x^n_j - x^{n-1}_i)^2 &= 2\nu(x^{n-1}_i)\Delta t_d.
\end{aligned}
\tag{2.11}
$$

Assuming that the redistribution radius scales as $O(\Delta t_d^{1/2})$, it can be shown that the global truncation error of scheme (2.11) behaves as $O(\Delta t_d^{1/2-\epsilon})$, where ϵ is a small positive real number, as shown in Appendix A. The procedure works in the same way for higher-order spatial accuracy [23]. The redistribution formulae (2.11) reduce to those in [64] for the case of constant diffusivity.

2.3 Redistribution onto a uniform grid – modified interpolation kernels

To determine f_{ij}^n from the given redistribution formulae, we need to specify the target particle locations x_i^n. In the original treatment [64], the neighboring particles of each source particle were chosen as the target particles, i.e., the set of x_i^{n-1} and that of x_i^n were taken to be the same. More particles were introduced if the number of neighboring particles was not sufficient to achieve the desired accuracy. Although this approach makes the entire process grid-free, the complex procedure necessary to deal with the arbitrariness of the number and the locations of the target particles makes the original redistribution method expensive, especially in three-dimensional simulations where the number of particles easily reaches several millions. In this section, we provide an alternative formulation to address this difficulty.

From the formulation described in the previous section, the following fact can be easily recognized: it is not necessary to keep the same particle locations before and after each redistribution step, i.e., the set of x_i^{n-1} and that of x_i^n in (2.9) need not be the same. For example, we can simply take a set of uniform grid points as the target particle locations to develop a redistribution formula for each source particle. In that case, the arbitrariness in the number and locations of target particles is eliminated, and the complex procedure of finding the fractions is replaced by a much simpler one.

Since multi-dimensional generalization is straightforward, we consider the one-dimensional case first. We concentrate on the case of constant diffusivity first. Suppose we have an equally-spaced grid, located at $x = -\Delta x$, 0, and Δx. We interpret these grid points as the target particle locations, i.e., $x_1 = -\Delta x,\ x_2 = 0$, and $x_3 = \Delta x$. Given that a source particle is located at $x = x_0$, where $|x_0| < \frac{\Delta x}{2}$, the corresponding

redistribution formula, to the lowest order in $\mathbf{R}$, is given by:

$$\begin{aligned} \sum_{j=1}^{3} f_{0j} &= 1, \\ \sum_{j=1}^{3} f_{0j}(x_j - x_0) &= 0, \\ \sum_{j=1}^{3} f_{0j}(x_j - x_0)^2 &= 2\nu\Delta t_d. \end{aligned} \tag{2.12}$$

Solving these equations explicitly, we obtain the following redistribution fractions.

$$\begin{aligned} f_{01} &= \frac{2\nu\Delta t_d - x_0\Delta x + x_0^2}{2\Delta x^2}, \\ f_{02} &= \frac{\Delta x^2 - 2\nu\Delta t_d - x_0^2}{\Delta x^2}, \\ f_{03} &= \frac{2\nu\Delta t_d + x_0\Delta x + x_0^2}{2\Delta x^2}. \end{aligned} \tag{2.13}$$

Although these expressions are enough for implementation, rewriting them in the form of an interpolation kernel is more convenient for further discussion. For a given particle distribution $\underline{u}^n$ in the form of (2.3), we define the interpolated particle distribution $\underline{u}^{n+1}$ as

$$\begin{aligned} \underline{u}^{n+1}(x) &= \sum_{j\in\mathbf{Z}} \delta(x - j\Delta x) \int_{\mathbf{R}} \lambda\left(\frac{j\Delta x - x'}{\Delta x}\right) \underline{u}^n(x')dx' \\ &= \sum_{i=1}^{N} \Gamma_i^n \left(\sum_{j\in\mathbf{Z}} \lambda\left(\frac{j\Delta x - x_i^n}{\Delta x}\right) \delta(x - j\Delta x)\right). \end{aligned} \tag{2.14}$$

The interpolated particle distribution has particles only at $x = j\Delta x$, where $j \in \mathbf{Z}$. We call λ the interpolation kernel, since it relates the initial particle distribution and the interpolated distribution. Usually λ is of compact support. Thus the interpolation of a particle is only done over its nearest grid points. Since (2.14) exhibits some

similarity to (2.9), we can easily convert (2.13) to the following interpolation kernel:

$$\Lambda_2(\xi,c)=\begin{cases}\frac{1}{2}(1-|\xi|)(2-|\xi|)+c^2 & : \quad \frac{1}{2}\le|\xi|<\frac{3}{2}\\ 1-|\xi|^2-2c^2 & : \quad |\xi|<\frac{1}{2}\\ 0 & : \quad \frac{3}{2}\le|\xi|\end{cases} \tag{2.15}$$

where $c=\sqrt{\nu\Delta t_d}/\Delta x$. The corresponding redistribution formulae approximate the diffusion process with a global truncation error $O(h)$, where $h=\sqrt{\Delta t_d}$ [64], if c is kept constant during refinement. The notation Λ_2 has been chosen intentionally. This expression yields one of the classical 'inviscid' interpolation kernels given in [14] at the limit of $c\to 0$, where it was also denoted as Λ_2. One may realize that Λ_2 becomes the TSC (triangular-shaped cloud) interpolation kernel when $c^2=1/8$. This fact can be used to estimate the effective kinematic viscosity induced by the numerical diffusion when one uses the TSC interpolation kernel for remeshing.

The procedure given above can be generalized to other kernels. Two of the most widely used interpolation kernels, Λ_3 and M_4', can also be extended to account for diffusion as follows.

$$\Lambda_3(\xi,c)=\begin{cases}1-2c^2+|\xi|\left(3c^2-\frac{1}{2}\right)-\xi^2+\frac{|\xi|^3}{2} & : \quad |\xi|<1\\ (2-|\xi|)\left(\frac{1}{6}(3-|\xi|)(1-|\xi|)+c^2\right) & : \quad 1\le|\xi|<2\\ 0 & : \quad 2\le|\xi|\end{cases} \tag{2.16}$$

and

$$M_4'(\xi,c)=\begin{cases}1-\frac{5\xi^2}{2}+\frac{3|\xi|^3}{2}-c^2\left(2-9\xi^2+6|\xi|^3\right) & : \quad |\xi|<1\\ \frac{1}{2}(2-|\xi|)^2(1-|\xi|-2c^2+4c^2|\xi|) & : \quad 1\le|\xi|<2\\ 0 & : \quad 2\le|\xi|\end{cases} \tag{2.17}$$

Λ_3 is continuous, and $M_4'\in C^1(\mathbf{R})$. Λ_3 approximates the diffusion process with a global truncation error $O(h^2)$, and M_4', $O(h)$. When $c^2=1/6$, these two kernels coincide.

So far, we have discussed the one-dimensional cases only. The multi-dimensional

generalization of these interpolation kernels can be achieved in a trivial way for a uniform Cartesian grid. One can obtain redistribution fractions in $\mathbf{R}^d$ simply by using the tensor product of the redistribution fractions obtained by the interpolation kernel acting on each coordinate. The resulting redistribution fractions automatically satisfy the redistribution formulae given in [64].

The idea of redistributing particle strength onto uniform grid points can also be applied to the case of variable diffusivity. Here, we present the interpolation kernel satisfying (2.11).

$$
\begin{aligned}
&\Lambda_3'(\xi, c, d_\nu) \\
&\quad = \begin{cases}
\frac{1}{6}(2-\xi)\left(6c^2 + 3d_\nu(2-\xi) + (1-\xi)(3-\xi)\right) & : \ 1 \le \xi < 2 \\
\frac{1}{2}\left(2 + 2c^2(3\xi - 2) - \xi\left(1 - \xi(\xi-2) - d_\nu(4-3\xi)\right)\right) & : \ 0 \le \xi < 1 \\
\frac{1}{2}\left(2 - 2c^2(3\xi + 2) + \xi\left(1 - \xi(\xi+2) + d_\nu(4+3\xi)\right)\right) & : -1 \le \xi < 0 \\
\frac{1}{6}(2+\xi)\left(6c^2 - 3d_\nu(2+\xi) + (1+\xi)(3+\xi)\right) & : -2 < \xi < -1 \\
0 & : \quad 2 \le |\xi|
\end{cases}
\end{aligned}
\tag{2.18}
$$

where $c^2 = \nu \Delta t_d / \Delta x^2$ and $d_\nu = \frac{\Delta t_d}{\Delta x} \frac{\partial \nu}{\partial x}$. ν and $\frac{\partial \nu}{\partial x}$ should be evaluated at the source particle location. Because only three equations are available in (2.11), while there are four unknown redistribution fractions, we imposed an additional condition for the third order moment, i.e., $\sum_j f_{ij}^n (x_j^n - x_i^{n-1})^3 = d_\nu \Delta x^3$. The resulting kernel is continuous, and approximates the diffusion process with a global truncation error $O(h^{M'})$ for all $M' < 1$, as shown in Appendix A. As the notation implies, this expression gives Λ_3 in (2.16) when $d_\nu = 0$.

Again, multi-dimensional generalization can be made simply by taking tensor products. The procedure of multi-dimensional generalization gives redistribution formulae which are different from those obtained directly from the Galerkin formulation given in [23]. For instance, in $\mathbf{R}^2$, for $k_1 = k_2 = 1$, $\underline{G}_{k,i}^n$ is $O(h^4)$ if it is obtained by taking tensor products. On the other hand, according to [23], $\underline{G}_{k,i}^n$ must be exactly zero under the same condition. However, as one can clearly see in this example, the difference only contributes at a higher order than the error considered, hence these

two different formulae are equivalent within the error considered.

The actual implementation of these interpolation kernels to simulate diffusion in vortex methods is a straightforward generalization of the original redistribution method [64]. To solve the Navier-Stokes equation in the velocity-vorticity formulation, we employ the viscous splitting algorithm [14, 48]: the evolution of the flow field is considered in discrete time steps. In each step, the vortex elements are first convected, and then diffused by interpolation, i.e., the algorithm consists of substeps where the convective and the diffusive effects are considered separately. In this way, the computational advantages of Lagrangian vortex methods, that is, minimal dispersion/dissipation during the computation of convection, no restriction from the CFL condition, and optimal utilization of computational elements, are automatically inherited without being compromised, because convection is still dealt with in completely Lagrangian way.

It is convenient to define appropriate notations for different step sizes, because the time step for diffusion is often chosen as a multiple of that for convection at high Reynolds number. Thus, from here on, the convection time step size is denoted by Δt_c, while the diffusion time step size is denoted by Δt_d. If there is no need to distinguish between different time steps, as in Appendix A, we use Δt as Δt_d.

Due to the core overlap condition imposed during the convection substep, the grid size for interpolation, Δx, should be chosen such that $\Delta x < \sigma$, where σ is the radius of the core function. The choice of Δt_d and Δx is further restricted by the stability bound on c^2 associated with each interpolation kernel. These stability bounds will be discussed in Section 2.4. To meet all these conditions simultaneously, one may first decide on σ by considering the spatial resolution required for the solution, and then decide on a value of Δx that satisfies the overlap condition. After that, Δt_d can be chosen as a multiple of Δt_c in the range of valid values for Δt_d, which should be decided by stability consideration.

We note that the use of these interpolation kernels for treating diffusion has the following advantages. First, the use of a uniform grid eliminates the expensive linear optimization process used to find the fraction in the original redistribution scheme,

and results in a very efficient diffusion scheme. The high computational load resulting from the optimization process was one of the most critical weaknesses of the original vorticity redistribution method [14]. The second is its simplicity. An inviscid vortex code can be expanded easily to treat viscous flows. If the code already has a routine for remeshing onto a uniform grid, simply modifying the kernel leads to a viscous flow code. Finally, the two processes, remeshing and diffusion, are treated in one step in such a way that the dispersive errors introduced by remeshing are controlled by the concomitant diffusion process, and provides an easy way to guarantee the stability of remeshing.

On the other hand, there are several potential weaknesses. The application of the method might require the generation of a large data set for the storage of the grid points, as in other implementations of global remeshing. However, only the grid points near the support of the particle distribution are relevant. If the support of particle distribution is large, one may still avoid the problem of generating a large data array by partitioning particles into several small clusters and performing interpolation for each cluster separately. An elegant strategy of tree-structured grid storage is available [75], and can be easily adopted for the current scheme. The order of approximation of the interpolation kernels presented here is relatively low. Λ_3, which has the highest order among the interpolation kernels given, is first-order in time and second-order in space. However, constructing higher-order interpolation kernels is possible, though we do not pursue it in this paper.

We end this section with few comments concerning the relation between the method proposed here and other diffusion simulation approaches. The first is the finite difference method. One may treat diffusion and remeshing by first performing remeshing through an inviscid interpolation kernel, then by applying an explicit finite difference scheme on the remeshed particle distribution. Such a two-step approach is valid, but there are differences between this and our one-step approach. The two-step approach does not in general yield particle distribution identical to that obtained by the modified interpolation kernels. For instance, suppose that we have only one source particle initially. If one first applies the inviscid Λ_3 to this particle and then

uses the three-point centered finite difference formula in space and the explicit Euler scheme in time to treat diffusion, the support of resulting particle distribution covers six grid points in general, which is larger than that covered by the modified Λ_3. If one uses the four-point one-sided finite difference formulae for the outermost remeshed particles to limit the support of resulting particle distribution, some of moment conditions are violated. Actually, Λ_3 given here represents the only particle distribution covering four points with all the moments up to the third order correct. Our one-step approach usually results in more efficient utilization of grid points.

We also note that a similar idea of using a grid to simulate diffusion was proposed in [46]. However, this early treatment was based on the concept of resampling [14], i.e., the redistribution fraction onto each grid point is determined by the local value of the fundamental solution, not by matching the moments. Since each moment corresponds to an integral property such as the total circulation, the current scheme has better conservation properties. For example, the current method preserves the linear impulse in the case of constant diffusivity, where the method in [46] cannot. Finally, we note that the use of a quadrature rule and the nature of semi-discretization make it conceptually difficult to incorporate the idea of remeshing within PSE directly. This is one reason why the discussion has been made on the basis of the redistribution method.

2.4 Error analysis of interpolation kernels

In this section, we analyze the error characteristics of the extended interpolation kernels presented in the previous section. The purpose of this analysis is to obtain the stability bound of each kernel. We discuss the dissipative or dispersive characteristics of the error for the low-frequency modes. Since the high-frequency modes are all well damped. We also show that the dispersive nature of these interpolation kernels is changed by the addition of diffusion.

To this end, we consider the one-dimensional linear advection-diffusion equation

with constant flow speed U, i.e.,

$$\frac{\partial u}{\partial t} + U\frac{\partial u}{\partial x} = \nu\frac{\partial^2 u}{\partial x^2}. \tag{2.19}$$

If we employ a typical operator splitting algorithm, the advection step is solved by particle methods without introducing any additional error at each time step. One can simply discretize the initial condition using particles, and displace the particles to obtain the field at any time instance. The error is introduced during the diffusion step, or equivalently during the remeshing step, by the application of an interpolation kernel.

Let Δt be the time step for interpolation and Δx be the grid size. We denote $x_j = j\Delta x$ as the fixed location of the jth grid point and $\underline{u}_j^n$ as the strength of the particle located at x_j immediately following the nth remeshing step. We assume for convenience that $0 < C \equiv \frac{U\Delta t}{\Delta x} < \frac{1}{2}$. Since interpolation is made onto the nearest grid points of the source particle, $U\Delta t$ can be arbitrarily large. This restriction makes it possible to interpret the resulting evolution equation of $\underline{u}_j$ as an Eulerian scheme, making the analysis easier. The results obtained from this analysis are not affected by the removal of this restriction, since we can always use a transform $x' = x - nt\Delta x/\Delta t$, where n is chosen such that the flow speed measured in the new coordinate system satisfies the restriction.

We first consider Λ_2. Since particles are always remeshed onto the uniform grid points at the end of the step, the position of the jth particle at the beginning of a new time step is x_j. In the advection step, the particles are displaced by $U\Delta t$, i.e., $\tilde{x}_j^n = x_j + U\Delta t$, and $\tilde{u}_j^n = \underline{u}_j^n$, where $\tilde{x}_j$ is the location of the displaced jth particle, and $\tilde{u}_j$ is its strength. In the remeshing step, the displaced particles are interpolated onto the uniform grid points. Thus, we have

$$\begin{aligned}\underline{u}_j^{n+1} = \underline{u}_{j-1}^n \Lambda_2\left(\frac{x_j - \tilde{x}_{j-1}^n}{\Delta x}, c\right) \\ + \underline{u}_j^n \Lambda_2\left(\frac{x_j - \tilde{x}_j^n}{\Delta x}, c\right) + \underline{u}_{j+1}^n \Lambda_2\left(\frac{x_j - \tilde{x}_{j+1}^n}{\Delta x}, c\right)\end{aligned} \tag{2.20}$$

Again, $c = \frac{\sqrt{\nu \Delta t}}{\Delta x}$. This formula actually gives the Lax-Wendroff scheme when $c^2 = 0$.

To analyze the error characteristics from this expression, one usually calculates the amplification factor and the phase speed error [10]. The analysis is performed in the wavenumber space. We take the Fourier transform of (2.20) using the following substitution.

$$\underline{u}_j^n = \sum_\theta \underline{v}_\theta^n e^{ij\theta}, \tag{2.21}$$

where $i = \sqrt{-1}$, and $\theta = 2\pi k \Delta x$. Reorganizing (2.20) by using this substitution, we can find

$$\underline{v}_\theta^{n+1} = g(C, c, \theta) \underline{v}_\theta^n, \tag{2.22}$$

where

$$g(C, c, \theta) = 1 - c^2 - C^2 + \left(c^2 + \frac{C^2}{2} + \frac{C}{2} \right) e^{-i\theta} + \left(c^2 + \frac{C^2}{2} - \frac{C}{2} \right) e^{i\theta}. \tag{2.23}$$

From this amplification factor, we first obtain the stability bound. In practice, particles can be placed anywhere, and hence we do not have any control over C and θ. Thus, we need to obtain the range of c where $|g(C, c, \theta)| \leq 1$ for all $0 \leq C \leq 1/2$ and $0 \leq \theta \leq 2\pi$. Either analytically or numerically, we can compute $|g(C, c, \theta)|^2$ to obtain this range of valid c. For Λ_2, the range of valid c is $c^2 \leq 3/8$. Within this range, the l^2 norm of the discretized field variable is decreased by the application of Λ_2.

To analyze the error characteristics of the low-frequency modes, we compare the effect of dispersion and that of dissipation, in an order of magnitude sense. The exact solution in the wavenumber space is given by:

$$v_\theta^{n+1} = e^{-i2\pi k U \Delta t - 4\pi^2 \nu k^2 \Delta t} \underline{v}_\theta^n = e^{-iC\theta - c^2\theta^2} \underline{v}_\theta^n. \tag{2.24}$$

This implies that the rate of norm decay and the phase speed error should be analyzed in the following way.

$$g(C, c, \theta) = e^{-iC\theta + iA(C,c,\theta) - c^2\theta^2 - B(C,c,\theta)}, \tag{2.25}$$

where $A(C, c, \theta)$ represents the phase speed error and hence the dispersive effect, and $B(C, c, \theta)$ represents the rate of additional norm decay and hence the effect of numerical dissipation. It is hard to get exact expressions of $A(C, c, \theta)$ and $B(C, c, \theta)$, but we can get the following asymptotic formulae for the leading order terms by taking the logarithm of (2.23) and expanding it in series.

$$\begin{aligned} A(C, c, \theta) &= \frac{1}{6} C(1 - 6c^2 - C^2)\theta^3 + O(\theta^5), \\ B(C, c, \theta) &= \frac{1}{24}\left(12c^4 - 3C^2(C^2 - 1) - 2c^2(1 + 6C^2)\right)\theta^4 + O(\theta^6). \end{aligned} \tag{2.26}$$

This analysis shows that the leading order error induced by the application of Λ_2 is strictly dominated by its dispersive component at the low-frequency regimes, i.e., as $\theta \to 0$. When $c^2 \leq 1/8$, the leading order term of $A(C, c, \theta)$ is greater than or equal to 0 for all $0 \leq C \leq 1/2$ and $0 \leq \theta \leq 2\pi$. Thus these low-frequency modes show lagging phase error, and induce spurious oscillations at the trailing edges of the wave packets [69, 71]. Especially when c^2 is very small, these unphysical oscillations can survive dissipation for a time long enough to couple with other parts of the equations in more complex equations, e.g., the Euler equation or the Navier-Stokes equation at high Reynolds number.

If the equation of interest is extremely sensitive to such spurious oscillations, one may completely suppress these oscillations by enforcing the monotonicity preservation condition [43, 71]. To achieve this, one can simply adjust c^2 to make these interpolation kernels non-negative by choosing Δx and Δt_d appropriately. For Λ_2, when $1/8 \leq c^2 \leq 3/8$, the interpolation kernel is guaranteed to be non-negative everywhere. A non-negative interpolation kernel gives non-negative redistribution fractions, and hence makes the resulting scheme TVD, which guarantees the preservation of monotonicity [43, 71]. However, since these interpolation kernels have been successfully used with $c^2 = 0$ in many previous inviscid vortex simulations [38], we conclude that the use of non-negative interpolation kernels may not lead to serious instability in vortex simulations. In other applications, there are still possibilities that these spurious oscillations may be troublesome.

It is interesting to see that the dispersion relation can be significantly modified by the addition of diffusion: especially when $c^2 > 1/8$, the low frequency modes may show leading phase error for certain values of C. This threshold actually coincides with the lower bound of the range of c^2 yielding Λ_2 non-negative.

For Λ_3 and M_4', we only state the results briefly. For Λ_3, the amplification factor is given by

$$\begin{aligned} g(C,c,\theta) = C\left(c^2+\frac{1}{6}(C-1)(C+1)\right)e^{-2i\theta} \\ +\left(c^2+C-3c^2C+\frac{C^2}{2}-\frac{C^3}{2}\right)e^{-i\theta} \\ +1-2c^2-\frac{C}{2}+3c^2C-C^2+\frac{C^3}{2} \\ +(1-C)\left(c^2-\frac{1}{6}(2-C)C\right)e^{i\theta}. \end{aligned} \tag{2.27}$$

When $c^2 \le 1/2$, $|g(C,c,\theta)| \le 1$ for all $0 \le C \le 1/2$ and $0 \le \theta \le 2\pi$. This gives the stability bound as $c^2 \le 1/2$. We can also get the asymptotic expressions for $A(C,c,\theta)$ and $B(C,c,\theta)$.

$$\begin{aligned} A(C,c,\theta) &= \frac{1}{60}C(2+C-C^2-10c^2)(1-3C+2C^2)\theta^5+O(\theta^7), \\ B(C,c,\theta) &= \frac{1}{24}\left(12c^4-c^2(2+12C-12C^2)\right. \\ &\qquad \left.+C(2-C-2C^2+C^3)\right)\theta^4+O(\theta^6). \end{aligned} \tag{2.28}$$

For small values of c^2, the leading order term in $A(C,c,\theta)$ is greater than or equal to 0, and the application of Λ_3 may also result in spurious oscillations at the trailing edge. To suppress these oscillations completely, one can choose $1/6 \le c^2 \le 1/2$ to make Λ_3 non-negative.

For M_4', we get

$$\begin{aligned} g(C,c,\theta) = &\left(3c^2C^2 - 2c^2C^3 - \frac{C^2}{2} + \frac{C^3}{2}\right)e^{-2i\theta} \\ &+ \left(c^2 + \frac{C}{2} + 2C^2 - 9c^2C^2 - \frac{3}{2}C^3 + 6c^2C^3\right)e^{-i\theta} \\ &+ 1 - 2c^2 - \frac{5C^2}{2} + 9c^2C^2 - 6c^2C^3 + \frac{3C^3}{2} \\ &+ \left(c^2 - \frac{C}{2} + C^2 - 3c^2C^2 - \frac{C^3}{2} + 2c^2C^3\right)e^{i\theta}. \end{aligned} \tag{2.29}$$

The stability bound is given by $c^2 \leq 1/2$. The asymptotic expressions for $A(C,c,\theta)$ and $B(C,c,\theta)$ are given by

$$\begin{aligned} A(C,c,\theta) &= \frac{1}{6}C(1-6c^2)(1-3C+2C^2)\theta^3 + O(\theta^5), \\ B(C,c,\theta) &= \frac{1}{24}\left(12c^4 - 2c^2(1+24C^2-48C^3+24C^4)\right. \\ &\qquad \left. +9C^2(C-1)^2\right)\theta^4 + O(\theta^6). \end{aligned} \tag{2.30}$$

Again, the leading order term in $A(C,c,\theta)$ is greater than or equal to 0 for $c^2 \leq 1/6$, and hence the low-frequency modes show lagging phase error. Interestingly, when $c^2 > 1/6$, $A(C,c,\theta)$ becomes non-positive for any C, and the low-frequency modes show leading phase error. The non-negativity of M_4' can be achieved by choosing $1/6 \leq c^2 \leq 1/2$. Again, the threshold of the radical change of the dispersion relation for low-frequency modes coincides with the lower bound of c^2, yielding non-negativity.

For Λ_3', it is hard to get a precise stability bound, since there is another parameter d_ν. Numerical calculation of the upper bound of $|g(C,c,\theta)|$ shows that $|d_\nu|$ should remain small when c^2 is small. However, for moderate values of c^2, the restriction on d_ν is not severe. We also note that d_ν approaches 0 if one refines the resolution while keeping c^2 constant. Thus, for most cases, one can just check the bound on c^2, for which one may consult the case of Λ_3. The region of non-negativity for Λ_3' is a convex

set in (c^2, d_ν) plane, whose boundary is described by the following set of equations:

$$\begin{aligned} c^2 - 1/2 = 0, \quad 4 + 9d_\nu^2 - 24c^2 = 0, \\ 20 + 27|d_\nu| - 162c^2|d_\nu| + 54|d_\nu|^3 - 2(7 - 18c^2 + 9d_\nu^2)^{3/2} = 0. \end{aligned} \tag{2.31}$$

2.5 Numerical examples

In this section, we discuss the results of a number of computations using the modified interpolation kernels. We provide three numerical examples of three-dimensional vortex simulations. Next, a nonlinear reaction-diffusion problem is solved to demonstrate the applicability of the method to cases of spatially varying diffusion coefficient.

2.5.1 Vortex rings

The behavior of vortex rings has been studied intensively, and hence they serve as good examples to check the capability of a numerical method [65]. We show results of three examples: evolution of a vortex ring at an intermediate Reynolds number, asymptotic drift of a vortex ring, and a case of side-by-side collision of two vortex rings.

We first briefly discuss the numerical method. A viscous splitting algorithm is employed. During the convection step, we solve the equations of motion for inviscid incompressible flow in vorticity transport form:

$$\begin{aligned} \frac{D\boldsymbol{\omega}}{Dt} =& \boldsymbol{\omega} \cdot \nabla \mathbf{u}, \\ \nabla \cdot \mathbf{u} =& 0, \end{aligned} \tag{2.32}$$

where $\boldsymbol{\omega} = \nabla \times \mathbf{u}$, and $\mathbf{u}$ is the velocity. The numerical solution proceeds by discretizing the vorticity field onto overlapping vector elements, each centered at $\boldsymbol{\chi}_i^c$ with volume dV_i and vorticity $\boldsymbol{\omega}_i$:

$$\boldsymbol{\omega}(\mathbf{x}, t) = \sum_i^N [\boldsymbol{\omega}_i dV_i](t) f_\sigma(\mathbf{x} - \boldsymbol{\chi}_i^c(t)). \tag{2.33}$$

The vorticity associated with each element is localized by a radially symmetric core function f_σ of radius σ, where $f_\sigma(\mathbf{x}) = \frac{1}{\sigma^3} f(\frac{|\mathbf{x}|}{\sigma})$. We use the low-order algebraic kernel as the core function [45, 74]. Each vortex element is described by a 'stick,' decomposing the particle strength $[\boldsymbol{\omega}_i dV_i](t)$ into a positive scalar weight Γ_i times a material line element $\delta\boldsymbol{\chi}_i(t)$. The vector $\delta\boldsymbol{\chi}_i$ points in the direction of the vorticity, and is ascribed to two nodes. Nodes are simply advected by the velocity field:

$$\frac{d\boldsymbol{\chi}_i}{dt} = \mathbf{u}(\boldsymbol{\chi}_i). \tag{2.34}$$

Advecting the nodes accounts for the material line element deformation, and thus for stretching and tilting of the vorticity $[\boldsymbol{\omega}_i dV_i]$. A second order predictor/corrector scheme with adaptive time-step control is used for time integration of the ordinary differential equations in (2.34), where the velocity at each node $\mathbf{u}(\boldsymbol{\chi}_i)$ is evaluated by an adaptive tree-code [45]. When $|\delta\boldsymbol{\chi}_i|$ of a given element exceeds 0.9σ, a new node is added halfway between the original two nodes. The parallel implementation of the adaptive tree-code is achieved by domain decomposition using the k-means clustering technique [50].

During the diffusion step, we use Λ_3 to interpolate the particle strength $[\boldsymbol{\omega}_i dV_i]$ of each vortex element onto target particles on a uniform grid. Following the interpolation, we eliminate particles with $|\boldsymbol{\omega}_i dV_i| < |\boldsymbol{\omega} dV|_{\text{del}}$ to control the problem size. Next, each target particle on the grid is converted back into a stick, having its center $\boldsymbol{\chi}_i^c$ at the grid point and $|\delta\boldsymbol{\chi}_i| = 0.6\sigma$. Because $|\delta\boldsymbol{\chi}_i|$ defines the length scale at which $\nabla\mathbf{u}$ is evaluated for the calculation of stretching, one should choose $|\delta\boldsymbol{\chi}_i|$ comparable to σ, which defines the spatial resolution of the simulation. If $|\delta\boldsymbol{\chi}_i|$ is too small, stretching is evaluated at a length scale that is not well resolved. On the other hand, $|\delta\boldsymbol{\chi}_i|$ should not be too large to avoid a quick increase in number of elements, since we add a new node when $|\delta\boldsymbol{\chi}_i| > 0.9\sigma$. Our $|\delta\boldsymbol{\chi}_i|$ is chosen via a tuning process considering these conditions. After the conversion of the target particles into sticks, the code can start the convection step again using these sticks as its initial condition.

All of the following simulations were performed on the IBM SP-RS/6000 located

at the National Energy Research Scientific Computing Center (NERSC).

Evolution of a vortex ring at an intermediate Reynolds number

The first example is a single vortex ring at $Re_\Gamma = \Gamma/\nu = 500$. A ring of radius R and core radius a is initially placed at the $y = 0$ plane. The core of the ring is represented by its azimuthal vorticity:

$$\omega_\phi = \frac{K}{\pi}\frac{\Gamma}{a^2}\exp\left\{-K\left(\frac{R^2}{a^2} + \frac{r^2}{a^2} - \frac{2Rr}{a^2}\sin\theta\right)\right\}, \tag{2.35}$$

where $r = \sqrt{x^2+y^2+z^2}$, $\tan\theta = (\sqrt{x^2+z^2})/y$, and $K = (2.24182)^2/4$. To make the initial distribution smooth, an image ring was placed across the axis of symmetry so that $\omega_\phi = 0$ at the y-axis. The ring has unit circulation and unit radius, i.e., $\Gamma = 1$ and $R = 1$. The core radius is chosen to be $a/R = 0.35$. This set of parameters makes the initial conditions identical to those of the axisymmetric spectral simulation performed by Stanaway *et al.* [66, 67].

We performed two different runs. The first is a fully three-dimensional simulation at $\Delta t_c = \Delta t_d = 0.5$, $\sigma = 0.1$, $\Delta x = 0.07$, $|\boldsymbol{\omega} dV|_{\text{del}} = 10^{-8}$. In the second case, a 20 degree section of the vortex ring is simulated at higher spatial resolution, where $\Delta t_c = \Delta t_d = 0.25$, $\sigma = 0.05$, $\Delta x = 0.035$, $|\boldsymbol{\omega} dV|_{\text{del}} = 10^{-10}$. If an element lies outside the 20 degree section, the element is rotated into the domain using azimuthal symmetry. Since the fully three-dimensional run did show a symmetry in the azimuthal direction during the period of interest, the simulation using the 20 degree section is expected to behave similarly.

The results are reported in the following dimensionless variables, which were also used in [66, 67]. The dimensionless speed of the vortex ring centroid is given by

$$\overline{U} = U_c \frac{(I_0/\rho)^{1/2}}{\nu^{3/2}}, \tag{2.36}$$

where I_0 is the initial linear impulse of the ring, and U_c is the speed measured in the

computational units. We also use dimensionless time, which is scaled as

$$\overline{t} = t\frac{\nu^2}{I_0/\rho}, \tag{2.37}$$

and shifted to match the initial time reported in [66, 67].

In Figure 2-1, the speed of the vortex ring centroid is plotted. For comparison, the curve reported in [66, 67] is also shown. The values are underestimated in the lower resolution run, but the higher resolution run shows a close match. At the later stage, where diffusion plays a dominant role in establishing the vorticity distribution, close agreement is observed at both resolutions. The circulation of the vortex ring is plotted in Figure 2-2. Unlike the initial speed, which is more strongly affected by convection than diffusion, the evolution of the circulation is well captured even by the lower resolution run.

We also show vorticity contours of the high resolution run on the $z = 0$ plane in Figure 2-3. We have chosen the same instances as those reported in [66, 67] for one-to-one comparison. The contour levels remain the same for all times in this figure. To recover the contour levels used in [66, 67], we have matched the diameter of the outermost solid contour at the initial condition, and the difference between the solid lines is set to be a factor of 10 larger than between the dashed ones. Comparing Figure 2-3 to that reported in [66, 67], we see that our simulation does reproduce the details of the vortex ring correctly. Even the subtle structure of the tail is well matched. We also note that the linear impulse of the ring is preserved within 0.9% for the duration of the simulation in both of our simulations. The number of vortex elements at the end of the simulation was around 500,000 for both of our simulations.

Asymptotic drift of a vortex ring

The second example is the long-time asymptotic drift of a vortex ring. The centroid speed under these conditions was studied by Rott and Cantwell [60], and we compare the result of our simulation to these theoretical estimates.

Initially, we place a Stokes vortex ring at the $y = 0$ plane. The vorticity distribu-

tion of a Stokes vortex ring is given by

$$\omega_\phi = \frac{I_0/\rho}{8\pi^{3/2}(\nu t_I)^2} \sin\theta\eta \exp(\eta^2), \tag{2.38}$$

where $\eta = r/\sqrt{4\nu t_I}$. r and θ are defined in the same way as in the previous example. The ring has unit linear impulse, i.e., $I_0/\rho = 1$, and the kinematic viscosity is chosen to be $\nu = 1$ for simplicity. With this choice, the only parameter that must be specified is the initial time t_I, which is chosen to be $t_I = 1/900$. The initial Reynolds number is $Re_I = (I_0/\rho)^{1/2}/(\nu t_I)^{1/2} = 30$. The numerical parameters used are: $\Delta t_c = \Delta t_d = 0.0003$, $\sigma = 0.05$, $\Delta x = 0.03$, $|\boldsymbol{\omega} dV|_{\text{del}} = 10^{-12}$. To limit the size of the simulation, we again follow the evolution of a 20 degree section of the ring, assuming azimuthal symmetry. The 20 degree section of the Stokes vortex ring is initially discretized into more than 80,000 elements, which gives smaller inter-particle distance than that specified by Δx. Still, the initial centroid speed of the vortex ring is naturally underestimated, since the numerical parameters, such as σ, are chosen to match the resolution required for the later stage. Note that our purpose is to study the long-time asymptotic drift, where diffusion is expected to dominate the dynamics.

The speed of the long-time asymptotic drift of a single vortex ring is given as follows [60]:

$$\overline{U} = \frac{7}{15}\left(8\pi\overline{t}\right)^{-3/2} \approx 0.0037038\overline{t}^{-3/2}. \tag{2.39}$$

This theoretical result was also well verified by the axisymmetric simulations of Stanaway *et al.* [66, 67]. As shown in Figure 2-4, where the speed of the vortex ring centroid is plotted, the result of our simulation matches (2.39) well as $\overline{t}$ increases.

Figure 2-5 and Figure 2-6 show the evolution of the circulation and that of the kinetic energy respectively. From the expression of the Stokes vortex ring, it can be shown that the circulation must evolve as $\overline{t}^{-1}$, and that the kinetic energy must evolve as $\overline{t}^{-3/2}$. Our simulation matches these trends exactly. The linear impulse of the ring is preserved within 0.04% for the duration of the simulation. The error in the linear impulse increases mostly at the initial stage, where convection still affects the evolution of the vortex ring. At the later stage, where diffusion dominates

the evolution, the error in the linear impulse does not increase much, showing that interpolation indeed preserves the linear impulse. The number of vortex elements at the end of the simulation was around 300,000.

Side-by-side collision of two vortex rings

The final example of vortex calculations is the interaction of two vortex rings; the case studied by Kida *et al.* [35]. As an initial condition, two identical vortex rings are placed side-by-side. The centers of the vortex rings are placed on the x axis, separated by a distance s. The radius of each ring is R. We use a Gaussian vorticity distribution within the core:

$$\omega_\phi = \omega_0 \exp\left\{-\left(\frac{r}{a}\right)^2\right\}, \tag{2.40}$$

where r is the distance from the core centerline, ω_0 is the maximum vorticity at the core center. The nominal circulation of the vortex ring is $\pi\omega_0 a^2$. Note that (2.40) is equivalent to (2.35) with the proper change of variables. We use different representations to simplify the comparison with the reference cases.

A set of parameters similar to Case I in [35] is chosen, namely, $R = 0.982$, $a = 0.393$, $s = 3.65$, $\omega_0 = 23.8$, and $\nu = 0.01$, which makes $Re_\Gamma = 1153$ based on the nominal circulation. The rings are not inclined with respect to the $y = 0$ plane. This condition is not identical to that of Case I in [35], since the simulation performed in [35] was spatially periodic, while our rings are isolated in $\mathbf{R}^3$. Due to periodicity, the evolution of the vortex rings in [35] turned out to be slower. Thus the comparison between these two cases can be qualitative only.

The numerical parameters used are the following: $\Delta t_c = 0.05$, $\Delta t_d = 0.1$, $\sigma = 0.2$, $\Delta x = 0.090909$, and $|\boldsymbol{\omega} dV|_{\text{del}} = 5 \times 10^{-7}$. The vortex rings move toward the $x = 0$ plane, as they travel in the y direction, through their mutual induction. They approach each other, and collide along the $x = 0$ plane as shown in Figure 2-7. The collision promotes the establishment of large vorticity gradients, which are then gradually annihilated by diffusion. Eventually, the two rings merge into a distorted

single ring. The evolution of colliding rings shown in Figure 2-7 is similar to that depicted in [35]. In particular, one can recognize the formation of threads on the front of the vortex tube, which are remnants of the anti-parallel vortices at the contact point. These threads were also observed in [35].

The interaction can be seen in Figures 2-8 and 2-9, where the contours of ω_z and ω_x are plotted, respectively. As depicted in Figure 2-8, the outer cores move upward faster than the inner cores, and induce a flow that forces the inner cores toward the $x = 0$ plane. As the inner cores collide, the outer vortex tubes extend across the $x = 0$ plane resulting in the formation of bridges, as shown in Figure 2-9. During this first reconnection, the circulation of each of the inner cores decreases rapidly, while the circulation of each of the bridges increases, which can be seen in Figure 2-10. This transfer of circulation was also observed in [35]. The number of vortex elements for this simulation remains around 450,000 by the end of the simulation. The linear impulse is preserved within 0.7%.

Finally, we note that the computational time spent for the interpolation step remains indeed small compared to that spent on the calculation of convection for all the simulations reported in this paper. The difference becomes more pronounced as the number of vortex elements increases. In a numerical experiment using 2 million vortex elements on 384 SP POWER3 processors, the computational time for one interpolation step was less than 10% of the computational time of one single prediction step.

2.5.2 Nonlinear reaction-diffusion system

In this section, we show that the interpolation kernels can be used for treating nonlinear problems as well. We consider the following one-dimensional reaction-diffusion problem.

$$\frac{\partial \theta}{\partial t} = \frac{\partial}{\partial x}\left(\theta^2 \frac{\partial \theta}{\partial x}\right) - 2\theta\left(\frac{\partial \theta}{\partial x}\right)^2 \quad \text{for} \quad x \in (0,1), t > 0, \tag{2.41}$$

where the initial and the boundary conditions are given as follows:

$$\theta(x,0) \;=\; \theta_I(x) \;=\; \frac{2}{3+2x}, \tag{2.42}$$

$$\frac{\partial\theta}{\partial x} = 0 \;\text{ for }\; x = 0 \;\text{ and } 1,\; t > 0. \tag{2.43}$$

Equation (2.41) models thermal conduction in solid crystalline molecular hydrogen, and the following analytical solution was obtained in [57]:

$$\begin{aligned} \theta =& \overline{\theta} + \pi^{-1/2} \int_{\mathbf{R}} A'(\hat{x} + 2t^{1/2}\beta) \exp(-\beta^2) d\beta, \\ x =& \overline{\theta}\hat{x} + \pi^{-1/2} \int_{\mathbf{R}} A(\hat{x} + 2t^{1/2}\beta) \exp(-\beta^2) d\beta, \end{aligned} \tag{2.44}$$

in which $\hat{x}$ is an extensible distance coordinate,

$$\overline{\theta} = \left(\int_0^1 \theta_I(x)^{-1} dx \right)^{-1} = \frac{1}{2}, \tag{2.45}$$

and A is odd, of period $2/\overline{\theta}$, and given over a half period by solving

$$\int_0^{A(\gamma)+\overline{\theta}\gamma} \theta_I(x)^{-1} dx = \gamma, \tag{2.46}$$

which yields

$$A(\gamma) = \begin{cases} \frac{1}{2}\left(-3 - \gamma + \sqrt{9+8\gamma}\right) & : \quad 0 \le \gamma \le 2 \\ -A(-\gamma) & : \quad -2 < \gamma < 0 \\ \text{periodic in } 4 & : \quad \text{otherwise} \end{cases} \tag{2.47}$$

A' is the derivative of A. The expression in (2.44) can be easily integrated numerically to obtain the pointwise value of the solution with high accuracy.

To solve the problem numerically, we employ the following procedure:

1. Initialize the particles: set $n = 0$, $x_j^n = (j - 1/2)\Delta x$, and $\Gamma_j^n = \theta_I(x_j^n)\Delta x$.

2. Solve for reaction first. The equation $\frac{\partial\theta}{\partial t} = -2\theta\left(\frac{\partial\theta}{\partial x}\right)^2$ is modeled by a set

of ordinary differential equations $\frac{\partial \Gamma_j}{\partial t} = -2\Gamma_j \left(\underline{\partial_x \theta}_j\right)^2$ for the particles, where $\underline{\partial_x \theta}_j = \underline{\partial_x \theta}(x_j)$ is the numerical approximation of $\left(\frac{\partial \theta}{\partial x}\right)_{x=x_j}$. Similarly, we denote the numerical approximation of $\theta(x_j)$ as $\underline{\theta}_j = \underline{\theta}(x_j)$. The ordinary differential equations are discretized in time using the improved polygon method [8].

3. Solve for diffusion. The equation $\frac{\partial \theta}{\partial t} = \frac{\partial}{\partial x}\left(\theta^2 \frac{\partial \theta}{\partial x}\right)$ is approximated by remeshing using the Λ_3' interpolation kernel (2.18). $\nu(x_j)$ and $\left(\frac{\partial \nu}{\partial x}\right)_{x=x_j}$ are evaluated from the values of $\underline{\theta}_j$ and $\underline{\partial_x \theta}_j$. in this case, the absence of convection forces the particles to stay at the grid location all the time. Hence, to demonstrate the capability of the method in performing remeshing and diffusion concurrently, the uniform grid for the target particle locations is obtained by shifting the initial particle locations by a distance randomly selected at each time step, i.e., $x_j^n = x_j^0 + \rho^n$, where ρ^n is a random number in $[-\frac{\Delta x}{2}, \frac{\Delta x}{2})$. To satisfy the boundary condition, the particles generated outside the domain during the remeshing process are reflected back into the domain. For example, a particle at $x_j^n < 0$ is moved to $-x_j^n$ at the end of the diffusion substep without changing its strength. In a similar way, we move the particles with $x_j^n > 1$ to $2 - x_j^n$.

4. Advance time by Δt and repeat steps (2) and (3).

To evaluate $\underline{\theta}(x)$ and $\underline{\partial_x \theta}(x)$, we use the following expressions.

$$\begin{aligned} \underline{\theta}(x) &= \sum_{i=1}^{N} \Gamma_i \left(f_\sigma(x - x_i) + f_\sigma(x + x_i) + f_\sigma(x - 2 + x_i)\right), \\ \underline{\partial_x \theta}(x) &= \frac{\partial \underline{\theta}}{\partial x} = \sum_{i=1}^{N} \Gamma_i \left(f_\sigma'(x - x_i) + f_\sigma'(x + x_i) + f_\sigma'(x - 2 + x_i)\right). \end{aligned} \tag{2.48}$$

The two additional terms in the summation represent the image particles included to satisfy the boundary condition. We use a core function $f_\sigma \in C_c^4(\mathbf{R})$:

$$f_\sigma(x) = \frac{1}{\sigma} f\left(\frac{x}{\sigma}\right), \tag{2.49}$$

where

$$f(x) = \begin{cases} \frac{693}{512}(1 - 5x^2 + 10x^4 - 10x^6 + 5x^8 - x^{10}) & : \quad |x| < 1 \\ 0 & : \quad 1 \leq |x| \end{cases} \tag{2.50}$$

For supp $f_\sigma = [-\sigma, \sigma]$, the image particles included in (2.48) are enough to satisfy the correct boundary conditions for $\sigma < 1$. Other core functions may be used as long as they are of compact support and in $C_B^3(\mathbf{R})$, which is required to obtain convergence in L^∞ as shown in Appendix A.

Computations were performed for $t = [0, 0.011]$ in 4-byte precision on a Pentium 4 workstation. We chose $\Delta t/\Delta x^2 = 1.1$ to satisfy the non-negativity constraint (2.31). Figure 2-11 and Table 2.1 show the convergence of the approximate solution to the analytical solution with the numerical parameters being refined. Note that both σ and $\Delta x/\sigma$ should approach zero to suppress noise at high wavenumbers. One can also notice that the numerical error is more prominent near the boundary. The initial conditions with their images are only continuous at the boundary, and hence the error near the boundary in the initial discretization is larger than that in the domain interior. However, the overall trend of convergence is clear.

Table 2.1: L^∞ error for different numerical parameters at $t = 0.011$

	$\sigma/\Delta x = 3$	$\sigma/\Delta x = 6$
$\Delta x = 0.1$	1.0266×10^{-2}	
$\Delta x = 0.05$	4.7675×10^{-3}	
$\Delta x = 0.01$	8.7498×10^{-3}	8.6109×10^{-4}
$\Delta x = 0.005$		4.6580×10^{-4}

2.6 Summary

A scheme is proposed to treat diffusion and remeshing, simultaneously, in Lagrangian vortex methods. Interpolation kernels similar to those that have been used for remeshing of particle distributions in inviscid vortex simulations are obtained by utilizing the moment-based redistribution method. The stability properties of the new interpolation kernels were investigated by using analogies to Eulerian schemes. Numerical

examples show that the scheme works well in test problems. Results suggest that the scheme can be successfully applied to complex problems, including cases in which nonlinear diffusion plays an important role.

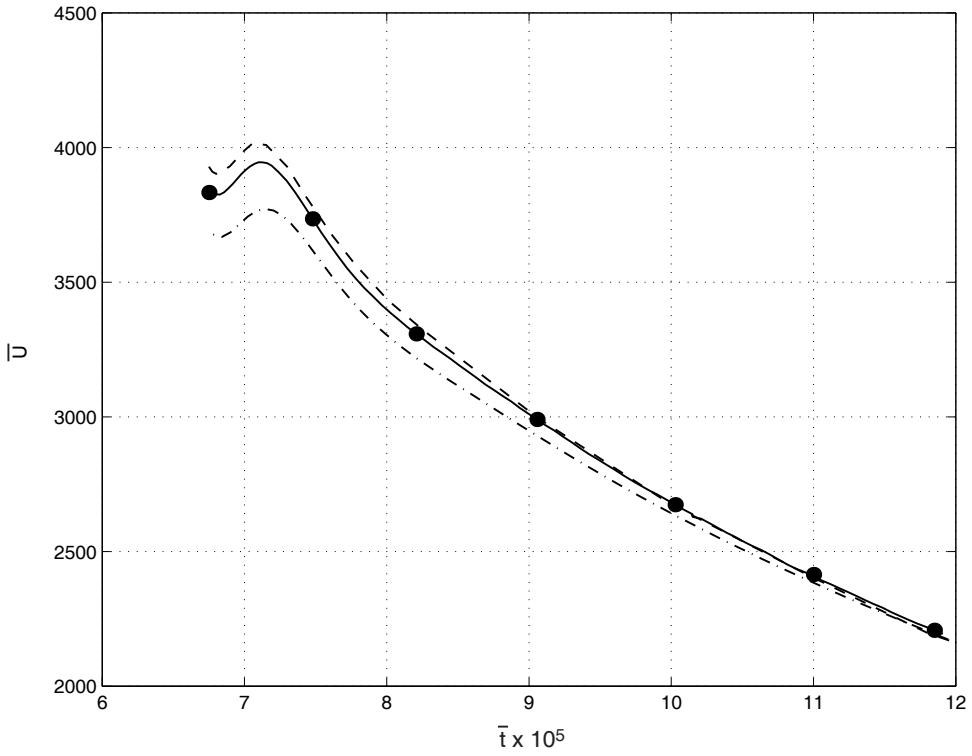

Figure 2-1: Speed of the vortex ring verses time. Solid, 20 degree section simulation at high resolution; Dash-dot, full simulation at low resolution; Dashed, Stanaway *et al.* [66, 67]. Dots on the solid curve correspond to the instances shown in Figure 2-3.

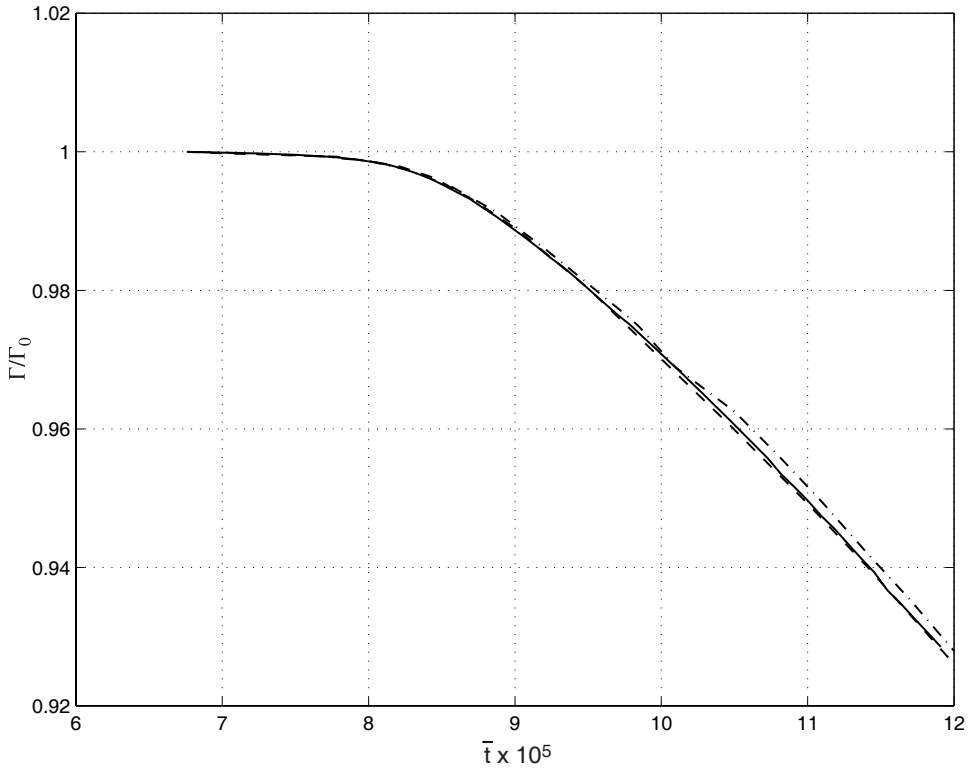

Figure 2-2: Circulation of the vortex ring verses time. Solid, 20 degree section simulation at high resolution; Dash-dot, full simulation at low resolution; Dashed, Stanaway *et al.* [66, 67].

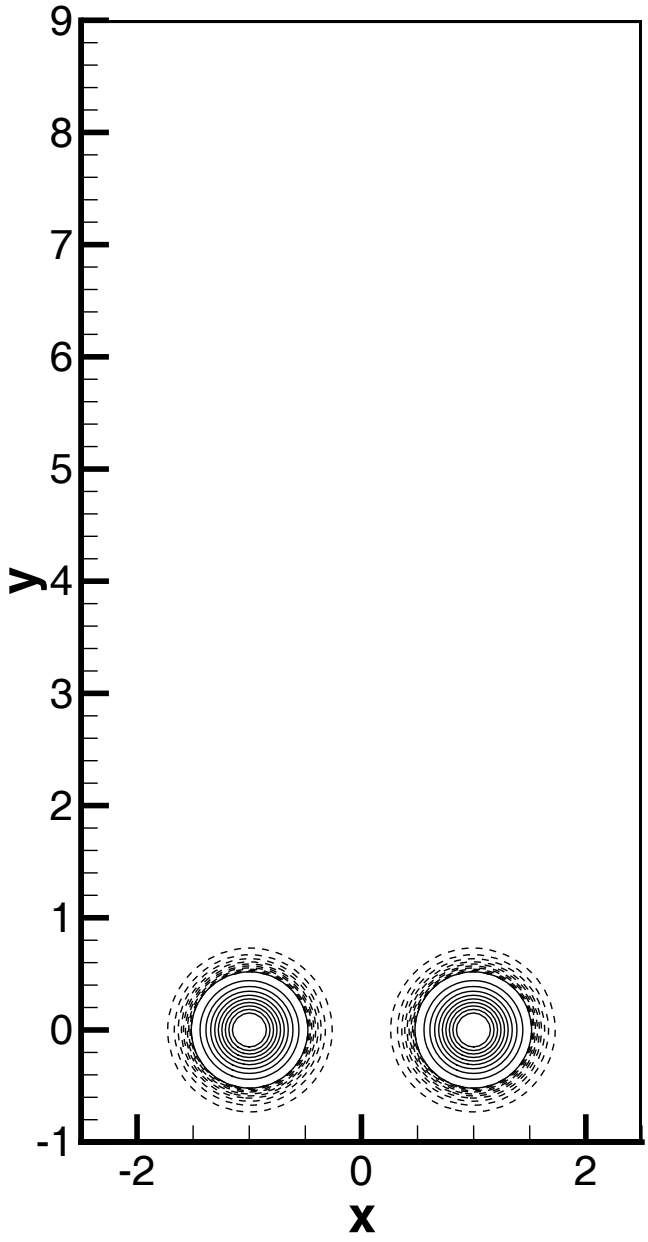

(a) $\overline{t} = 6.75 \times 10^{-5}$

Figure 2-3: The evolution of a single vortex ring. Vorticity contour at several instants in time. The contour levels for dashed lines vary from $|\omega_z| = 0.024$ to $|\omega_z| = 0.24$. The contour levels for solid lines vary from $|\omega_z| = 0.24$ to $|\omega_z| = 2.4$. For lines of the same type, the vorticity varies linearly.

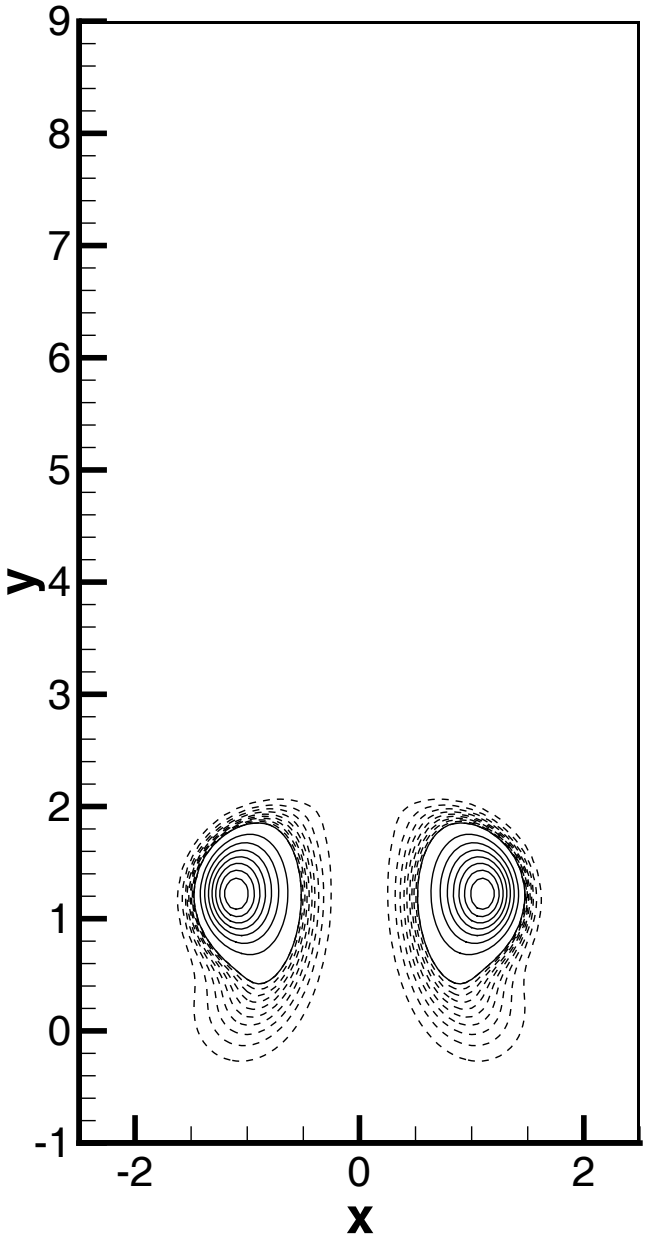

(b) $\overline{t} = 7.48 \times 10^{-5}$

Figure 2-3: Continued from the previous page.

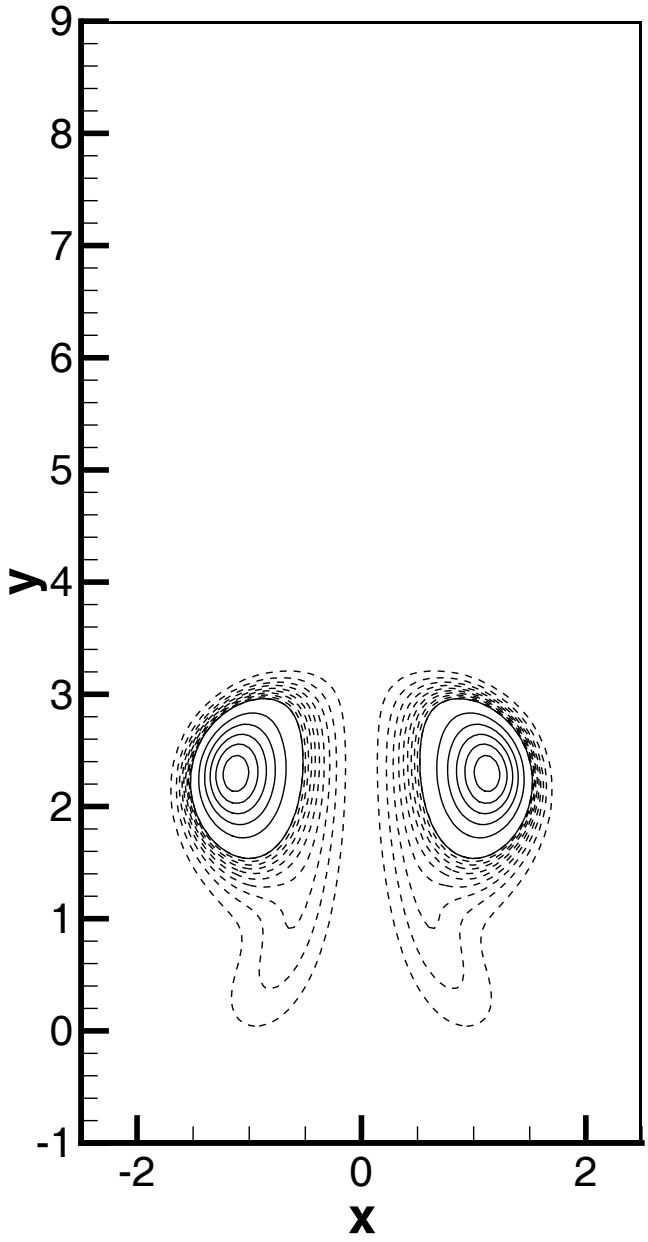

(c) $\overline{t} = 8.21 \times 10^{-5}$

Figure 2-3: Continued from the previous page.

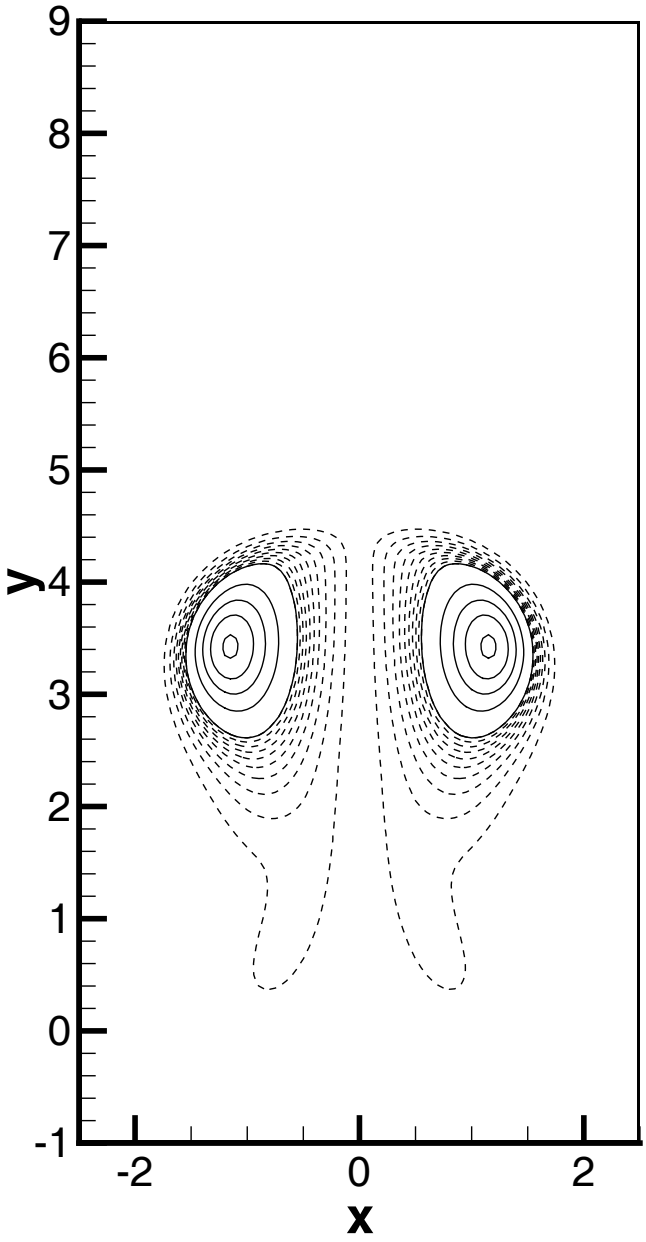

(d) $\overline{t} = 9.06 \times 10^{-5}$

Figure 2-3: Continued from the previous page.

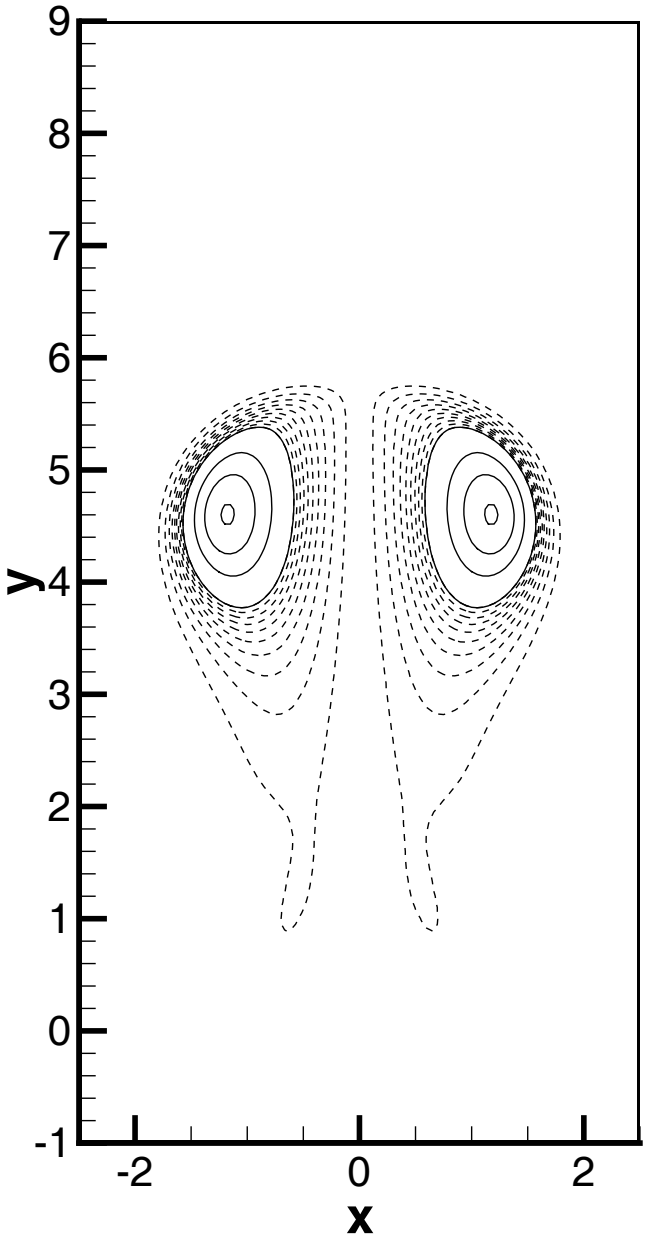

(e) $\overline{t} = 10.03 \times 10^{-5}$

Figure 2-3: Continued from the previous page.

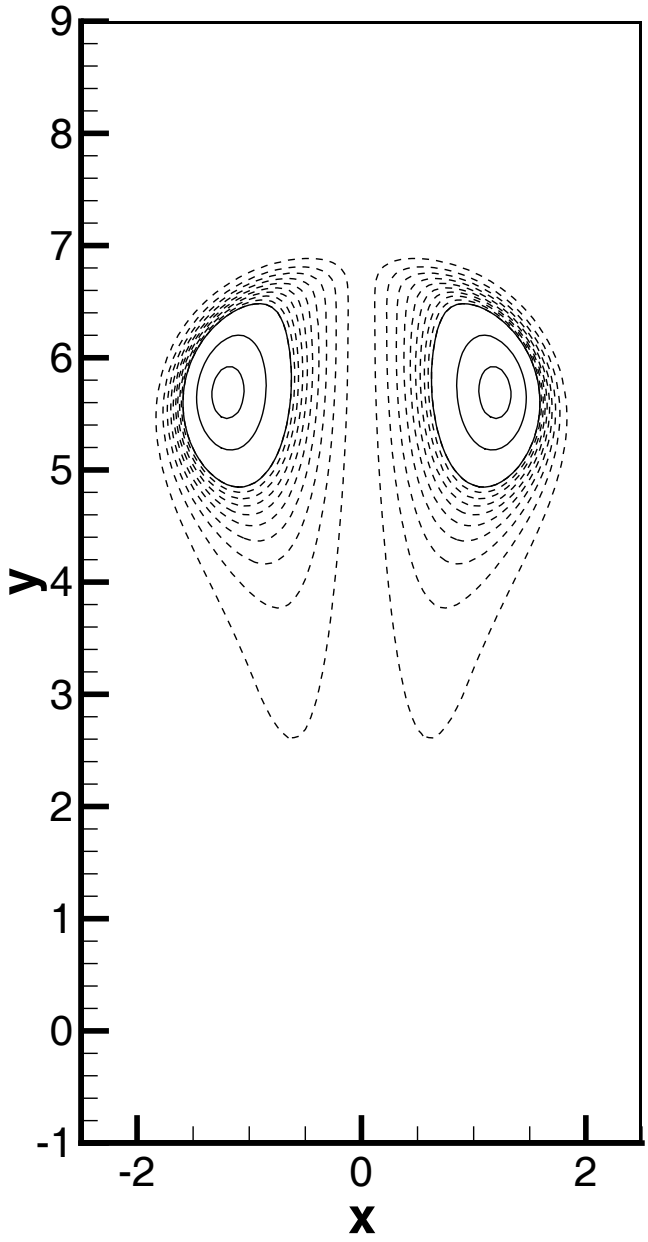

(f) $\overline{t} = 11.00 \times 10^{-5}$

Figure 2-3: Continued from the previous page.

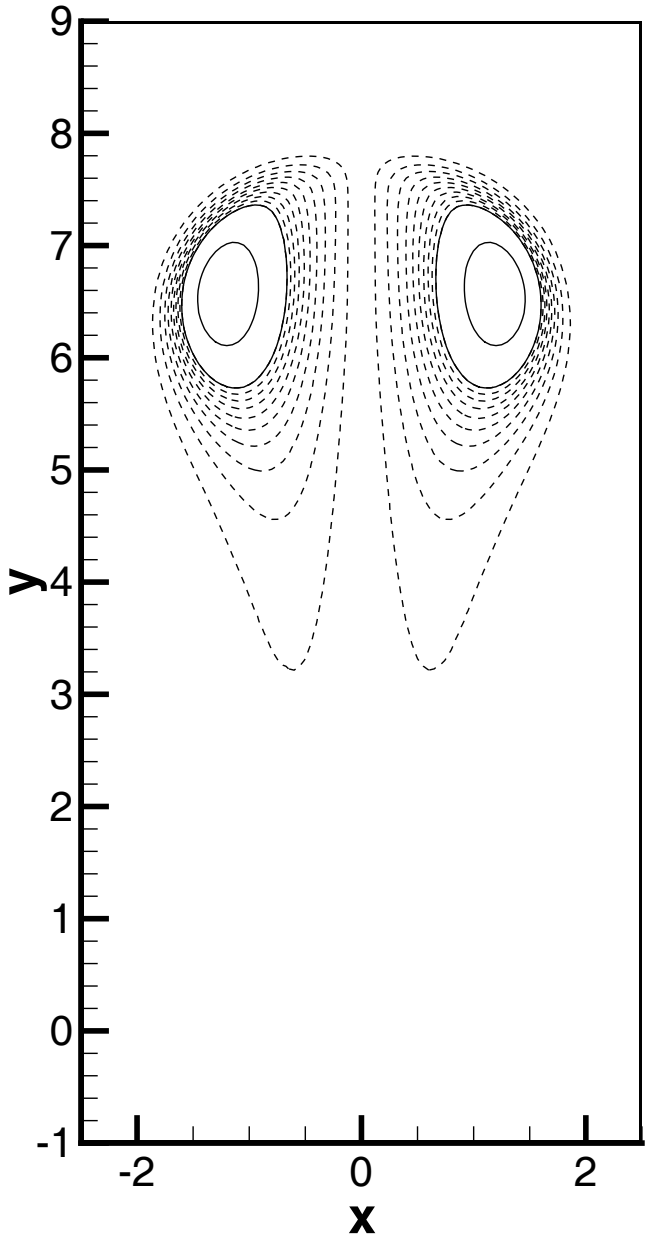

(g) $\overline{t} = 11.85 \times 10^{-5}$

Figure 2-3: Continued from the previous page.

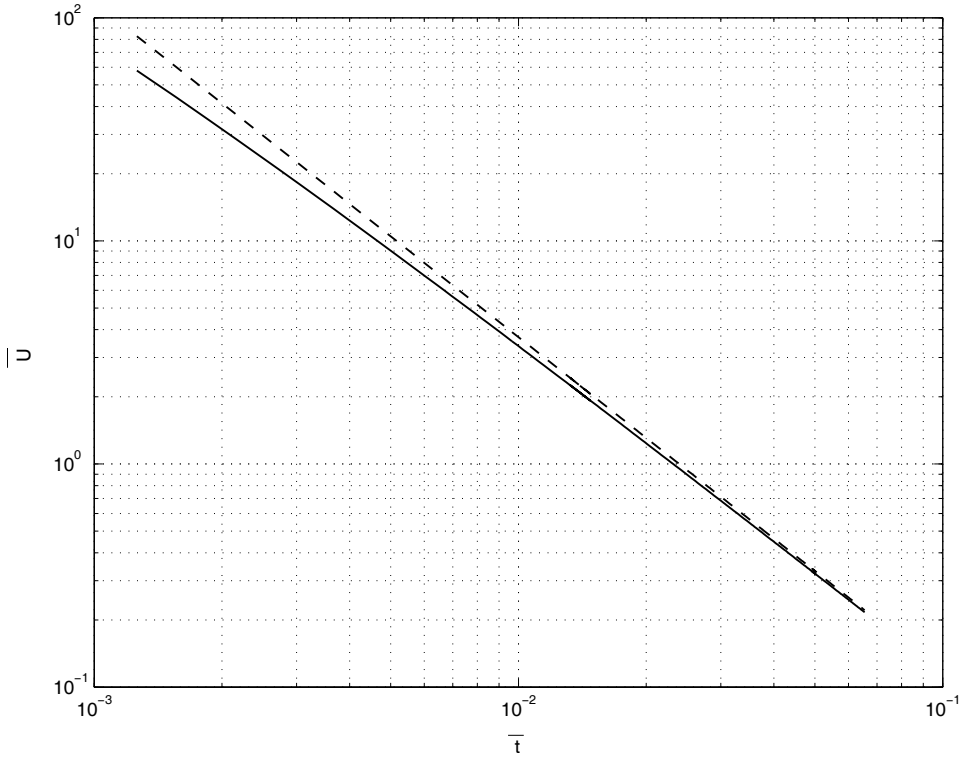

Figure 2-4: Speed of the vortex ring verses time. Solid, present study; Dashed, Eq. (2.39) [60].

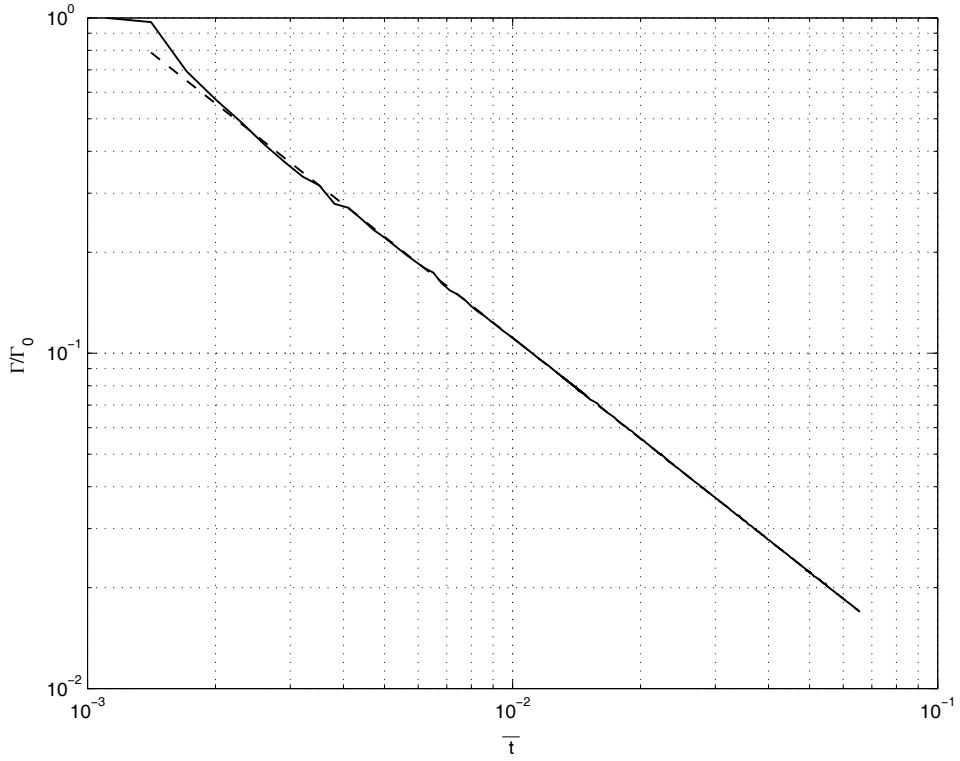

Figure 2-5: Circulation of the vortex ring verses time. Solid, present study; Dashed, a line proportional to $\overline{t}^{-1}$.

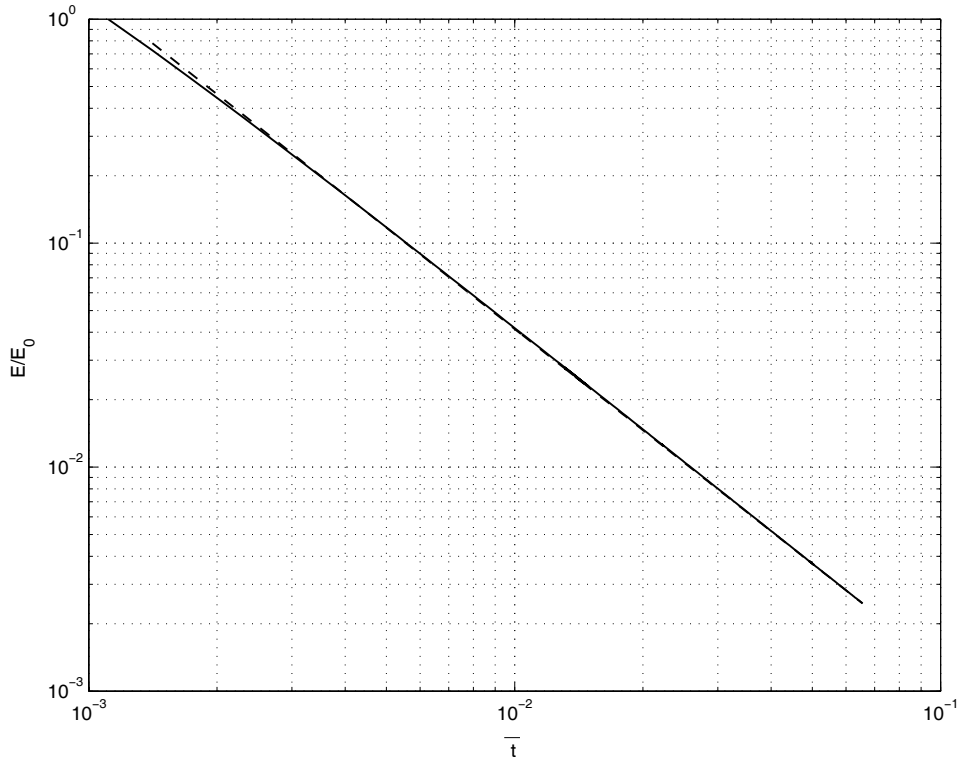

Figure 2-6: Kinetic energy of the vortex ring verses time. Solid, present study; Dashed, a line proportional to $\overline{t}^{-3/2}$.

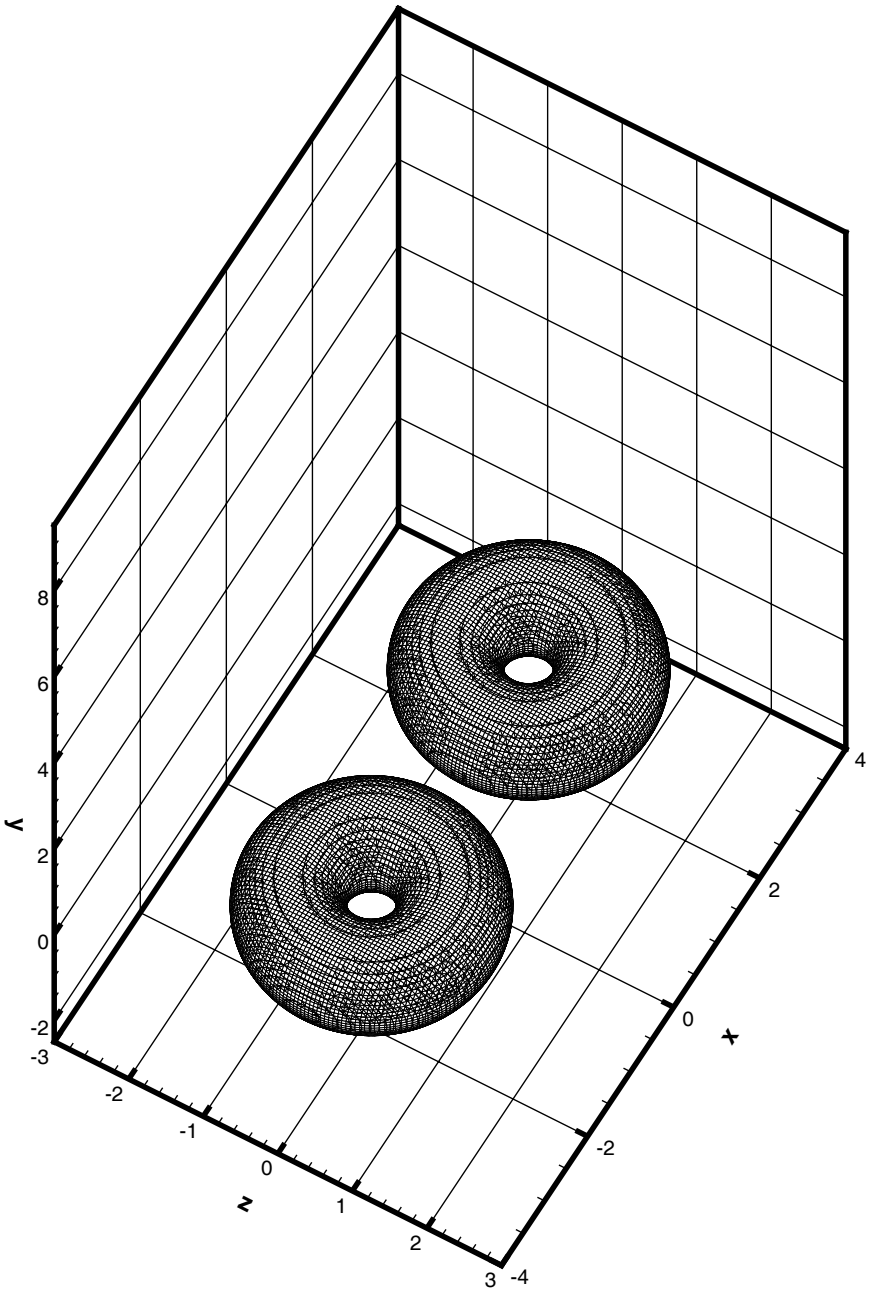

(a) $t = 0.0$

Figure 2-7: Iso-surfaces of the vorticity norm $|\boldsymbol{\omega}| = 2.0$.

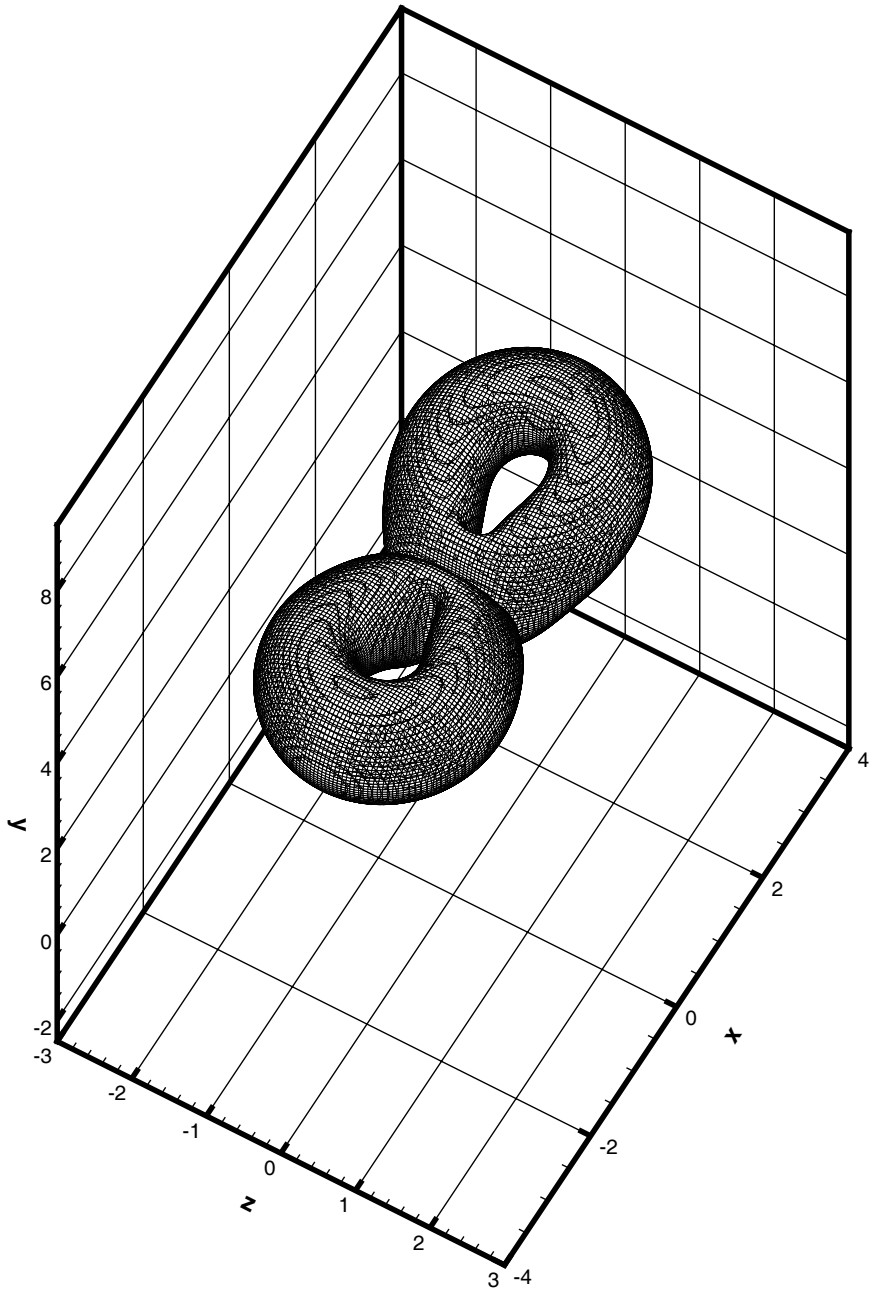

(b) $t = 3.0$

Figure 2-7: Continued from the previous page.

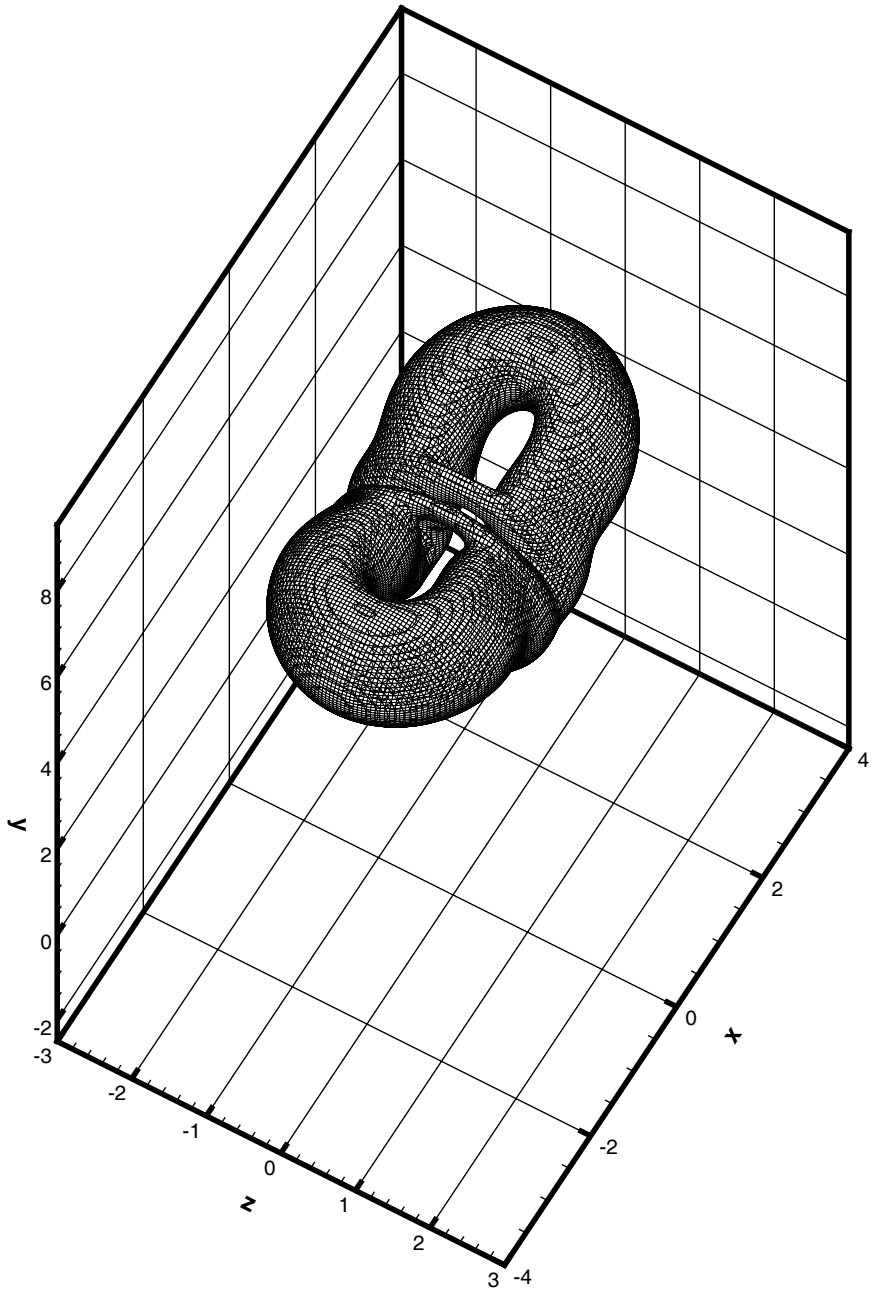

(c) $t = 4.0$

Figure 2-7: Continued from the previous page.

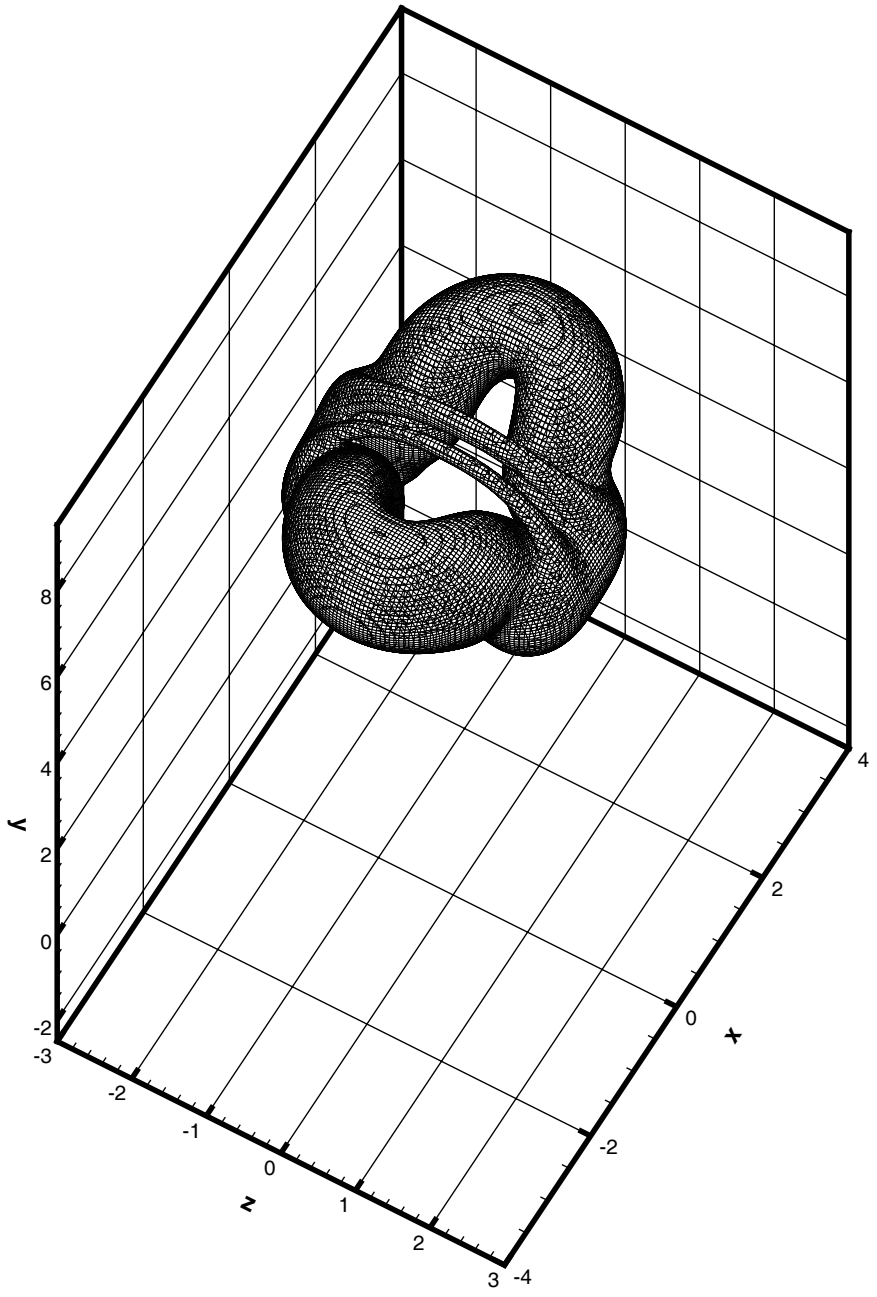

(d) $t = 5.0$

Figure 2-7: Continued from the previous page.

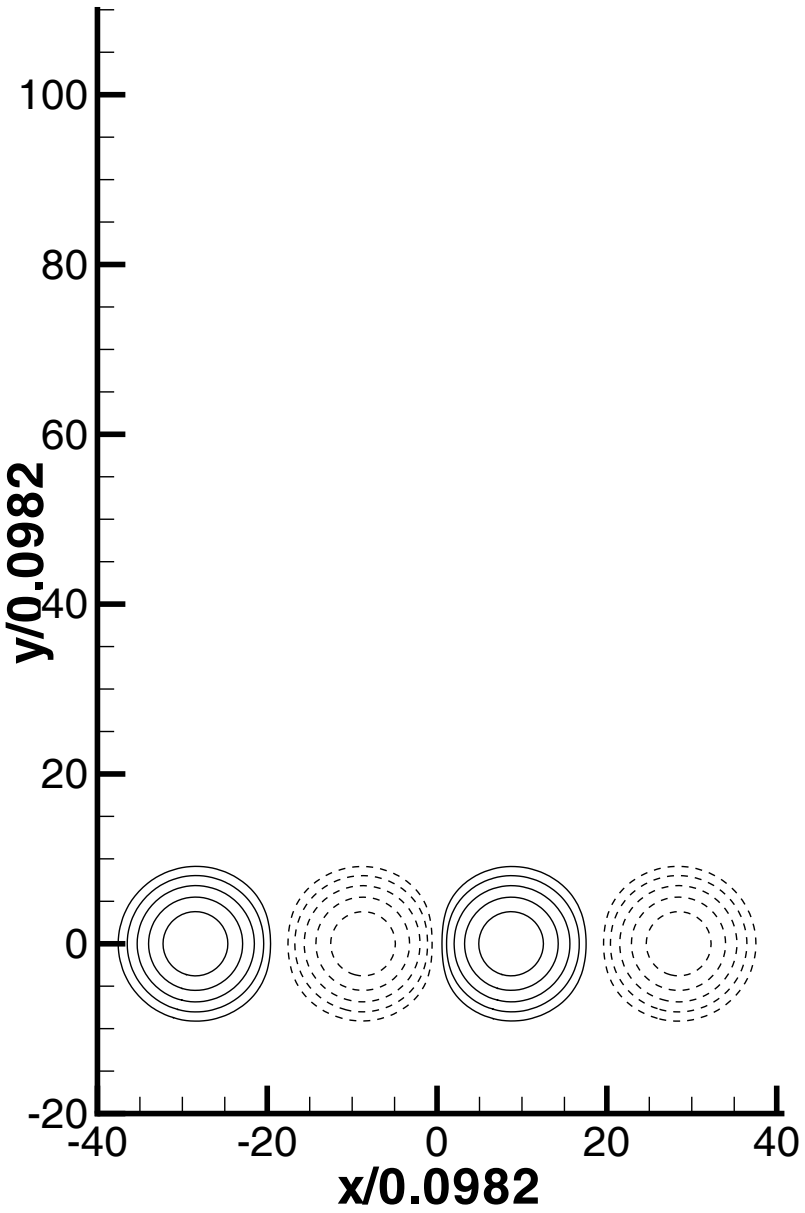

(a) $t = 0.0$

Figure 2-8: Contour of ω_z at $z = 0$. Levels plotted are 0.5, 1, 2, 4, and 8. Solid and dashed lines represent positive and negative values respectively.

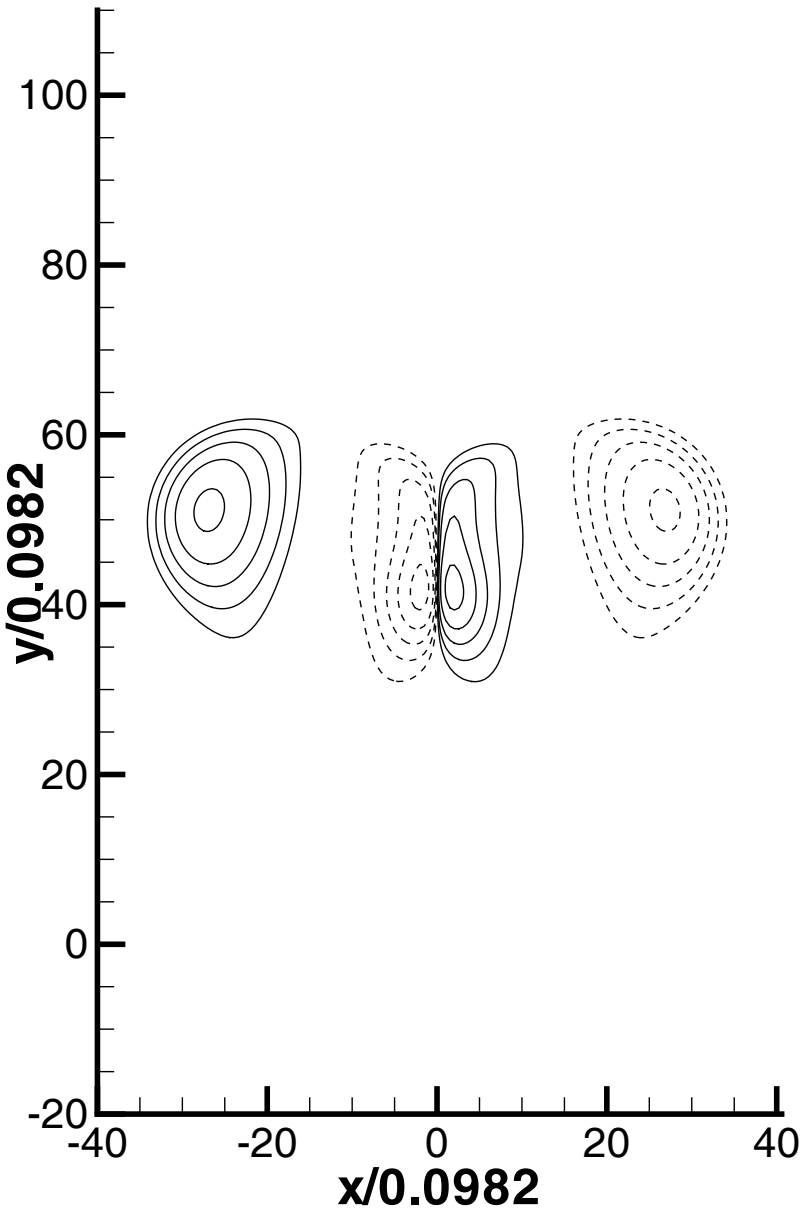

(b) $t = 3.0$

Figure 2-8: Continued from the previous page.

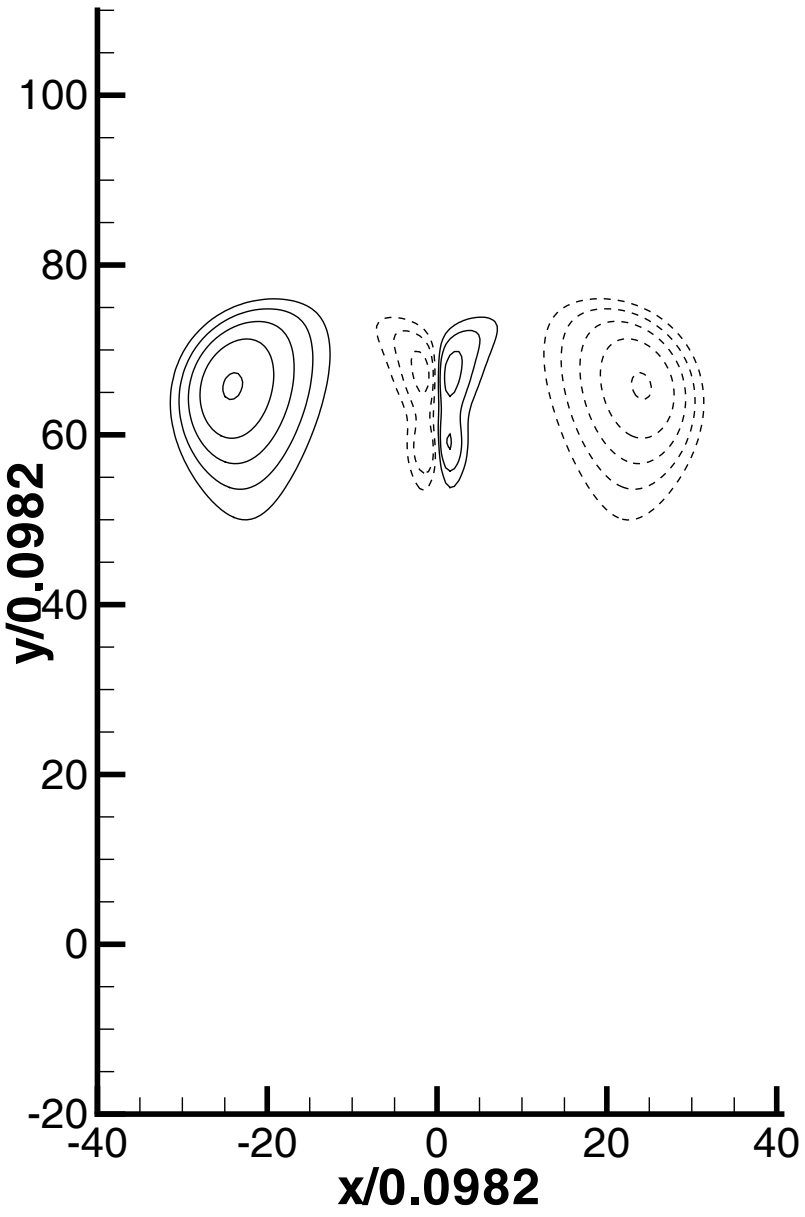

(c) $t = 4.0$

Figure 2-8: Continued from the previous page.

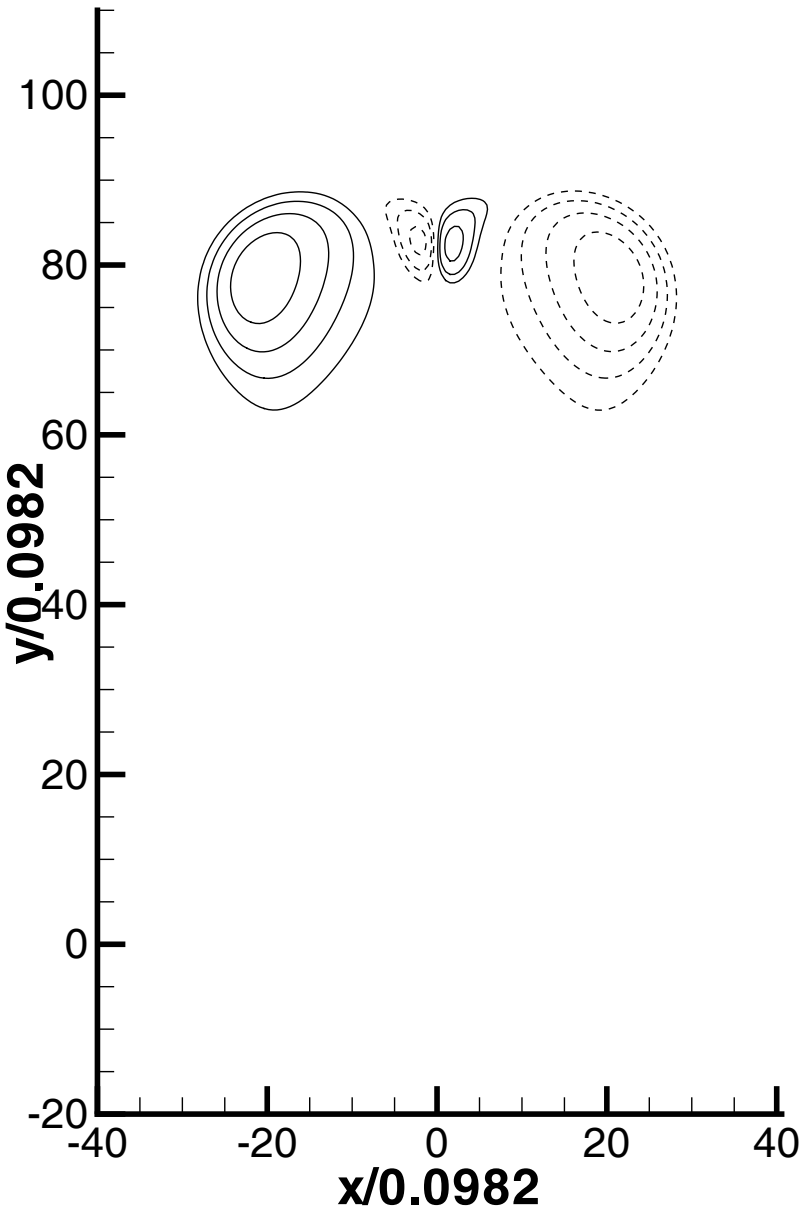

(d) $t = 5.0$

Figure 2-8: Continued from the previous page.

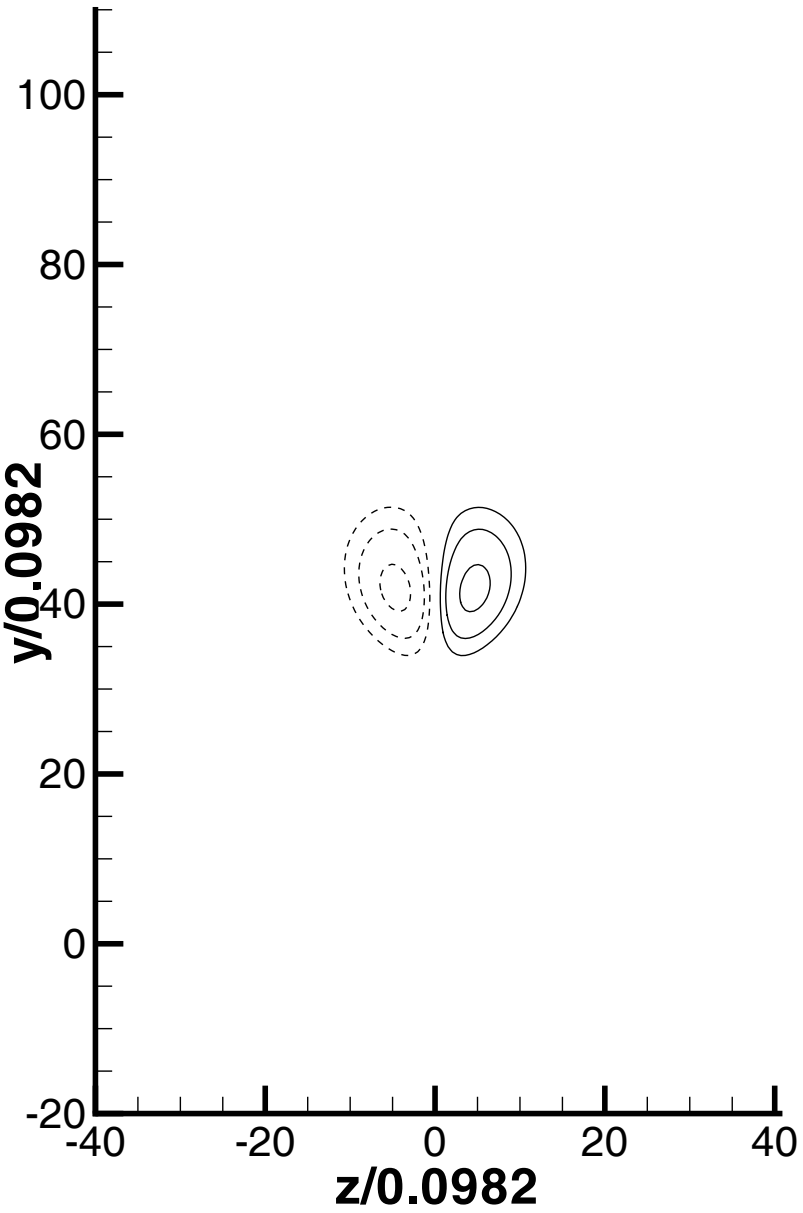

(a) $t = 3.0$

Figure 2-9: Contour of ω_x at $x = 0$. Levels plotted are 0.5, 1, 2, 4, and 8. Solid and dashed lines represent positive and negative values respectively.

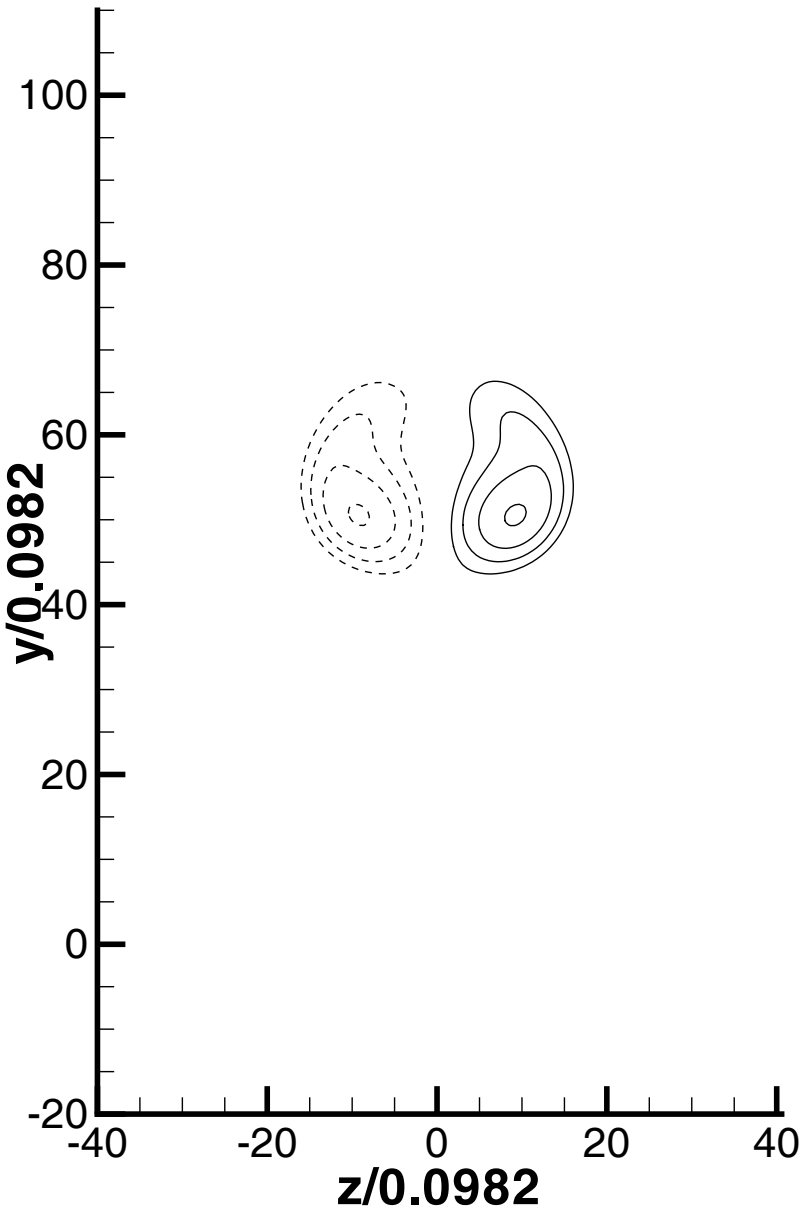

(b) $t = 4.0$

Figure 2-9: Continued from the previous page.

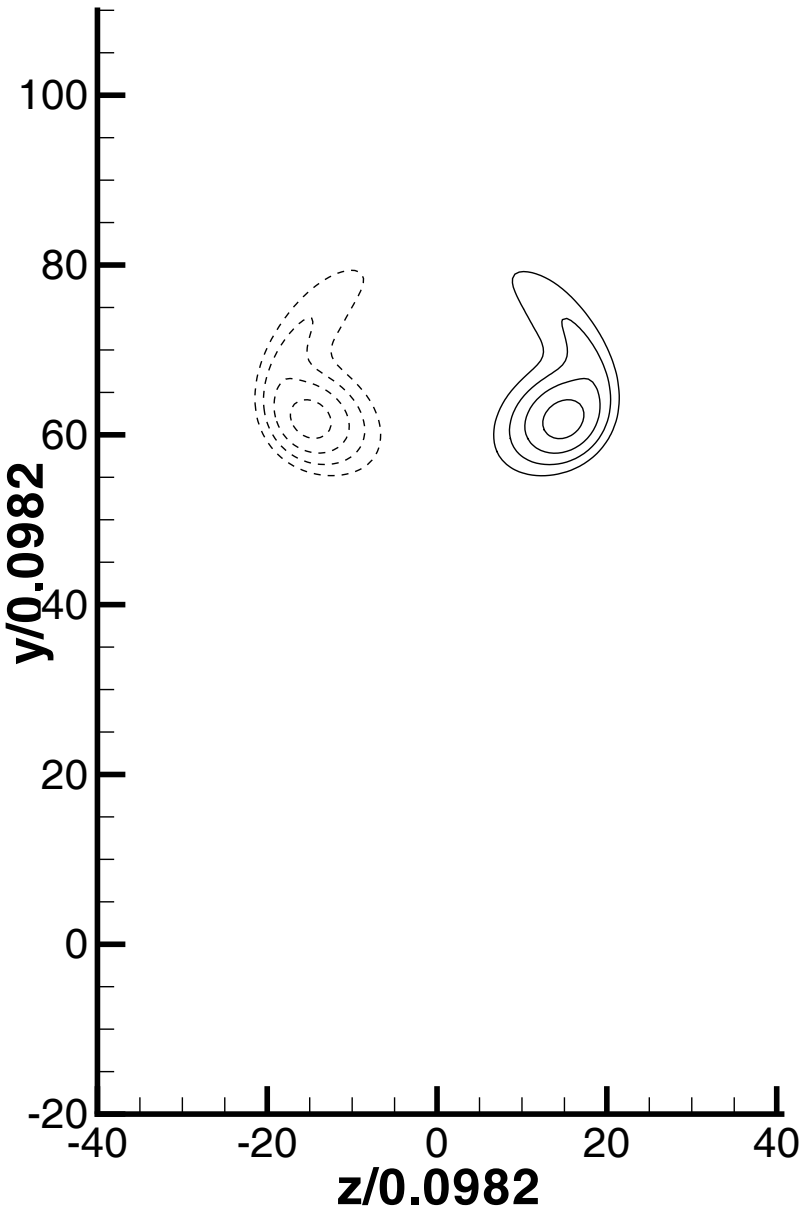

(c) $t = 5.0$

Figure 2-9: Continued from the previous page.

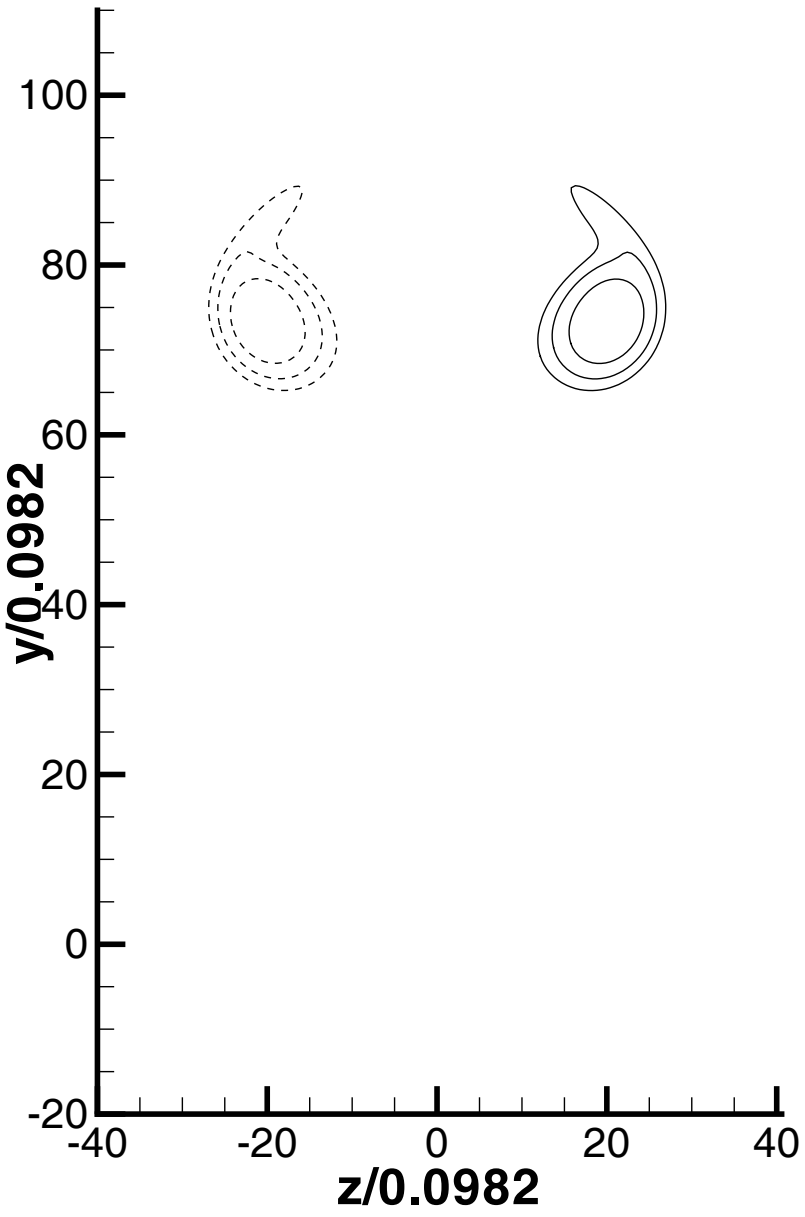

(d) $t = 6.0$

Figure 2-9: Continued from the previous page.

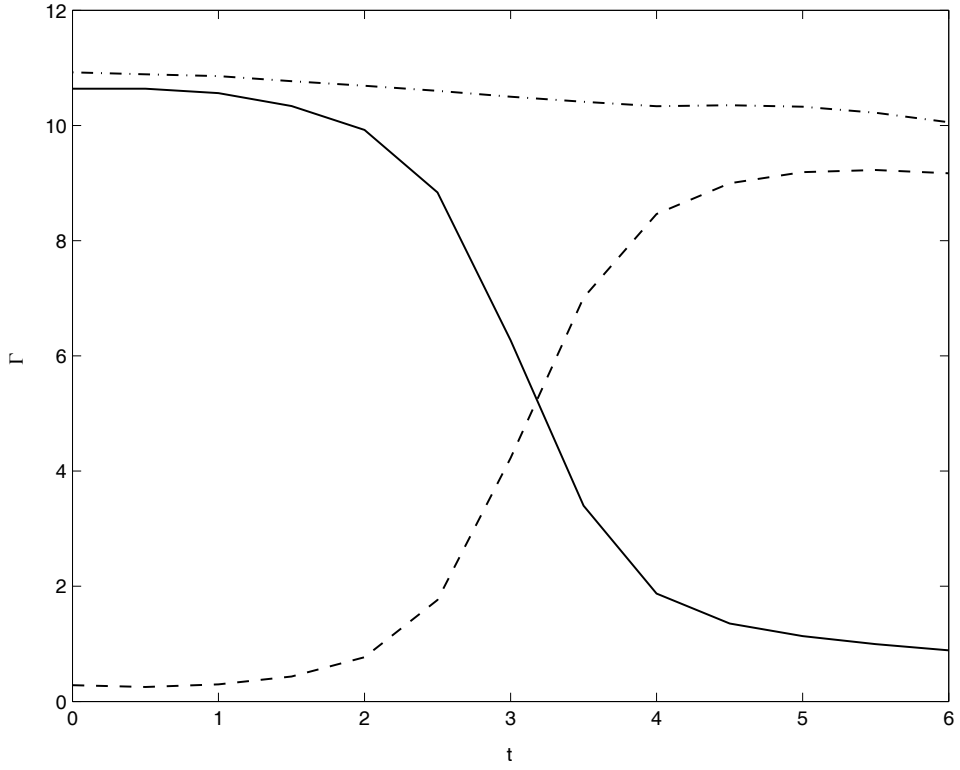

Figure 2-10: Evolution of circulation around interacting vortex tubes. Solid, circulation around the cross-section of an inner core on the $z = 0$ plane; dashed, circulation around the cross-section of a bridge on the $x = 0$ plane; dash-dot, the sum of these two circulations.

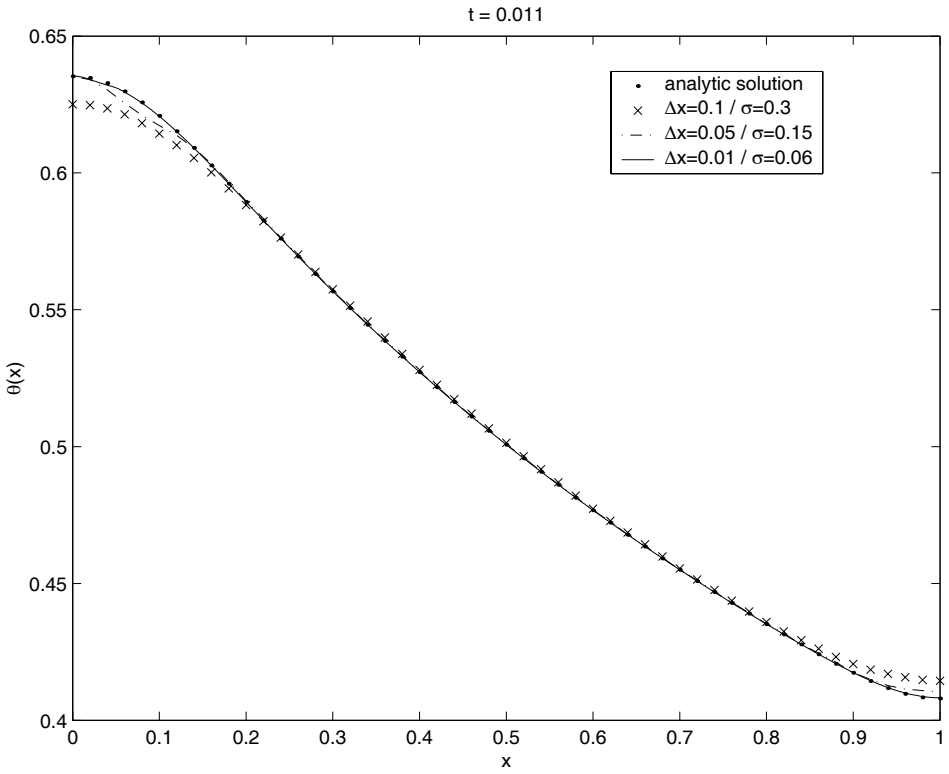

Figure 2-11: Profiles at $t = 0.011$ for different numerical parameters compared against the analytical solution obtained from (2.44)

Chapter 3

Vorticity Formulation of Transverse Jets

In this chapter, we present vorticity formulation of transverse jets. Details of numerical implementation are discussed, though the main part of the scheme is more or less the same to the numerical method used to investigate vortex rings, given in the previous chapter. The new components in this chapter are boundary conditions and vorticity introduction mechanisms, since the computational domain is not any more $\mathbf{R}^3$. Redundancy in description is maintained to ensure the presentation in this chapter self-contained, so that one needs to consult only this chapter to understand the results of simulations given in the following chapters.

3.1 Governing equations and numerical formulation

3.1.1 Governing equations

Equations of motion for viscous, incompressible flow may be written in the following velocity-vorticity formulation, where $\boldsymbol{\omega} = \nabla \times \mathbf{u}$:

$$\frac{D\boldsymbol{\omega}}{Dt} = \boldsymbol{\omega} \cdot \nabla \mathbf{u} + \nu \Delta \boldsymbol{\omega}, \quad \nabla \cdot \mathbf{u} = 0, \tag{3.1}$$

Using the Helmholtz decomposition, we may write

$$\mathbf{u} = \mathbf{u}_\omega + \mathbf{u}_p, \tag{3.2}$$

where $\mathbf{u}_\omega$ is recovered by the Biot-Savart law

$$\mathbf{u}_\omega(\mathbf{x}, t) = -\frac{1}{4\pi}\int_\Omega \frac{(\mathbf{x}-\mathbf{x}')\times\boldsymbol{\omega}(\mathbf{x}', t)}{|\mathbf{x}-\mathbf{x}'|^3} d\mathbf{x}' = \mathbf{K}\star\boldsymbol{\omega}, \tag{3.3}$$

where the following notation is used:

$$(\mathbf{F}\star\mathbf{G})(\mathbf{x}) \equiv \int_\Omega \mathbf{F}(\mathbf{x}, \mathbf{y})\times\mathbf{G}(\mathbf{y}) d\mathbf{y}, \tag{3.4}$$

and

$$\mathbf{K}(\mathbf{x}, \mathbf{y}) = -\frac{1}{4\pi}\frac{\mathbf{x}-\mathbf{y}}{|\mathbf{x}-\mathbf{y}|^3}. \tag{3.5}$$

$\mathbf{u}_p$ is a divergence-free potential velocity field ($\mathbf{u}_p = -\nabla\phi$) to satisfy a prescribed normal velocity on the boundary of the given domain Ω:

$$\Delta\phi = 0 \quad \text{in} \quad \Omega, \qquad \mathbf{n}\cdot\mathbf{u}_\omega + \mathbf{n}\cdot\mathbf{u}_p = \mathbf{n}\cdot\mathbf{u} \quad \text{on} \quad \partial\Omega \tag{3.6}$$

Vorticity is generated at the boundary, and introduced either by a separated flow or by the action of diffusion. Together, these equations completely describe the motion of an incompressible, viscous flow.

3.1.2 Three-dimensional vortex methods

A three-dimensional vortex element method [42, 14] is used to perform the simulation of an unsteady, incompressible transverse jet at a finite Reynolds number. We employ a viscous splitting algorithm: the evolution of the flow field is considered in discrete fractional steps, where the vorticity field is first convected and then diffused [14, 48]. The algorithm consists of substeps where the convective and the diffusive effects are considered separately. In this way, the computational advantages of Lagrangian vor-

tex methods, that is, minimal dispersion/dissipation, no restriction from the CFL condition, and optimal utilization of computational elements, are automatically inherited without being compromised.

During the convection substep, we solve the equations of motion for inviscid incompressible flow in vorticity transport form:

$$\frac{D\boldsymbol{\omega}}{Dt} = \boldsymbol{\omega} \cdot \nabla \mathbf{u}, \quad \nabla \cdot \mathbf{u} = 0. \tag{3.7}$$

Numerical solution of this equation proceeds by discretization of the vorticity field onto overlapping vector elements, each centered at χ_i^c with volume dV_i and vorticity ω_i:

$$\boldsymbol{\omega}(\mathbf{x}, t) \approx \sum_i^N [\boldsymbol{\omega}_i dV_i](t) f_\sigma(\mathbf{x} - \boldsymbol{\chi}_i^c(t)). \tag{3.8}$$

The vorticity associated with each element is localized by a radially symmetric core function f_σ of radius σ, where $f_\sigma(\mathbf{x}) = \frac{1}{\sigma^3} f(\frac{|\mathbf{x}|}{\sigma})$. Here we employ the Rosenhead-Moore kernel as the core function [58, 52], which yields

$$\mathbf{u}_\omega(\mathbf{x}, t) \approx \sum_i^N -\frac{1}{4\pi} \frac{\mathbf{x} - \boldsymbol{\chi}_i}{\left(|\mathbf{x} - \boldsymbol{\chi}_i|^2 + \sigma^2\right)^{3/2}} \times [\boldsymbol{\omega}_i dV_i] \tag{3.9}$$

from the Biot-Savart law (3.3). Each vortex element is described as a 'stick' by expressing the particle strength $[\boldsymbol{\omega}_i dV_i](t) = \Gamma_i(t)\boldsymbol{\delta\chi}_i(t)$, where $\boldsymbol{\delta\chi}_i(t)$ represents a material line element. The positive scalar weight Γ_i is the circulation contained in the material line element. The vector $\boldsymbol{\delta\chi}_i$ points in the direction of the vorticity, and is described with two nodes. Each node is simply advected by the velocity field:

$$\frac{d\boldsymbol{\chi}_i}{dt} = \mathbf{u}(\boldsymbol{\chi}_i). \tag{3.10}$$

Advecting the nodes accounts for deformation of the material line element $\boldsymbol{\delta\chi}_i$, and thus for stretching and tilting of the vorticity. A second order predictor/corrector scheme with adaptive time-step control is used for time integration of the ordinary differential equations in (3.10), where the velocity at each node $\mathbf{u}(\boldsymbol{\chi}_i)$ is evaluated

by an adaptive tree-code [45]. When $|\boldsymbol{\delta\chi}_i|$ of a given element exceeds 0.9σ, a new node is added. The parallel implementation of the adaptive tree-code is achieved by a domain decomposition using the k-means clustering technique [50].

During the diffusion substep, a modified interpolation kernel is used [73]. At each step, the solution of the diffusion equation is approximated by a new set of particles, which lie on a uniform grid over a region encompassing the support of the particle distribution from the previous step. These new set of particles is obtained by interpolating each particle from the previous step onto its neighboring grid points, i.e., for each grid point, whose index is given as j,

$$[\boldsymbol{\omega}_j dV_j]^{n+1} = \sum_i^N f_{ij} [\boldsymbol{\omega}_i dV_i]^n, \tag{3.11}$$

where f_{ij} is the redistribution fraction from the ith particle to the grid point. f_{ij} is obtained by using the interpolation kernel Λ_3 [73]:

$$f_{ij} = \Lambda_3\left(\frac{x_j - x_i}{\Delta x}\right)\Lambda_3\left(\frac{y_j - y_i}{\Delta x}\right)\Lambda_3\left(\frac{z_j - z_i}{\Delta x}\right) \tag{3.12}$$

where

$$\Lambda_3(\xi; c) = \begin{cases} 1 - 2c^2 + |\xi|\left(3c^2 - \frac{1}{2}\right) - \xi^2 + \frac{|\xi|^3}{2} & : \quad |\xi| < 1 \\ (2 - |\xi|)\left(\frac{1}{6}(3 - |\xi|)(1 - |\xi|) + c^2\right) & : \quad 1 \le |\xi| < 2 \\ 0 & : \quad 2 \le |\xi| \end{cases} \tag{3.13}$$

Here $c = \sqrt{\nu \Delta t_d}/\Delta x$, which represents the ratio between the diffusion length scale and the grid size Δx. Δt_d is the time step size for the diffusion substep, which can be different from the time step size for the convection substep Δt_c. Usually, to have enough resolution in convection calculation, Δt_c is chosen to be a fraction of Δt_d, and in that case, a few convection substeps are performed for one diffusion substep.

After interpolation, we eliminate particles with $|\boldsymbol{\omega}_j dV_j| < |\boldsymbol{\omega} dV|_{\text{del}}$ to control the problem size. The value of $|\boldsymbol{\omega} dV|_{\text{del}}$ is chosen to be at least two order of magnitude

smaller than the strength of elements showing the vortical structures we are interested in. Finally, each particle on the grid is converted back into a stick, having its center $\boldsymbol{\chi}_j^c$ at the grid point that it lies on and $|\boldsymbol{\delta\chi}_j| = 0.6\sigma$. This conversion completes the entire step including convection and diffusion.

3.1.3 Computational domain and boundary conditions

The coordinate system we use in computation is the same as that shown in Figure 1-3. The center of the jet nozzle exit is at the origin. All variables are made dimensionless by d, the jet diameter, and U_∞, the speed of the crossflow. The jet velocity, V_j, is specified by the jet-to-crossflow momentum ratio r, i.e., $r = V_j/U_\infty$. The crossflow is directed in the positive x direction, and the jet centerline is aligned with the y axis. The plane of $y = 0$ is considered as a solid wall, except at the jet orifice. We impose symmetry across $z = 0$. This assumption has been verified by full three-dimensional simulations without imposed symmetry at similar conditions, for shorter runs.

To enforce the normal-velocity boundary condition at $y = 0$ during each convection substep, an image vorticity distribution is placed in $y < 0$ during the evaluation of velocity:

$$\boldsymbol{\omega}_{\text{img,conv}}(x, y, z) = -\omega_x(x, -y, z)\hat{\mathbf{e}}_x + \omega_y(x, -y, z)\hat{\mathbf{e}}_y - \omega_z(x, -y, z)\hat{\mathbf{e}}_z. \tag{3.14}$$

The jet outflow is represented by a semi-infinte cylindrical vortex sheet of radius $1/2$ extending from $y = 0$ to $y = -\infty$, with strength $\boldsymbol{\gamma} = -2r\hat{\mathbf{e}}_\theta$. For numerical implementation, this column of vortex sheet is terminated at $y = -5$, which is enough for the domain we are interested in. The crossflow velocity is modeled by a potential $\phi_\infty = -x$.

During each diffusion substep, wall-tangential vorticity is treated with the homogeneous Neumann boundary condition, i.e., $\frac{\partial \omega_x}{\partial y} = \frac{\partial \omega_z}{\partial y} = 0$, at $y = 0$. On the other hand, wall-normal vorticity flux is given in order to satisfy $\nabla \cdot \boldsymbol{\omega} = 0$ at $y = 0$. This condition for wall-normal vorticity is, in practice, only important for the case with the full no-slip boundary condition, where substantial wall-normal vorticity may exist

near the boundary. Just as in velocity evaluation, this apparently complicated set of boundary conditions are implemented by placing an image in $y < 0$:

$$\boldsymbol{\omega}_{\text{img,diff}}(x, y, z) = -\boldsymbol{\omega}_{\text{img,conv}}(x, y, z). \tag{3.15}$$

Finally, to control the number of vortex elements, we gradually increase our deletion cutoff $|\boldsymbol{\omega} dV|_{\text{del}}$ from $x = 7$, and we delete all the elements with $x \geq 10$ as the exit boundary condition. We have not seen a severe impact on the near-field jet evolution from this exit boundary treatment, but there is possibility that the far-field evolution of our jet might have been affected.

3.2 Vorticity introduction at the boundary of the domain

The scheme presented in the previous section describes how vorticity behaves in the computational domain, i.e., $y > 0$ in this case. In this section, we describe how to introduce vorticity into the domain, which is equally important.

3.2.1 No-slip boundary condition in vortex methods

As described in the previous section, our numerical scheme relies on splitting of the vorticity transport equation into an inviscid and a viscous part. Implementation of the no-slip boundary condition in this case is complicated by the fact that the convection substep in the algorithm can only handle the impermeability of the solid wall, which is, in our case, treated by having an image vorticity distribution, i.e, (3.14), during the calculation of the velocity field. As the result, the diffusion substep in the algorithm starts with a velocity field violating its boundary condition [14].

A typical way to resolve the difficulty is to include another substep just before the start of the diffusion substep. In the substep, which is referred as the generation substep, a singular vorticity distribution at the boundary, i.e., a vortex sheet, with a strength just enough to cancel the jump of the tangential component of the velocity

is created. This vortex sheet newly generated enables the diffusion substep to start with a velocity field that does satisfy the no-slip boundary condition. The newly generated vortex sheet has to be considered as part of the interior vorticity in the subsequent substeps, and the diffusion substep immediately regularizes the singular vortex sheet into a regular boundary layer. We refer the tangential component of the velocity on the wall recorded just before the generation step as the slip velocity and denote it as $\mathbf{u}_{\text{slip}}$.

Just after the generation substep, the tangential velocity on the wall is zero as long as we consider the vortex sheet generated as part of the interior vorticity. Subsequent convection and diffusion substeps cause deviation from the no-slip boundary condition, which is again cancelled by the vortex sheet generated during the next generation step. In this sense, the no-slip boundary condition is satisfied at the order of Δt during overall computation. Accordingly, each generation step, except the very first generation step, introduces a new vortex sheet, whose strength per unit area is $O(\Delta t)$. That is, at each time step, we introduce a new vorticity distribution of its strength $O(\Delta t)$ into the computational domain from the solid wall boundary to satisfy the no-slip boundary condition at the solid wall.

3.2.2 Modeling of boundary generation of vorticity for transverse jets

The description provided in the previous section provides a glimpse on the generic strategy used in vortex methods to satisfy the no-slip boundary condition over the solid wall. Though it is also true in our case that vorticity is introduced into the computational domain through the no-slip boundary condition, this route of introduction is not the only one source of vorticity in transverse jets. We have two major sources of vorticity. One is the advected jet shear layer developed from the jet nozzle pipe, and the other is the vortex sheet introduced to satisfy the no-slip boundary condition. On top of these vortex sheets, we need to consider the solenoidality of the vortex sheet generated at each time step. Such special issues about transverse jets

are discussed here in details.

In the case of transverse jets, as briefly introduced in the previous paragraph, vorticity is introduced into the domain from two sources:

1. Vorticity is introduced from the jet shear layer developed from the jet nozzle pipe at $y < 0$. The introduction of vorticity is purely convective. We refer it as $\boldsymbol{\gamma}_j$.

2. A vortex sheet is formed on the wall ($y = 0$) as previously described. We refer this vortex sheet as $\boldsymbol{\gamma}_w$. The vortex sheet has two routes toward the computational domain of $y > 0$. On one hand, it may be introduced to the domain via viscous diffusion. On the other hand, it may be introduced to the domain by being lifted at the jet nozzle exit, purely through advection. This route is derived by considering the solenoidal continuation of $\boldsymbol{\gamma}_w$, which is referred as $\boldsymbol{\gamma}_c$.

Figure 3-1 schematically shows each of these sources. Major coordinate variables are also shown in the figure. In the following, we describe each of them in details.

Vorticity produced in the jet boundary layer at $y < 0$ is represented by a single sheet of azimuthal vorticity. Introducing this vorticity into the flow as a cylindrical vortex sheet, we have

$$\boldsymbol{\gamma}_j = -r\hat{\mathbf{e}}_\theta \quad \text{for} \quad y \ll 1 \tag{3.16}$$

in the jet column.

The azimuthal vorticity given in (3.16) does not provide a complete picture of the jet near field, however. For $\rho > 1/2$, a vortex sheet is formed on $y = 0$:

$$\boldsymbol{\gamma}_w = \hat{\mathbf{e}}_y \times \mathbf{u}_{\text{slip}}, \tag{3.17}$$

where $\mathbf{u}_{\text{slip}}$ is the slip velocity on the surface of the wall. The wall vortex sheet, $\boldsymbol{\gamma}_w$, is solenoidal by construction for $\rho > 1/2$, since

$$\int_{0^-}^{0^+} (\nabla \cdot \boldsymbol{\gamma}_w)\, dy = \int_{0^-}^{0^+} \left(\frac{\partial \omega_x}{\partial x} + \frac{\partial \omega_z}{\partial z} \right) dy + \omega_{y,y=0^+} - \omega_{y,y=0^-} = 0. \tag{3.18}$$

We have used the following relations:

$$\omega_x = u_z \delta(y), \tag{3.19}$$

$$\omega_z = -u_x \delta(y), \tag{3.20}$$

$$\omega_{y,y=0^-} = 0, \tag{3.21}$$

and

$$\int_{0^-}^{0^+} \left(\frac{\partial \omega_x}{\partial x} + \frac{\partial \omega_z}{\partial z} \right) dy = \left(\frac{\partial u_z}{\partial x} - \frac{\partial u_x}{\partial z} \right) \Big|_{y=0} = -\omega_{y,y=0^+} \tag{3.22}$$

This solenoidality is, however, violated at $\rho = 1/2$, unless each vortex filament is continued from the wall ($\rho > 1/2$ and $y = 0$) to the jet column ($\rho = 1/2$ and $y > 0$) in an appropriate way.

To make an appropriate connection, we separate $\boldsymbol{\gamma}_w$ into azimuthal and radial components, and examine how each component behaves at the jet nozzle boundary. The azimuthal component, $\gamma_{w,\theta} = \boldsymbol{\gamma}_w \cdot \hat{\mathbf{e}}_\theta$, is simply advected by the local velocity, which is assumed to be $V_j \hat{\mathbf{e}}_y/2 = r\hat{\mathbf{e}}_y/2$, without experiencing any tilting or stretching. Thus, writing $\boldsymbol{\gamma}_c = \gamma_{c,y}\hat{\mathbf{e}}_y + \gamma_{c,\theta}\hat{\mathbf{e}}_\theta$, we have

$$\gamma_{c,\theta}|_{\rho=1/2,y=0} = \gamma_{w,\theta}|_{\rho=1/2,y=0}\,. \tag{3.23}$$

In the following, we define $f(\theta) \equiv \gamma_{w,\theta}|_{\rho=1/2,y=0}$. The radial component, $\gamma_{w,\rho} = \boldsymbol{\gamma}_w \cdot \hat{\mathbf{e}}_\rho$, on the other hand, does experience tilting towards the direction of the jet. At the nozzle boundary, solenoidality requires that

$$|\boldsymbol{\gamma}_w| = |\boldsymbol{\gamma}_c|. \tag{3.24}$$

This is obtained by applying the divergence theorem to the vortex filament, which essentially states that the circulation should remain constant along each vortex filament. Additionally considering the sense of rotation ω_ρ experiences across the jet

shear layer, we find

$$\gamma_{c,y}|_{\rho=1/2,y=0} = -\gamma_{w,\rho}|_{\rho=1/2,y=0}\,. \tag{3.25}$$

In the following, we define $g(\theta) \equiv -\gamma_{w,\rho}|_{\rho=1/2,y=0}$.

Now, we extend (3.23) and (3.25) to $y > 0$ by enforcing $\boldsymbol{\gamma}_c$ to be solenoidal. For $y \ll 1$, we assume that the jet column is a cylinder heading straight upward. We apply $\nabla \cdot \boldsymbol{\omega} = 0$ on this cylindrical surface, which yields

$$\frac{\partial \gamma_{c,y}}{\partial y} + 2\frac{\partial \gamma_{c,\theta}}{\partial \theta} = 0. \tag{3.26}$$

Integrating (3.26) from $y = 0$, we get

$$\boldsymbol{\gamma}_c = f(\theta)\hat{\mathbf{e}}_\theta + (g(\theta) - 2yf'(\theta))\hat{\mathbf{e}}_y. \tag{3.27}$$

By summing (3.16) and (3.27), the complete jet column vortex sheet for $y \ll 1$ is now given as follows:

$$\boldsymbol{\gamma}_j + \boldsymbol{\gamma}_c = (-r + f(\theta))\hat{\mathbf{e}}_\theta + (g(\theta) - 2yf'(\theta))\hat{\mathbf{e}}_y. \tag{3.28}$$

(3.17) and (3.28) completely describe the vortex sheet on the wall and that on the jet column, respectively. The only thing assumed is that $\mathbf{u} = V_j\hat{\mathbf{e}}_y/2$ over the jet nozzle boundary.[1] Note that this condition is actually what we impose around the jet nozzle boundary, i.e., a boundary condition, rather than an assumption. However, as discussed previously, the no-slip boundary condition is satisfied during the overall computation procedure only at the order of $O(\Delta t)$. That is, the simulated flow field does not have to satisfy the condition exactly at the very instance we generate $\boldsymbol{\gamma}_w$ or $\boldsymbol{\gamma}_c$. Since the deviation of the slope of the jet shear layer surface from the straight upward direction for $y \ll 1$ is estimated to be at most $O(\Delta t/r)$, it is safe to assume this condition in our cases with relatively high r.

[1]The cylindrical geometry of the jet column, assumed during the derivation, is essentially a condition derived from this assumption on the jet velocity field. The integration of the velocity field leads to a cylindrical jet column straight upward.

In Figure 3-1, the geometry of each vortex sheet is schematically illustrated. These vortex sheets represent vorticity newly generated at the boundary at each instance, but their behaviors are different. The vortex sheet on the jet column (3.28) is located at $y > 0$, and experience the influence of both convection and diffusion. On the other hand, the vortex sheet on the wall (3.17) leaves the wall only by diffusion. Before leaving the wall, it does not affect the flow in $y > 0$, since its effect is exactly cancelled by its image (3.14). This is a particularly important observation, since an unseparated thin wall vortex sheet, whose boundary layer thickness is much smaller than major jet structures, can be effectively modeled by preventing the wall vortex sheet from diffusing into the domain of $y > 0$. With this statement in mind, in the rest of this section, we describe two numerical approaches to discretize (3.17) and (3.28).

3.2.3 Numerical implementations

Here, two numerical approaches to discretize (3.17) and (3.28) are presented. The first method allows the wall vortex sheet to diffuse, while the second method does not. Comparing the results, we can evaluate how the separation of the wall vortex sheet affects the behavior of the jet.

In the first approach, the full no-slip boundary condition is implemented along the solid wall, and both the wall vortex sheet and the jet vortices evolve as described by the governing equations. To account for the wall vortex sheet, the surface of the wall is divided into triangular and rectangular elements. Each surface element has its area, dA_i, and a collocation point at its center, $\mathbf{x}_{col,i}$. Just before each diffusion substep, slip velocity at each collocation point is computed. Once the slip velocity, $\mathbf{u}_{\text{slip},i} = \mathbf{u}(\mathbf{x}_{col,i})$, is obtained, a vortex element with its strength $[\boldsymbol{\omega}_i dV_i] = (\hat{\mathbf{e}}_y \times \mathbf{u}_{\text{slip},i}) dA_i$ is generated at the collocation point.[2]

To account for the jet column vortex sheet, we introduce new elements near the

[2]When $\mathbf{u}_{\text{slip}}$ is evaluated for each collocation point on the plane of $y = 0$, a vortex element close to the collocation point, i.e., within a distance comparable to σ, is interpreted as having its core size smaller than σ, proportional to its distance from the plane of $y = 0$. The reason for this special treatment is to avoid the cancellation of vorticity due to the existence of the image of the vortex element, which may otherwise lead to excessive vorticity introduction to the computational domain.

nozzle boundary every Δt_{noz} time units. Each new set of vortex elements introduced near the jet nozzle boundary is the discretized version of (3.28) for $0 < y < r\Delta t_{noz}/2$, which corresponds to the vorticity introduced into the flow during the period of Δt_{noz}. We thus introduce elements so that their centers lie at $y = r\Delta t_{noz}/4$. In the azimuthal direction, we divide it among n_θ vortex elements. Taking the center of each element as the collocation point, we obtain the following expression for the total strength of the vortex elements:

$$\begin{aligned}[\boldsymbol{\omega}_i dV_i] &= \left(-\frac{r^2}{4} + \frac{r}{4} f(\theta)\right) \hat{\mathbf{e}}_\theta \Delta t_{noz} \Delta\theta \\ &+ \left(\frac{r}{4} g(\theta) - \frac{r^2 \Delta t_{noz}}{8} f'(\theta)\right) \hat{\mathbf{e}}_y \Delta t_{noz} \Delta\theta, \end{aligned} \tag{3.29}$$

where $\Delta\theta = 2\pi/n_\theta$. $f(\theta)$ and $g(\theta)$ are computed by evaluating $\mathbf{u}_{\text{slip}}$ at the nozzle boundary.[3] Note that this approach completely accounts for all the interactions between the wall vortex sheet and the jet column.

In the other approach, which was used in [51], the wall vortex sheet exists due to the slip induced by the crossflow, but is assumed to stay at the wall without being diffused into the computational domain of $y > 0$. Neglecting the feedback from the vorticity in the domain, we approximately express the wall vortex sheet as $\boldsymbol{\gamma}_w = -\hat{\mathbf{e}}_z$. As mentioned earlier, since $\boldsymbol{\gamma}_w$ never leaves the wall due to lack of diffusion, we do not have to explicitly generate vortex elements for $\boldsymbol{\gamma}_w$. The existence of this vortex sheet only affects the jet at the nozzle boundary, where nontrivial $\boldsymbol{\gamma}_c$ is generated by the solenoidal connection of vortex filaments. Since $f(\theta) = -\cos\theta$ and $g(\theta) = \sin\theta$ in this case, substitution into (3.29) gives new vortex elements near the jet nozzle

[3] In principle, $\mathbf{u}_{\text{slip}}$ should be evaluated just outside of the jet shear layer, i.e., at $\rho = d/2^+$, since the jet shear layer forms a sharp discontinuity in the velocity field. For the jet shear layer is smoothed with a core function in actual numerical implementations, the best location to evaluate $\mathbf{u}_{\text{slip}}$ may show dependency on the core size σ, which is left as a subject of further study.

boundary every Δt_{noz} time units:

$$\begin{aligned}[\boldsymbol{\omega}_i dV_i] &= \left(-\frac{r^2}{4} - \frac{r}{4}\cos(\theta)\right)\hat{\mathbf{e}}_\theta \Delta t_{noz}\Delta\theta \\ &+ \left(\frac{r}{4}\sin(\theta) - \frac{r^2\Delta t_{noz}}{8}\sin(\theta)\right)\hat{\mathbf{e}}_y \Delta t_{noz}\Delta\theta. \end{aligned} \tag{3.30}$$

The expression (3.30) is identical to the expression given by [51]. Note that (3.29) is more rigorously derived here by considering the solenoidality of the vorticity field. (3.30) is just a special case with the assumption that $\boldsymbol{\gamma}_w = -\hat{\mathbf{e}}_z$.

We name the former as the *full no-slip boundary condition* and the later as the *reduced vorticity influx model*. Comparing the results of these two distinct vorticity introduction mechanism, we can identify the effects of wall-vortex separation on the behavior of transverse jets. Especially, many of near-field vortical structures, including tornado-like foci experimentally observed on the lee side of the jet [33], are the results of the separation of the wall boundary layer, and hence they are excluded a priori in the reduced model, where the effect of the wall boundary layer is only implicitly included by its solenoidal continuation, i.e., $\boldsymbol{\gamma}_c$.

In the following chapters, we first investigate jets with the reduced vorticity influx model. Then, the results with the full no-slip boundary condition are presented in order to emphasize how differently the jet near-field behaves. There, we get near-field vortical structures including tornado-like foci, which contribute to the formation of counter-rotating vorticity.

3.3 Numerical scheme summarized

An overview of the numerical scheme is given in this section for quick reference. For cases with the full no-slip boundary condition, each computational step proceeds as follows:

1. Given a filament configuration, by using a second order predictor/corrector scheme with adaptive time-step control, (3.10) is integrated to treat the convection substep. Since Δt_c is a fraction of Δt_{noz}, multiple convection substeps

are performed before proceeding to the next substep. For cases with the full no-slip boundary condition, we set $\Delta t_{noz} = \Delta t_d$.

2. New vortex elements corresponding to $\boldsymbol{\gamma}_w$ are created to satisfy the no-slip boundary condition.

3. By using (3.11), particles are interpolated to a uniform grid to treat the diffusion substep. At the end of the substep, the interpolated particle distribution is converted to filaments.

4. New vortex elements corresponding to $\boldsymbol{\gamma}_j$ and $\boldsymbol{\gamma}_c$ are created, according to (3.29).

5. t is advanced by Δt_{noz}.

For cases with the reduced vorticity influx model, each computational step proceeds as follows:

1. Given a filament configuration, by using a second order predictor/corrector scheme with adaptive time-step control, (3.10) is integrated to treat the convection substep. Since Δt_c is a fraction of Δt_{noz}, multiple convection substeps are performed before proceeding to the next substep.

2. If t is a multiple of Δt_d, which is usually a multiple of Δt_{noz} for cases with the reduced vorticity influx model, particles are interpolated to a uniform grid by using (3.11). At the end of this diffusion substep, the interpolated particle distribution is converted to filaments.

3. New vortex elements corresponding to $\boldsymbol{\gamma}_j$ and $\boldsymbol{\gamma}_c$ are created, according to (3.30).

4. t is advanced by Δt_{noz}.

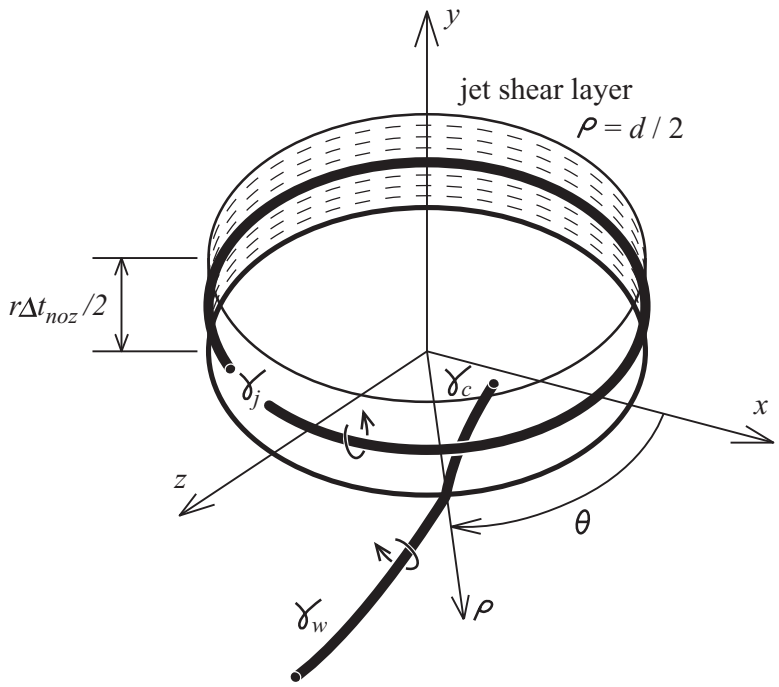

Figure 3-1: Schematic illustration of vortex sheets near the jet nozzle exit. The circle at $\rho = 1/2$ and $y = 0$ represents the jet nozzle boundary. $\boldsymbol{\gamma}_w$ represents the wall vortex sheet on $y = 0$, $\boldsymbol{\gamma}_j$ and $\boldsymbol{\gamma}_c$ form the jet column for $y \ll 1$.

Chapter 4

Results: Vorticity Dynamics of Transverse Jets

4.1 Transverse jets with the reduced vorticity influx model

Two cases are investigated with the reduced vorticity influx model: one with $r = 7$ (Case I) and the other with $r = 10$ (Case II). Both cases are having the same Reynolds number based on the crossflow speed, $Re_\infty = U_\infty d/\nu = 245$. The Reynolds numbers based on the jet flow speed are $Re_j = V_j d/\nu = 1715$ and 2450 respectively. The core size, σ, is chosen to be 0.1, which was the value used in [51]. The grid size for interpolation, Δx, is 0.035, which gives the overlap ratio, $\sigma/\Delta x$, around 3 to ensure smooth recovery of the velocity field. Both simulations are performed with $\Delta t_d = 0.06$. Δt_{noz} is set to be 0.02 in Case I, and is set to be 0.01 in Case II, to ensure overlap between vortex elements subsequently introduced around the jet nozzle boundary. Δt_c is automatically adjusted.

Jets are started at $t = 0$ and then allowed to evolve for a while to acquire statistically stationary states. Jet centerline-streamline trajectories are monitored until statistically stationary states are obtained. Jet trajectories have been settled down, roughly at $t = 12.0$ in Case I, and at $t = 15.0$ in Case II. Analysis is performed for the

data obtained after these instances. An example of computational element distribution is plotted in Figure 4-1. Computational elements are located only in part of the entire computational domain, which results in efficient utilization of memory. The number of vortex elements in Case I is plotted in Figure 4-2. Initially, the number of vortex elements almost linearly grows as the jet penetrates into the computational domain. The growth is attenuated at the instance around $t = 6$, when vortex elements start to advect out through the exit plane placed at $x = 7$. Case II shows a similar trend, but uses more elements, since the jet penetrates the computational domain deeper. The number of vortex elements used in Case II is about twice of that used in Case I.

We present the jet trajectory, and describe a few notable vortical structures including the counter-rotating vortex pair. The mechanism behind the formation of the counter-rotating vortex pair is investigated with Lagrangian diagnostics. The mechanism bears great similarity to what we have discovered in our previous inviscid simulations [51]. Finally, since a rapid transition from large-scale coherent structures to small-scale structures is observed in our simulations, the mechanism leading to the proliferation of small-scale structures is investigated.

4.1.1 Trajectories and overall flow features

The trajectory for each case is provided by the jet centre streamline shown in Figure 4-3. The streamline for Case I is obtained by averaging the velocity field during $t \in [12.0, 17.6]$, while that for Case II is obtained for $t \in [15.0, 20.0]$. In Figure 4-3, our results are compared against two references. One is the widely referred correlation (1.2), which was obtained by Margason [49]. Trajectories with $r = 7$ and $r = 10$ are plotted based on the correlation. The other set of data was experimentally obtained by Keffer and Baines [32]. Though there is some tendency that the penetration of the jet into the crossflow is underestimated in Case I, Figure 4-3 clearly shows that our trajectories are within a reasonable range.

The averaged streamlines are also compared to the scaling laws, i.e., (1.3) and (1.4), developed by Hasselbrink and Mungal [28], in Figure 4-4. As one may see, the

matching is not perfect. This discrepancy is actually expected, since these scaling laws are proposed for relatively high jet-to-crossflow momentum ratios ($r \geq 20$), as discussed in Chapter 1. Considering the fact that $r = 7$ and 10 in our simulations, it is understandable for the near-field scaling law to show difference from our jet trajectory. Rather the more remarkable thing is that the far-field 1/3 power law is closely followed by the streamline of Case II, where $r = 10$. The far-field 1/3 power law does seem to be more robust, because it is less affected by subtle conditions near the exit of the jet.

It should be noted that the discussion on trajectories is only tentatively presented here. The objective of the comparison here is rather to show the validity of our simulation results. The trajectories we have observed in both cases are in physically reasonable ranges, suggesting the mechanistic descriptions of vorticity dynamics given in the following subsections are likely observed in real transverse jets.

Instantaneous snapshots of vorticity iso-surfaces for Case I are given in Figures 4-5 and 4-6. To give better insights on the overall flow features, we also plot the mirror image across the $z = 0$ plane, though the simulation is performed only in one of the half spaces. Two of the most important features can be readily identified: the roll-up of the jet shear layer at the windward side, resulting from a mechanism similar to the Kelvin-Helmholtz instability, and the counter-rotating vortex pair at the lee side. While both structures have been reported in our previous inviscid study [51], the vortical structures in Figures 4-5 and 4-6 are more readily identifiable, since this result is obtained at the stationary state, not during the early transient period. A few discrepancies from the previous simulation results should be pointed out. For instance, the roll-up of the shear layer is delayed from what we have observed in [51]. This delay seems to be mainly due to the effect of viscosity, which attenuates the growth of the instability.

The flow field exhibits much unsteadiness. As described in the previous paragraph, the periodic roll-up of the jet shear layer, i.e., the Kelvin-Helmholtz instability, is one among various mechanisms showing unsteadiness. Additional complication of the flow field is observed further downstream, as shown in Figure 4-7, where we plot the

instantaneous jet centre streamline at $t = 12.0$ and the average jet centre streamline simultaneously. We also put contours for the velocity magnitude, i.e., $|\mathbf{u}|$ alongside. The downstream region of the jet is contaminated by much action of rather small-scale flow structures, as clearly seen in the contour lines. With such unsteadiness, the undulating instantaneous jet centre streamline naturally deviates from the average one. Small-scale vortical structures are also shown in Figure 4-5. Especially, we note that there exists rather a sudden transition from the large-scale coherent structures into the small-scale structures in Case I.

The sudden transition from the large scales to the small scales can also be observed in velocity power spectra. Figure 4-8 shows the power spectra of the spanwise fluctuation velocity u'_z at three different locations. Near the jet nozzle exit, where the Kelvin-Helmholtz instability of the jet shear layer is the dominant unsteady dynamics, the energy is mostly concentrated around $St = fd/U_\infty \approx 3.5$, where f stands for the frequency. This peak frequency corresponds to the frequency of the roll-up at the windward side. The Strouhal number based on the jet is given by $St_j \equiv St/r$, which is around 0.5 in Case I. This is lower than that observed in [51], in which $St_j \approx 0.8$ was reported in a similar condition. As the structure propagates downstream, the frequency spectrum loses the signature of the roll-up rather quickly, and there is no distinct periodicity observed around one rd away from the jet nozzle exit. The coherency of the jet shear layer vortices is lost by the development of the small scales.

We emphasize that such a small-scale proliferation does not completely eliminate the signature of all the large-scale structures. Apparently, the signature of the periodic roll-up disappears quickly, but the counter-rotating vortices survive. We illustrate this point by presenting Figures 4-9 and 4-10, where contours of streamwise vorticity, i.e. ω_x, on the plane of $x/d = 3$. The instantaneous structure of the jet cross section is extremely complex and apparently dominated by small scales. However, although the vorticity field appears almost unorganized, it does preserve the signature of counter-rotating vortices. Following previous researchers [51, 76], we use a low-pass spatial filter to the streamwise vorticity field. A two-dimensional filter with cut-off

wavenumber $2/d$ is applied. Much more organized, clear counter-rotation is evident in the filtered vorticity field. Thus, it is obvious that the counter-rotating vortices, as an underlying structure, still survive the development of the small-scale structures for an extended region of jet downstream.

Case II shows similar flow features. Figure 4-11 shows the vorticity isosurfaces at $t = 16.0$. The roll-up of the jet shear layer happens on the windward side. The frequency of the roll-up phenomena is roughly $St_j \approx 0.5$, i.e., the same as that in Case I. The interaction of the jet shear layer vortices and the counter-rotating vortex pair leads to the breakdown of coherent structures into small-scale structures, contaminating large part of the computational domain as shown in Figure 4-12, where vorticity isosurfaces of a relatively low value is taken to emphasize the point. Once generated, these small-scale structures are weakened by viscosity. By increasing the value of vorticity magnitude, weak structures in the downstream are eliminated as shown in Figure 4-11. The sudden proliferation of the small-scale structures are triggered by a critical transition, which will be discussed in the later.

4.1.2 Shear layer roll-up and counter-rotating vorticity formation

We pursue mechanistic descriptions of vorticity dynamics in transverse jets. Since the vorticity dynamics is more properly depicted in the Lagrangian viewpoint rather than in the Eulerian one, a Lagrangian diagnostics, i.e., material element tracking, is employed. It should be noted that vorticity lines are not identical to material lines in viscous flows in general. Still, these two are well matched in our simulations. Only at relatively small scales, these lines show deviation from each other. We use the material elements as the surrogates of vortex filaments. These material elements gives appropriate descriptions on the development of large-scale vortical structures and their early breakdown into three-dimensional small-scale structures.

As we have pointed in the previous subsection, two major coherent vortical structures are identified: the roll-up of the shear layer at the windward side and the

counter-rotating vortex pair. To investigate the vorticity dynamics leading to the formation of these structures, we introduced ten material rings at the nozzle exit during $t \in [12.0, 12.36]$ in Case I. The snapshots showing the evolution of the material rings are given in Figures 4-13 and 4-14. The roll-up of the shear layer is manifested by the axial grouping of vortex filaments, which are represented by material rings in Figure 4-13. This grouping is usually visible on the windward side of the jet.

On the lee side, a complex out-of-plane distortion of the material line elements occurs, which eventually leads to the formation of the counter-rotating vortex pair. Upon introduction, the vorticity is primarily azimuthal and essentially aligned along material rings. The material rings shown in Figures 4-13(a) and 4-14(a), initially planar, gradually initiates out-of-plane distortion on the lee side. This deformation leads to the formation of a tongue-like structure, which forms two arms of the counter-rotating vortex pair as shown in Figures 4-13(b) and 4-14(b). Unlike our previous inviscid results in [51], the lift-up of the material line elements on the lee side precedes the roll-up of the shear layer. The roll-up of the shear layer is more severely affected by the effect of viscosity, as the growth rate of the instability is attenuated. However, the lift-up of the material line elements stays more robust against the effect of viscosity. This clearly shows that the roll-up of the shear layer, or equivalently the formation of accumulated vortex rings, is not a necessary condition for the formation of the counter-rotating vortex pair. The counter-rotating vortex pair can be independently formed from the velocity induced by the vorticity introduced previously, as claimed in [51].

At the very top of the tongue-like structure, material line elements are curving towards the windward side of the jet. While these material line elements become disorganized as they approach the windward side, they form vortex arcs with their counterparts on the windward side. The vortex arc formed by the lee side of the material rings has vorticity of the opposite sign to the vorticity contained in the arc formed from the windward side. A similar observation was made in [51]. At the later stages, some of the line elements are winding around the counter-rotating vortex pair. After that, these material line elements experience extensive stretching and folding,

creating a complex net of tangled vortices.

Case II shows similar behaviors, as shown in Figure 4-15 and 4-16. Here we only plot three material rings, which are introduced at $t = 15.0$, 15.16, and 15.36, respectively. The ring introduced at $t = 15.0$ shows extreme distortion by the time $t = 16.0$, leaving hints on the proliferation of small-scale structures, which will be dealt in the next subsection.

In summary, the material line elements exhibit repeating similarities in their evolution. Each segment transforms into two arcs, containing vorticity of opposite signs. These two arcs are connected by the vertical portion of each segment, which contains counter-rotating vorticity. This deformation of material rings, which roughly represent vortex filaments, leads to the counter-rotating vortex pair.

4.1.3 Development of small-scale structures

The sudden transition into small-scale structures has been reported elsewhere [76, 51], but the mechanism leading to the transition is not immediately clear. Here, we try to understand the mechanistic transformations of vorticity that lead to such a rapid transition.

To investigate the transition region more closely, most analysis is made for Case II. The higher value of r in Case II extends the transition region, so that one can have better snapshots for ongoing events than in Case I. Figures 4-17 and 4-18 provide aerial and windward views of the material ring introduced at $t = 15.0$, i.e., the first ring in Figures 4-15 and 4-16. The material line elements develop complex tangles initially around the counter-rotating vortex pair, while the windward side rolled-up vortices are maintaining their coherency. Due to the strong counter-rotating vortex pair on the lee-side of the jet, the windward-side of the material line elements, which represents the vortices rolled-up at the windward shear layer, tend to spiral around the counter-rotating vortices at the lee side. This spiral motion initiates the development of three-dimensional kink structures on each material ring, as shown in Figures 4-17(b) and 4-18(b). Once a kink structure forms, the segments with high curvature start stretching and folding by induction from its associated vorticity, which eventually

creates extremely complex three-dimensional structures.

Another way to investigate this complicated evolution is looking at the stretching rate of the vorticity field. Vorticity is intensified only by the action of the stretching rate, i.e., the strain rate aligned to its direction. Since viscosity only dissipates vorticity, to investigate only the mechanism of vorticity intensification, we may use the following estimate for the Lagrangian growth rate of $\frac{1}{2}|\boldsymbol{\omega}|^2$, i.e., $\frac{D}{Dt}\frac{1}{2}|\boldsymbol{\omega}|^2$:

$$\frac{D}{Dt}\left(\frac{1}{2}|\boldsymbol{\omega}|^2\right) = \boldsymbol{\omega}\cdot\frac{D\boldsymbol{\omega}}{Dt} = \boldsymbol{\omega}\cdot(\boldsymbol{\omega}\cdot\nabla\mathbf{u}) + \boldsymbol{\omega}\cdot(\nu\Delta\boldsymbol{\omega}) \leq \boldsymbol{\omega}\cdot(\boldsymbol{\omega}\cdot\nabla\mathbf{u})\,. \tag{4.1}$$

Thus, the exponent showing the growth rate of $\frac{1}{2}|\boldsymbol{\omega}|^2$ can be estimated by evaluating $\boldsymbol{\omega}\cdot(\boldsymbol{\omega}\cdot\nabla\mathbf{u})\,/\left(\frac{1}{2}|\boldsymbol{\omega}|^2\right)$. Since the exponent showing the growth rate of $|\boldsymbol{\omega}|$ is the half of that, which is $\boldsymbol{\omega}\cdot(\boldsymbol{\omega}\cdot\nabla\mathbf{u})\,/|\boldsymbol{\omega}|^2$. This expression gives the stretching rate of the vorticity field.

To visualize the consequence of the interaction between the Kelvin-Helmholtz rings on the windward side and the counter-rotating vortices on the lee side effectively, the contour lines of ω_y with the stretching rate field on planes of constant y are plotted at $t = 15.0$ in Figure 4-19. Close to the nozzle exit, e.g., at $y/d = 2.0$, a counter-rotating vortex, which can be recognized by a contour lines of ω_y, mostly exerts moderate stretching onto the windward side of the jet shear layer. As we proceed farther from the nozzle exit, the emergence of a region exhibiting strong stretching near the counter-rotating vortex becomes obvious. For instance, we see a concentrated region where intense stretching exists near $x/d = 0.5$ and $z/d = 0.2$ at $y/d = 3.0$. Just half diameter away, i.e., at $y/d = 3.5$, the region itself is stretched by and wound up against the counter-rotating vortex, which is a clear sign of development of strong azimuthal vorticity around the counter-rotating vortex. Once this winding up occurs, the counter-rotating vortex breaks down into pieces, as shown in the contour lines of ω_y at $y/d = 4.0$. A three-dimensional reconstruction of the isosurfaces of ω_y and stretching rate is provided in Figure 4-20. Around $y/d = 3.5$, a region experiencing strong stretching encircles the counter-rotating vortex that is visualized by the isosurfaces of ω_y, which exemplifies the winding up of the Kelvin-Helmholtz

vortices around the counter-rotating vortex. Soon after the winding up, isosurfaces of ω_y breaks down into pieces, giving birth to many small-scale vortices. A conceptual illustration of the mechanism is provided in Figure 4-21.

The overall dynamics of vorticity is also seen in Figure 4-22, where the temporal evolution of the length of each material ring (L) is plotted. t_0 is the time when each material ring is introduced at the jet nozzle exit. Just after its introduction, the rings are maintaining relatively stationary values of L, simply being advected by the jet flow. When it reaches an instance, when $t - t_0 \approx 0.4$, the lift-up of the lee-side segment of the material ring is started, leading to a gradual increase of L. Finally, the spiral motion starts to occur and the length of each ring shows exponential growth in time, which is a clear sign for the proliferation of small-scale structures. The growth rate of this later exponential increase is the average strain rate, in the direction of vorticity alignment, that is experienced by the material ring.

This mechanism of small-scale development is different from that previously reported in free jets [25]. In free jets, the rolled-up vortices at the shear layer attempt leapfrogging. During the process, the strong strain imposed and the increased radius of the front ring initiate vortex ring instability to develop three-dimensional vortical structures, which evolve into small-scale structures. Here, the process is initiated by the interaction between two vortical structures, one from the vortices rolled-up at the windward side and the other from the counter-rotating vortex pair. Since these two have almost perpendicular axis of rotation to each other, the interaction leads to instantaneous development of three-dimensionality, which explains why the breakdown process is so rapid in transverse jets. This process also bears similarity to the breakdown of a slender vortex filament [47], if we see the counter-rotating vortices as slender vortex filaments perturbed by azimuthal vorticity. An attempt to describe this process in this fashion can be found in earlier studies [33, 76]. However, the mechanism still needs to be distinguished in the sense that significant amount of azimuthal vorticity is instantaneously introduced into the counter-rotating vortex pair from the rolled-up vortices at the windward side, while a slender vortex develops azimuthal vorticity by deforming its own streamwise vorticity. Thus, flow reversal

must be accompanied along the vortex center in such a spontaneous breakdown of slender vortex filaments to sustain such deformation of vorticity. Such flow reversal is not apparent in our case, though significant slowing down of flow is expected [76]. This is a natural consequence, since azimuthal vorticity is supplied from external flow structures, i.e., rolled-up vortices at the windward side in the case of transverse jets. In this sense, the mechanism is rather best described as induced, not spontaneous, breakdown of counter-rotating vortex pairs.

Once the primary small-scale structures are developed in the lee side of the jet, these lee-side structures, in turn, start to perturb the vortices at the windward side. As described in the previous subsection, the lee-side vortices approach to the windward vortices by the action of counter-rotating vortex pair. By this time, these lee-side vortices are already extremely distorted by the mechanism described in the previous paragraph, and the action of these distorted vortices on the well-organized windward vortices enhances the development of three-dimensionality. With this secondary mechanism, the complete transition of both sides, i.e., windward and lee sides, is achieved.

In summary, we have found that the primary instability into small-scale breakdown is developed in the lee-side by the interaction between two structures, i.e., the vortices rolled up at the windward side and the counter-rotating vortex pair. This mechanism can be distinguished from that observed in free jets or even from that of slender vortex breakdowns.

4.2 Transverse jets with the full no-slip boundary condition

In the previous section, the vorticity transformation mechanism in transverse jets is investigated, using the reduced model. The formation of counter-rotating vortex pair is shown to be the result of the deformation of the jet shear layer vorticity, and the pattern of vorticity transformation closely follows the one previously observed

in our inviscid simulations [51]. The rapid proliferation of small-scale structures is observed, and we have identified the mechanism behind the development of small-scale structures as the induced breakdown of counter-rotating vortices.

The reduced model, however, is only capable of providing a partial picture. Unlike its idealized inviscid counterpart, real transverse jets experience the influence of separated vortices from the wall boundary layer. To investigate The transformation of the vorticity from the separated wall boundary layer, the full no-slip boundary condition should be used. In this section, we present one case, referred to Case III in the following. The condition is almost identical to that in Case I, where $Re_j = 1715$ and $r = 7$. The same numerical parameters for spatial discretization are used: $\sigma = 0.1$ and $\Delta x = 0.035$. Numerical parameters for time discretization are given as follows: $\Delta t_{noz} = \Delta t_d = 0.02$. The wall vortices are generated for $-7 \leq x < 7$, $-5 \leq z < 5$. Near the nozzle exit, the surface of the wall is discretized by triangular elements. Typical area of these elements is chosen to be smaller than Δx^2. Remaining part of the wall is discretized by square elements having their sides 0.025, which is smaller than Δx. To maintain solenoidality of wall vortices, we put mirror images of vortices across the planes of $z = -5$ and of $z = 5$. Computational element distribution is plotted in Figure 4-23. Computational elements are now spread over the solid wall to resolve the wall boundary layer. As the result, the number of vortex elements grows faster than in Case I as demonstrated in Figure 4-24.

Due to limited resources, the simulation of Case III is only performed for $t \leq 7.0$, while Case I is simulated even for $t > 12.0$. Due to the limited period of its evolution, the trajectory is not settled down yet, and the jet is still trying to penetrate deeper into the crossflow. However, the objective of the simulation is to capture the near-field jet structures. Although the far-field structures are still evolving, a relatively stationary state is achieved for the near-field structures. Thus, the near-field dynamics reported here can be considered as the epitome of real statistically stationary jets.

4.2.1 Overall flow features

The overall flow features show similarity to those observed with the reduced model in the previous section, though more complexity is exhibited. Figure 4-25 shows an instantaneous snapshot of vorticity iso-surfaces. We present the results of Case I ($z < 0$) and Case III ($z \geq 0$) side-by-side in the figure for comparison. The shear layer on the windward side shows rolled-up ring-like structures. The roll-up in Case III happens at a location more close to the jet nozzle exit than that in Case I. The ring-like structures in Case III are also more perturbed than those in Case I.

The lee-side structures of Case III show even more striking differences from those of Case I. The counter-rotating vortex pair in Case III does not really correspond to only one single pair any more. Rather, we observe two distinct strands on the side $z > 0$. One strand starts very near the wall at $x \approx 0$, and the other strand, which is more similar to that observed in Case I, forms at a location towards more downstream. In the direction of the jet stream, both strands show earlier formations than the counter-rotating vortex pair in Case I. These two strands remain separate near the nozzle, and then tangle and merge at a point two or three diameter above from the jet nozzle exit. Eventually they all roughly form one counter-rotating vortex pair in the large. Such additional structures we observe in Case III adds up complexity to the overall flow field, which results in birth of instabilities and proliferation of small scale structures. These structures absent in Case I should be considered as the result of the interaction between the jet and the separated wall boundary layer. Upright wake vortices, shed from the jet column [21], are not expected and indeed not observed in Case III, since the Reynolds number is relatively low [33].

Added complexity to the flow field and even more intense small-scale vortical structures downstream of the jet does not erase the signature of the counter-rotating vortices from Case III. Figures 4-26 and 4-27, equivalent to Figures 4-9 and 4-10 in Case I, are provided to show the underlying large-scale counter-rotating vortices. The instantaneous structure of the jet cross section in Case III is even more complex than that in Case I. Still, counter-rotation is evident in the filtered vorticity field. Counter-

rotation does exist, even in this much more complex flow field, as an underlying skeleton of the field.

Finally, we show the jet trajectory of Case III in Figure 4-28. The jet centre streamline is obtained by averaging the velocity field during $t \in [4.0, 7.0]$. For comparison, we also plot the stramline of Case I. The trajectory of Case III is more straight and penetrates deeper than that of Case I. It is quite surprising, since the jet is not mature and still evolving in Case III. The result with Case III matches more closely to the correlation obtained by Margason [49]. The deeper penetration seems to be the result of the difference in near-field counter-rotating vortex pair formation, which will be discussed in details later.

4.2.2 Near-wall flow structures

By satisfying the full no-slip boundary condition over the wall plate, the wall boundary layer, which is first created as a vortex sheet by the action of the uniform crossflow at $t = 0$, is growing into a layer of finite thickness. Figure 4-29 shows the crossflow-streamwise component of the velocity field on the centre plane. Since the jet is also started at $t = 0$, the immediate vicinity of the jet exhibits a transient behavior, as the jet is trying to penetrate into the crossflow. The immediate downstream of the jet requires longer time to be settled, since it takes time for the head of the jet to pass over that region. Weak flow reversal is indicated at $x/d = 1.1$ and $y/d < 0.4$ at $t = 4.0$. This weak reversed flow is due to the existence of a recirculation zone behind the jet column. In Figure 4-30, the velocity field on the plane of $y/d = 0.2$ is plotted. As clearly seen in this figure, a strong recirculating eddy exists behind the jet column. This eddy was not captured in previous inviscid simulations [12, 51]. The eddy indeed results from the separation of the wall boundary layer, which was absent in those previous simulations. The crossflow shows little or no penetration across the jet shear layer, which is the behavior truly observed in experiments [21].

The simulation reproduce many near-wall flow structures, which were previously reported by [33]. Figure 4-31 shows these near-wall flow structures identified at $t = 4.0$. The streamline patterns in Figure 4-31 show good agreements to those

in Figure 4-32, which was generated based on experiments with a similar condition by Kelso *et al.* [33]. Since the condition of Case III is identical to that of Case I, upright wake vortices, shedding from the jet column, are not expected due to low Reynolds number, and indeed our simulation does not exhibit them. Without such an intense unsteady structure, flow features identified instantaneously more or less remain invariant as time goes on.

Most of flow structures, especially those on the lee side, are well reproduced. The vertical centre-plane ($z = 0$) contains a node downstream of the jet, which was inferred from topological arguments and confirmed by dye visualization [33]. The flow pattern on the flat wall consists of a node on the centre-line, which is denoted by C in Figure 4-31, whose bifurcation lines extend downstream. A distinct focus, which is denoted by A in Figure 4-31, is observed on the plane of $y = 0.1$. The focus is similar to those spiraling foci found in [33], where the authors found two distinct foci, instead of one. The number of foci in our case is actually varying with the location where we make the cut. A slightly higher plane actually gives two foci, which are located near the roots of two strands of counter-rotating vorticity in Figure 4-25(b). The current plane is chosen, since other features like saddle points are more clearly identified in this plane than other cuts.

Figure 4-31(c) shows the wall vortices [33]. It is believed that these wall vortices are formed from the separated boundary layer downstream of the jet due to adverse pressure gradient and corresponding recirculation. From their surface dye visualization studies, Kelso *et al.* suggested that these wall vortices would be lifted away from the wall to merge with counter-rotating vortex pair. We show that such a merging really occurs by showing the evolution of vorticity lines later.

One thing we note is that horseshoe vortices, which are usually observed on the upstream of the jet, are not identified in Case III. Horseshoe vortices are formed from the separation of the wall boundary later due to adverse pressure gradient ahead of the jet column [21]. Apparently, the characteristic length scale of a horseshoe vortex depends on the boundary layer thickness upstream of the jet. For instance, Kelso *et al.* reported horseshoe vortices whose sizes are roughly from 1/5 to 1/10 of the

jet diameter [33]. On the other hand, Fric and Roshko showed horseshoe vortices with smaller sizes [21]. The boundary layer thickness in the case of Kelso *et al.* was from approximately 10.5 to 21 mm depending on the Reynolds number, which is comparable to their jet diameter 25.4 mm [34]. The boundary layer thickness in the case of Fric and Roshko is expected to be less than that.

In Case III, the development region of the wall boundary layer is spanned from a point 7 diameters away from the jet nozzle. From a rough estimate from the Blasius solution, the wall boundary layer thickness near the jet column should have its thickness around $0.85d$, if it is fully developed. With such a condition, from the previous discussion, the structure, if it did exist, would have its size similar to those reported in [33].

A few reasons can be considered:

1. The resolution we take is uniform over the entire domain, while the horseshoe vortices are fine structures confined within the wall boundary layer. One may needs to adopt higher resolution near the wall to resolve such a phenomenon. This argument, however, is at most questionable. A horseshoe vortex system has its typical length scale of δ and other structures with similar length scales are well captured.

2. Since our simulation period is short, the wall boundary layer is not yet fully developed. Note that the simulation is started without initializing the wall boundary layer in its fully developed condition. The time necessary to develop a boundary layer of thickness comparable to the jet diameter is roughly estimated from approximately 10 to 100 in Case III, which is clearly out of the time span we have computed.

3. The Reynolds number is too low to have a well-developed vortex system from the separated boundary layer.

Here, we expand the last point a little bit more. As discussed in Chapter 1, we have three dimensionless parameters controlling the flow field of a transverse jet, i.e., Re_∞,

r, and δ/d. Since a horseshoe vortex is believed to be formed from the separation of the wall boundary later due to adverse pressure gradient ahead of the jet column, an assumption is made that horseshoe vortices show rather weak dependency on r. With such an assumption, the controlling parameters reduces to two, i.e., Re_∞ and δ/d. At the limit of $\delta/d \to 0$, the flow becomes an air curtain. Additionally, we assume a laminar boundary layer, which is more or less stationary. With retained spanwise symmetry, the existence of a horseshoe vortex system at the limit of $\delta/d \to 0$ should be controlled by a single parameter, that is, $Re_\delta \equiv Re_\infty \delta/d$. The existence of a critical value, i.e., Re_δ^*, which demarcate the threshold between the occurrence and non-occurrence of horseshoe vortices, is expected by comparing two time scales of a horseshoe vortex of size δ, i.e., the time scale of diffusion, δ^2/ν, and the time scale of convection, δ/U_∞. Now, as we increase δ/d slightly, we expect that the fluid at the center plane experiences more and more stretching in the spanwise direction, which is generated by the flow bypassing the jet column, intensifying its spanwise vorticity. This additional effect of stretching gives more resistance against viscous dissipation to the horseshoe vortex system, and hence there is some possibility that Re_δ^* decreases as we increase δ/d. One way to verify this heuristic argument is initializing the wall boundary layer from the corresponding Blasius solution in cases with higher Reynolds numbers. Further investigation is necessary to confirm the hypothesis.

Our results on jet evolution are perhaps not affected by missing horseshoe vortices, since the impact of these horseshoe vortices is minimal to jet evolution, when r is relatively large. These horseshoe vortices do not have the same sense of rotation, when lifted from the wall, as the counter-rotating vortex pair or the upright wake vortices shedding from the jet column, which implies that it is not possible for the horseshoe vortices to contribute to the formation of these major structures. Rather, they tend to extend downstream [33] and are usually terminated within the wall boundary layer by the action of upright wake vortices [21]. The only vortical structures that may potentially result from these horseshoe vortices are the wall vortices downstream of the jet column, as shown in Figure 4-31(c). Yuan *et al.* [76] claimed that these wall vortices, which were called wake vortices by them, were originated from the legs of

the horseshoe vortices. However, even without clear signature of horseshoe vortices, we have wall vortices just downstream of the jet column, which implies that the wall vortices at the immediate vicinity of the jet column are not directly originated from the horseshoe vortices. Rather they result from recirculation, as discusses earlier in this section. With all these observations, we agree with Kelso *et al.* on that "the horseshoe vortex system seems to play only a minor role in the overall structure." As noted in Chapter 1, however, for $r < 1$, horseshoe vortices may have some chance to contribute on the formation of major jet structures.

Special attention should be given for the spiraling focus A, shown in Figure 4-31(b). The focus was referred as a tornado-like critical point by [33]. They suggested that this point was where the vorticity from the wall boundary layer was lifted away from the wall to merge eventually with counter-rotating vortices. The sense of rotation of the tornado-like structure emanating from the focus is the same as that of the counter-rotating vortices, and it may clearly contribute to the formation of counter-rotating vortices, if aligned properly. This is the topic of the following subsection.

4.2.3 Impact of near-wall structures on jet evolution

Previous inviscid simulations performed by Lagrangian vortex methods [12, 51] mostly attribute the formation of counter-rotating vortices to the deformation of the vorticity from the jet shear layer. Our simulation in the previous section, with the reduced model of vorticity introduction, also confirms that it is indeed the case. However, allowing the interaction between the boundary layer and the jet shear layer changes the picture significantly.

To examine the mechanism of counter-rotating vorticity formation under the impact of the wall boundary layer, we again use our Lagrangian technique of tracking material lines. Unlike in Case I and Case II, the vorticity line does not conform the material ring introduced at the jet nozzle exit. Many near-wall vortical structures, presented in the previous subsection, do indicate that there exist much richer near-field vortical structures than those represented by the reduced model. Thus, simply tracking material rings does not represent a correct picture of vorticity transforma-

tion. Rather, one should first identify the vorticity lines near the jet nozzle exit. Then, one can track these lines to identify possible mechanisms of vorticity transformation.

The identification of vorticity lines are made by numerical integration of the instantaneous vorticity field at $t = 4.0$. We show typical vorticity lines available near the wall in Figure 4-33. Two distinct groups can be readily identified. One group, which is represented by a slightly deformed ring around the jet nozzle, shows a structure similar to that of the vorticity lines created by the reduced model. These rings are slanted toward the upstream of the jet as those reported in [51], but the indentation is larger in our case.

The other group has its origin in the vorticity of the wall boundary layer. The vorticity of the wall boundary layer is entrained by the action of the jet as suggested by [33]. Most of the vorticity lines in this group shows unterminated, infinitely long shapes. The small ring located downstream of the jet is an exception, and it corresponds to the wall vortices shown in Figure 4-31(c). As discussed in the previous section, these wall vortices are not originated from the horseshoe vortices in our case.

The contribution of each of these groups to the formation of counter-rotating vorticity is qualitatively evaluated by tracking these vorticity lines as material lines. The results for the first group are shown in Figures 4-34 and 4-35. The ring first shows a further overall slanting of itself, and then the lee-side lift-up occurs. This lee-side lift-up generates two arms of counter-rotating vorticity, as described by [12] and [51]. However, since it happens so late, i.e., a few diameters away from the jet nozzle exit, the near-wall counter-rotating vorticity, shown at immediate vicinity of the jet nozzle exit, i.e., at $y/d < 2$ in Figure 4-25(b), obviously does not solely correspond to this later lift-up phenomenon. The lift-up of the lee-side of this ring-shaped vorticity line only contributes to the far-field counter-rotating vorticity located away from the jet nozzle exit.

Figures 4-36 and 4-37 show the evolution of the vorticity lines in the other group, originated from the separated wall boundary layer. The vorticity from the wall boundary layer clearly aligns itself to the near-wall counter-rotating vorticity. This tornado-like structure really corresponds to the focus A shown in Figure 4-25(b). From this

result, it is clear that the near-wall counter-rotating vorticity is primarily formed from the vorticity entrained from the wall boundary layer.

This result shows that the reduced vorticity influx model only partially explains counter-rotating vortex pair formation in real transverse jets. The model captures the evolution of part of near-wall vorticity as slanted vortex rings. However, not only these slanted vortex rings but also other wall vortices contribute to the formation of the counter-rotating vortex pair, and the latter is actually more important in the near field. Thus, the mechanism of counter-rotating vorticity formation suggested by the previous inviscid simulations either without the model [12] or with the model [51] provides only limited explanations on the formation of counter-rotating vorticity.

A more quantitative assessment is performed to substantiate the importance of these near-wall structures. Transversal cuts of the jets are made to generate contour plots of ω_y on planes of constant y. Figure 4-38 shows the results. The contour lines from Case I and those from Case III show radical differences. For instance, at a distance very small from the wall, e.g., at $y/d = 0.2$, Case I shows a single, well-defined region containing wall-normal vorticity around the jet nozzle boundary. This wall-normal vorticity corresponds to $\boldsymbol{\gamma}_c$, expressed by (3.30). On the other hand, Case III shows two clusters of wall-normal vorticity, i.e., one in $-0.5 \leq x/d \leq 0.5$ and the other in $x/d > 0.5$, indicating that the flow field of Case III does have two separate strands of counter-rotating vortices near the jet nozzle exit. While the vortex at $-0.5 \leq x/d \leq 0.5$ is similar to that identified in Case I in terms of its location, this vortex is still quite different in terms of its strength. Apparently, the vortex at $-0.5 \leq x/d \leq 0.5$ in Case III contains circulation about two times larger than that of the corresponding vortex in Case I. The other vortex in Case III is located completely outside of the jet nozzle boundary, i.e., at $x/d > 0.5$. From its location, we can conclude that this vortex is formed by the separation of the wall boundary layer vortices, i.e., from $\boldsymbol{\gamma}_w$ and not from $\boldsymbol{\gamma}_c$ or $\boldsymbol{\gamma}_j$. These two vortices, forming two strands of counter-rotation in Case III, evolve into two vortices, i.e., one at $x/d = 0.3$ and $z/d = 0.5$ and the other at $x/d = 0.7$ and $z/d = 0.2$, respectively, on the plane of $y/d = 1.0$. At this stage, there are also some signatures of ω_y developed on

the windward side of the jet, which correspond to wiggles in the jet vortices on the windward side. Note that the jet vortices on the windward side in Case III show a much earlier development of instabilities, as clearly seen in Figure 4-25. On the plane of $y/d = 2.0$, these signatures grow and small-scale structures contaminate the entire perimeter of the jet shear layer.

The evolution of circulation contained in counter-rotating vortices can be quantitatively examined by integrating ω_y on each half plane of constant y. We plot $\Gamma(y) = \int\int_{z>0} \omega_y dz dx$ in Figure 4-39. The circulation of streamwise vortices in Case III grows from 0 to a value around 4, though the circulation for $y/d > 0.5$ shows some undulation due to the early development of periodic roll-up on the windward side. The circulation in Case I roughly starts from 1 to a value around 2. The rates of growth are also qualitatively different. Case I shows a rather gradual increase of its circulation from $y/d = 0$ to $y/d \approx 1.0$, indicating that the increase is due to the gradual deformation of the jet shear layer. On the other hand, Case III shows a sharp increase within a relatively thin region near the wall. Actually, the circulation in Case III should start nominally from 0, since Case III satisfies the full no-slip boundary condition. Thus, the thin layer, where the sharp increase in the circulation is observed, is the wall boundary layer. Such a rapid increase of circulation clearly indicate that it is due to a sudden phenomenon, i.e., separation of the wall boundary layer, rather than continual deformation of the jet shear layer. On the other hand, the circulation in Case I starts at a value near 1 at $y/d = 0$, which indicates that this initial wall-normal vorticity is due to $\boldsymbol{\gamma}_c$. It is easy to check that the expression (3.30) gives unit wall-normal circulation when it is integrated.

We focus our eyes just the outside of the wall boundary layer, e.g. near $y/d = 0.2$. The value of the circulation in Case I is just 1, that is, only one quarter of that in Case III. From the fact that the vorticity from the wall boundary layer is usually much weaker than the vorticity from the jet shear layer, the difference between Case I and Case III is rather striking. Circulation per unit length of the jet column, $\frac{d\Gamma}{dl}\big|_j$, is about r times larger than circulation per unit length of the wall boundary, $\frac{d\Gamma}{dl}\big|_w$. That is, $\frac{d\Gamma}{dl}\big|_j \approx V_j \approx rU_\infty \approx r\,\frac{d\Gamma}{dl}\big|_w$. How can such weak vorticity form such an

intense tornado-like structure? In some sense, the terminology, i.e., a tornado-like structure, itself provides the answer. Dust devils ingest and tighten vorticity near the ground, which is lifted from the ground by convective updraft due to the Rayleigh-Taylor instability [5]. In transverse jets, this convective updraft is replaced by the entraining action of the jet. The jet provides a strong vertical flow lifting the wall boundary layer vorticity, making wall vorticity detached from the wall and aligned along the jet stream. Successive ingestion and tightening follows to form a strong tornado-like structure. The circulation of a vortex tube, which is generated by the entrainment of wall vorticity, is given by $\Gamma_{\text{ent}} = \frac{d\Gamma}{dl}\big|_w \times L_{\text{ent}}$, where L_{ent} represents the typical length of the domain where its wall vorticity is entrained into the jet. Entrainment processes of wall vortices are depicted in Figure 4-40. In the reduced vorticity influx model, we set $L_{\text{ent}} = d$ by allowing separation and entrainment only around the nozzle exit, and set $\frac{d\Gamma}{dl}\big|_w = U_\infty$ by neglecting any feedback from the jet to the wall vortex sheet. In reality, $L_{\text{ent}} > d$ as clearly seen in Figures 4-36 and 4-37, and $\frac{d\Gamma}{dl}\big|_w \neq U_\infty$ in general. More precisely, there exist two groups of wall boundary vortices entrained into the jet. One is the vortex tube similar to that in the reduced influx model. This group, denoted with the subscript ∞, extends spanwise into a point far from the jet nozzle exit, where the crossflow forms a wall boundary layer with $\frac{d\Gamma}{dl}\big|_{w,\infty} = U_\infty$ and $L_{\text{ent},\infty} > d$. The other has the shape of rings, and is formed in the recirculation zone behind the jet column. This group is denoted with the subscript r, standing for recirculation. The length of a typical recirculation zone is around the same as d, and its circulation per unit length, i.e., $\frac{d\Gamma}{dl}\big|_{w,r} \neq U_\infty$ in general. These two groups contribute to the formation of counter-rotating vortices together in reality. It is, hence, not surprising that the difference in circulation is so large.

The existence of the strong near-field counter-rotating vortices in Case III naturally leads to features different from Case I in further jet evolution. The following list summarizes our observations:

1. By having strong near-field counter-rotating vortices, the jet may resist more against the crossflow, which results in deeper penetration into the flow as shown in Figure 4-28.

2. Since the counter-rotating vortex pair is formed from the separated wall layer, the jet shear layer does not have to show lift-up of its lee side until it reaches further downstream. Instead, the circulation of the jet shear layer is maintained mostly in the azimuthal direction even on the lee side. As the result, the Kelvin-Helmholtz ring formation may occur earlier, and it may happen on the whole perimeter, not only on the windward side. Figure 4-25(b) shows accumulated ring structures on the lee side.

3. The Kelvin-Helmholtz rings in Case III may interact with the counter-rotating vortex pair earlier than in Case I, since the roots of counter-rotating vortex pair, formed from the tornado-like foci, are extended deeper to the nozzle exit. Since the location where azimuthal vorticity and streamwise vorticity is now located much more upstream than that in Case I, early three-dimensional structure development is possible.

4. The existence of multiple strands of counter-rotating vorticity leads to initiation of higher frequency excitation to the Kelvin-Helmholtz rings, which may result in proliferation of smaller scales.

With all these observations, it is suggested that the separated wall boundary layer critically affects the overall behavior of the jet near-field. The reduced vorticity influx model, on the other hand, only provides limited explanations. Care must be taken to interpret results from such a reduced model.

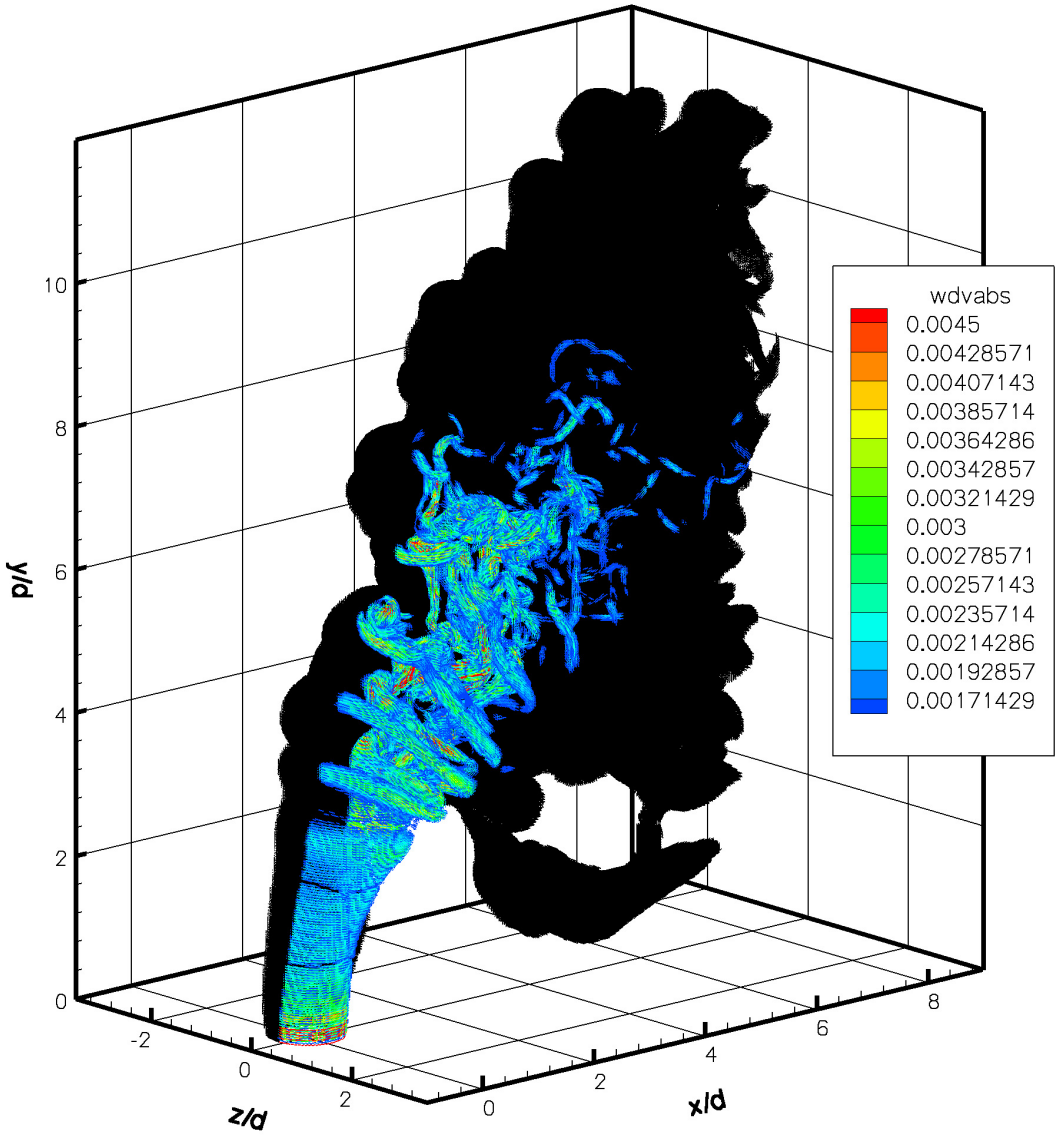

Figure 4-1: Perspective view of computational elements at $t = 12.0$ (Case I). The black cloud at $z/d < 0$ shows all the computational elements. The elements shown at $z/d > 0$ are those with $|\boldsymbol{\omega}_i dV_i| > 0.0015$, colored by $|\boldsymbol{\omega}_i dV_i|$.

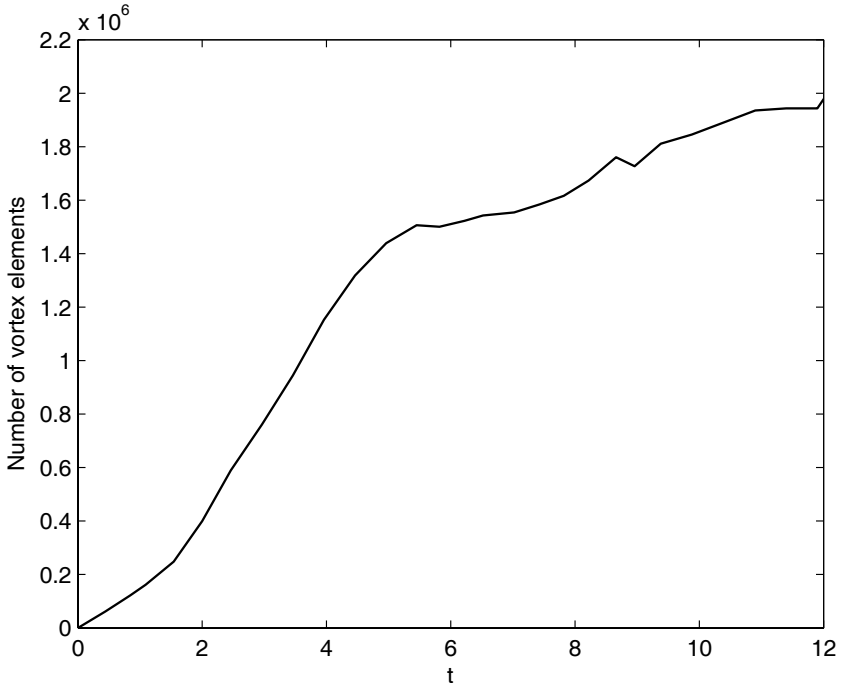

Figure 4-2: Number of vortex elements verses time (Case I).

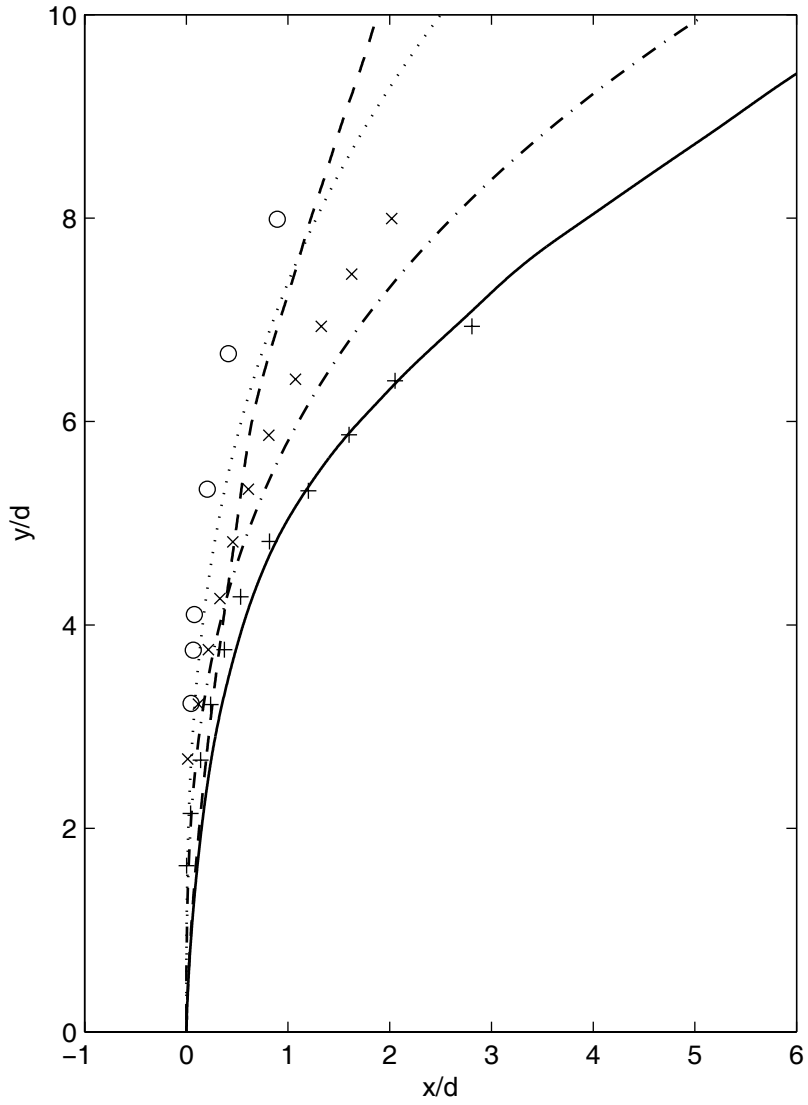

Figure 4-3: Computed trajectories verses experimental observations. Solid and dashed curves represent jet centre streamlines obtained for $t \in [12.0, 17.6]$ in Case I and $t \in [15.0, 20.0]$ in Case II, respectively. Upright crosses, slanted crosses, and circles represent the experimental data with $r = 6$, $r = 8$, and $r = 10$ obtained by Keffer and Baines [32], respectively. The dash-dot curve and dots represent an experimental correlation (1.2) for $r = 7$ and $r = 10$, respectively [49].

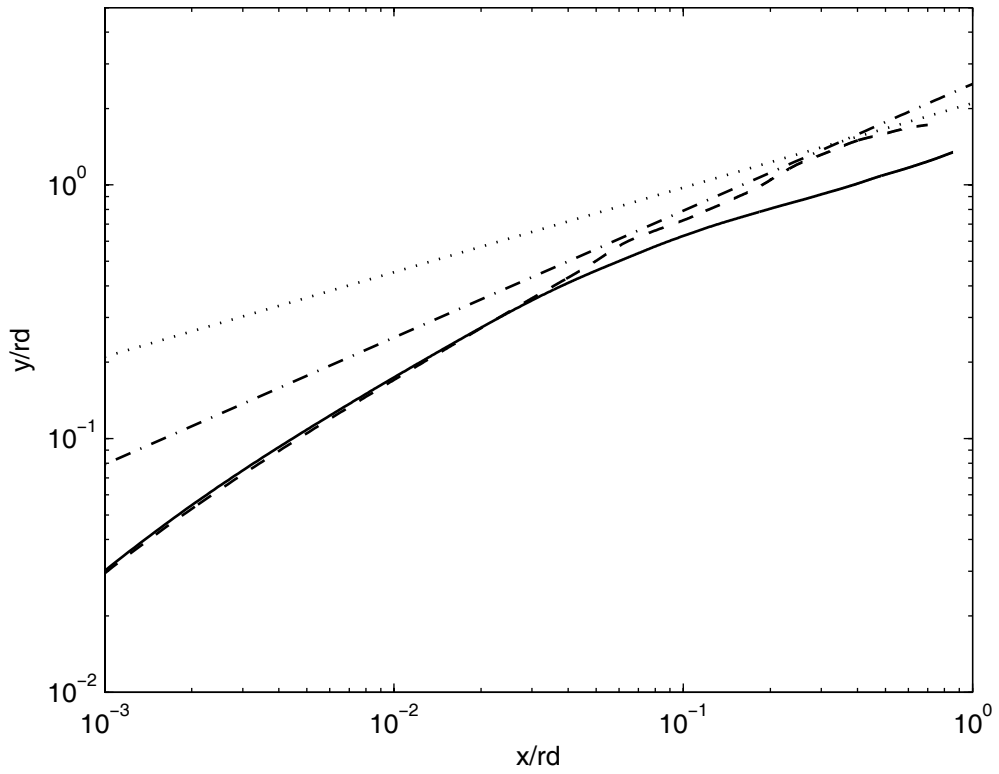

Figure 4-4: Computed trajectories verses scaling laws [28]. Solid and dashed curves represent jet centre streamlines obtained for $t \in [12.0, 17.6]$ in Case I and $t \in [15.0, 20.0]$ in Case II, respectively. The dash-dot curve represents the near-field scaling law (1.4). Dots represent the far-field scaling law (1.3).

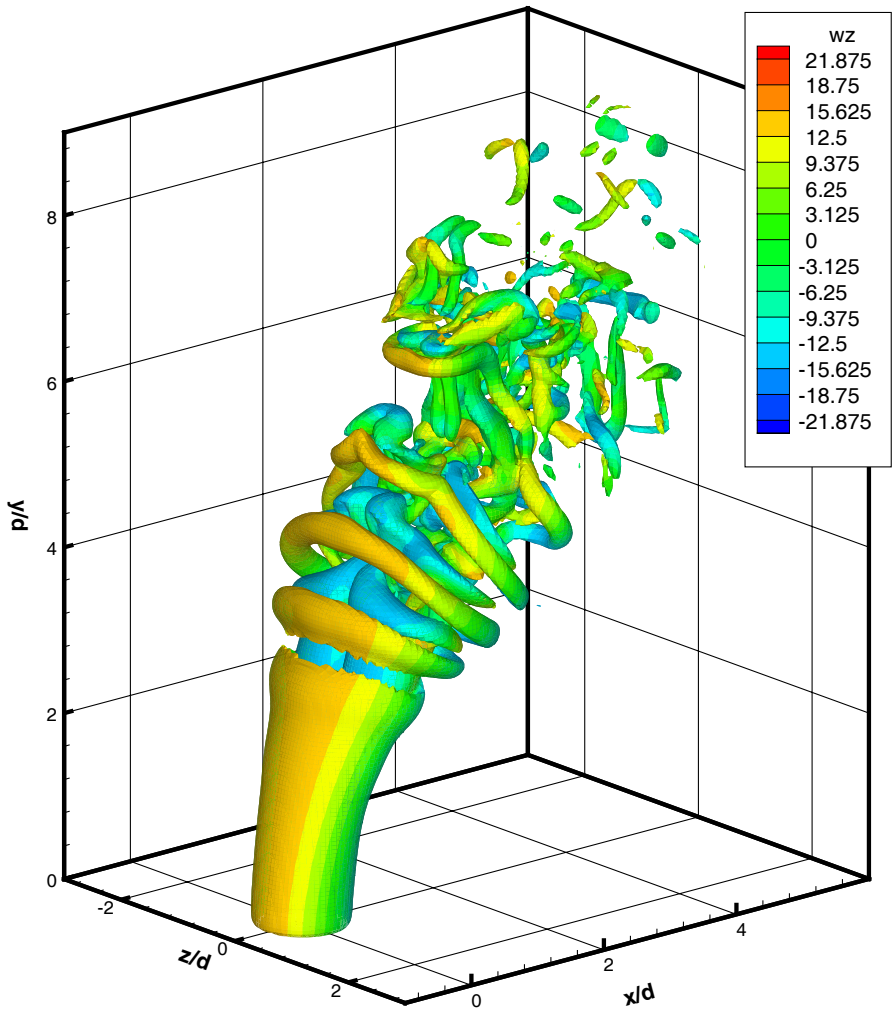

(a) windward side, colored by ω_z

Figure 4-5: Vorticity magnitude isosurfaces, $|\boldsymbol{\omega}| = 15$ at $t = 12.0$ at two perspectives (Case I).

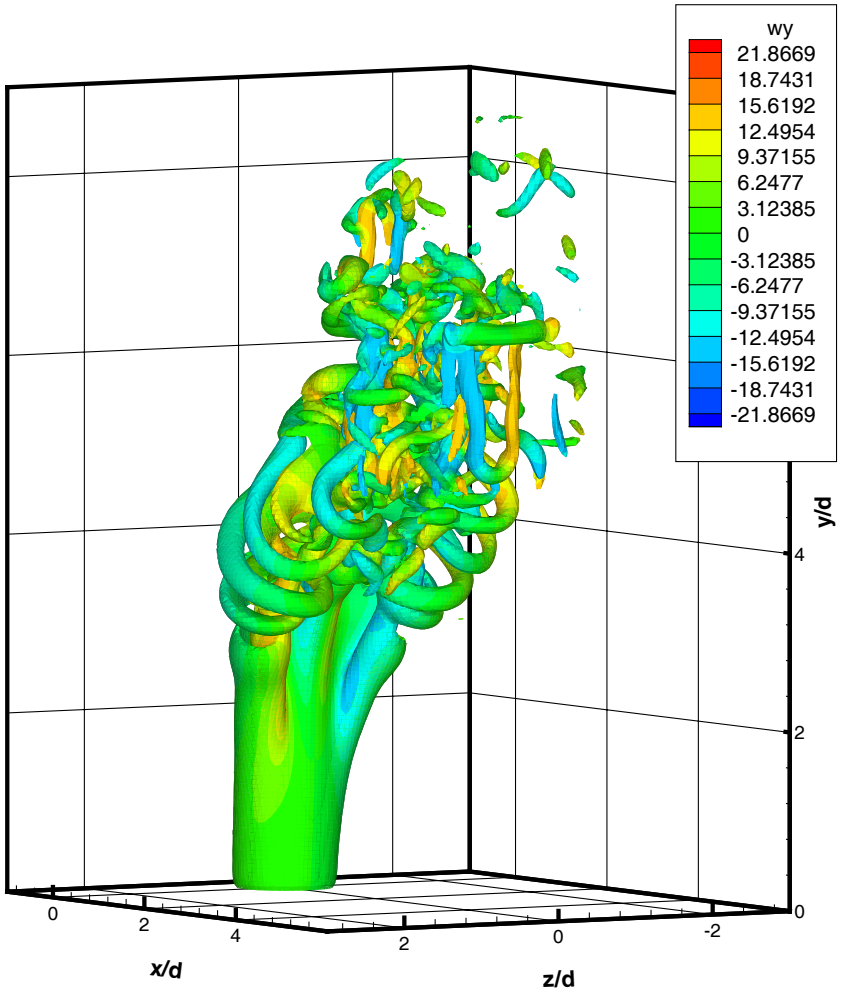

(b) lee side, colored by ω_y

Figure 4-5: Continued from the previous page.

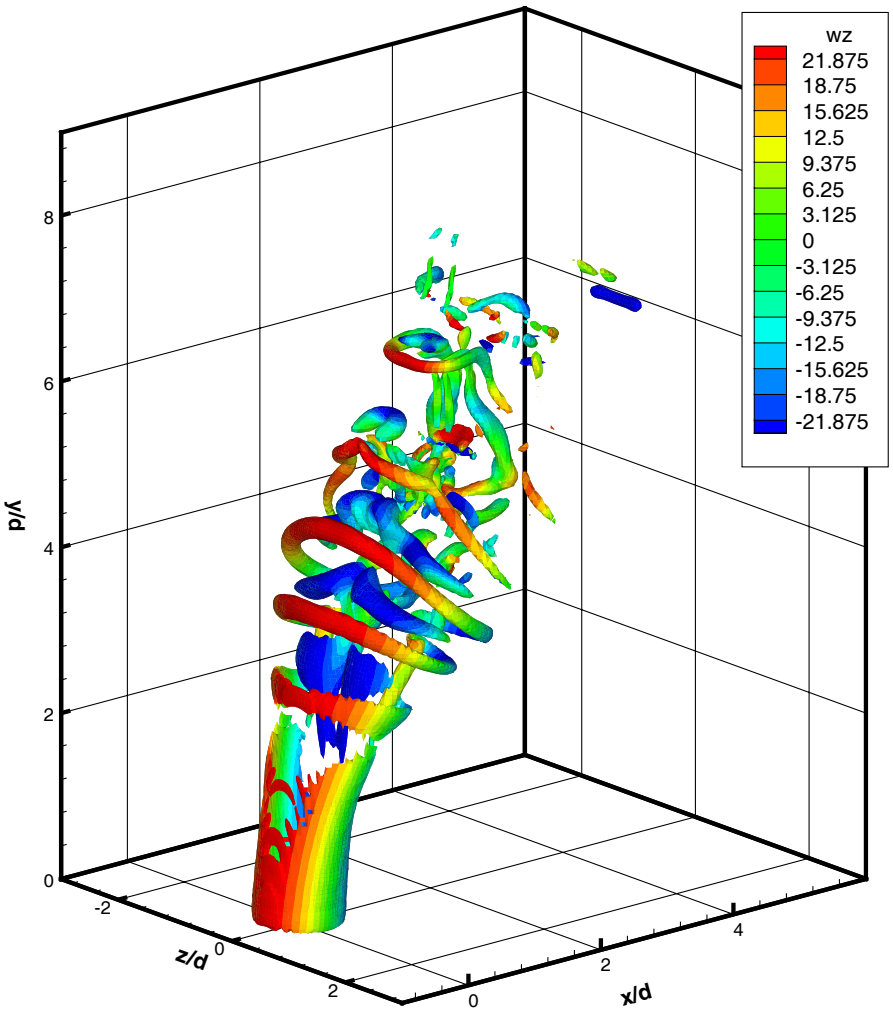

(a) windward side, colored by ω_z

Figure 4-6: Vorticity magnitude isosurfaces, $|\boldsymbol{\omega}| = 25$, at $t = 12.0$ at two perspectives (Case I).

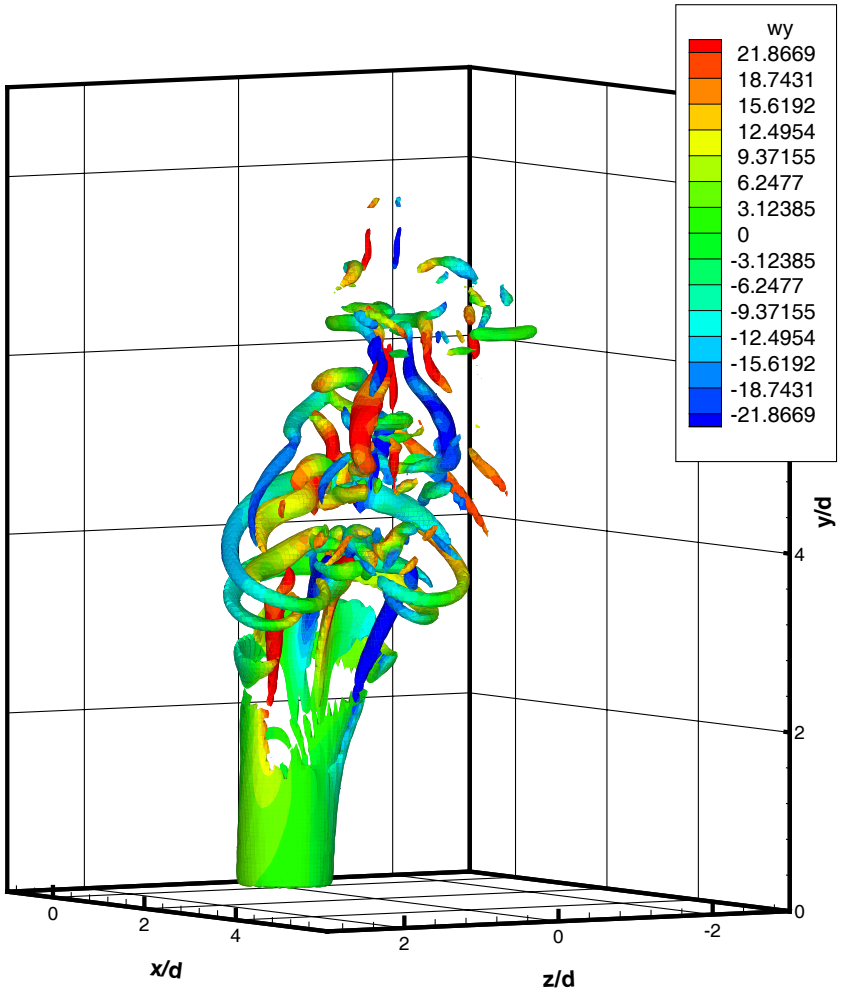

(b) lee side, colored by ω_y

Figure 4-6: Continued from the previous page.

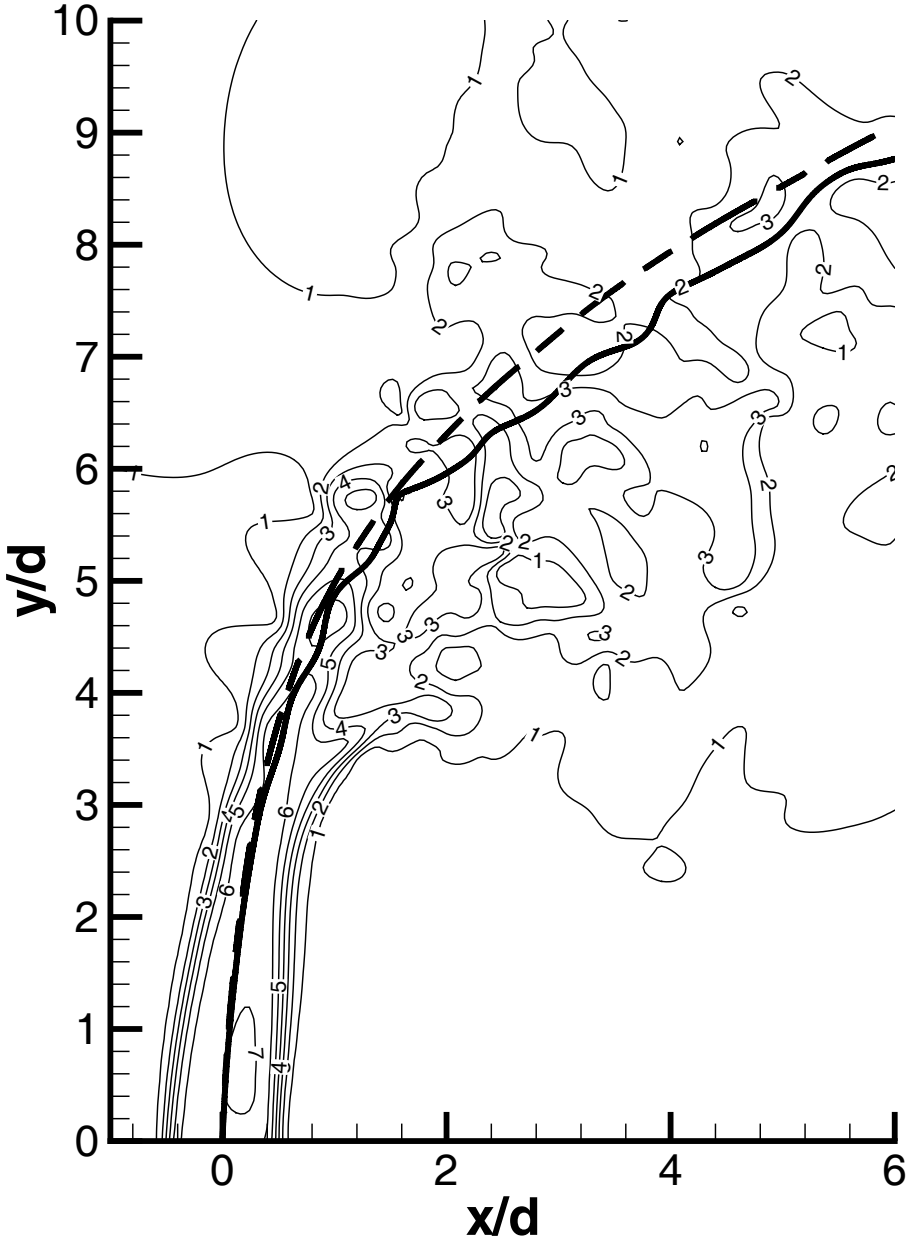

Figure 4-7: Computed trajectories and velocity magnitude contours in Case I. Thick solid and dashed curves represent the instantaneous jet centre streamline at $t = 12.0$ and the average jet centre streamline for $t \in [12.0, 17.6]$, respectively. The contours are obtained by the velocity magnitude, i.e., $|\mathbf{u}|$ at $t = 12.0$.

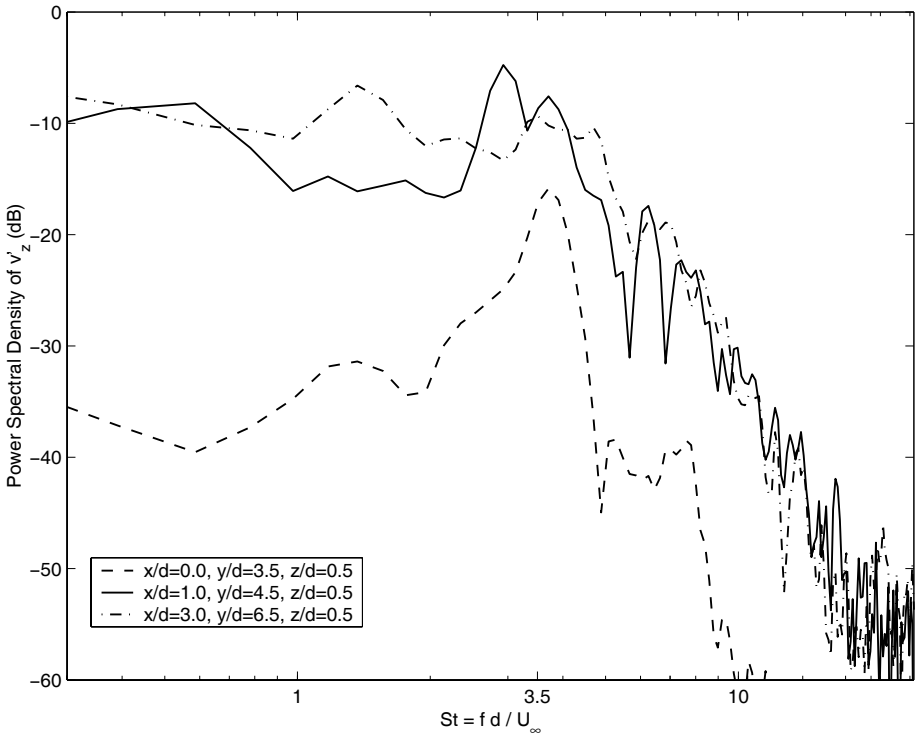

Figure 4-8: Power spectrum of u_z' collected at three spatial locations for $t \in [12.0, 17.6]$ (Case I).

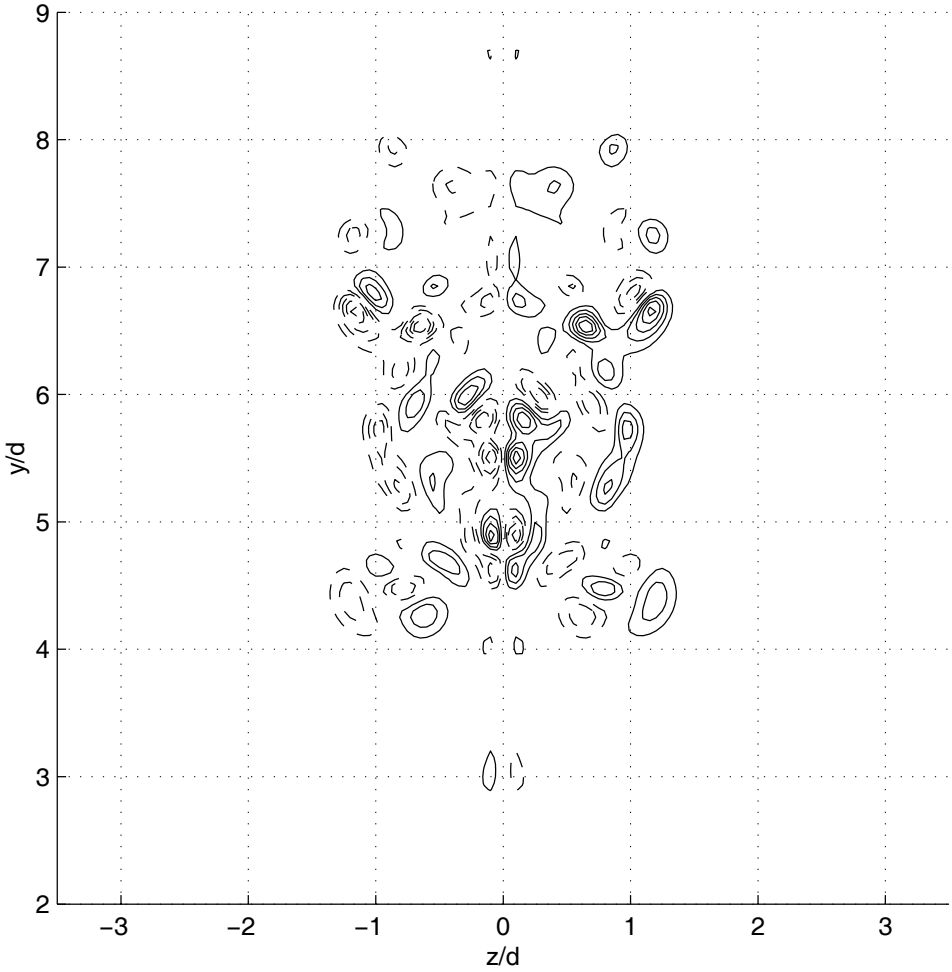

Figure 4-9: Crosssectional view showing the contours of ω_x at $x/d = 3.0$ and $t = 12.0$ (Case I). Dashed curves indicate negative values. The outer most lines indicate $\omega_x = \pm 4$. The difference between two adjacent levels is 4.

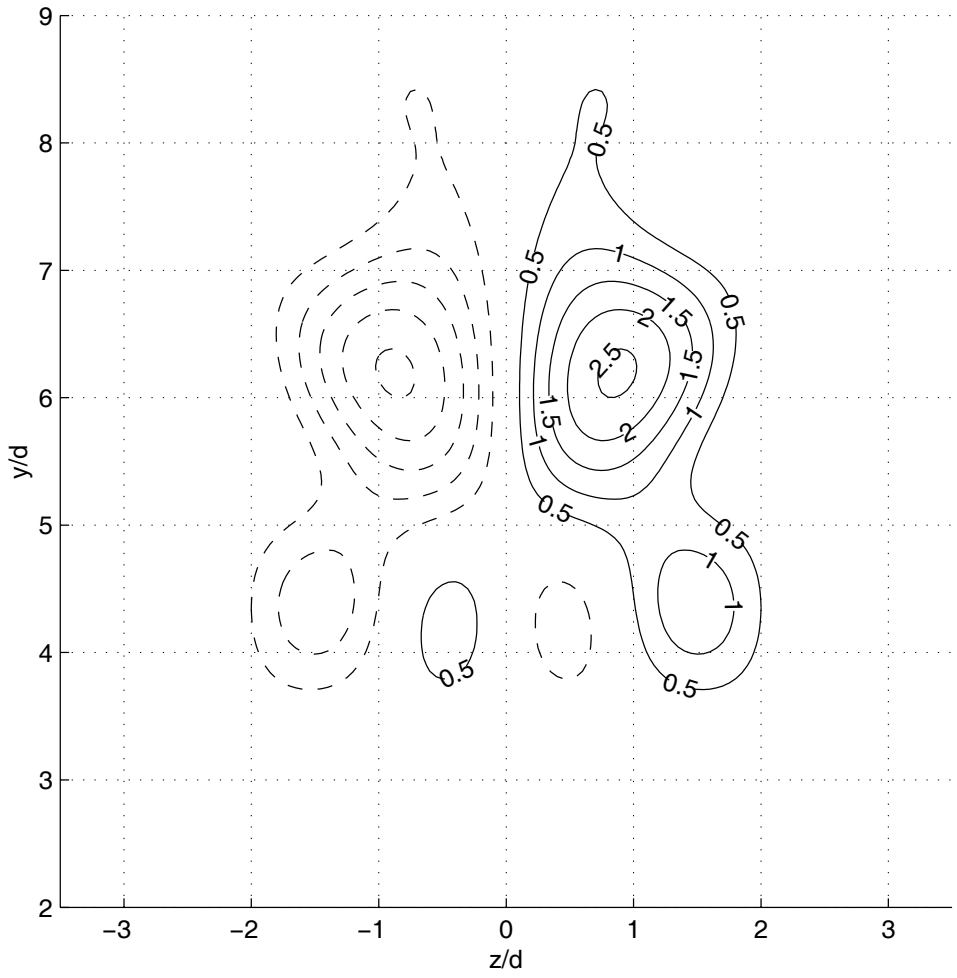

Figure 4-10: Crosssectional view showing the contours of filtered ω_x at $x/d = 3.0$ and $t = 12.0$ (Case I). Dashed curves indicate negative values.

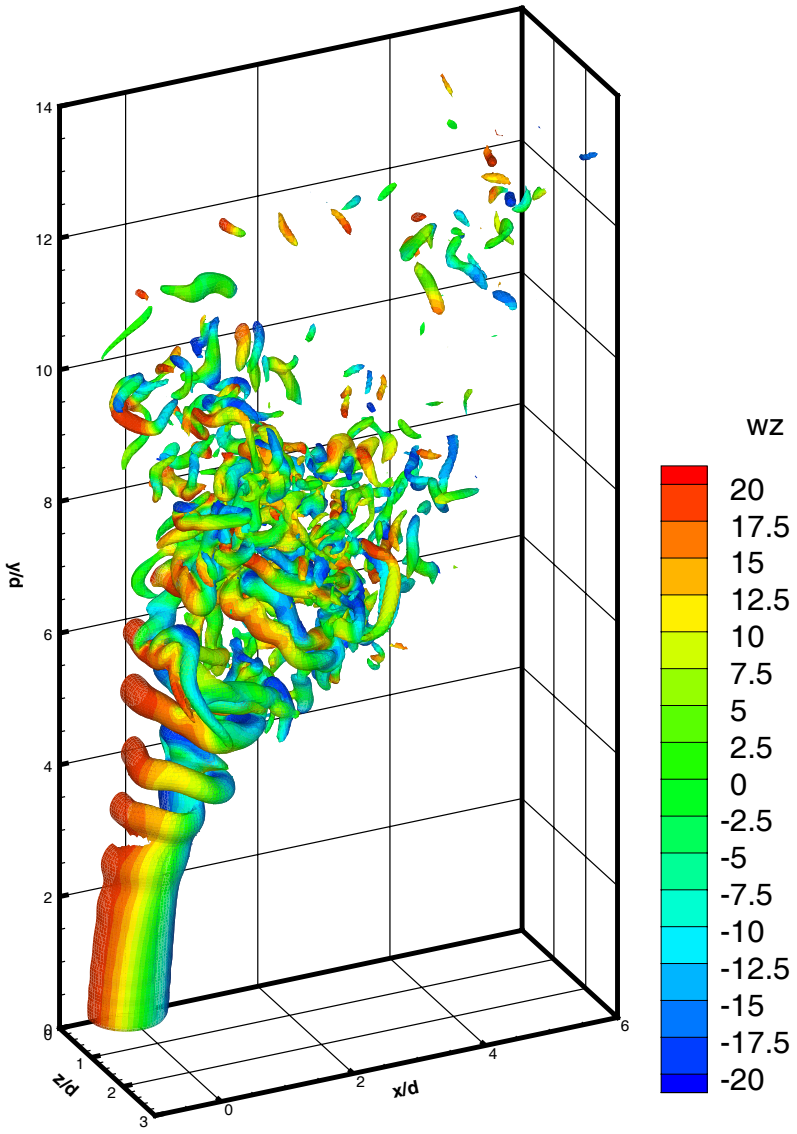

(a) outer view, colored by ω_z

Figure 4-11: Vorticity magnitude isosurfaces at $t = 15.0$, $|\boldsymbol{\omega}| = 20$ at two perspectives (Case II).

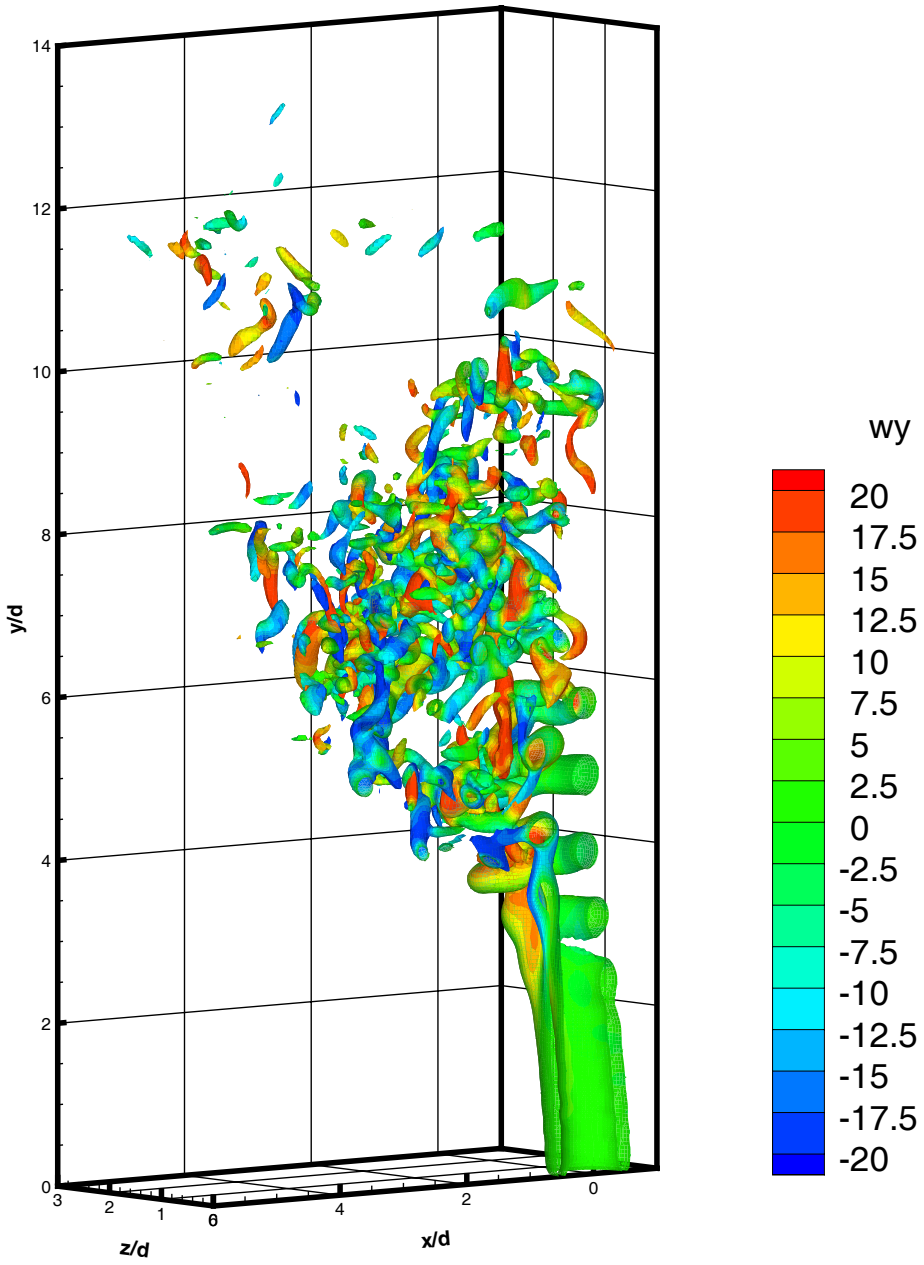

(b) inside view, colored by ω_y

Figure 4-11: Continued from the previous page.

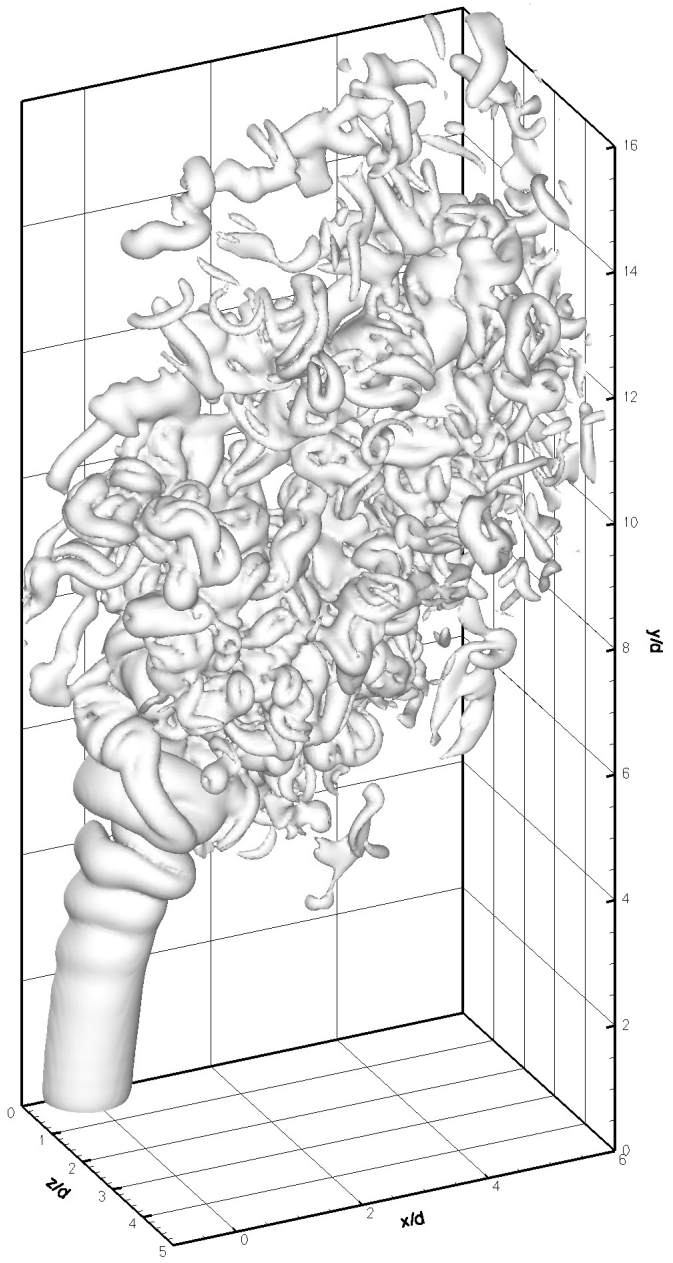

Figure 4-12: Vorticity magnitude isosurfaces at $t = 15.0$, $|\boldsymbol{\omega}| = 5$ (Case II).

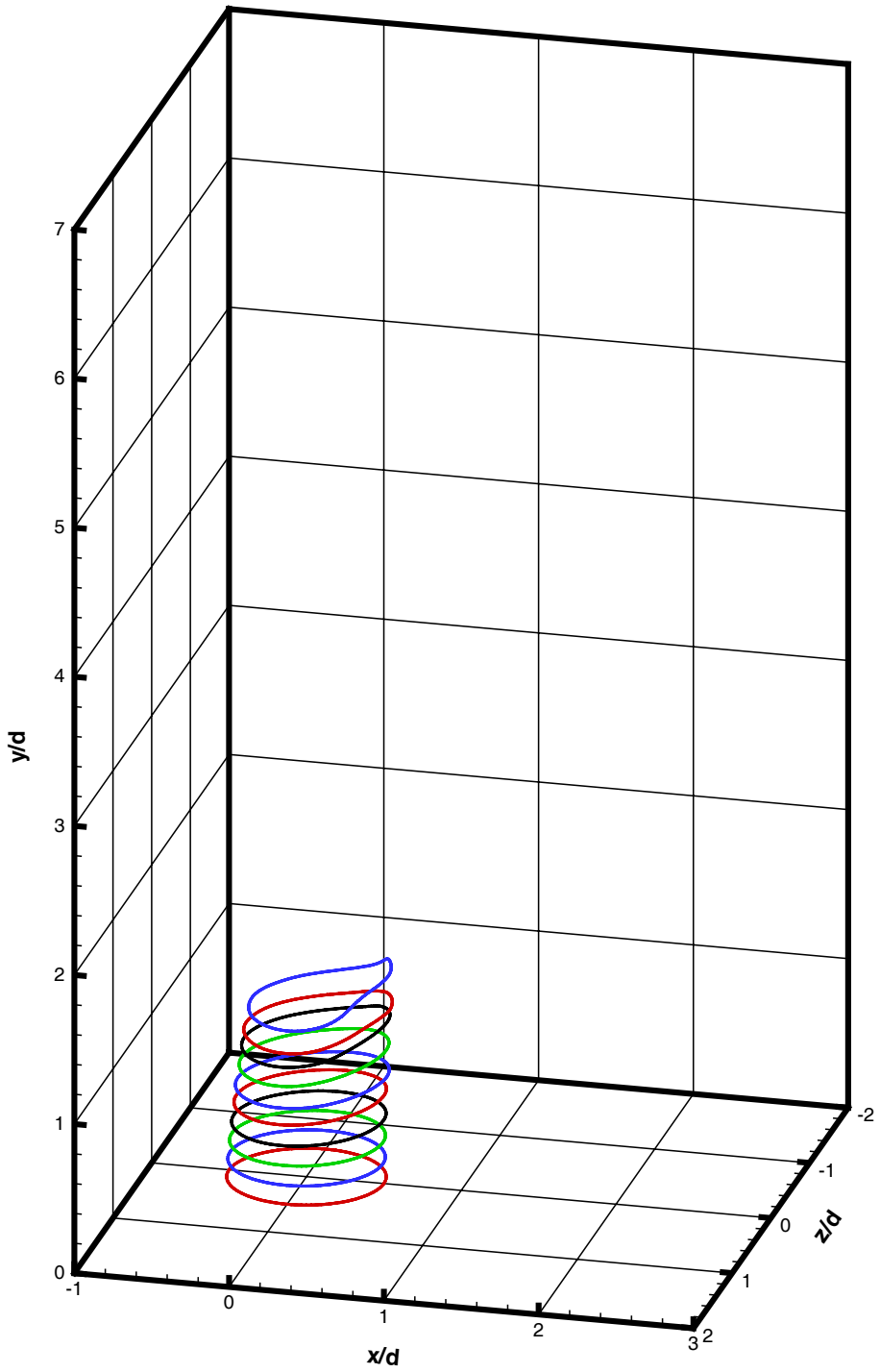

(a) $t = 12.36$

Figure 4-13: Side view of the evolution of material line elements introduced at the jet nozzle exit during $t \in [12.0, 12.36]$ (Case I).

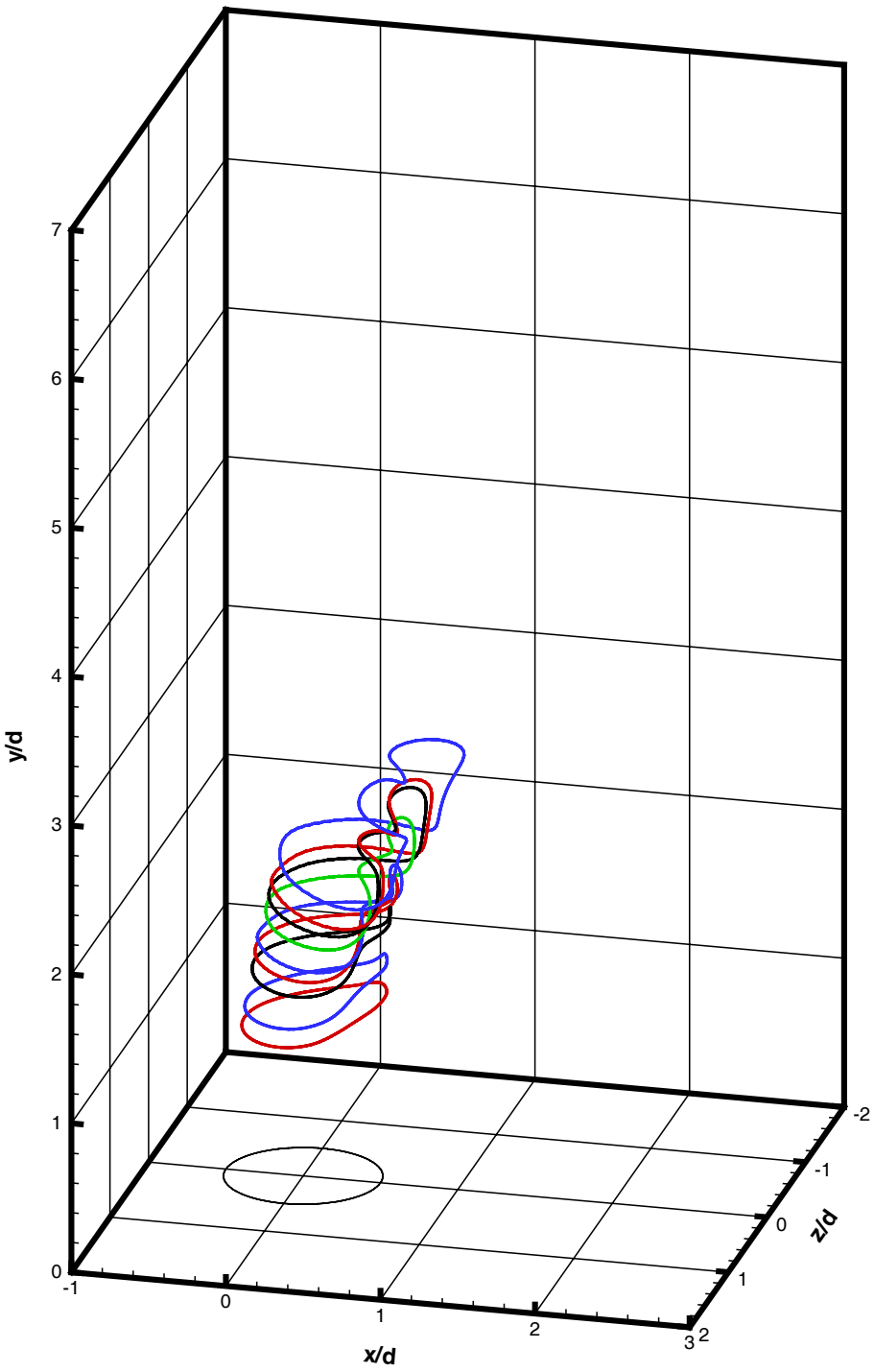

(b) $t = 12.68$

Figure 4-13: Continued from the previous page.

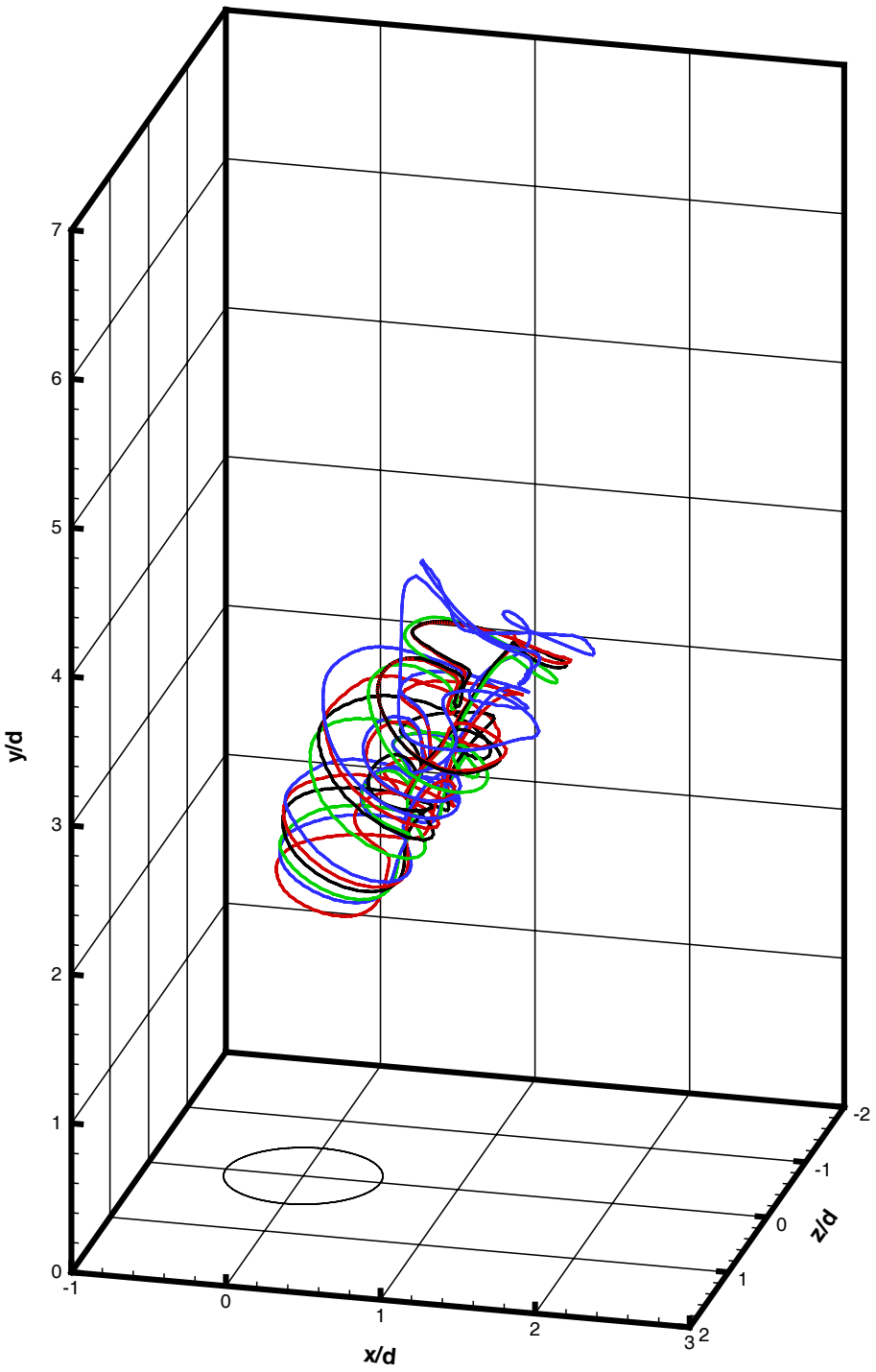

(c) $t = 13.00$

Figure 4-13: Continued from the previous page.

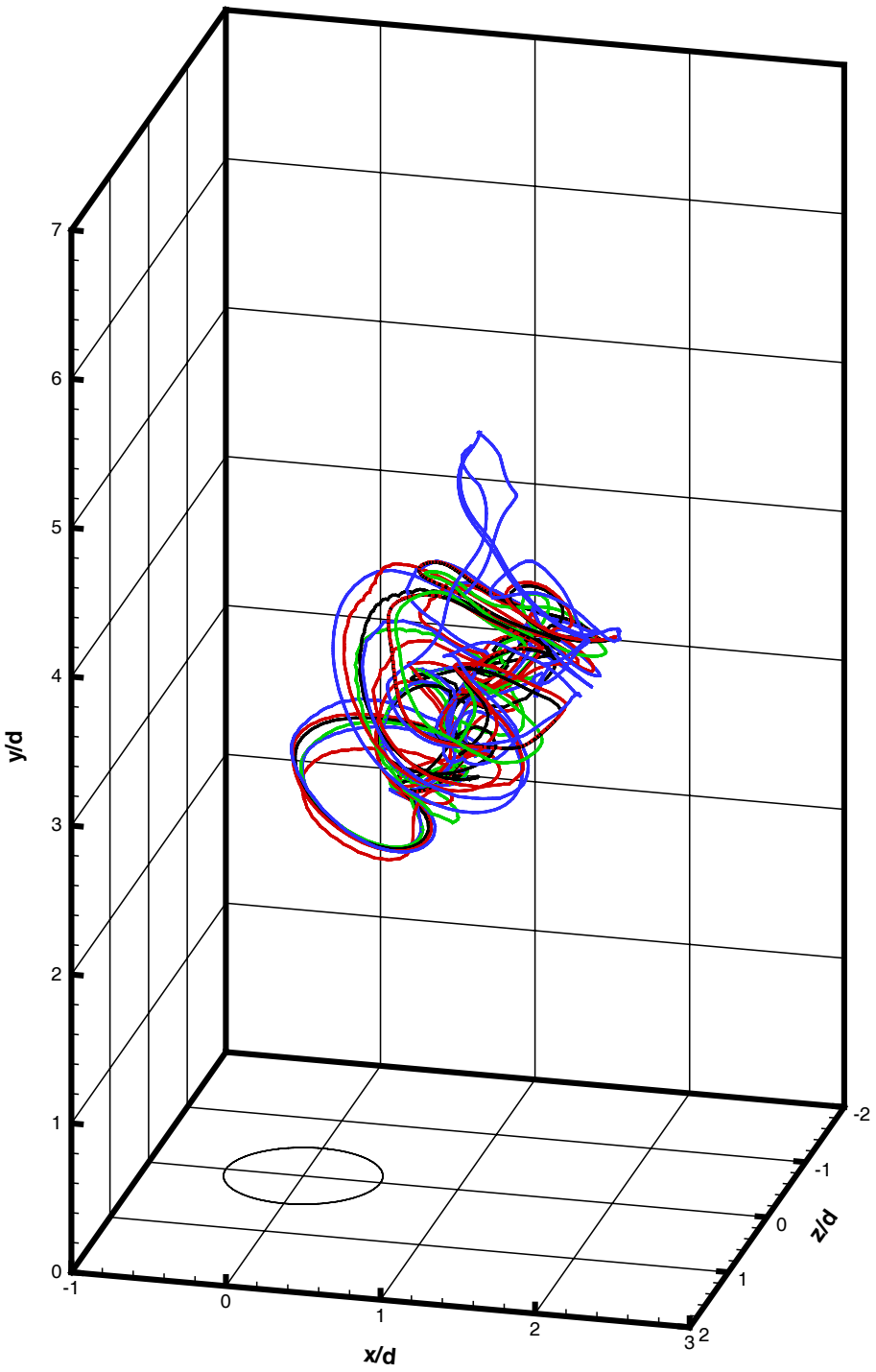

(d) $t = 13.16$

Figure 4-13: Continued from the previous page.

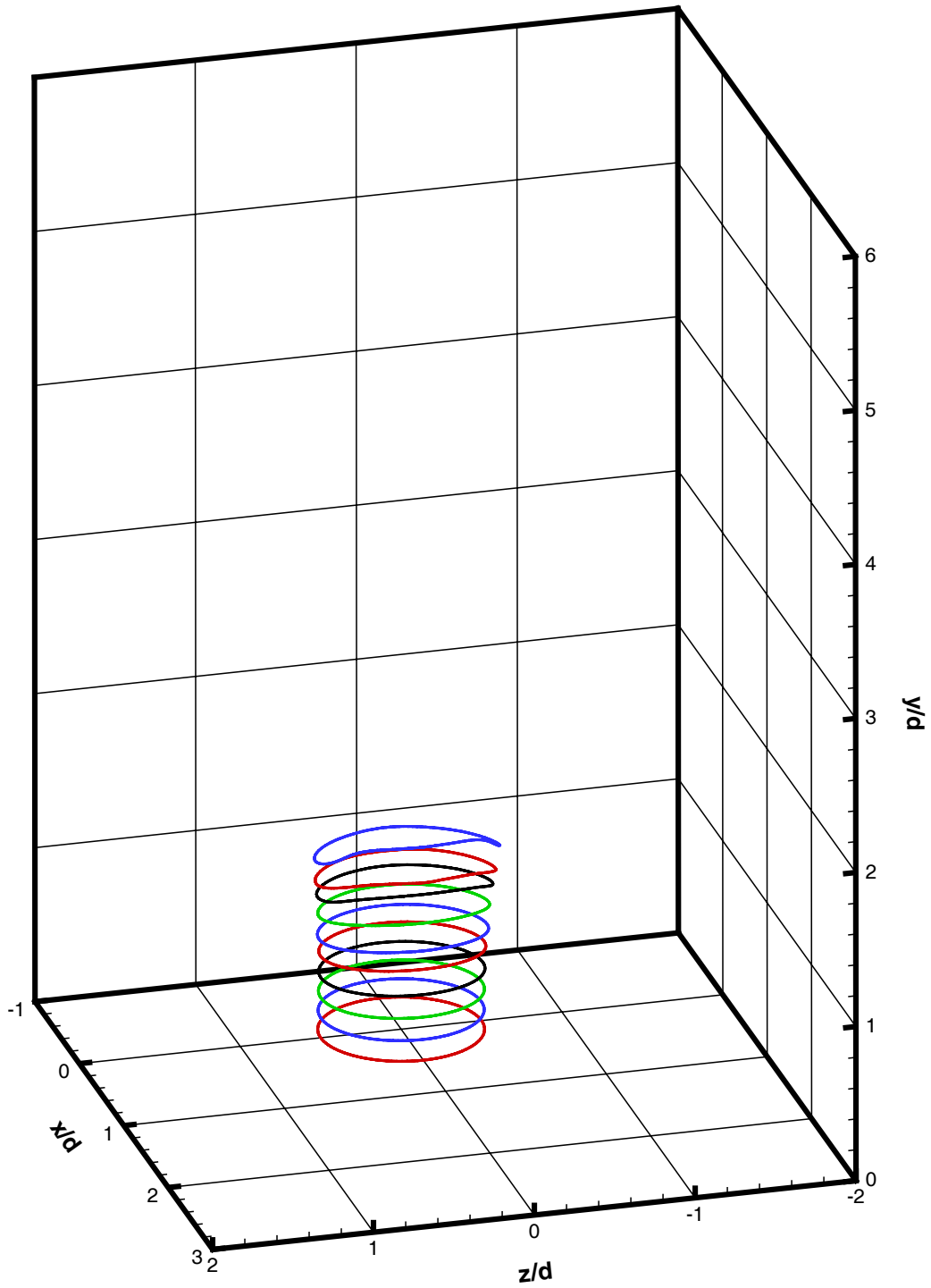

(a) $t = 12.36$

Figure 4-14: Front view of the evolution of material line elements introduced at the jet nozzle exit during $t \in [12.0, 12.36]$ (Case I).

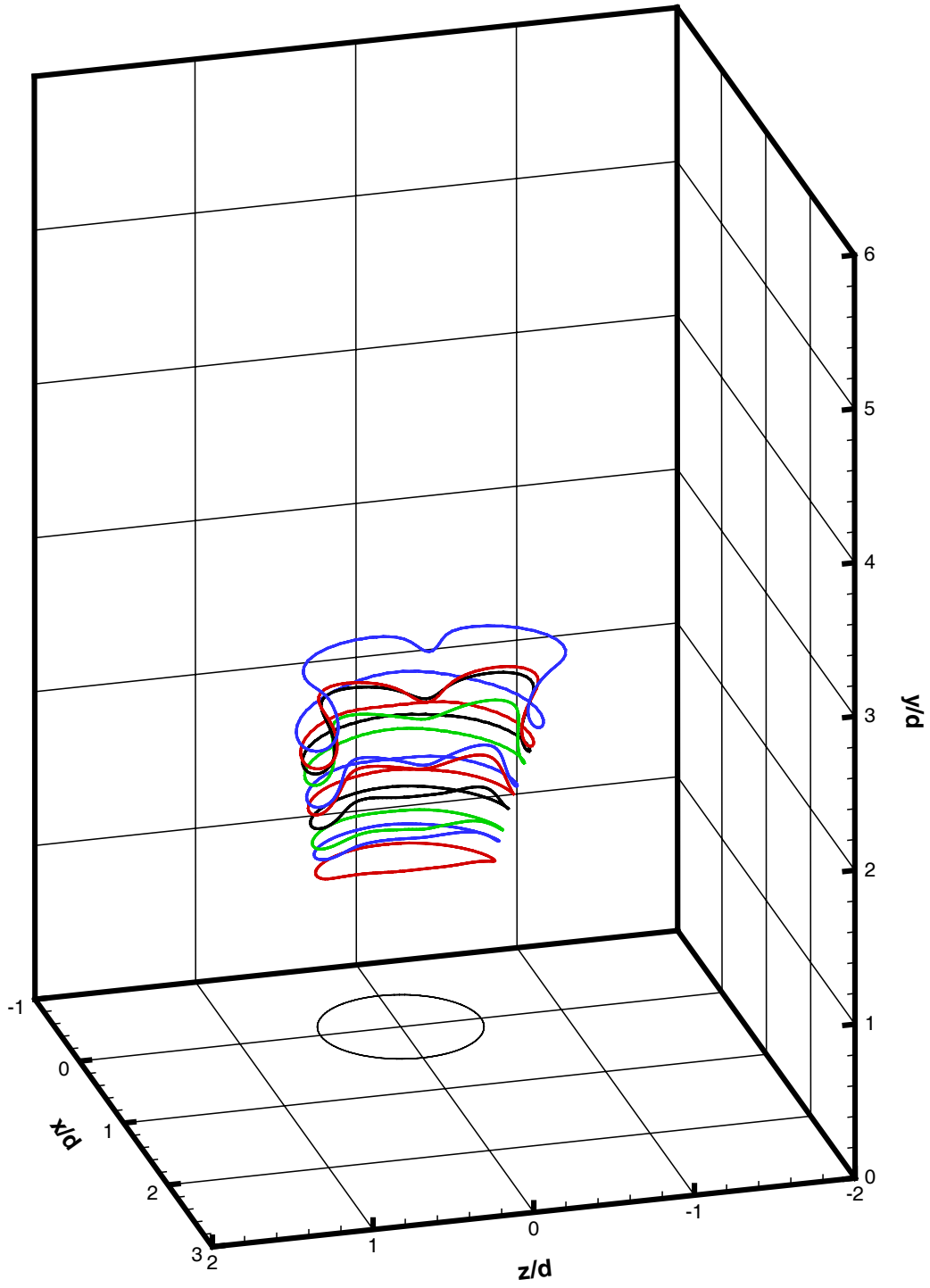

(d) $t = 12.68$

Figure 4-14: Continued from the previous page.

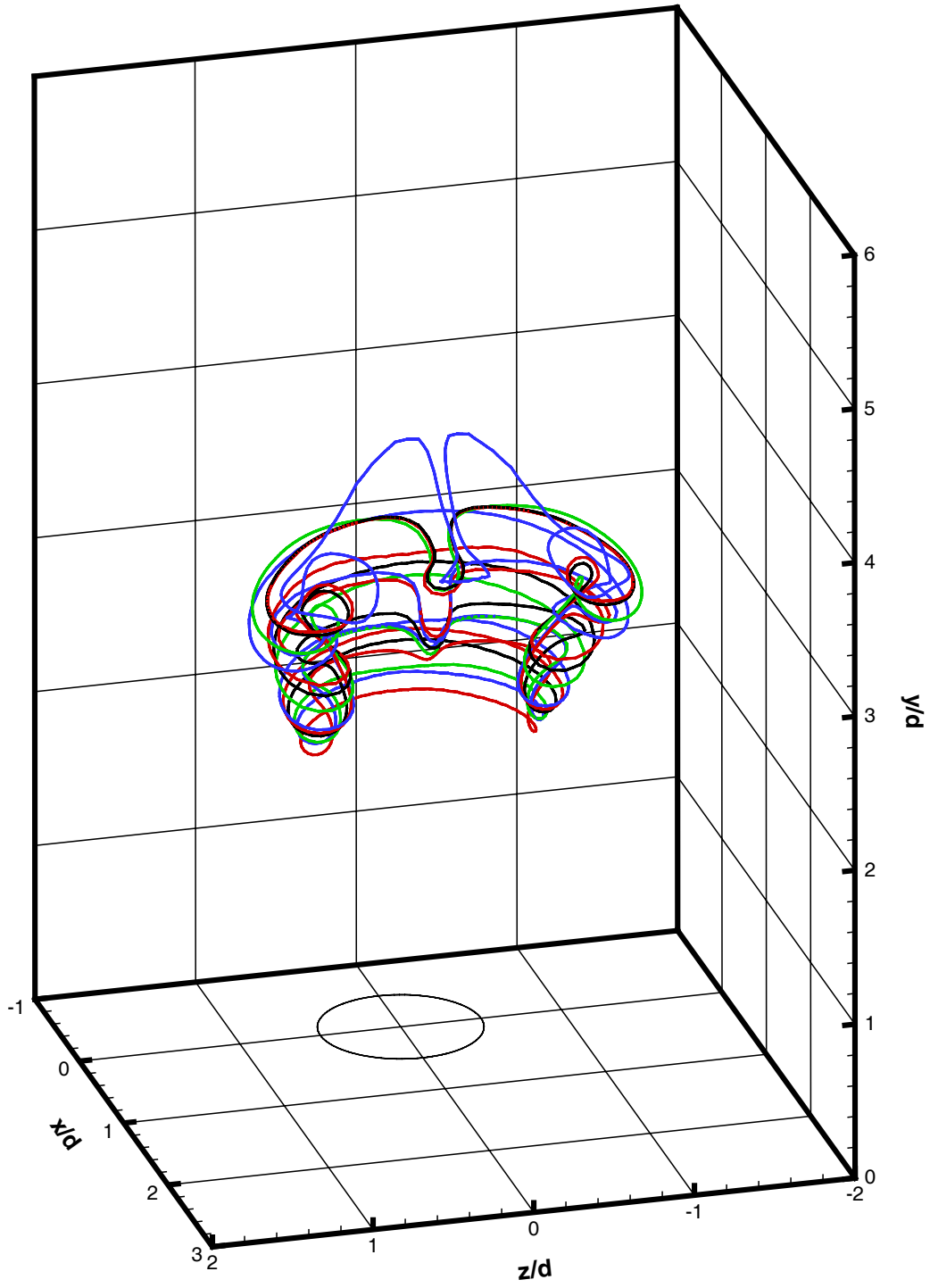

(c) $t = 13.00$

Figure 4-14: Continued from the previous page.

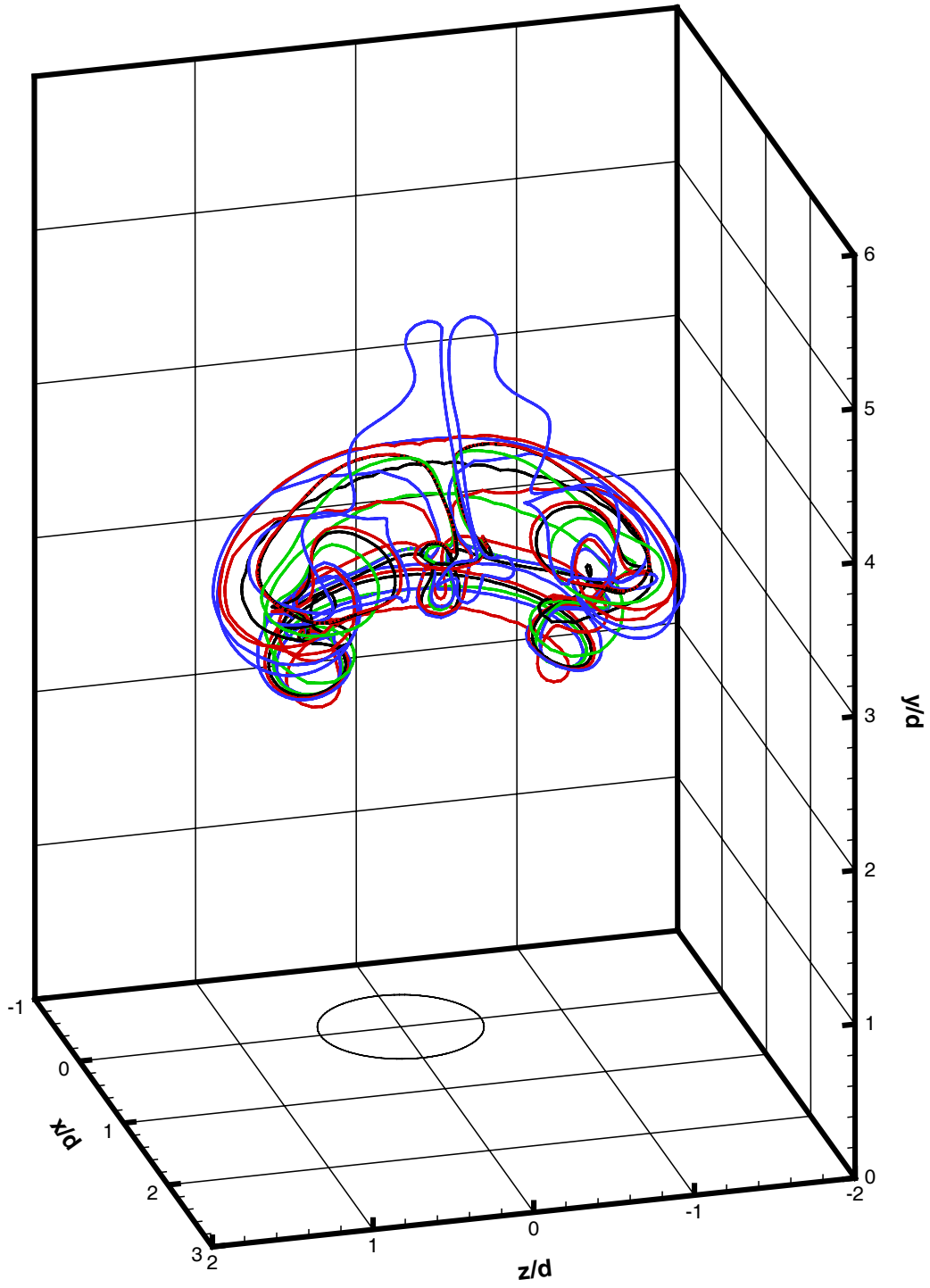

(d) $t = 13.16$

Figure 4-14: Continued from the previous page.

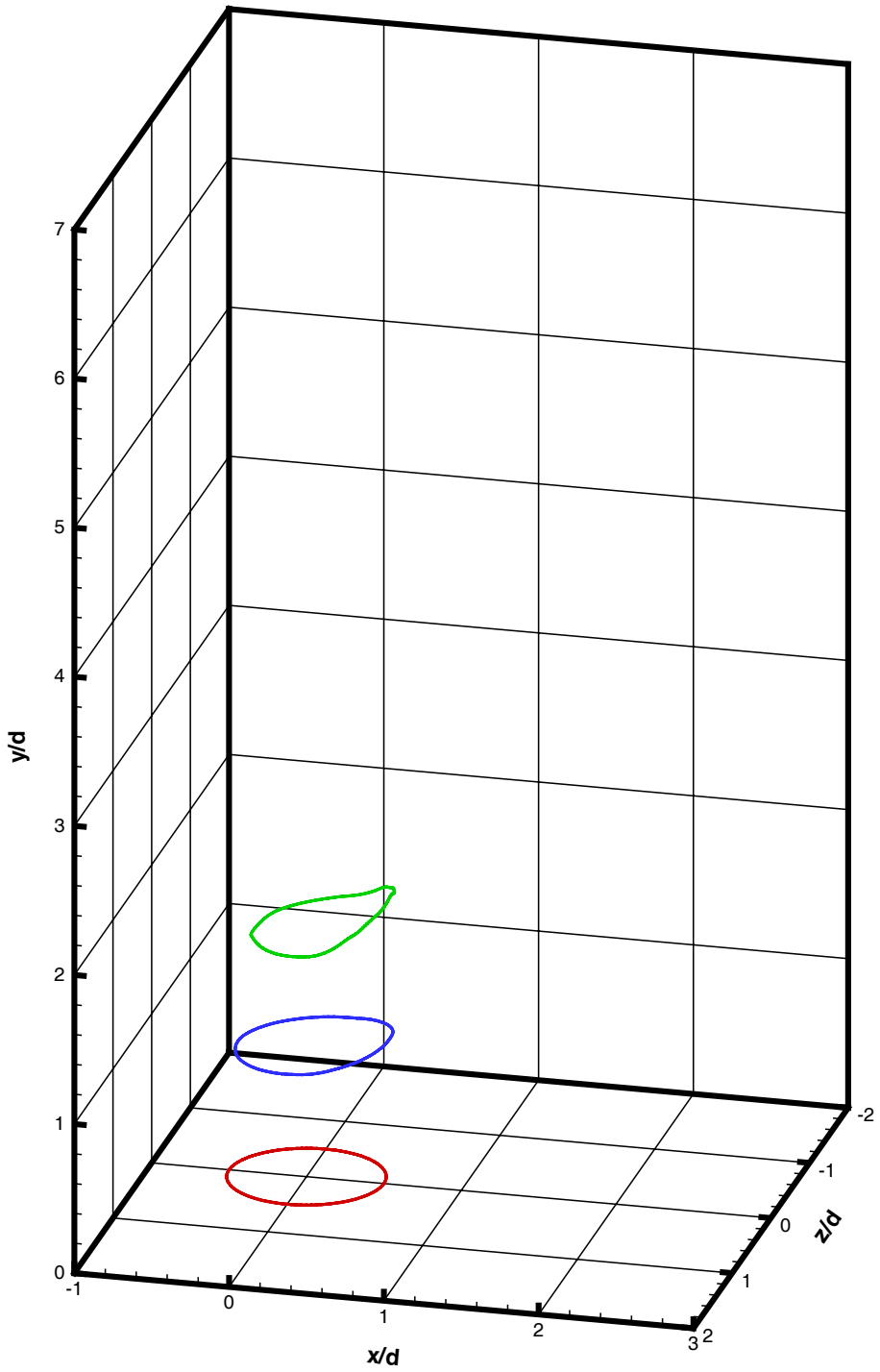

(a) $t = 15.36$

Figure 4-15: Side view of the evolution of material line elements introduced at the jet nozzle exit at $t = 15.0, 15.16, 15.36$ (Case II).

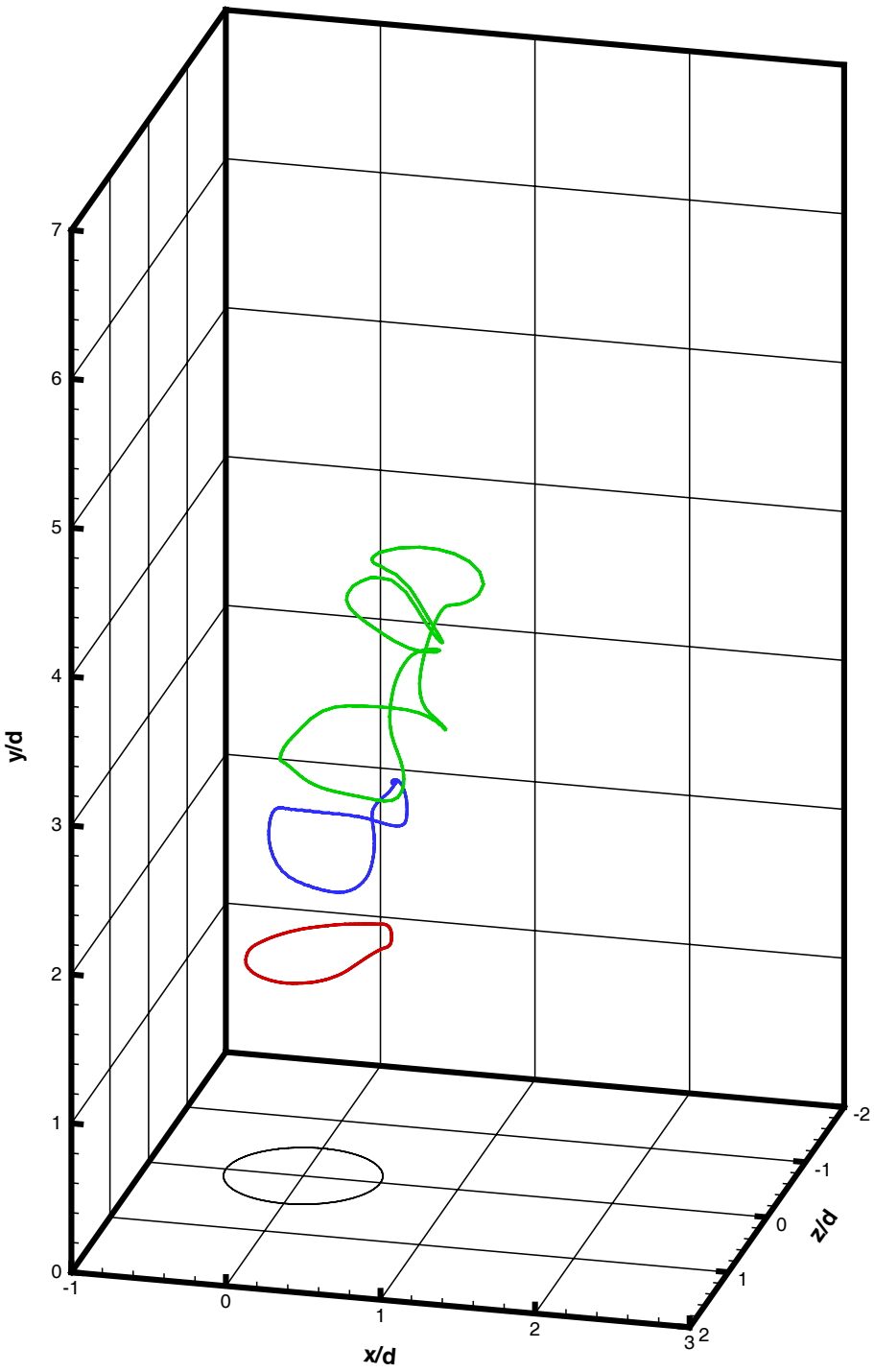

(b) $t = 15.68$

Figure 4-15: Continued from the previous page.

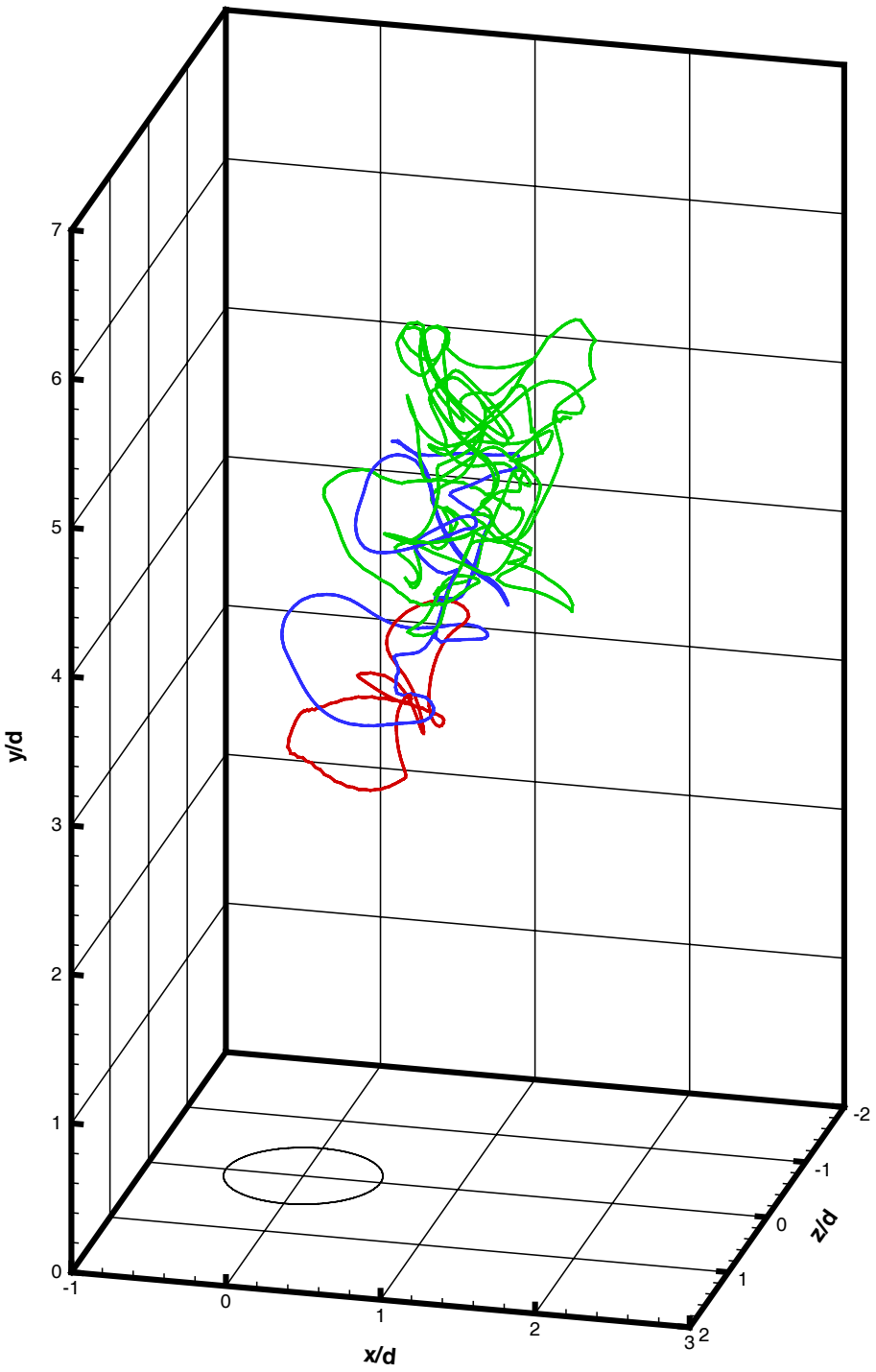

(c) $t = 16.00$

Figure 4-15: Continued from the previous page.

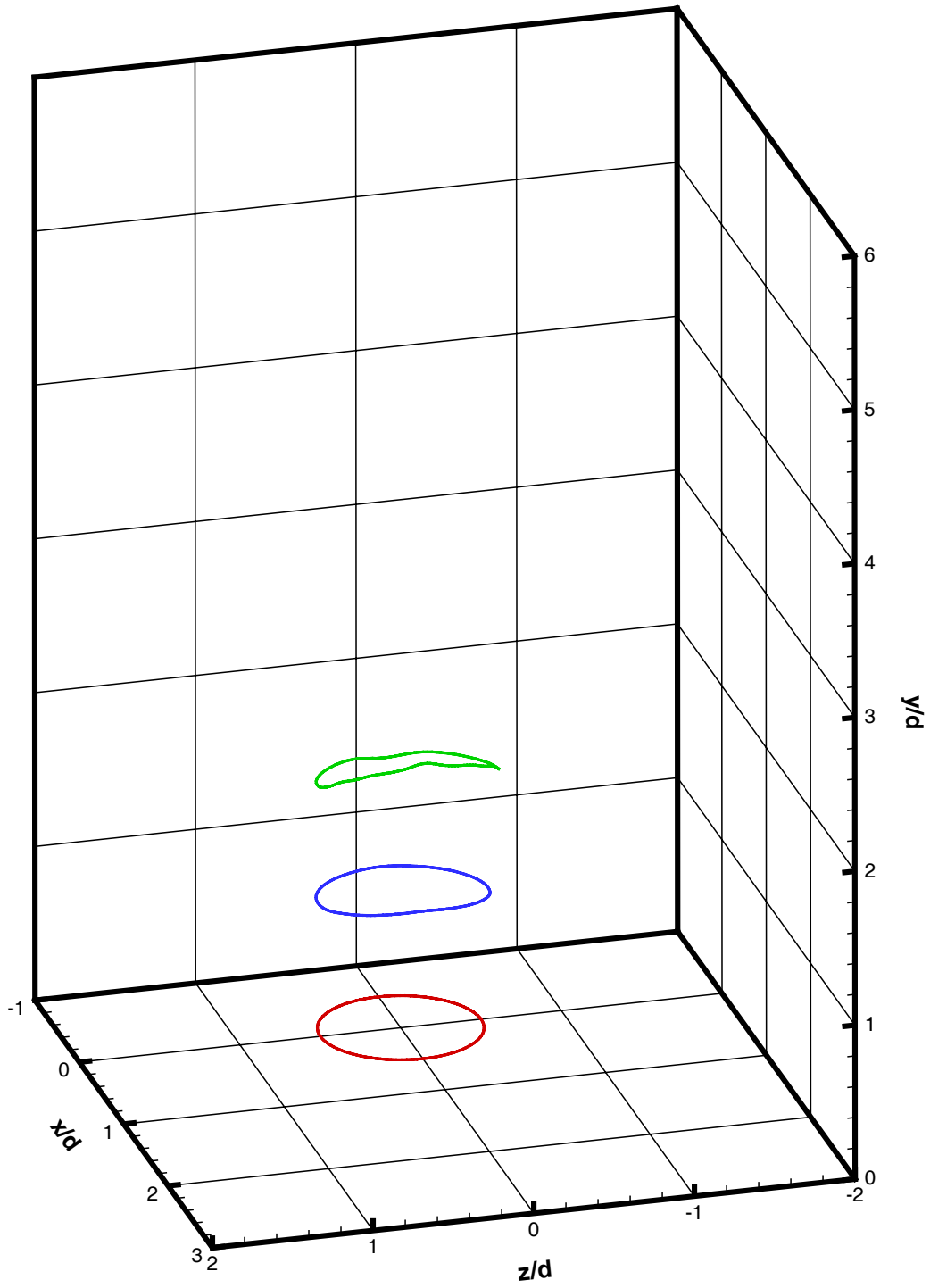

(a) $t = 15.36$

Figure 4-16: Front view of the evolution of material line elements introduced at the jet nozzle exit at $t = 15.0, 15.16, 15.36$ (Case II).

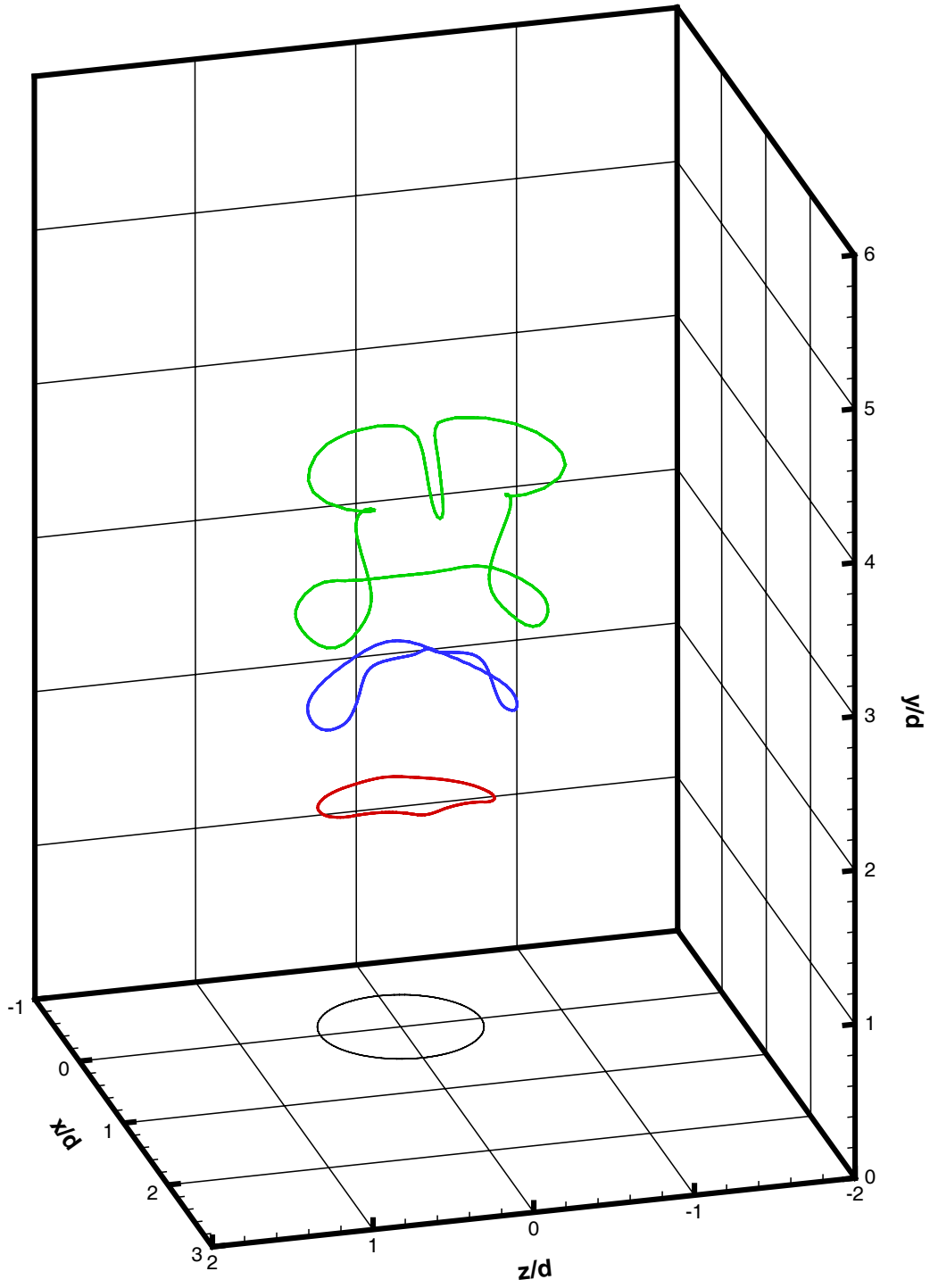

(b) $t = 15.68$

Figure 4-16: Continued from the previous page.

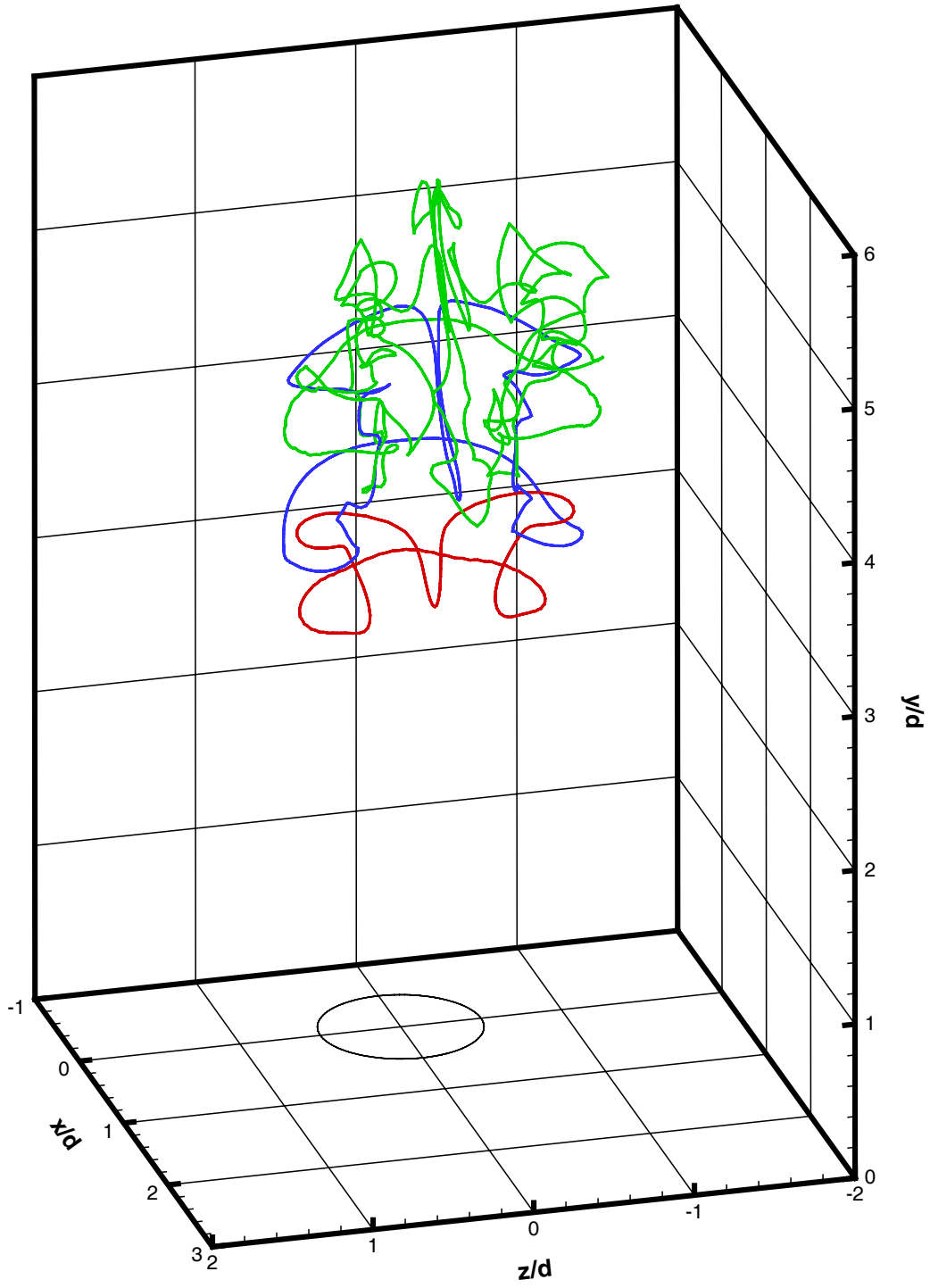

(c) $t = 16.00$

Figure 4-16: Continued from the previous page.

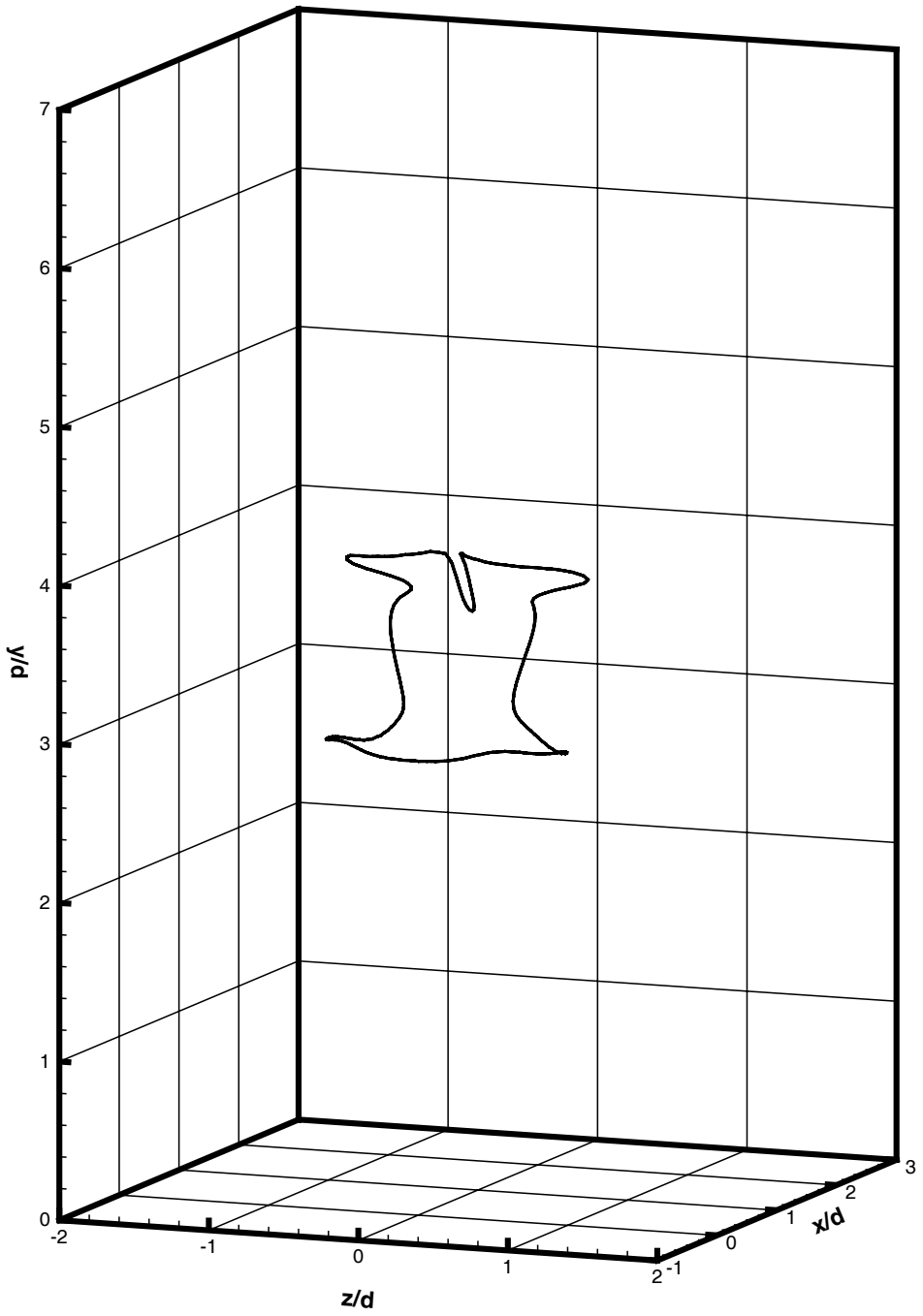

(a) $t = 15.68$

Figure 4-17: Evolution of a material ring, introduced at the jet nozzle exit at $t = 15.0$ (Case II).

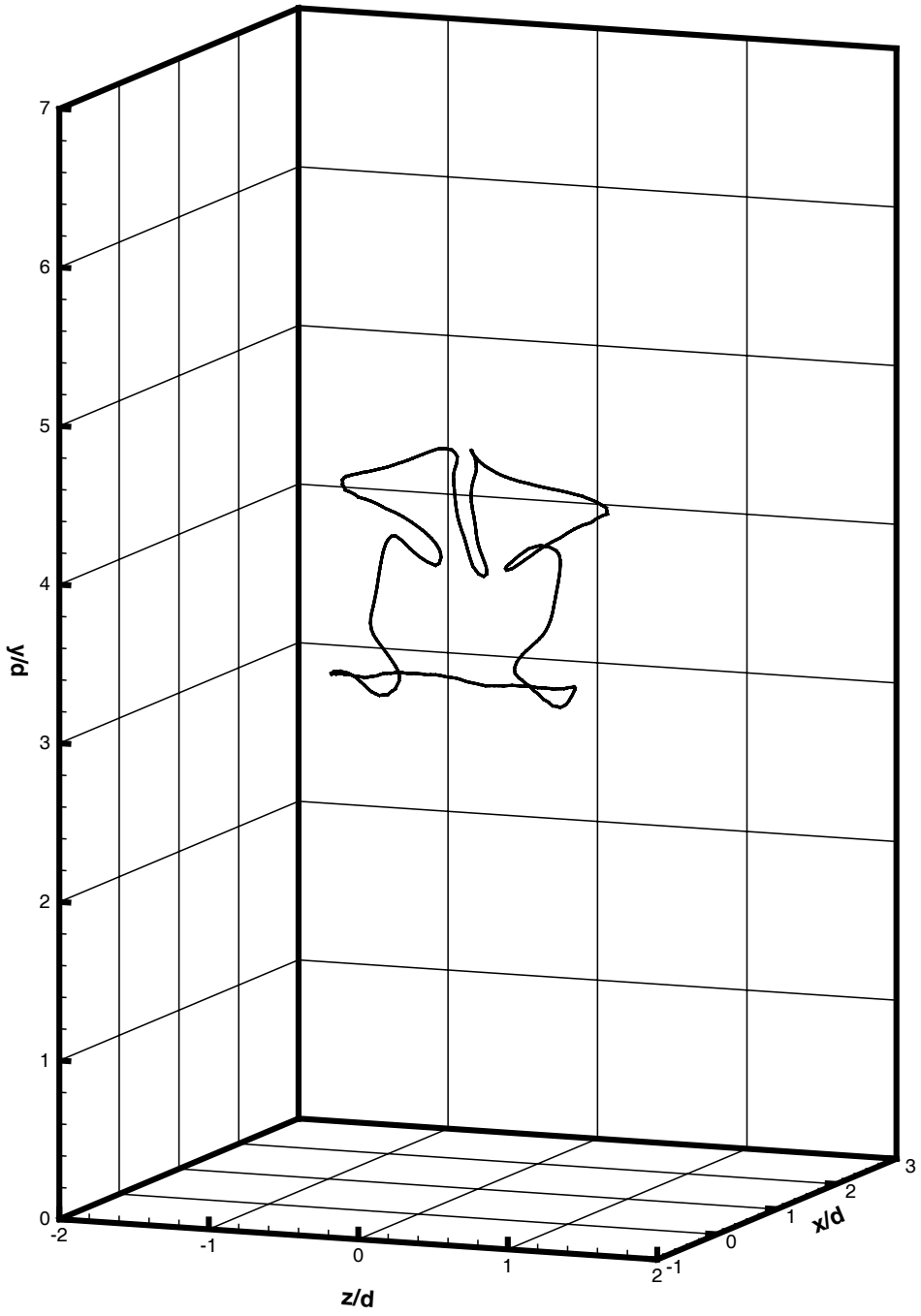

(b) $t = 15.76$

Figure 4-17: Continued from the previous page.

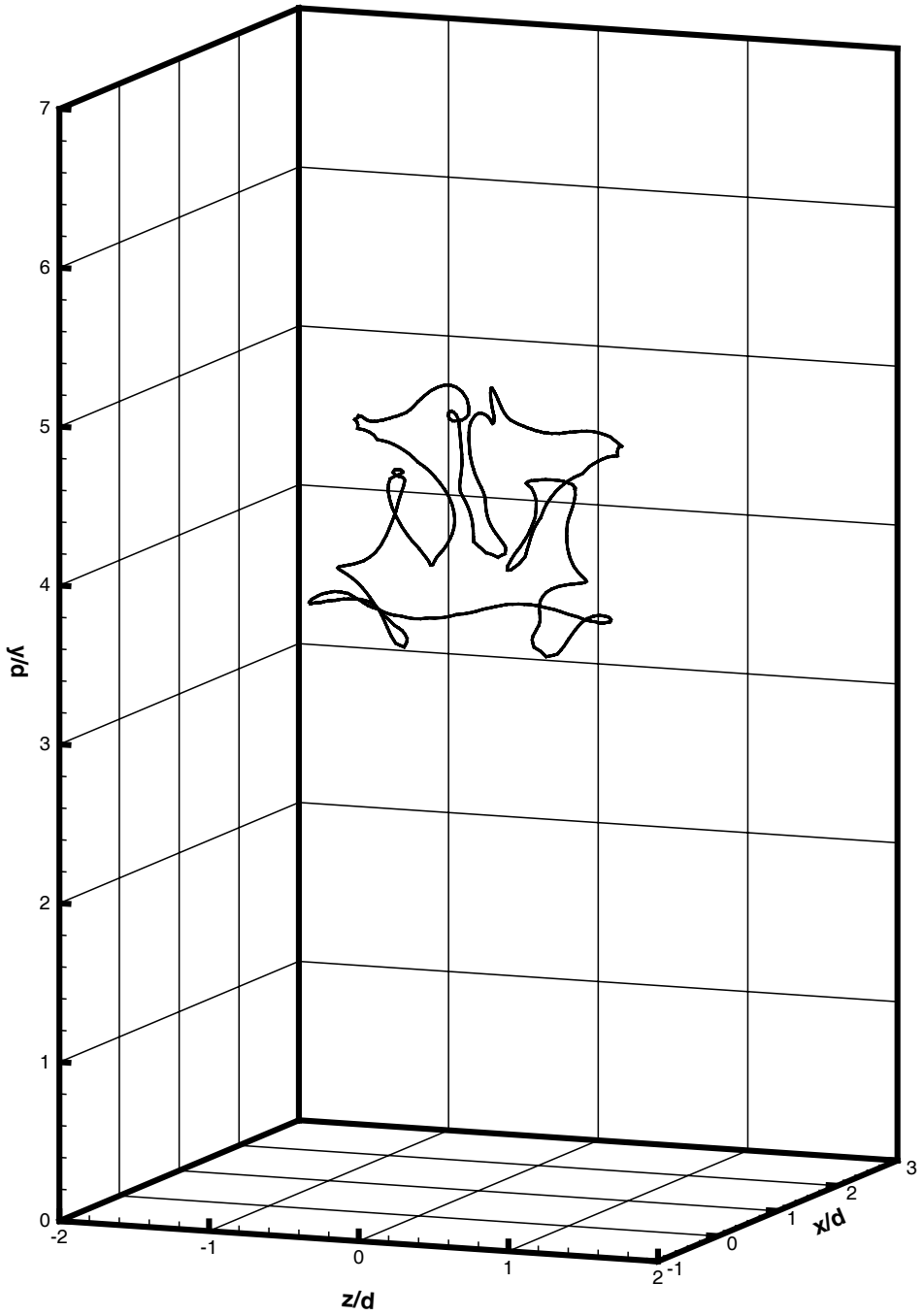

(c) $t = 15.84$

Figure 4-17: Continued from the previous page.

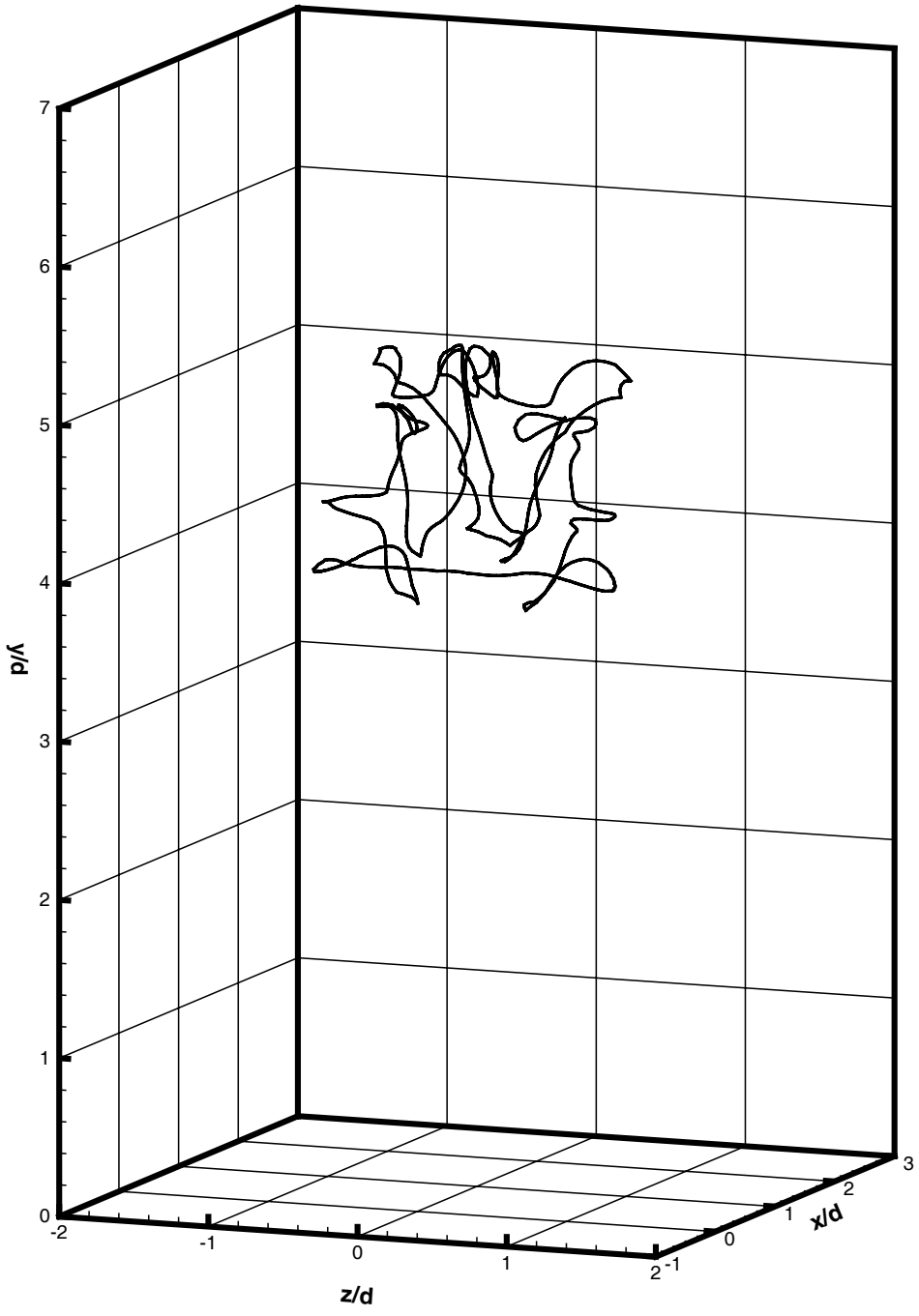

(d) $t = 15.92$

Figure 4-17: Continued from the previous page.

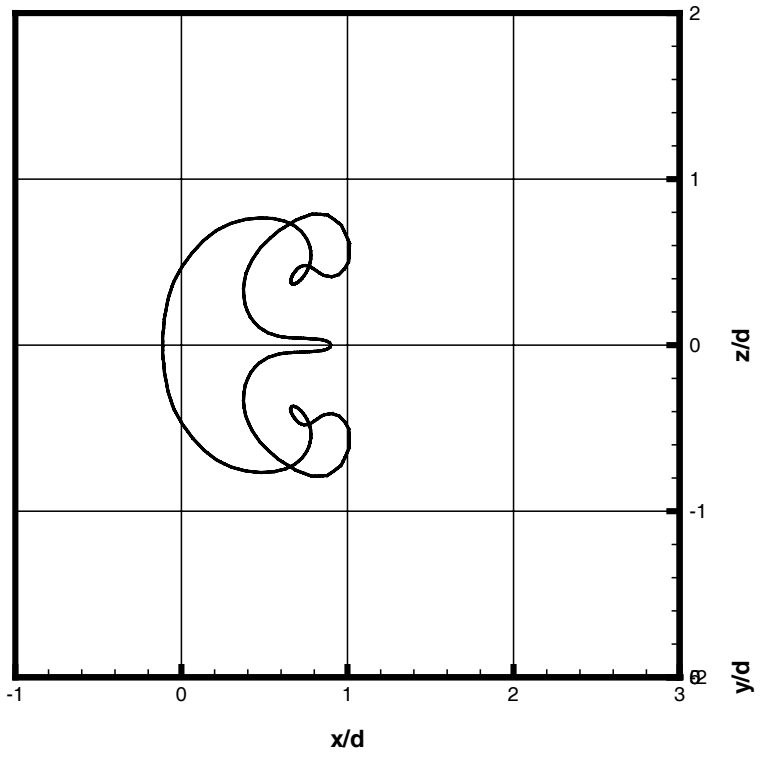

(a) $t = 15.68$

Figure 4-18: Evolution of a material ring, introduced at the jet nozzle exit at $t = 15.0$ (Case II).

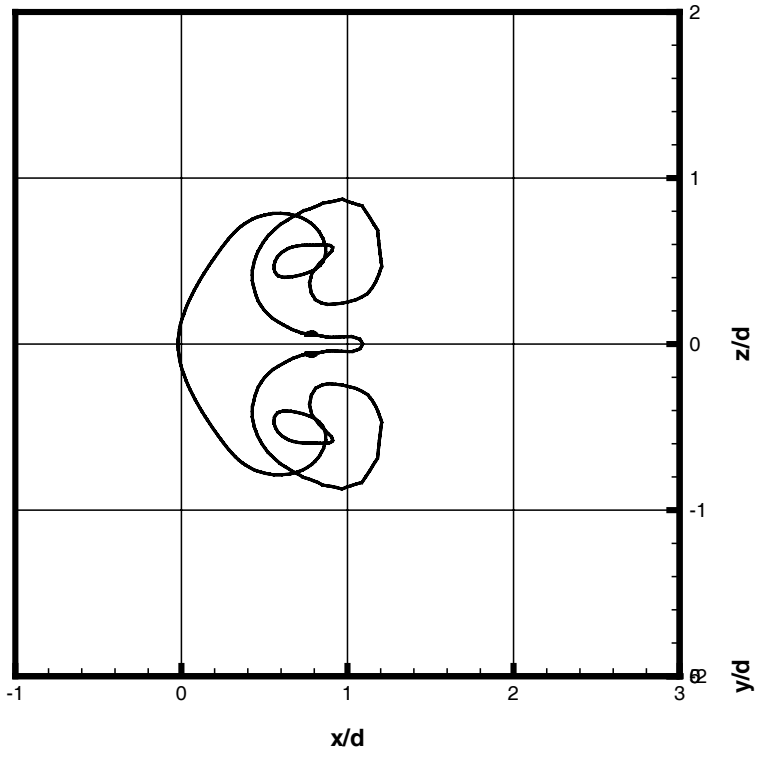

(b) $t = 15.76$

Figure 4-18: Continued from the previous page.

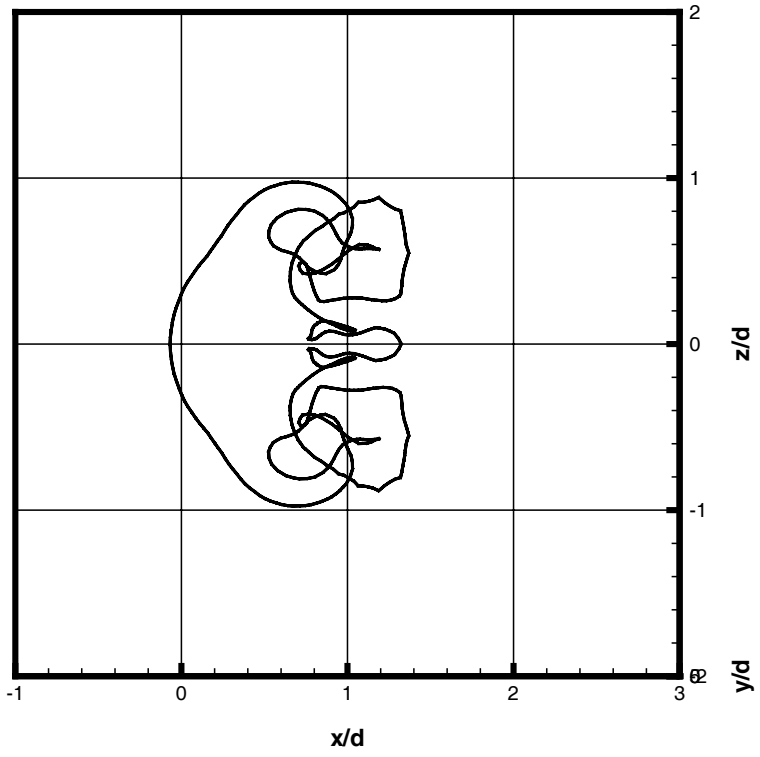

(c) $t = 15.84$

Figure 4-18: Continued from the previous page.

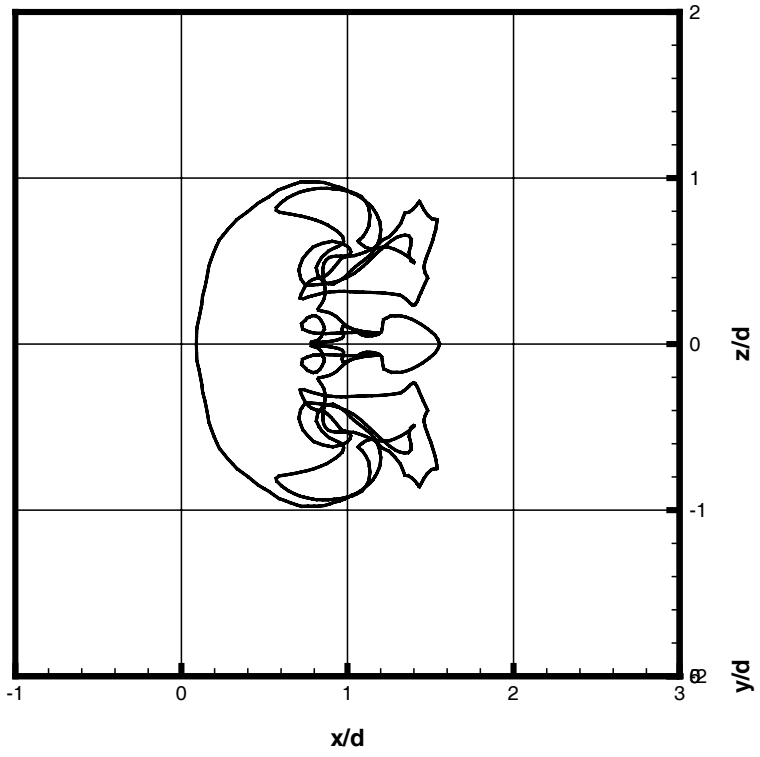

(d) $t = 15.92$

Figure 4-18: Continued from the previous page.

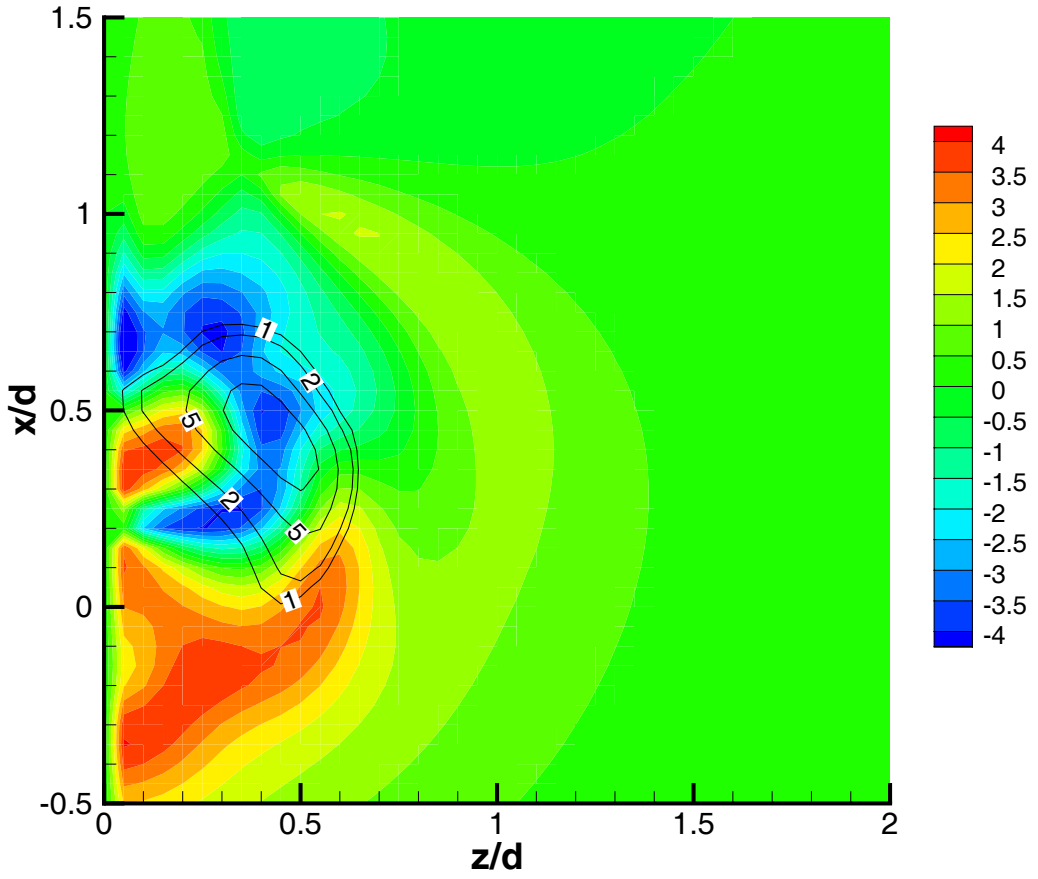

(a) $y/d = 2.0$

Figure 4-19: Contours of ω_y and the stretching rate on planes of constant y at $t = 15.0$ (Case II). Solid lines represent the contour lines of ω_y. Each plane is colored by the stretching rate, which is computed for $z/d \geq 0.05$.

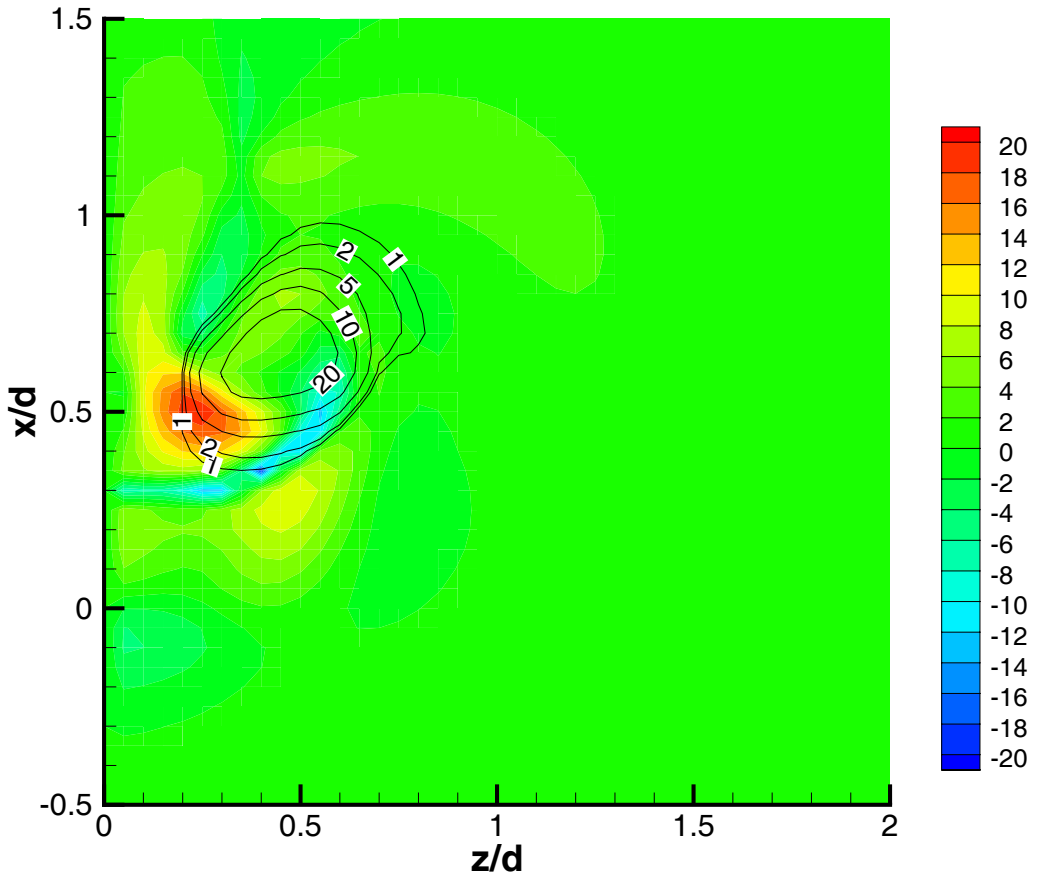

(b) $y/d = 3.0$

Figure 4-19: Continued from the previous page.

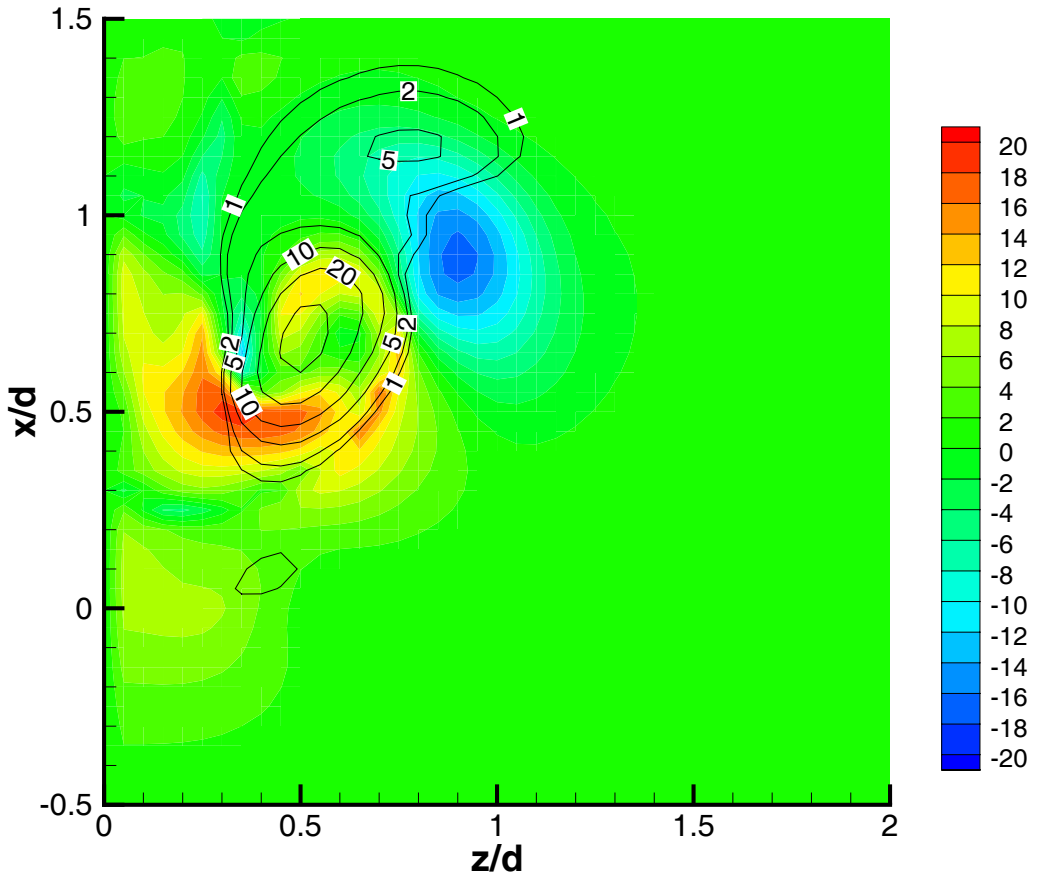

(c) $y/d = 3.5$

Figure 4-19: Continued from the previous page.

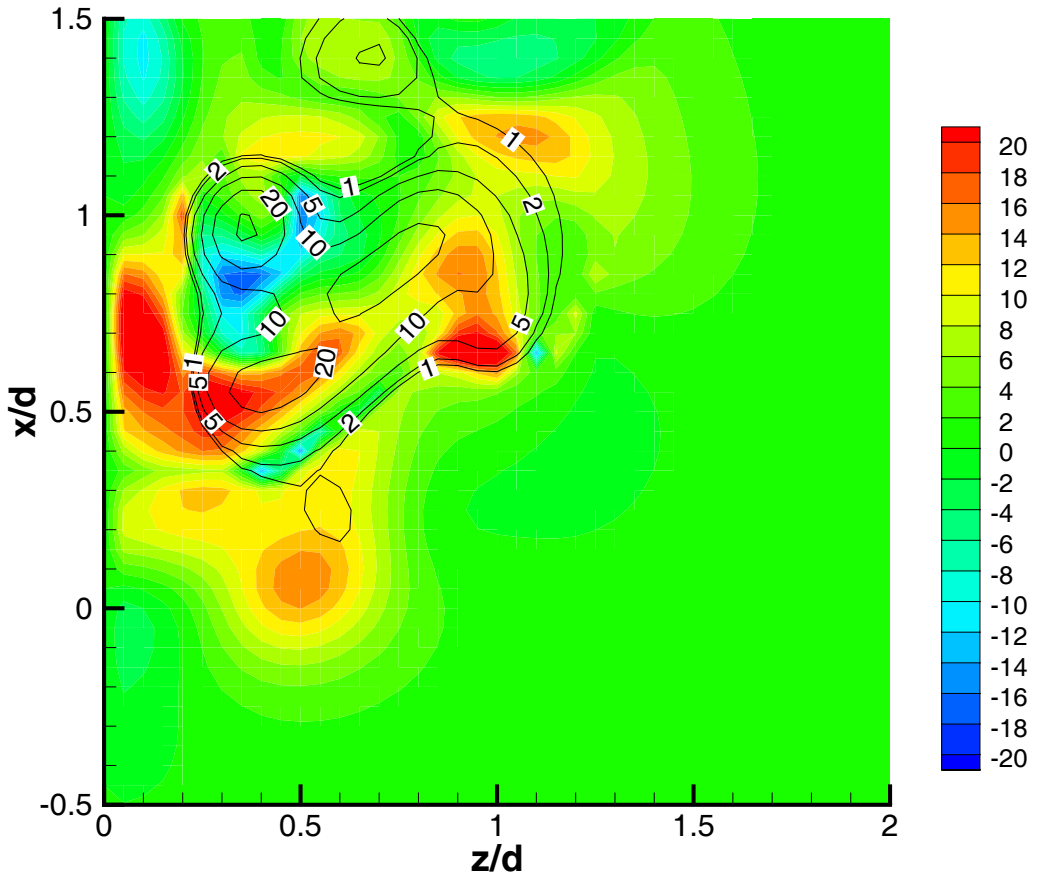

(d) $y/d = 4.0$

Figure 4-19: Continued from the previous page.

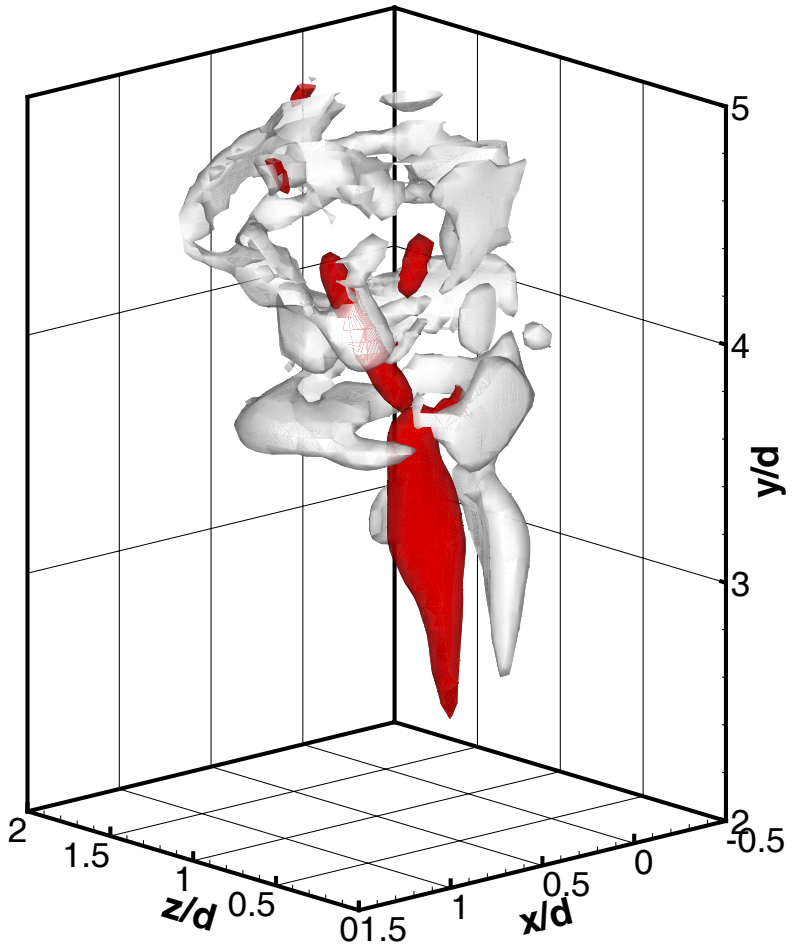

Figure 4-20: Three-dimensional visualization of isosurfaces of ω_y (red) and stretching rate (white) at $t = 15.0$ (Case II).

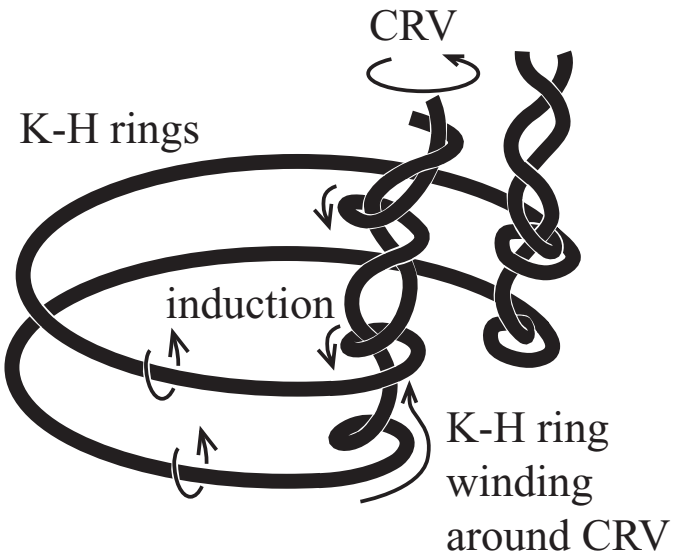

Figure 4-21: Schematic illustration of induced counter-rotating vortex breakdown. Vortex rings, which are formed from the Kelvin-Helmholtz instability on the windward side, wind around counter-rotating vortices. Kink-like structures are formed at the point of winding, and further instability breaks down the counter-rotating vortices through self and/or mutual induction.

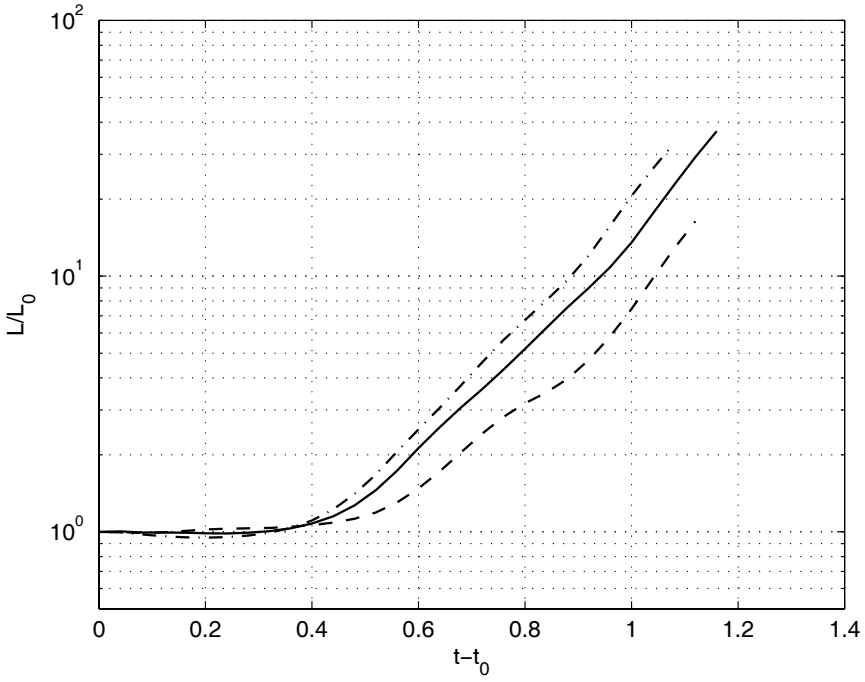

Figure 4-22: Evolution of the length of material rings, L, normalized by the initial length, L_0. The rings are introduced at the jet nozzle exit at $t = 15.0$ (solid), 15.04 (dashed), and 15.08 (dash-dot), respectively. t_0 denotes the time of the introduction of each ring (Case II).

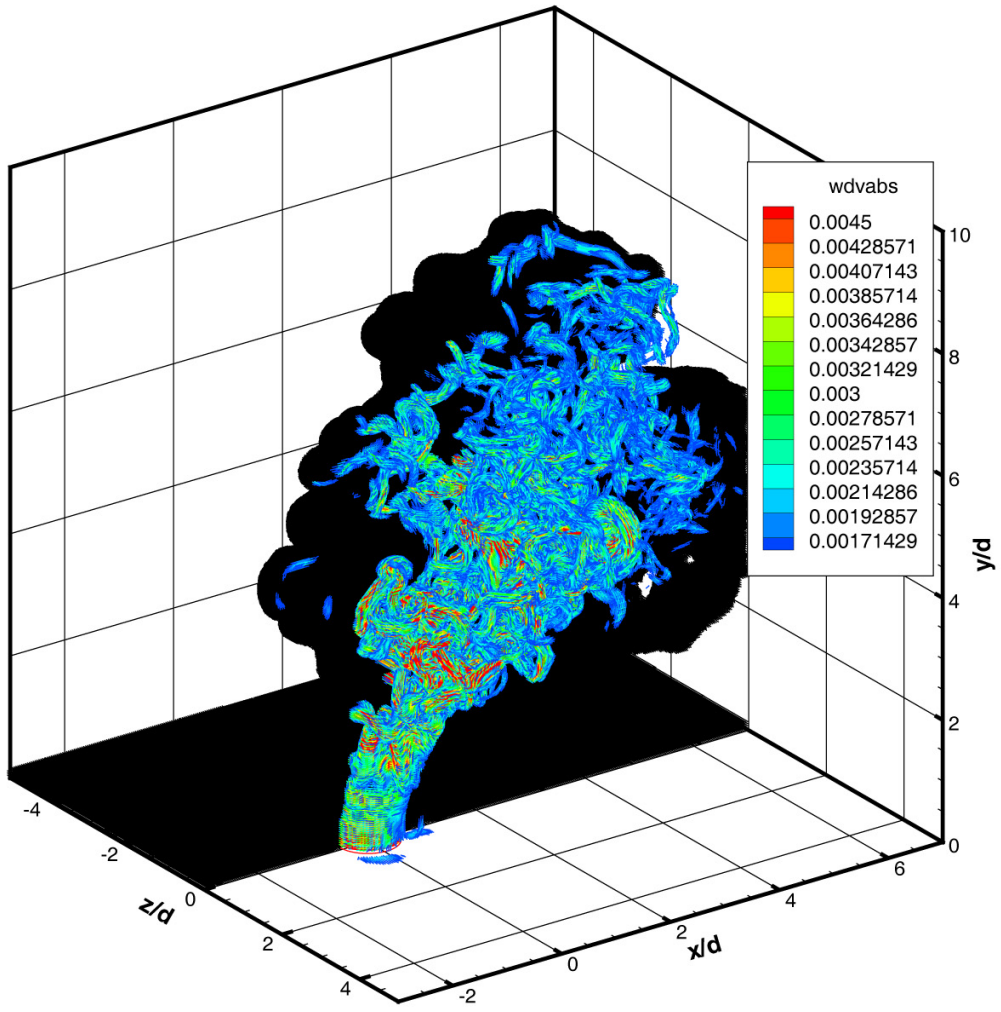

Figure 4-23: Perspective view of computational elements at $t = 4.0$ (Case III). The black cloud at $z/d < 0$ shows all the computational elements. The elements shown at $z/d > 0$ are those with $|\boldsymbol{\omega}_i dV_i| > 0.0015$, colored by $|\boldsymbol{\omega}_i dV_i|$.

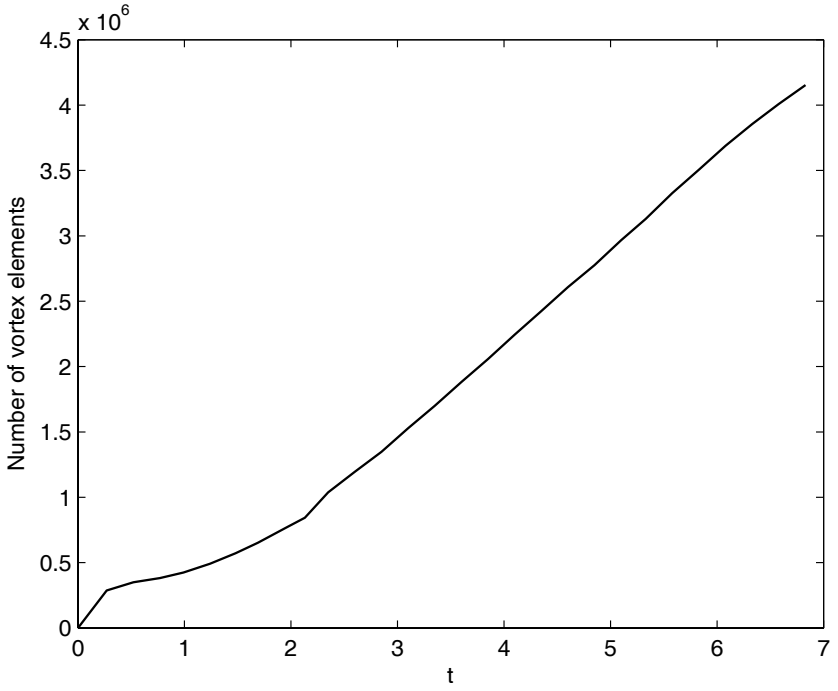

Figure 4-24: Number of vortex elements verses time (Case III).

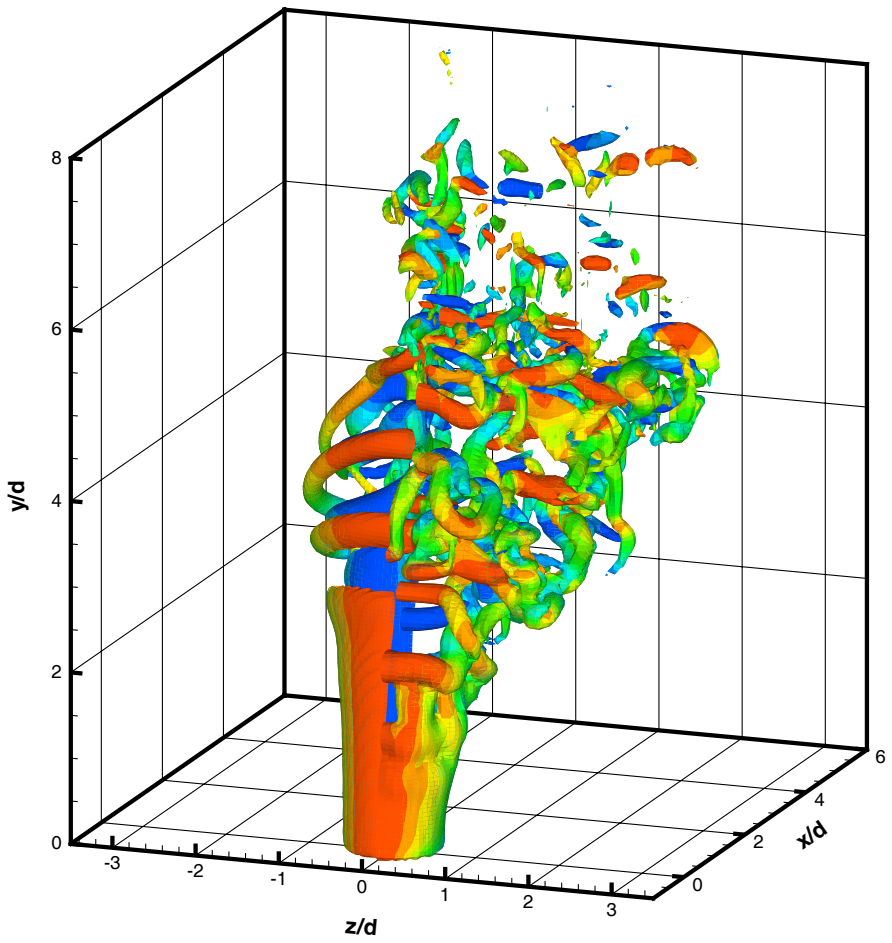

(a) windward side, colored by $-20 \leq \omega_z \leq 20$

Figure 4-25: Vorticity magnitude isosurfaces, $|\boldsymbol{\omega}| = 20$ at two perspectives. Isosurfaces in $z \geq 0$ are from Case III at $t = 4.0$. Isosurfaces in $z < 0$ are from Case I at t=12.0.

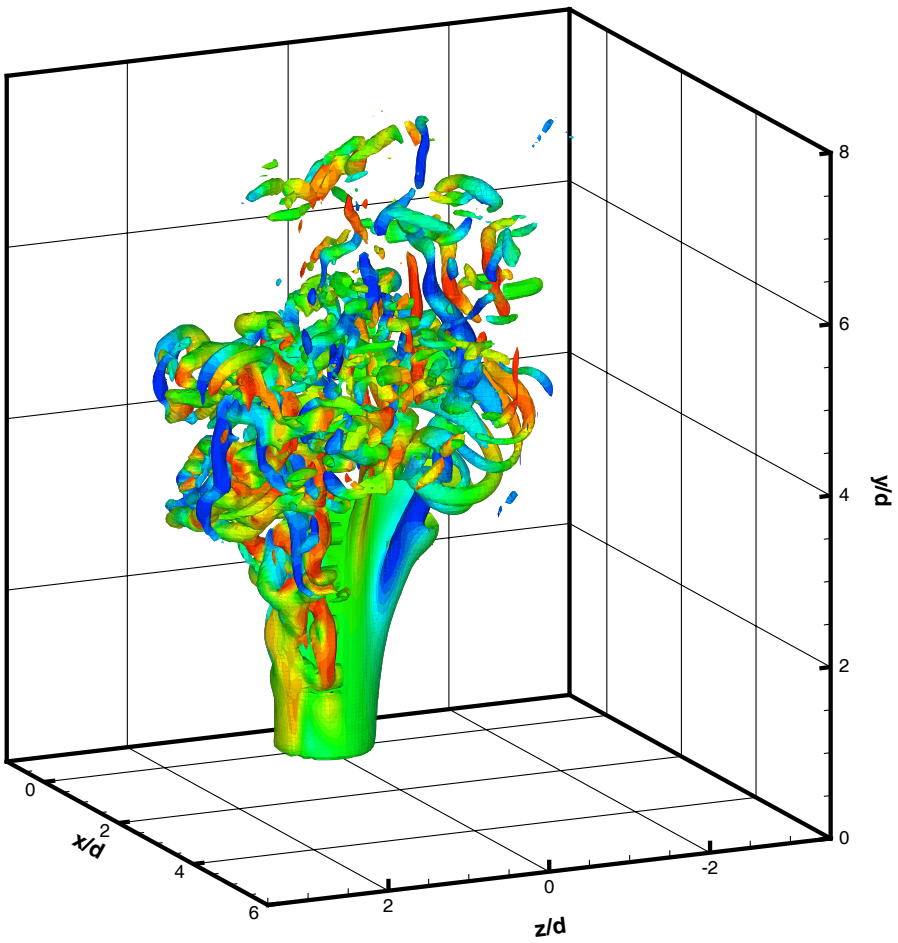

(b) lee side, colored by $-20 \leq \omega_y \leq 20$

Figure 4-25: Continued from the previous page.

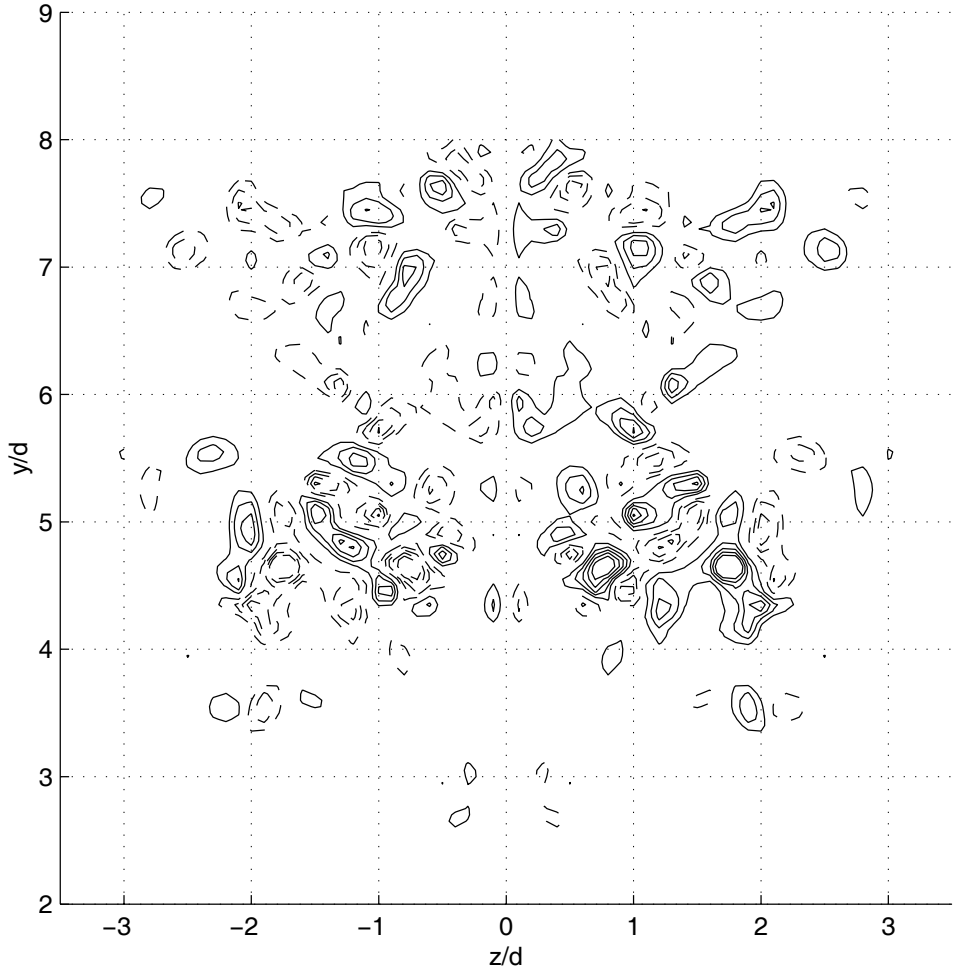

Figure 4-26: Crosssectional view showing the contours of ω_x at $x/d = 3.0$ and $t = 4.0$ (Case III). Dashed curves indicate negative values. The outer most lines indicate $\omega_x = \pm 4$. The difference between two adjacent levels is 4.

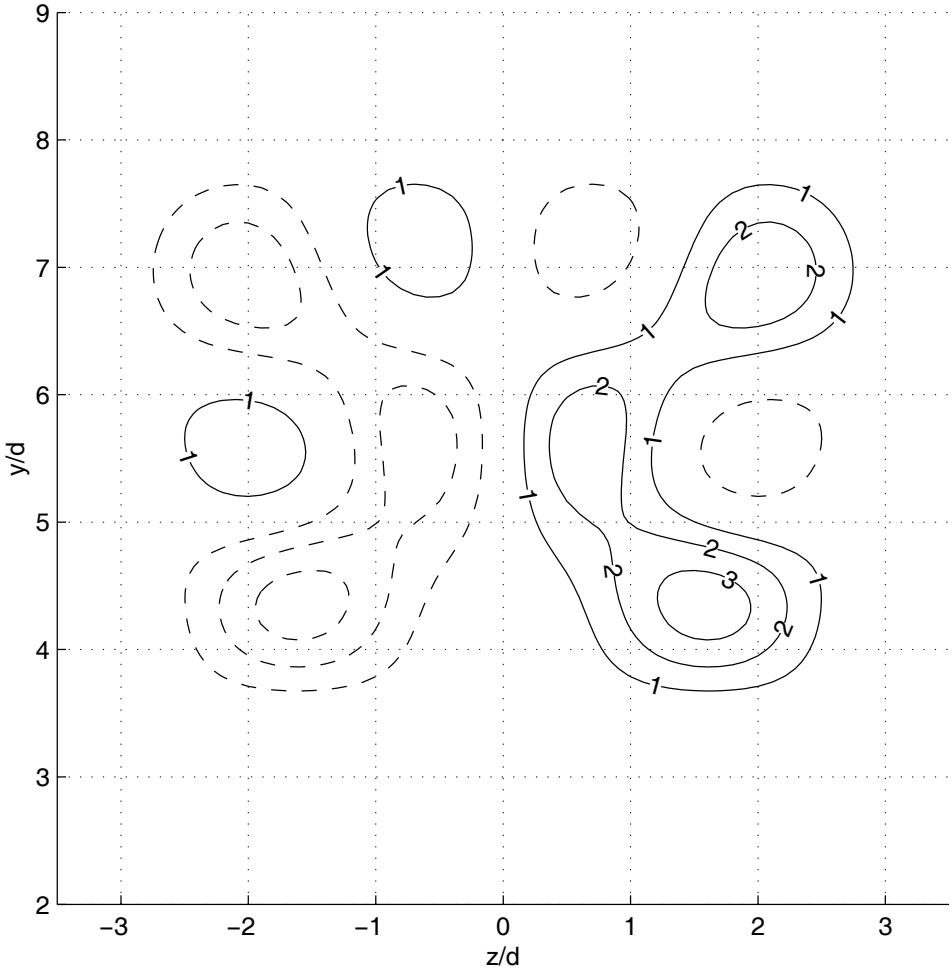

Figure 4-27: Crosssectional view showing the contours of filtered ω_x at $x/d = 3.0$ and $t = 4.0$ (Case III). Dashed curves indicate negative values.

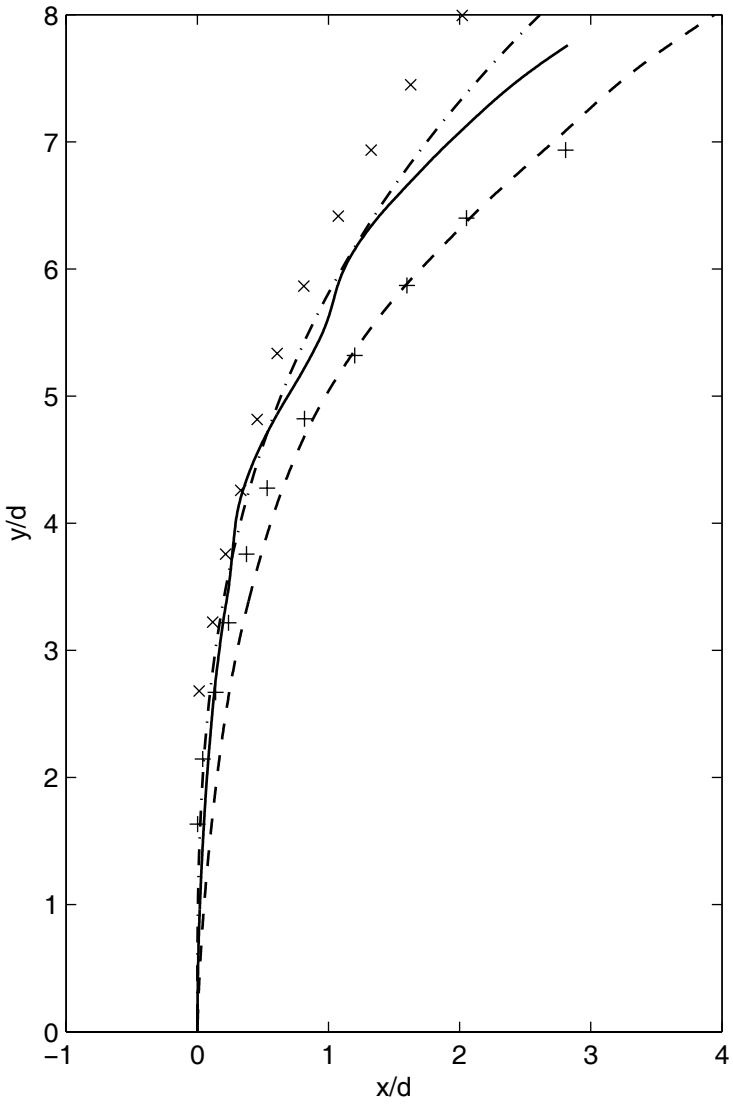

Figure 4-28: Computed trajectories verses experimental observations. Solid and dashed curves represent jet centre streamlines obtained for $t \in [4.0, 7.0]$ in Case III and $t \in [12.0, 17.6]$ in Case I, respectively. Upright crosses, slanted crosses, and circles represent the experimental data with $r = 6$ and $r = 8$ obtained by Keffer and Baines [32], respectively. The dash-dot curve represents an experimental correlation (1.2) for $r = 7$ [49].

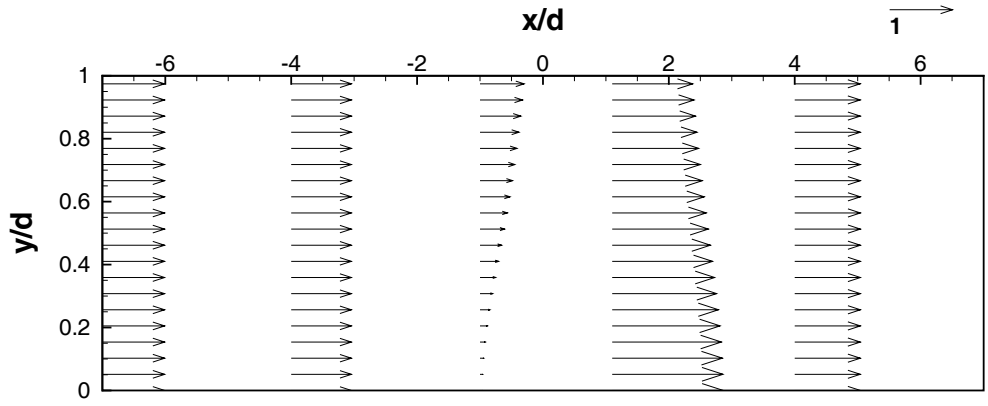

(a) $t = 0.0$

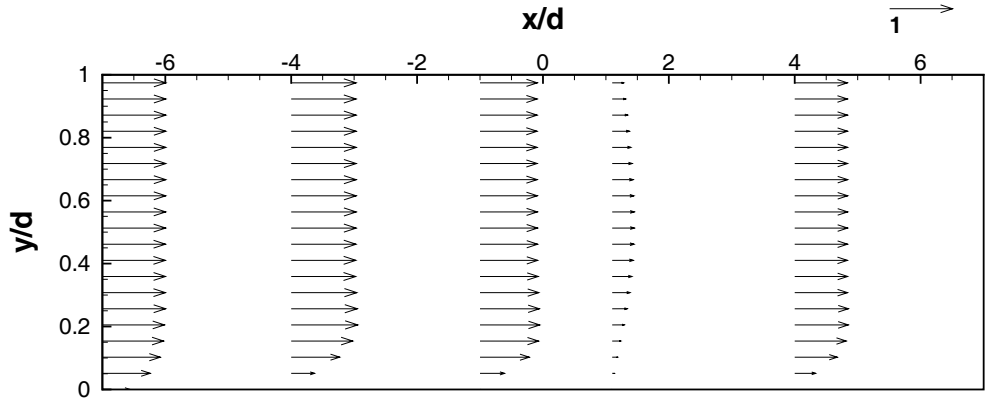

(b) $t = 2.0$

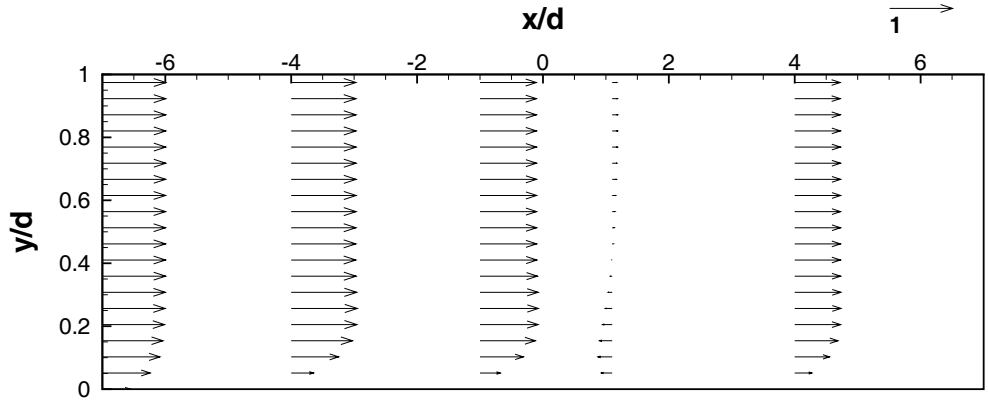

(c) $t = 4.0$

Figure 4-29: Evolution of the crossflow-streamwise velocity component, u_x, on the plane of $z/d = 0$, computed at $x/d = -7$, $x/d = -4$, $x/d = -1$, $x/d = 1.1$, and $x/d = 4$ (Case III). Reference vector of unit speed is plotted near the top right corner.

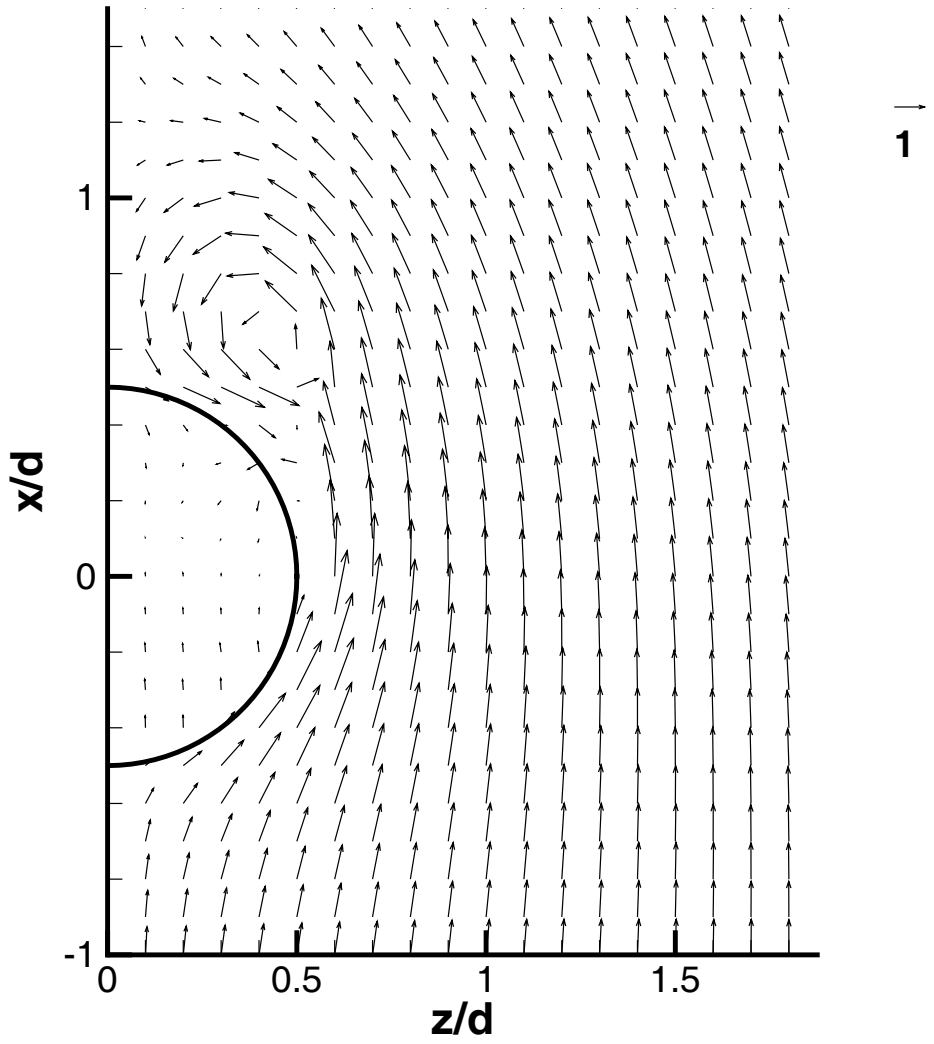

Figure 4-30: Velocity field on the plane of $y/d = 0.2$ at $t = 4.0$ (Case III). Reference vector of unit speed is plotted near the top right corner. The half circle indicates the location of the nozzle boundary.

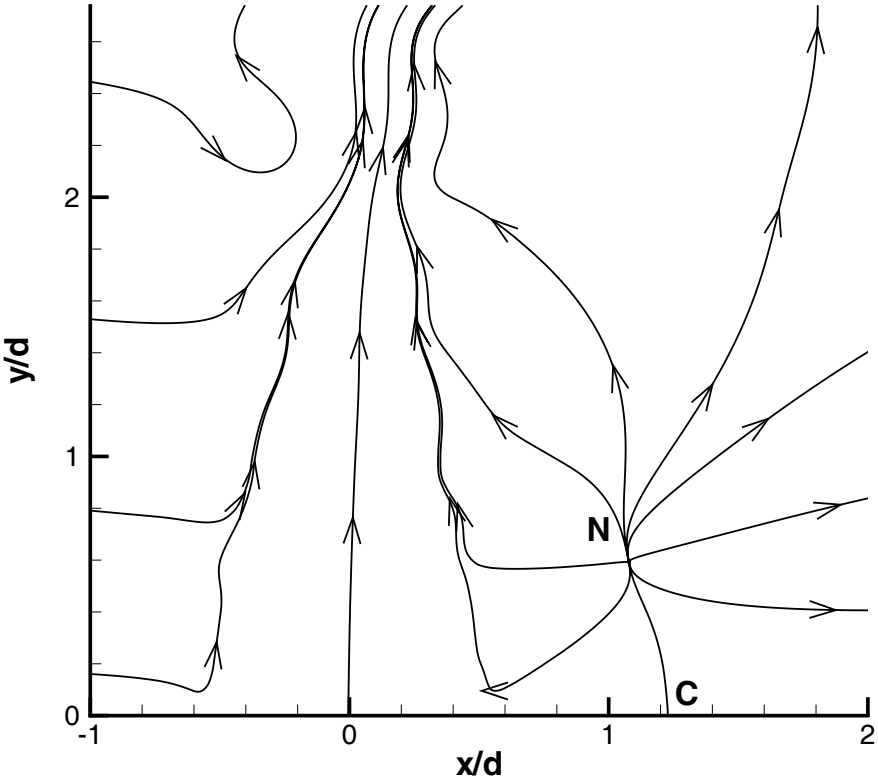

(a) $z = 0$

Figure 4-31: Near-wall flow structures demonstrated with instantaneous streamlines on three planes at $t = 4.0$ (Case III). S denotes a saddle point and N denotes a node on each plane.

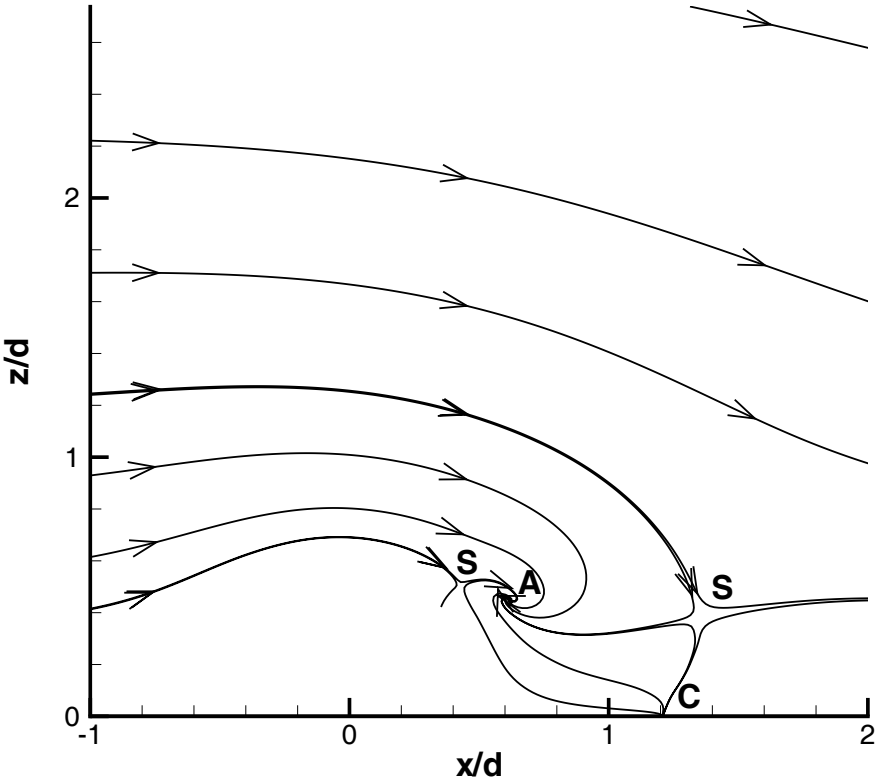

(b) $y = 0.1$

Figure 4-31: Continued from the previous page.

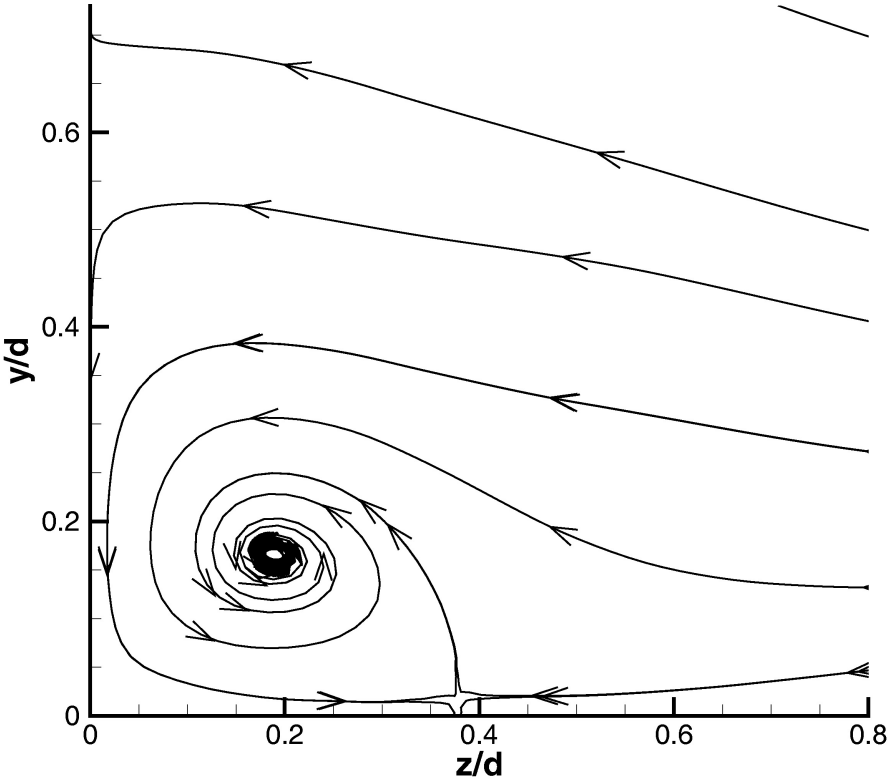

(c) $x = 0.8$

Figure 4-31: Continued from the previous page.

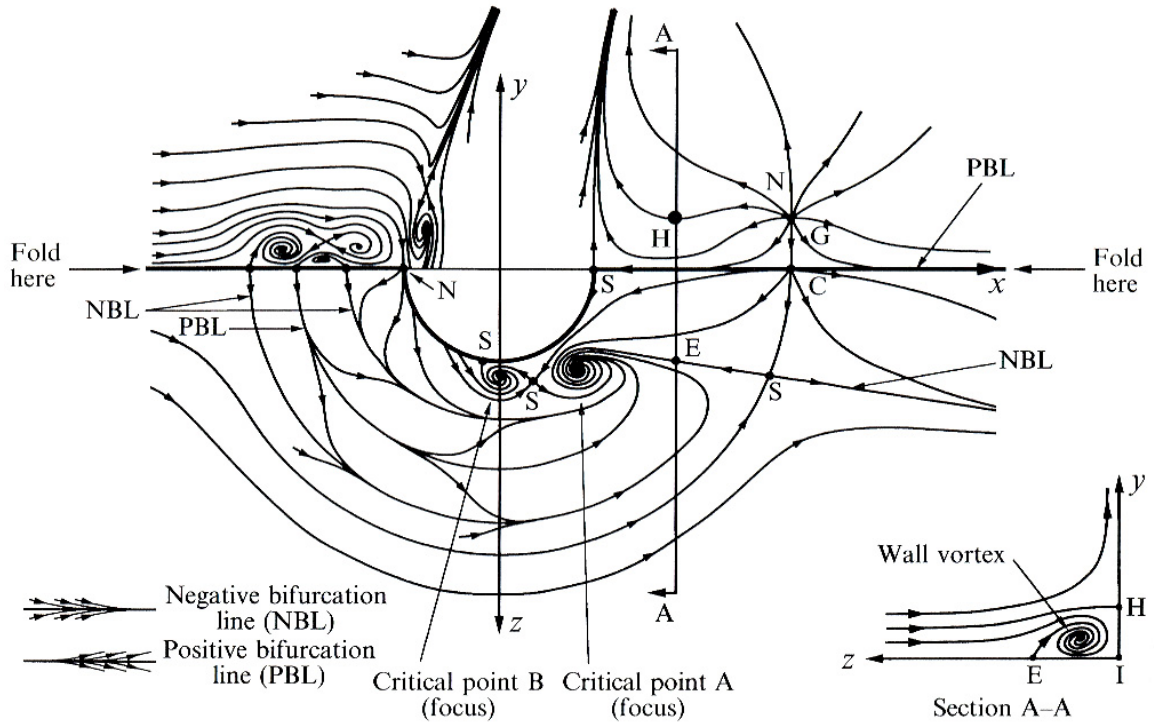

Figure 4-32: Composite streamline pattern, reproduced from [33]. S denotes a saddle point and N denotes a node. Reprinted with the permission of Cambridge University Press (invoice number: P03J 13028).

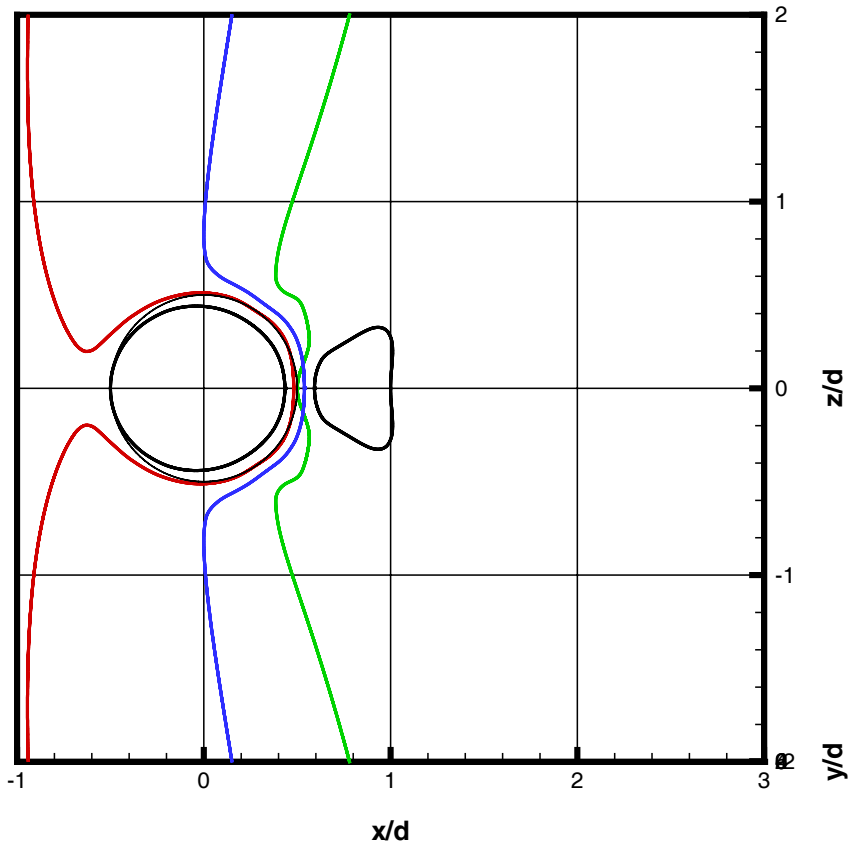

(a) top view

Figure 4-33: Vorticity lines identified near the wall at $t = 4.0$ (Case III).

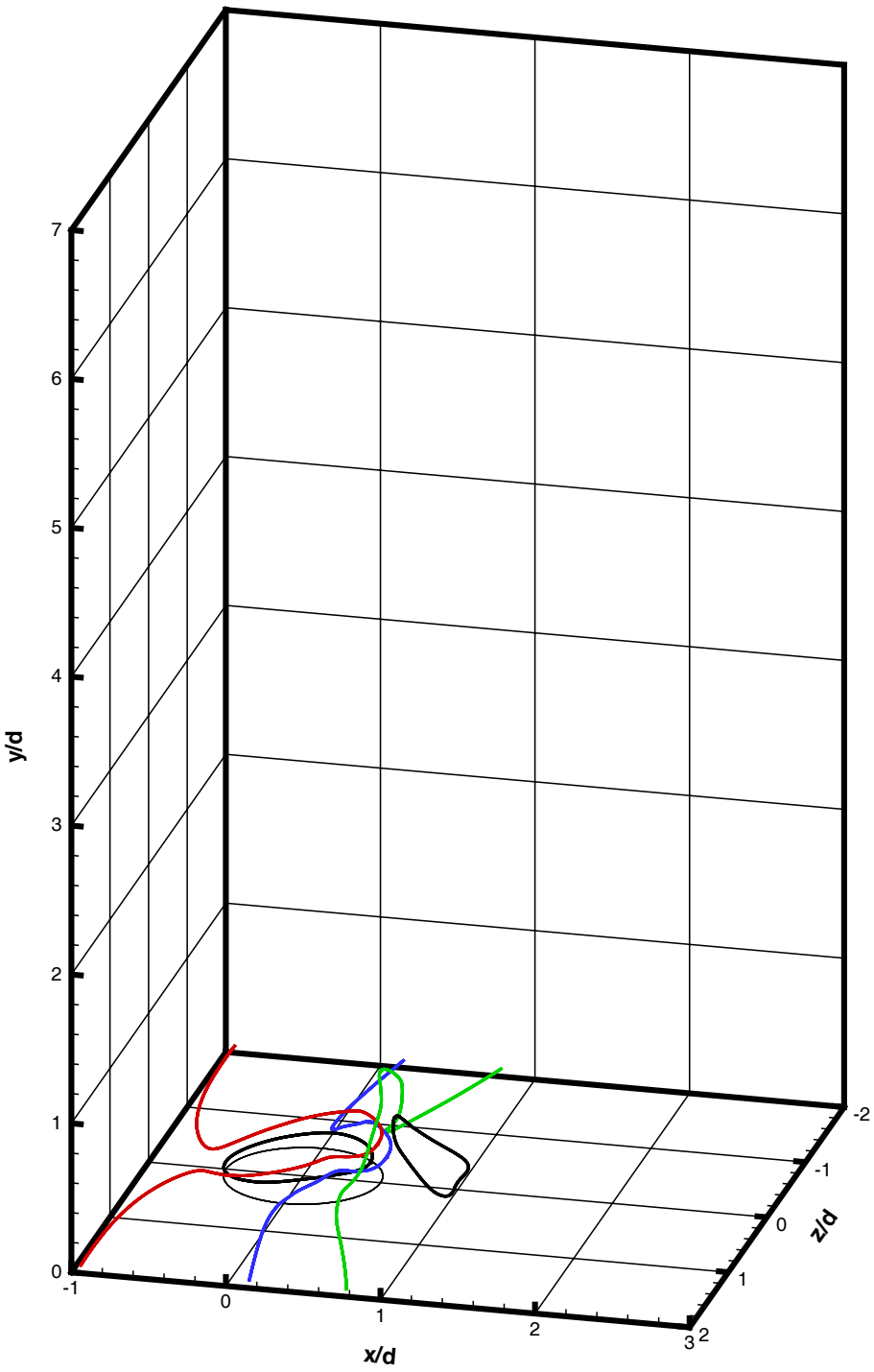

(b) side view

Figure 4-33: Continued from the previous page.

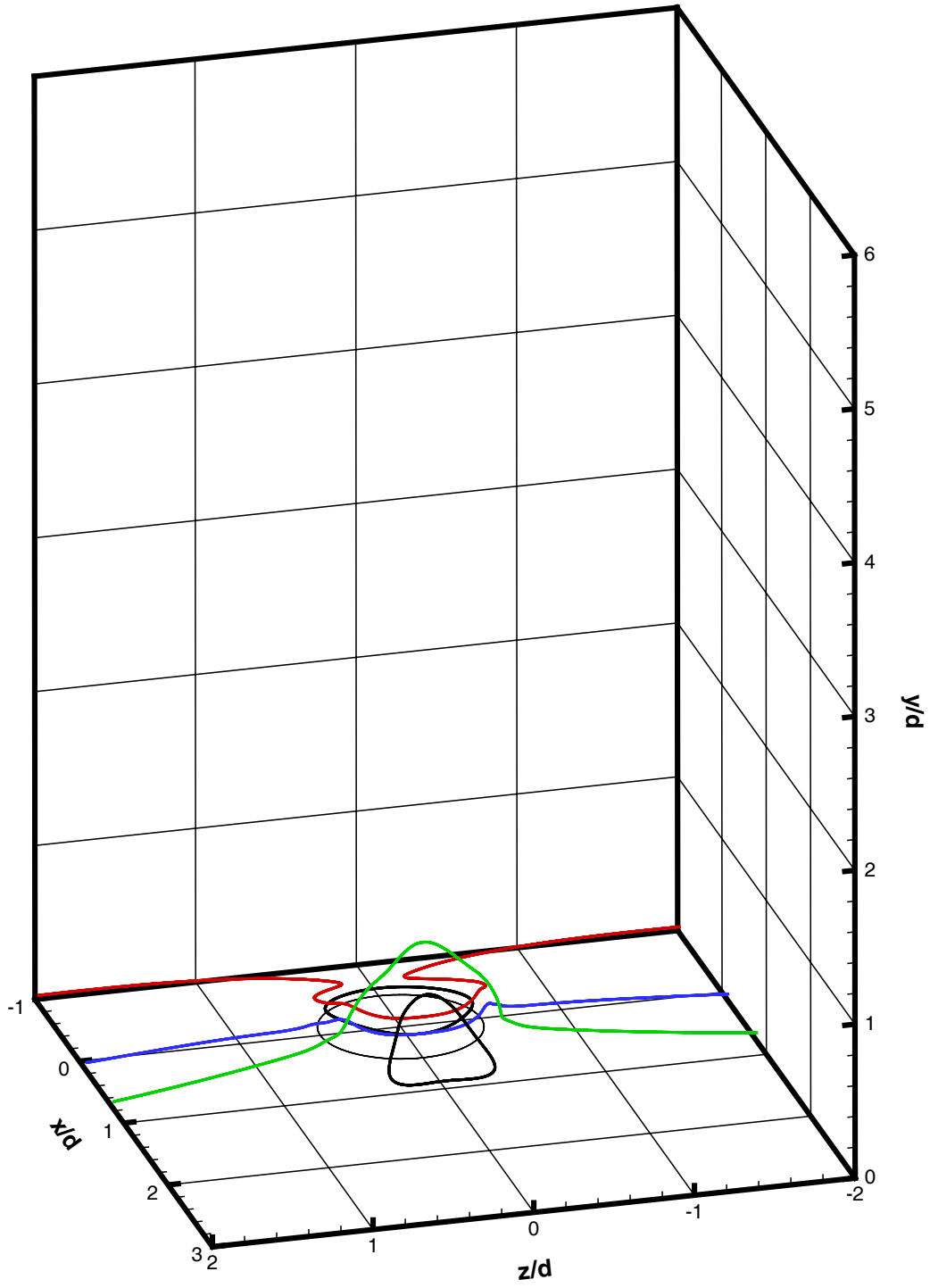

(c) front view

Figure 4-33: Continued from the previous page.

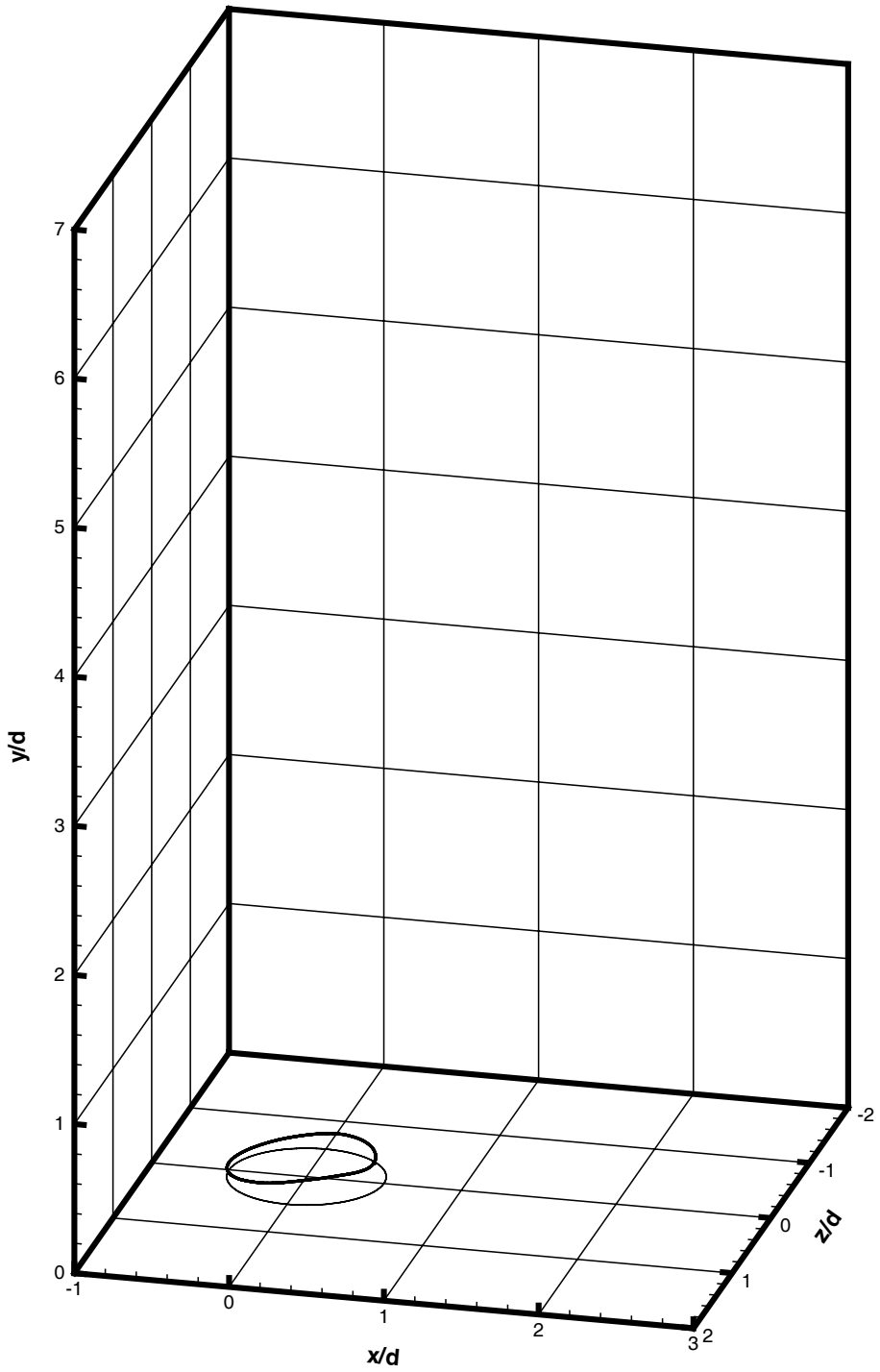

(a) $t = 4.00$

Figure 4-34: Side view of the evolution of a vorticity line introduced at the jet nozzle exit at $t = 4.0$ (Case III).

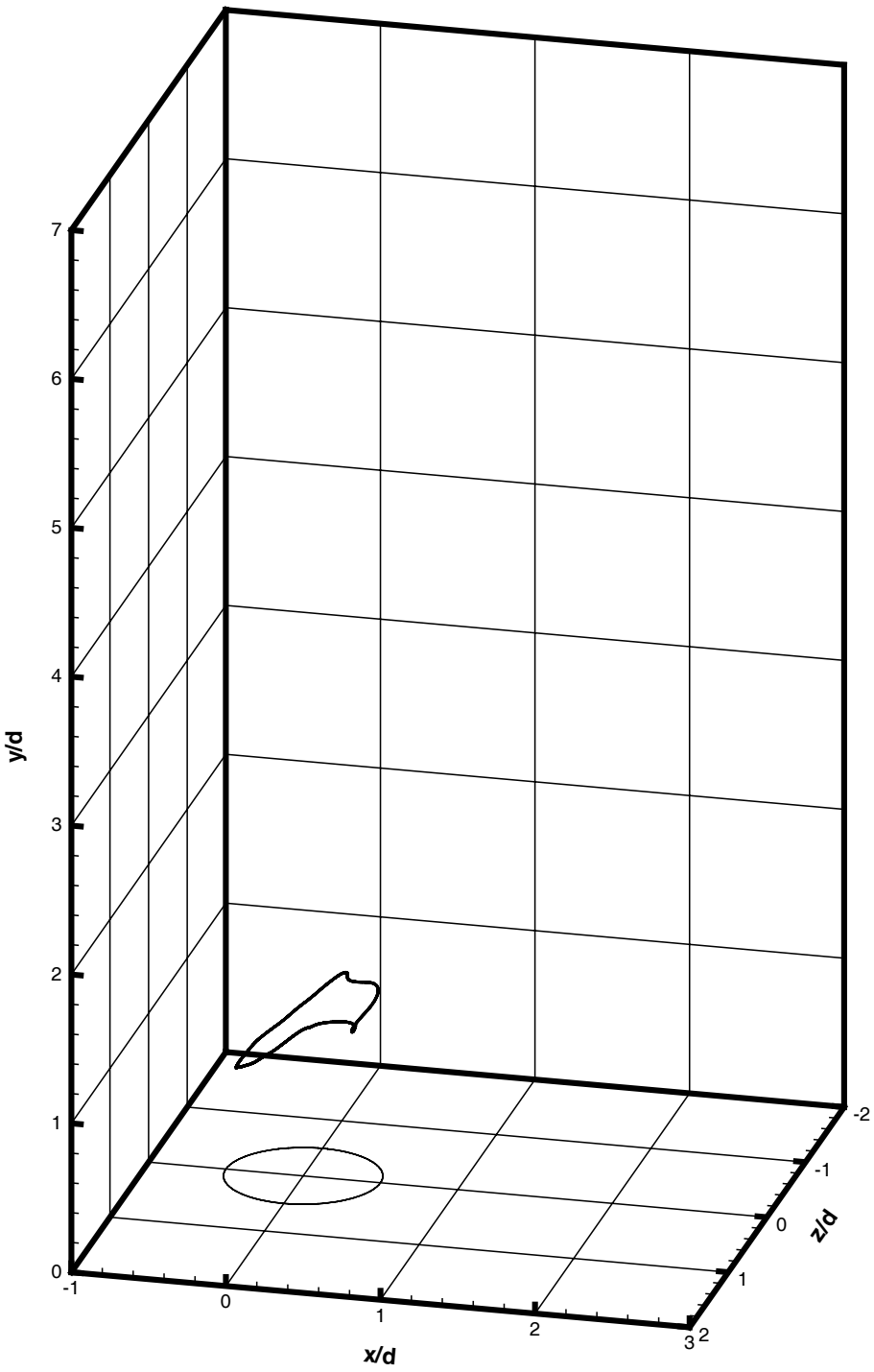

(b) $t = 4.36$

Figure 4-34: Continued from the previous page.

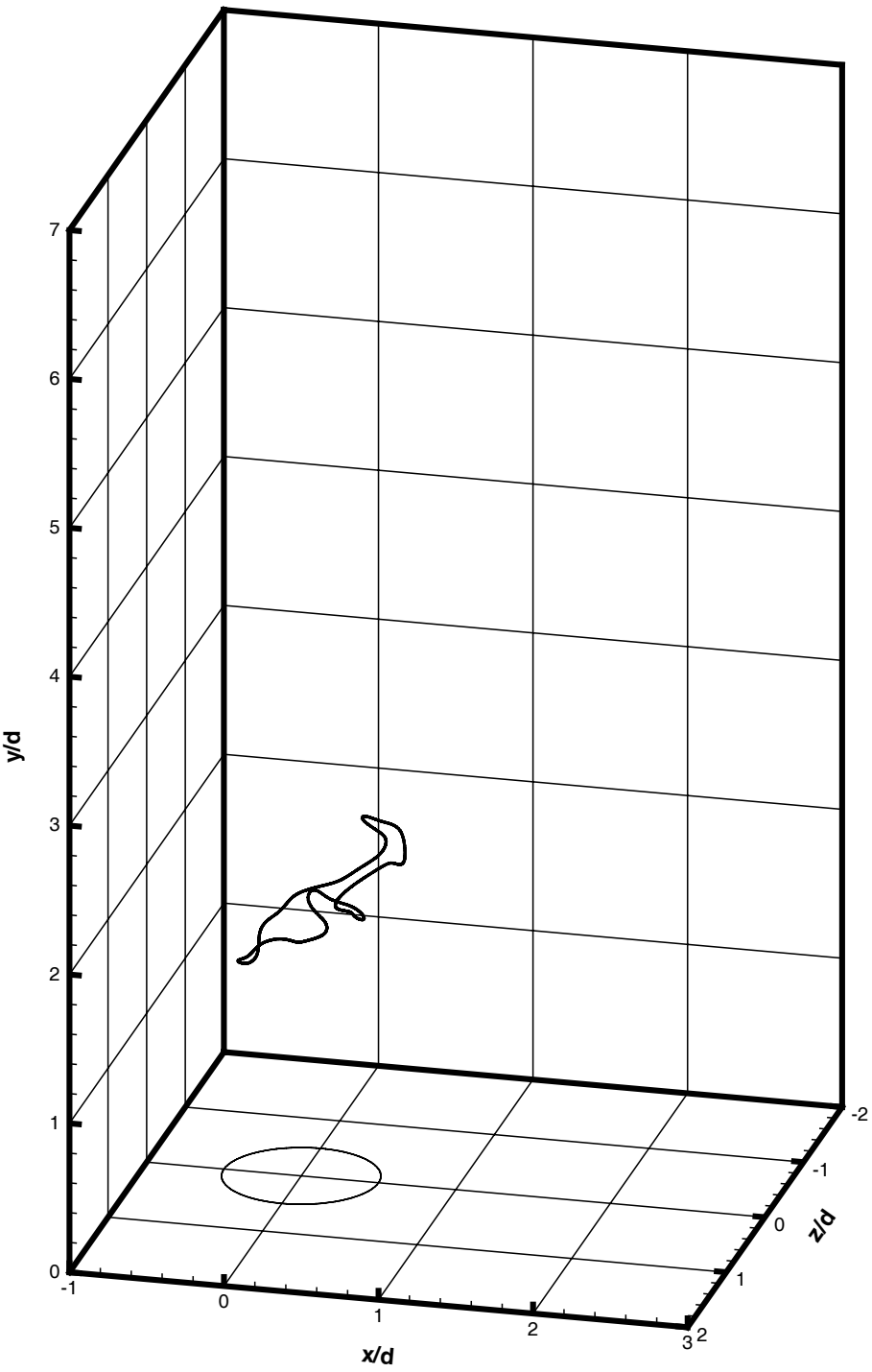

(c) $t = 4.68$

Figure 4-34: Continued from the previous page.

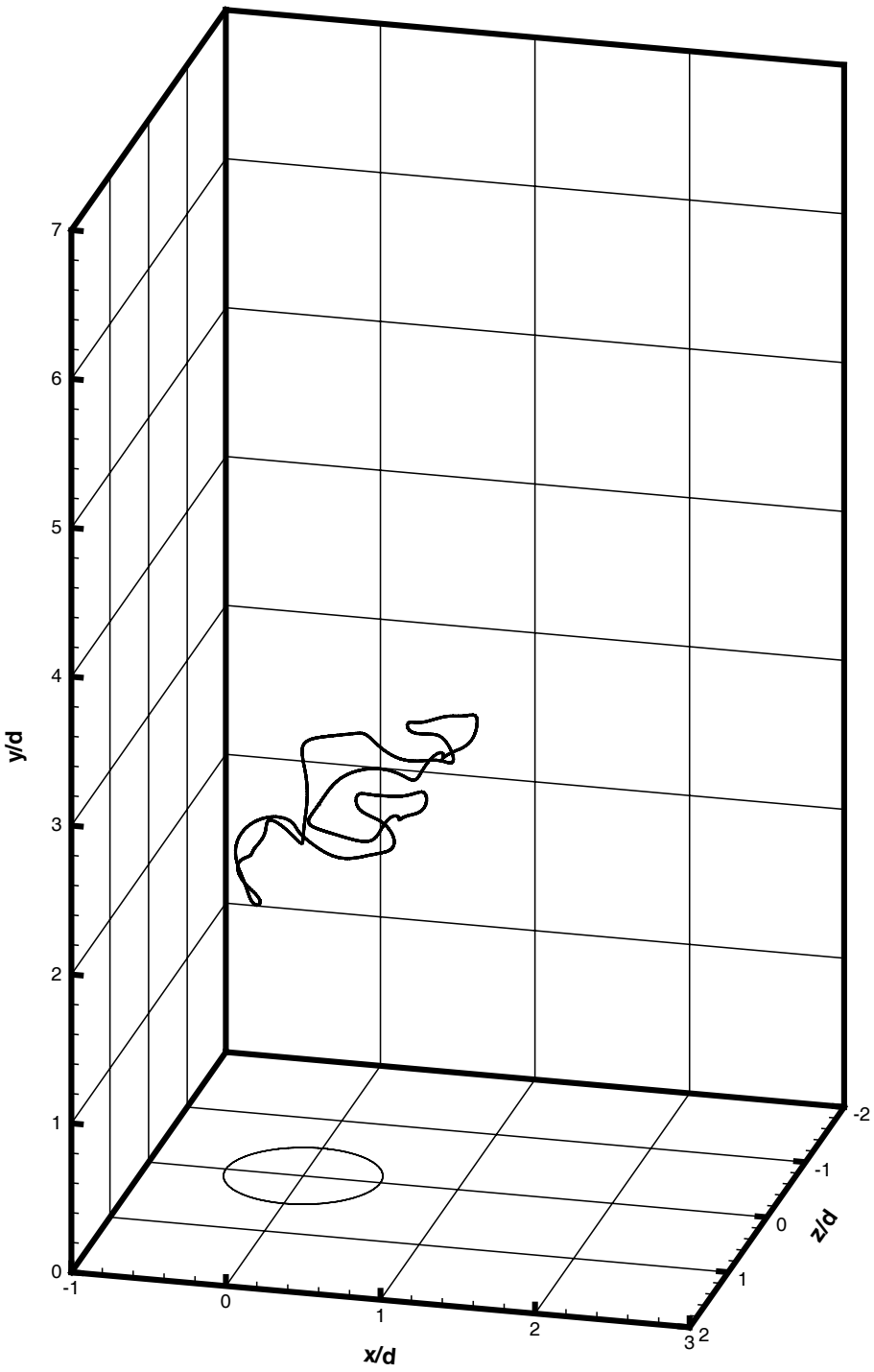

(d) $t = 5.00$

Figure 4-34: Continued from the previous page.

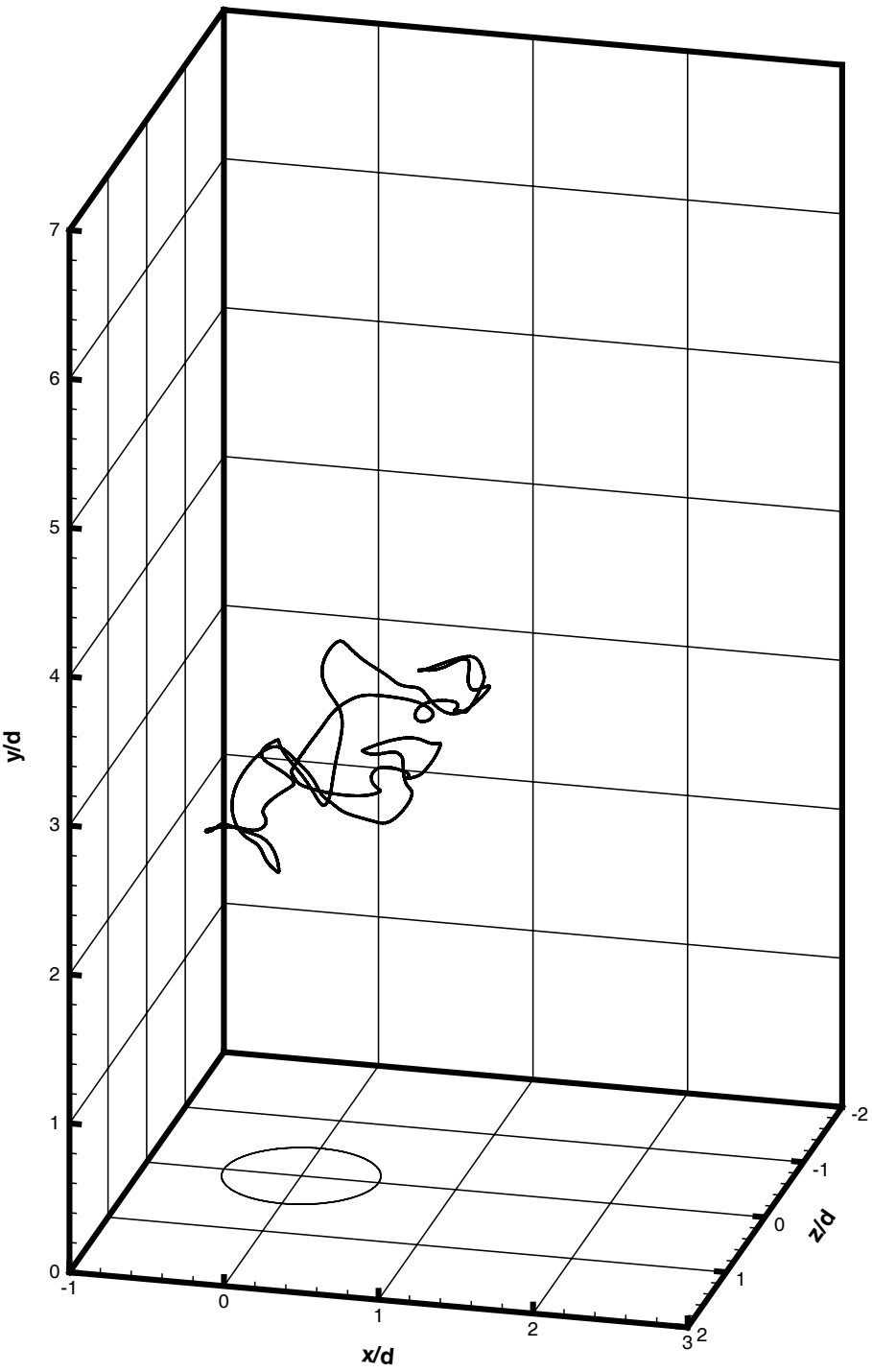

(e) $t = 5.20$

Figure 4-34: Continued from the previous page.

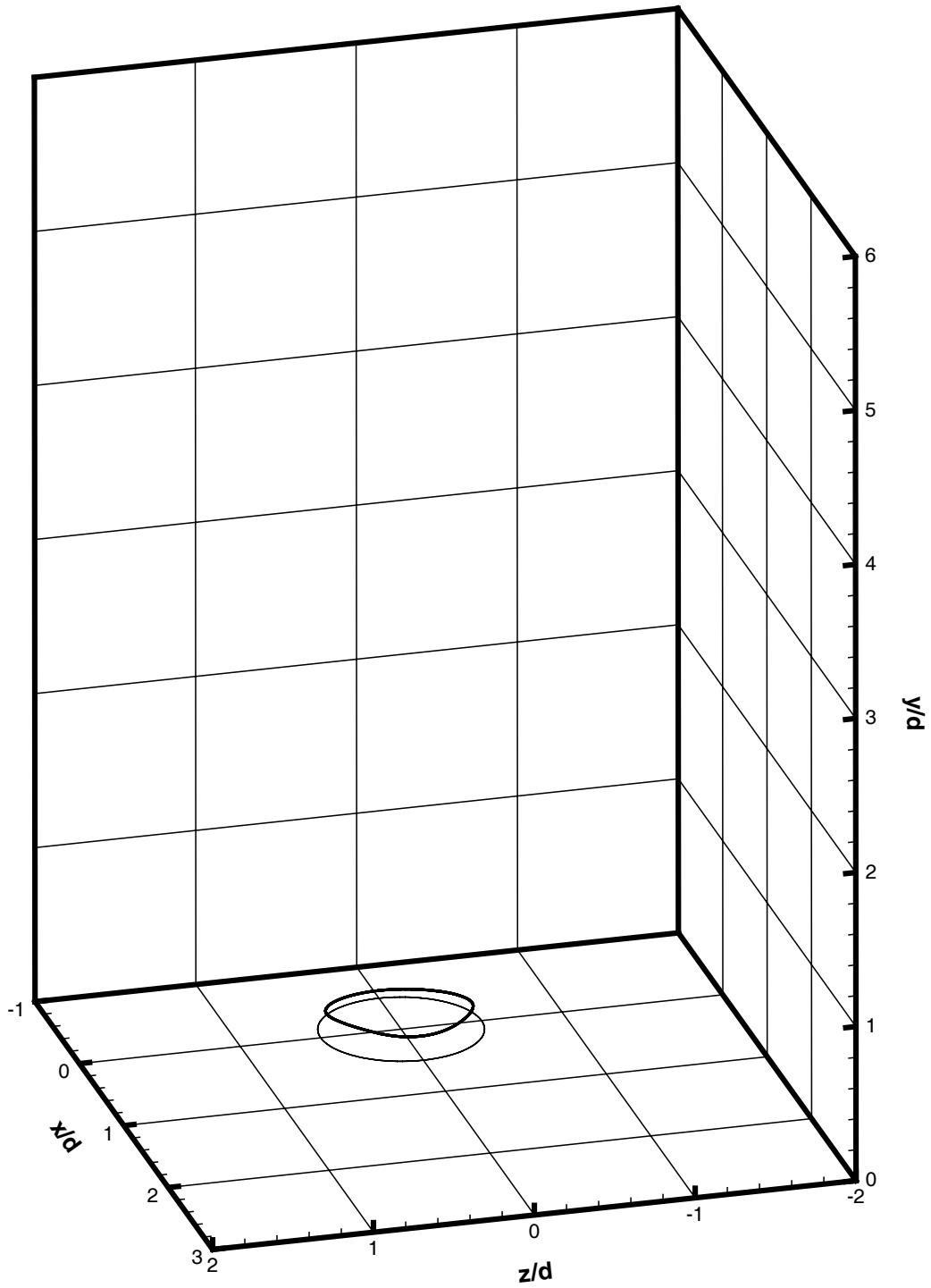

(a) $t = 4.00$

Figure 4-35: Front view of the evolution of a vorticity line introduced at the jet nozzle exit at $t = 4.0$ (Case III).

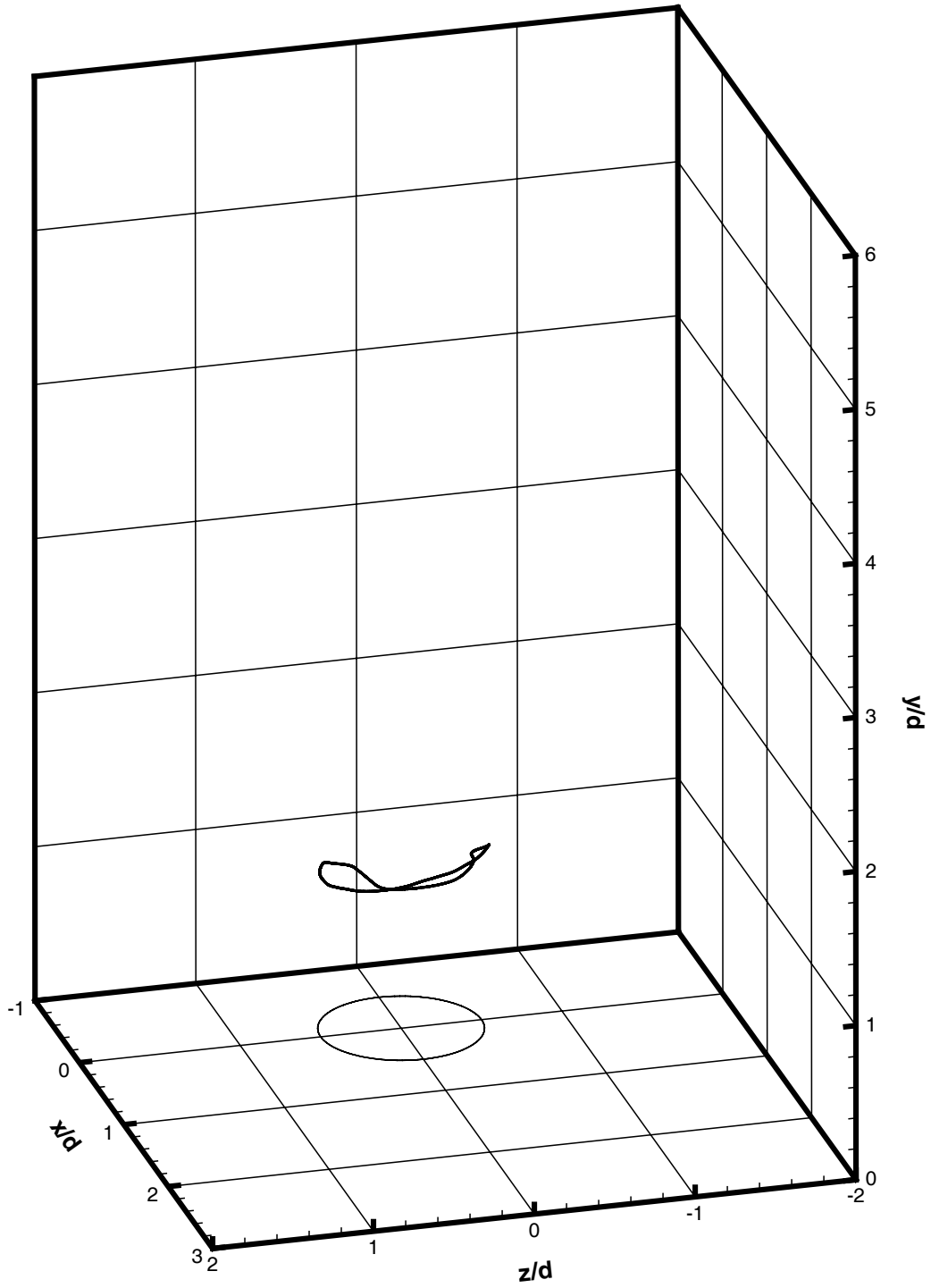

(b) $t = 4.36$

Figure 4-35: Continued from the previous page.

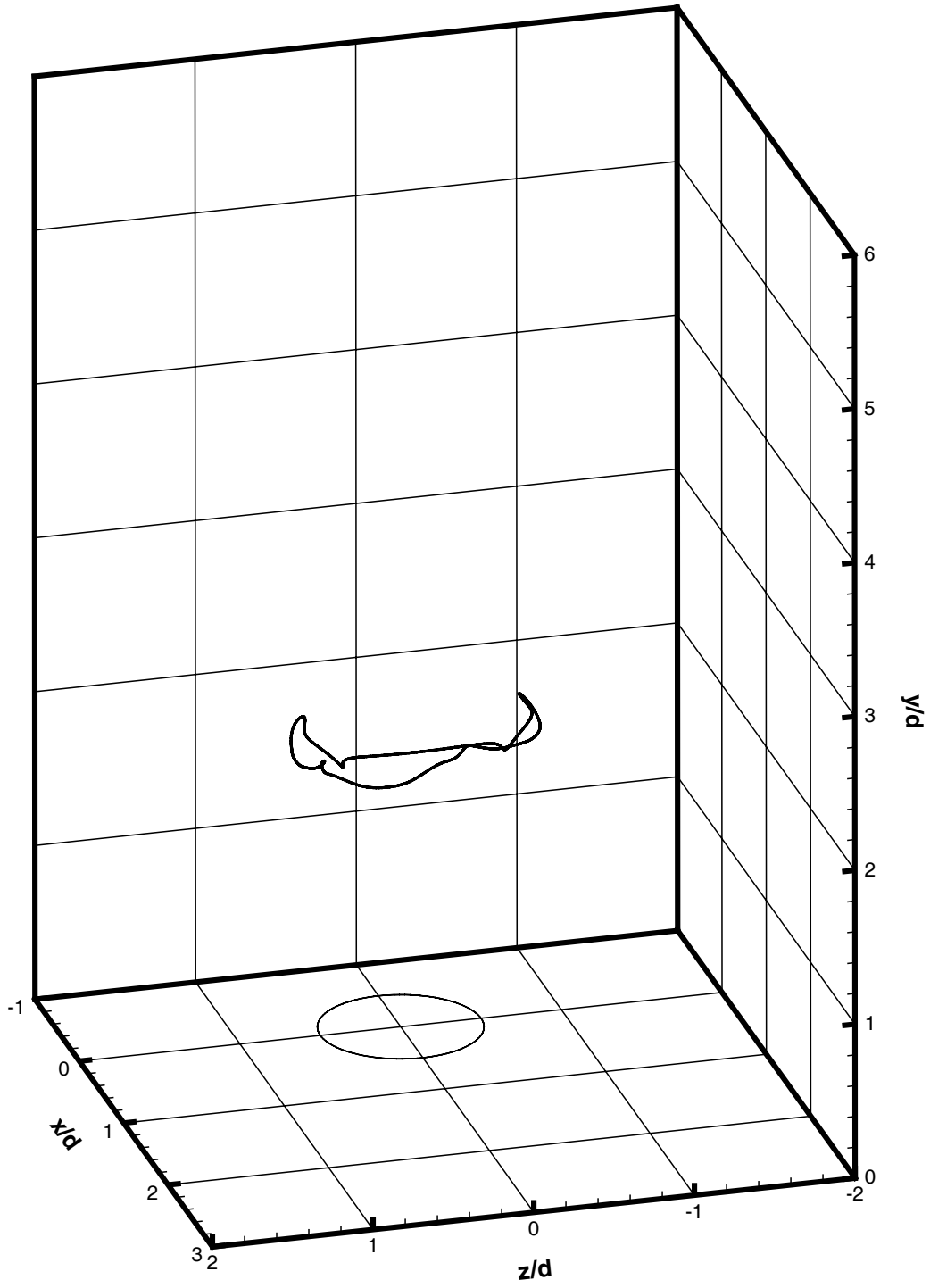

(c) $t = 4.68$

Figure 4-35: Continued from the previous page.

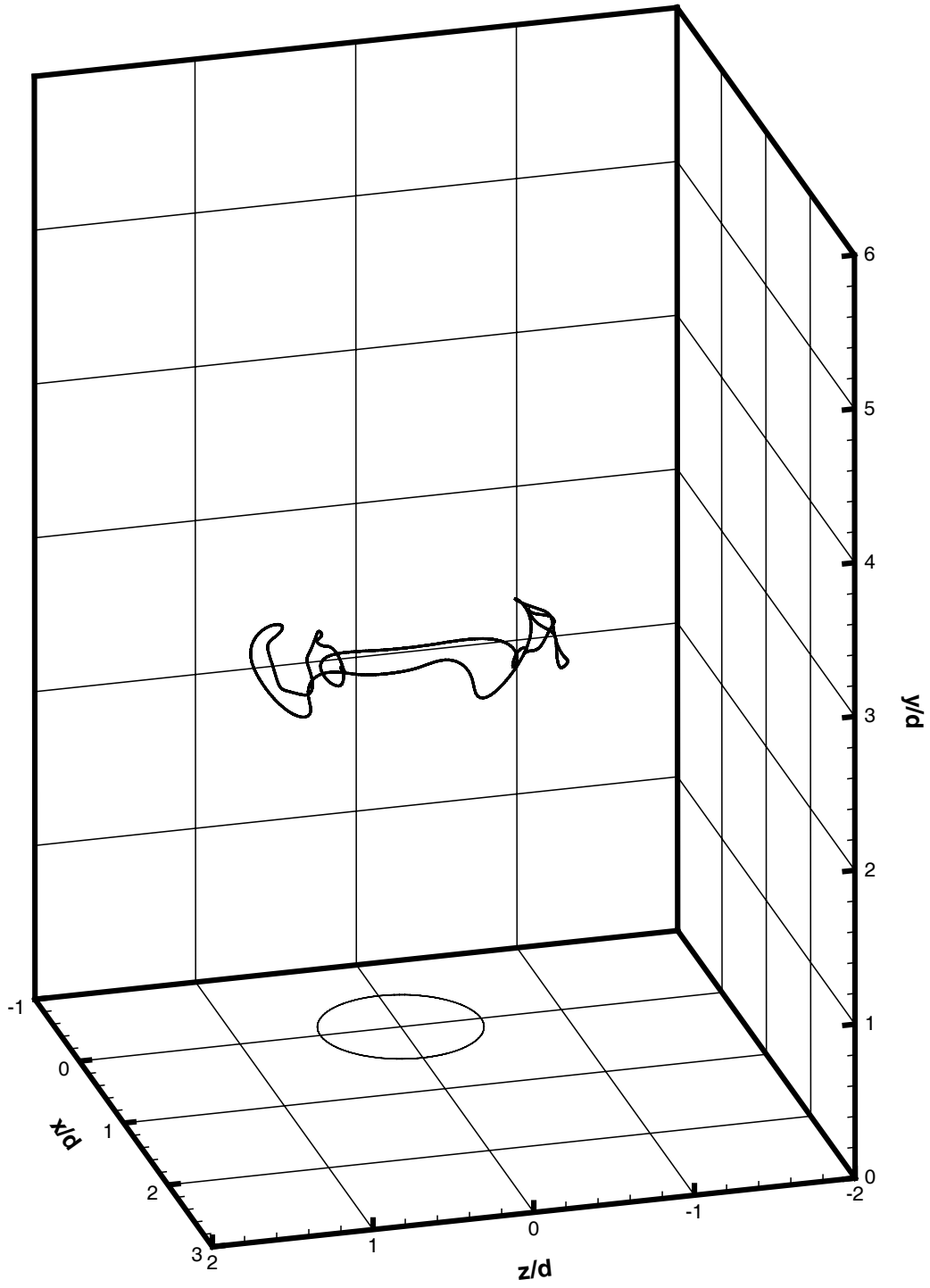

(d) $t = 5.00$

Figure 4-35: Continued from the previous page.

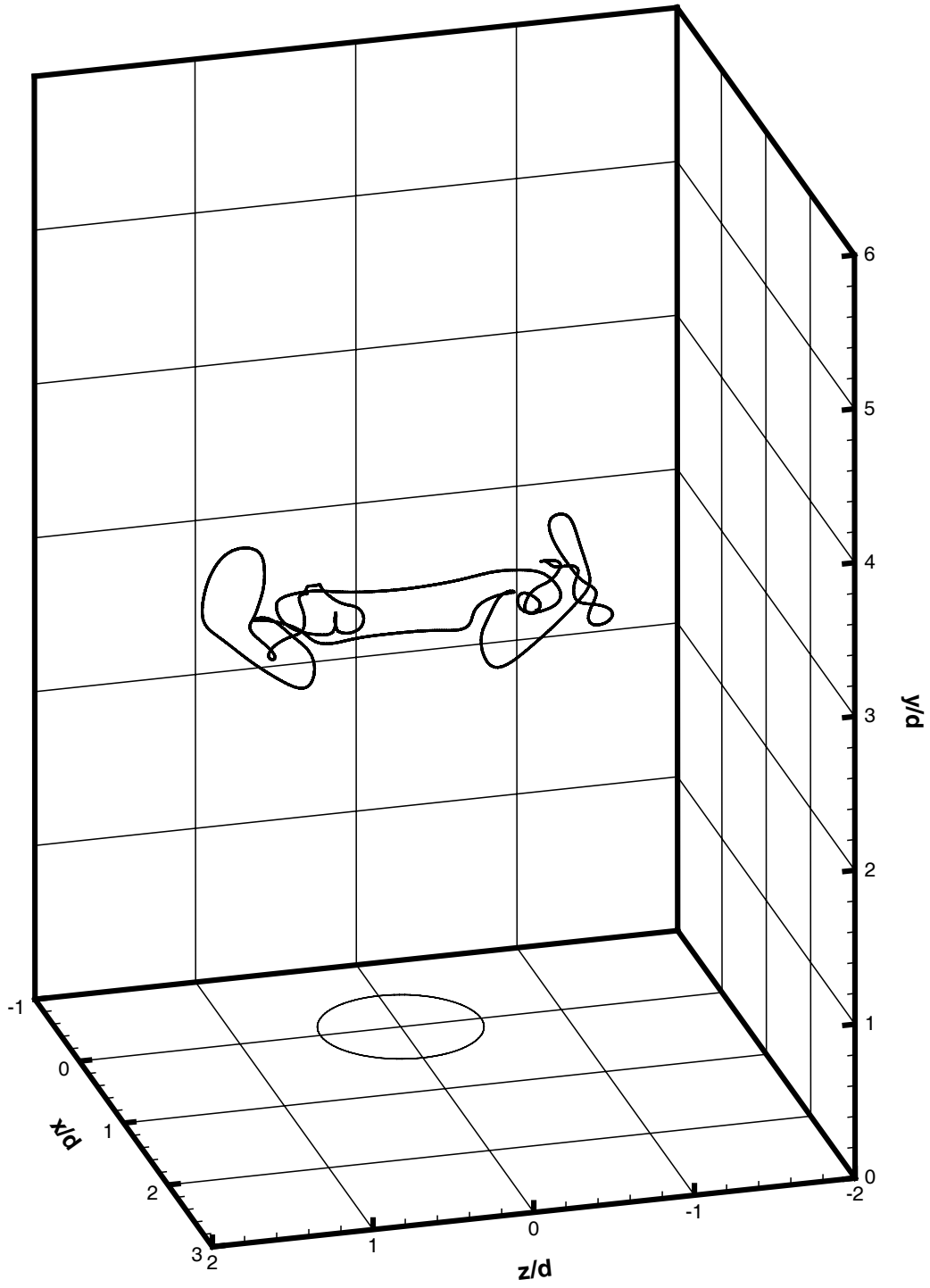

(e) $t = 5.20$

Figure 4-35: Continued from the previous page.

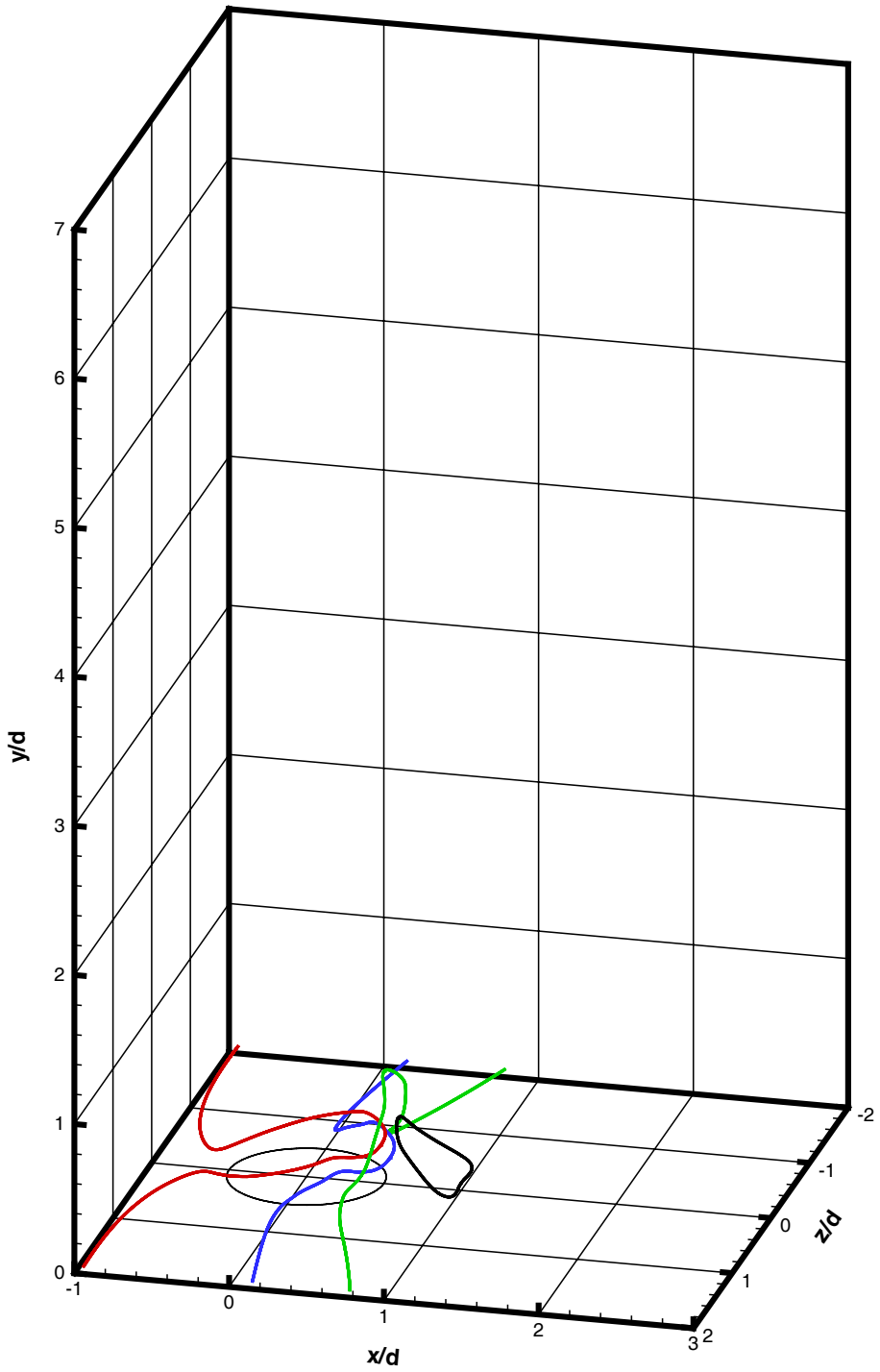

(a) $t = 4.00$

Figure 4-36: Side view of the evolution of vorticity lines introduced at the jet nozzle exit at $t = 4.0$ (Case III).

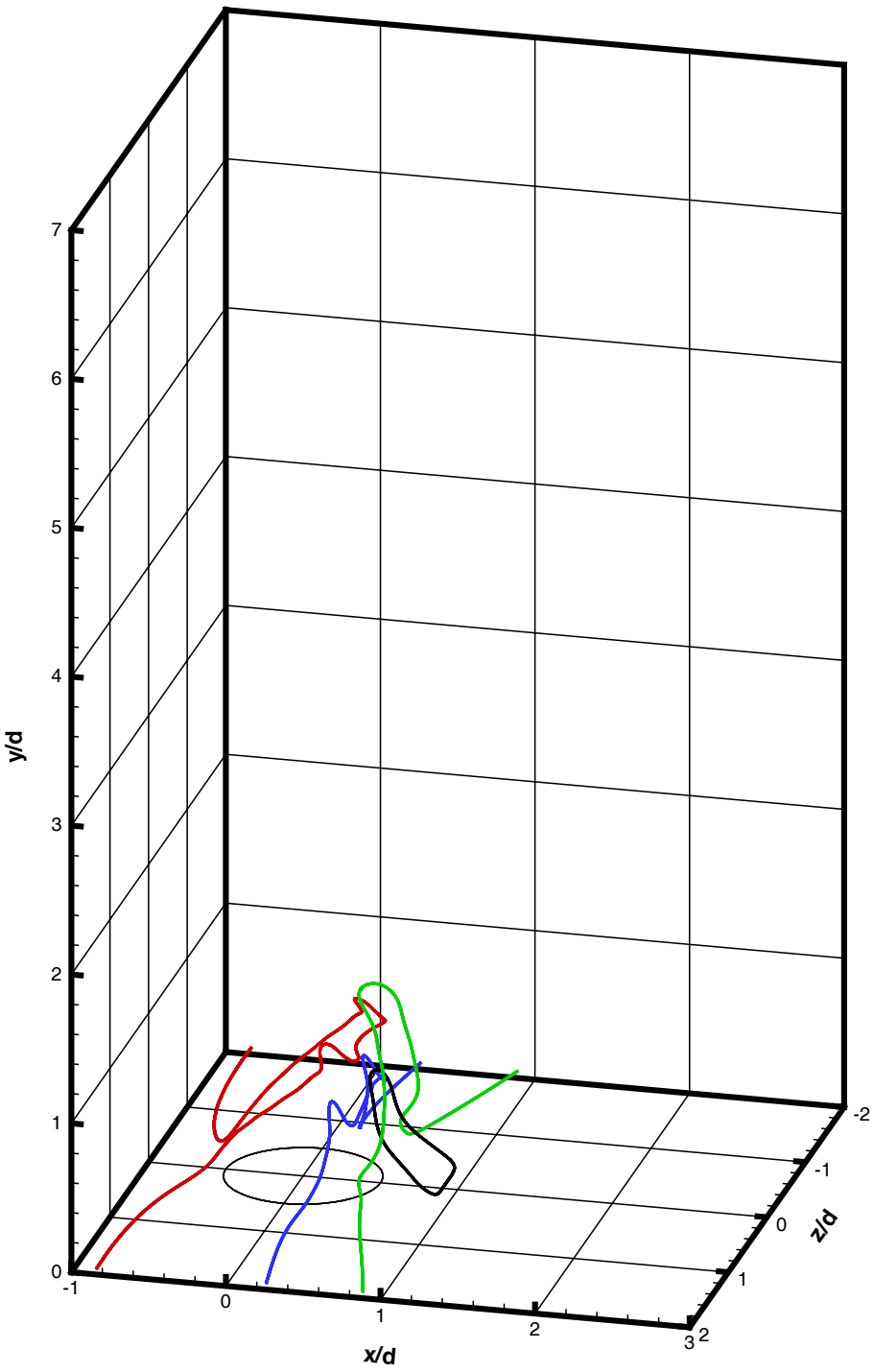

(b) $t = 4.36$

Figure 4-36: Continued from the previous page.

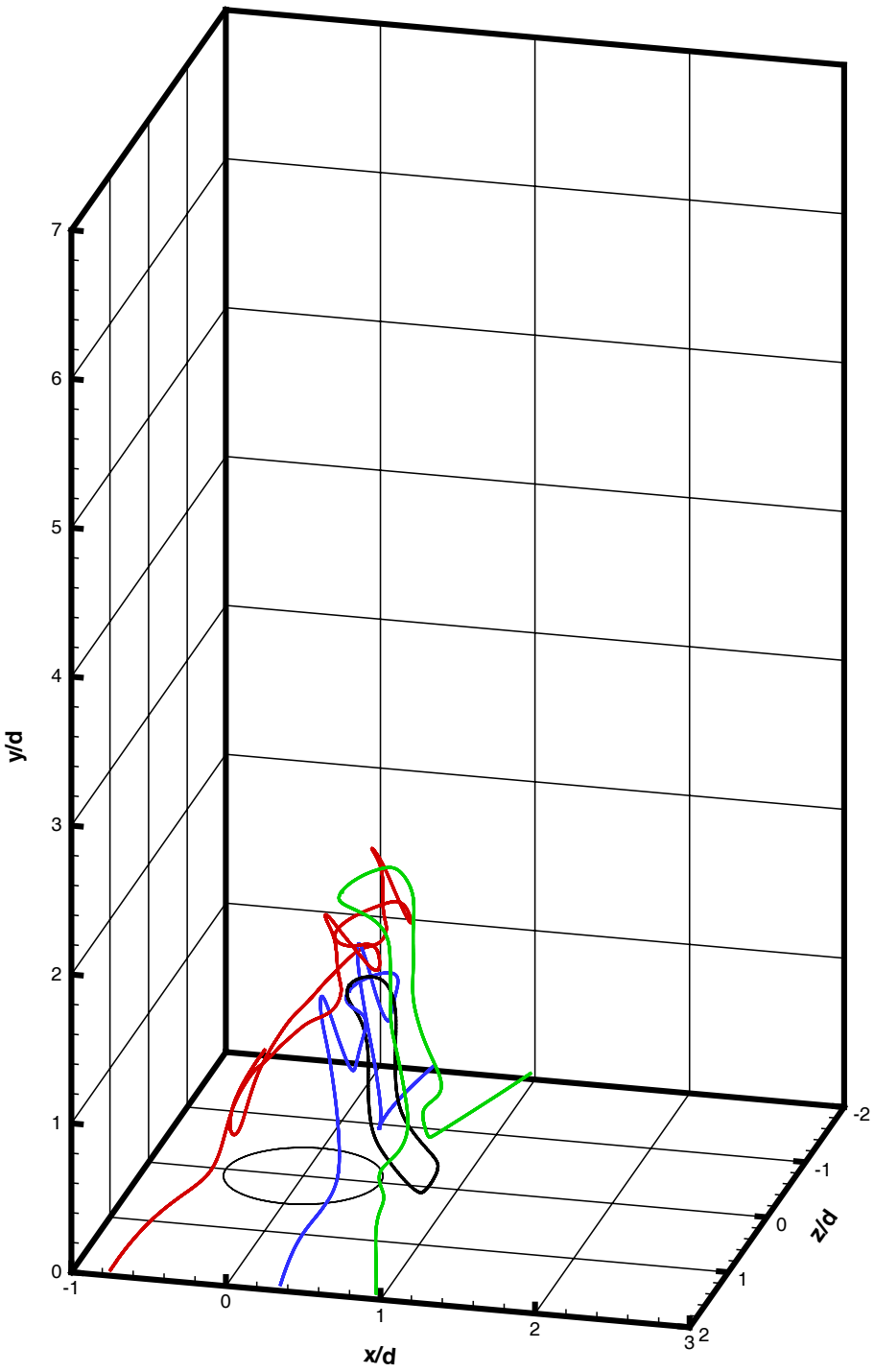

(c) $t = 4.68$

Figure 4-36: Continued from the previous page.

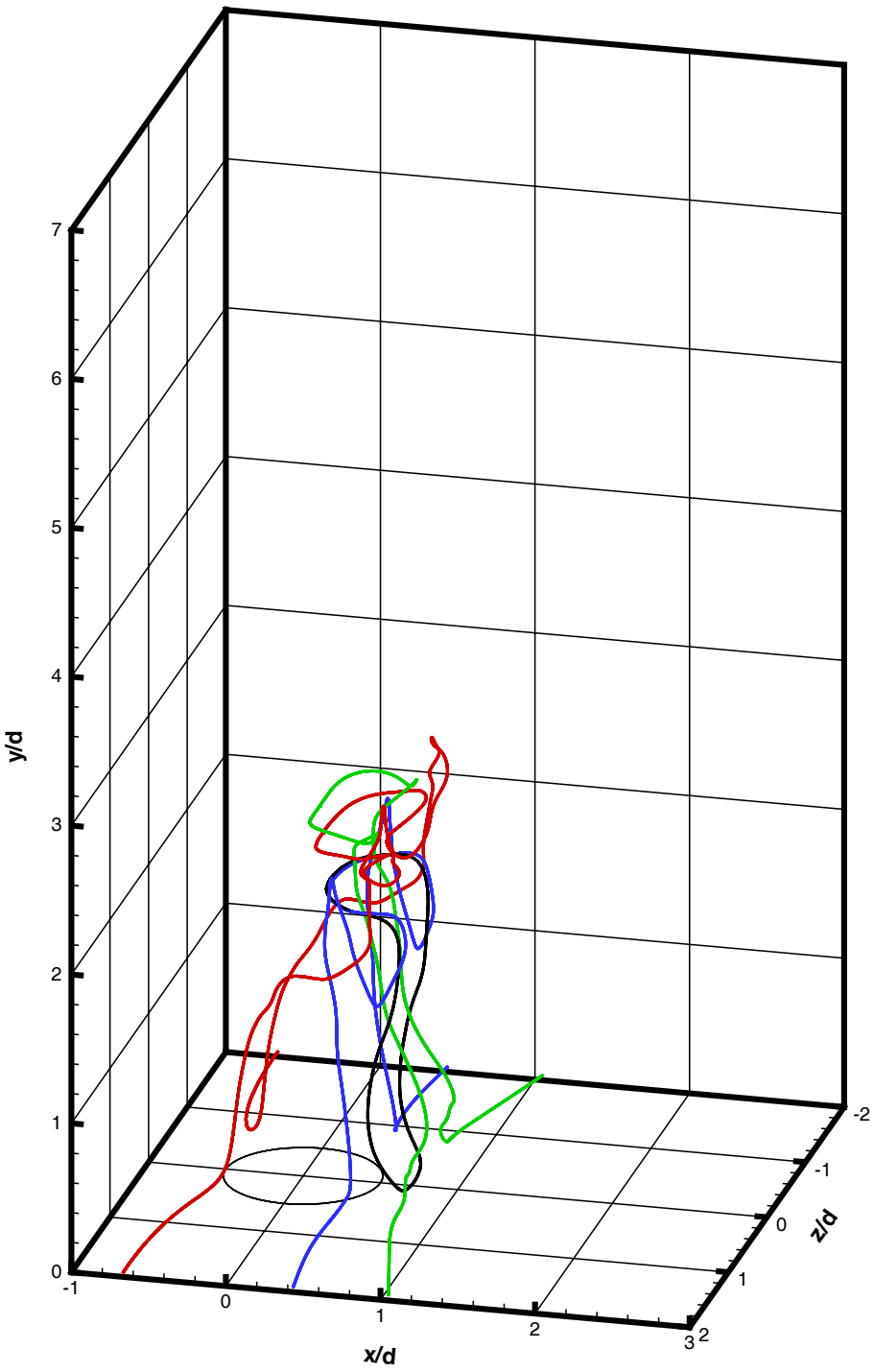

(d) $t = 5.00$

Figure 4-36: Continued from the previous page.

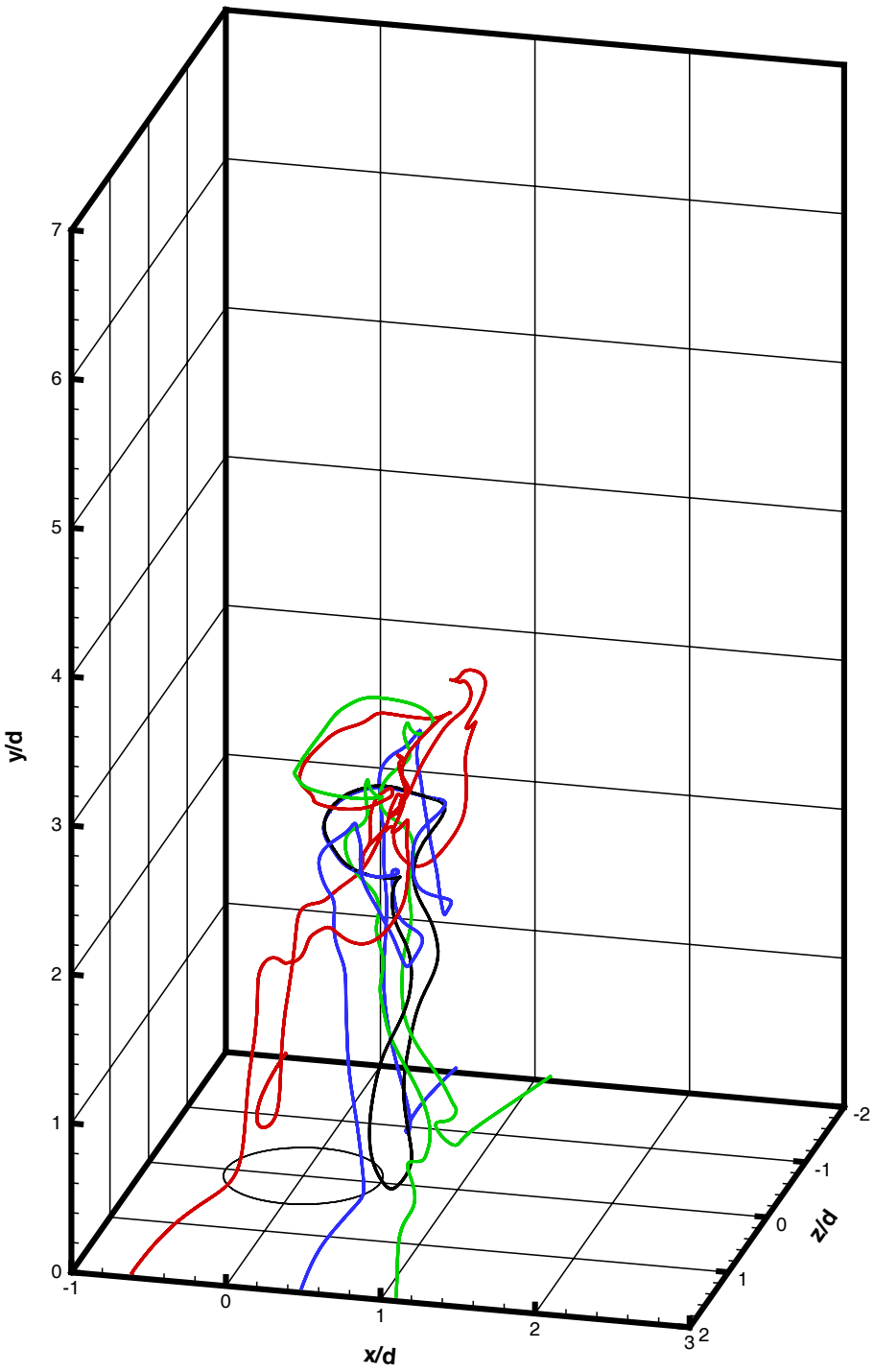

(e) $t = 5.20$

Figure 4-36: Continued from the previous page.

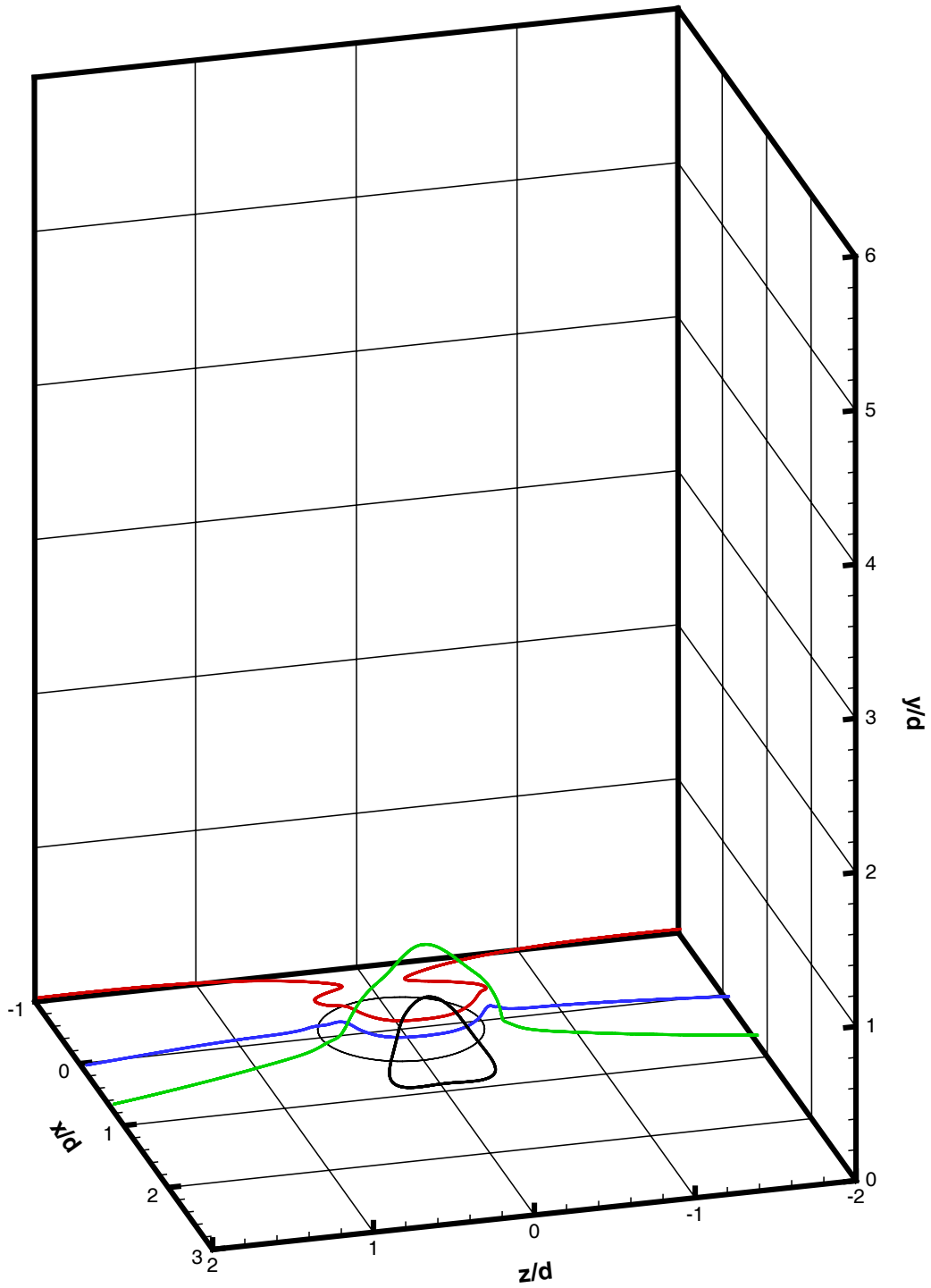

(a) $t = 4.00$

Figure 4-37: Front view of the evolution of vorticity lines introduced at the jet nozzle exit at $t = 4.0$ (Case III).

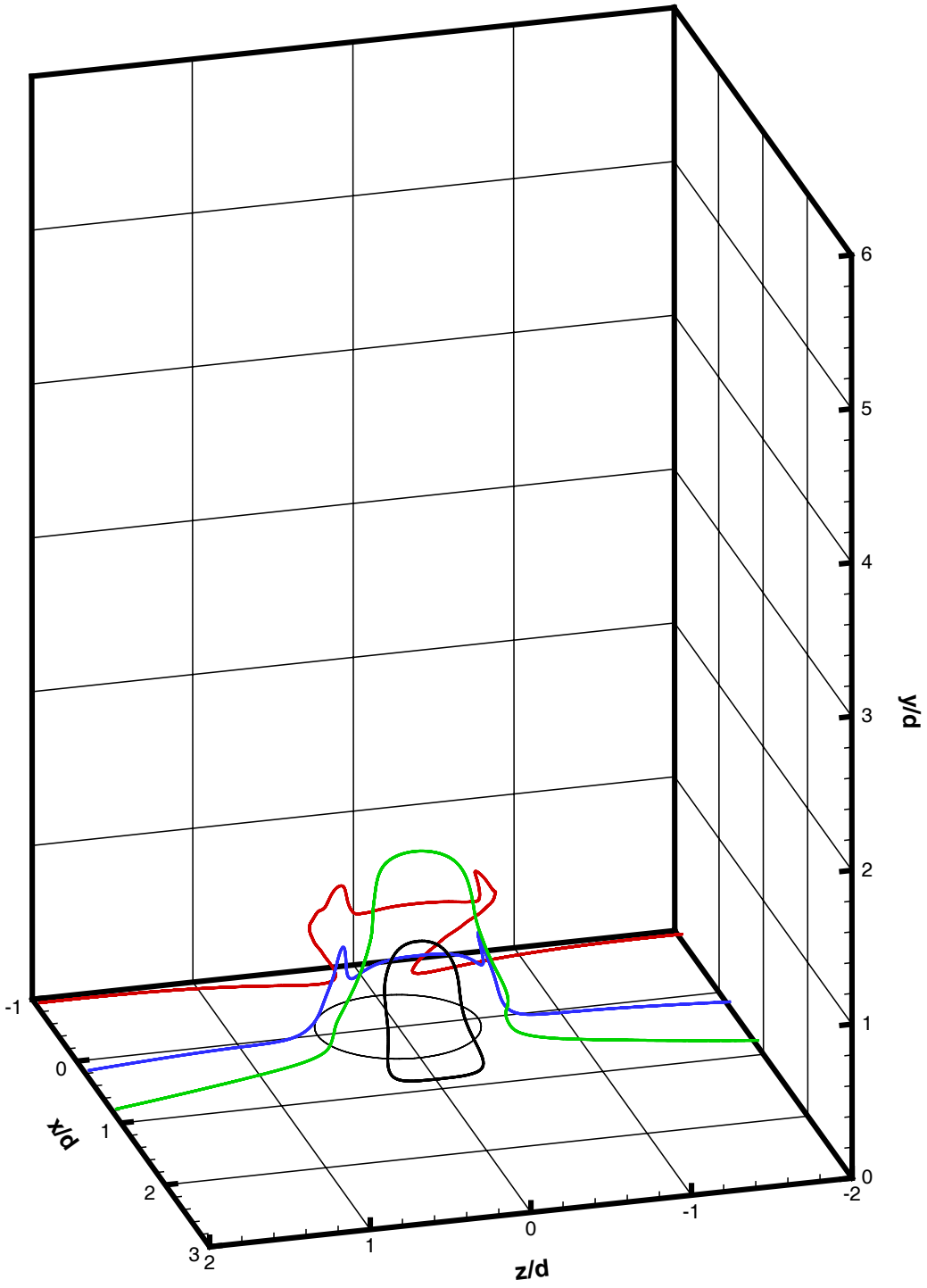

(b) $t = 4.36$

Figure 4-37: Continued from the previous page.

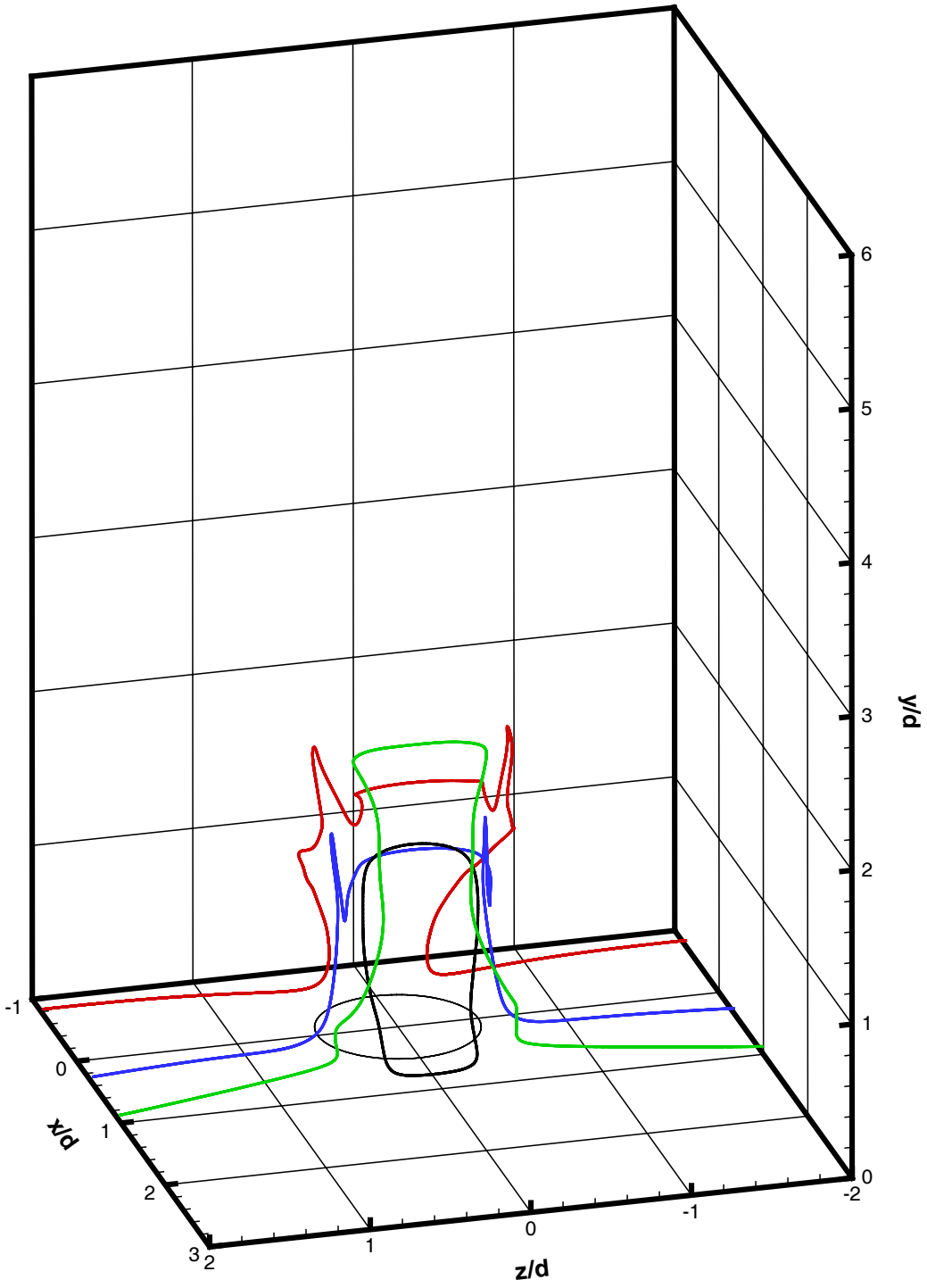

(c) $t = 4.68$

Figure 4-37: Continued from the previous page.

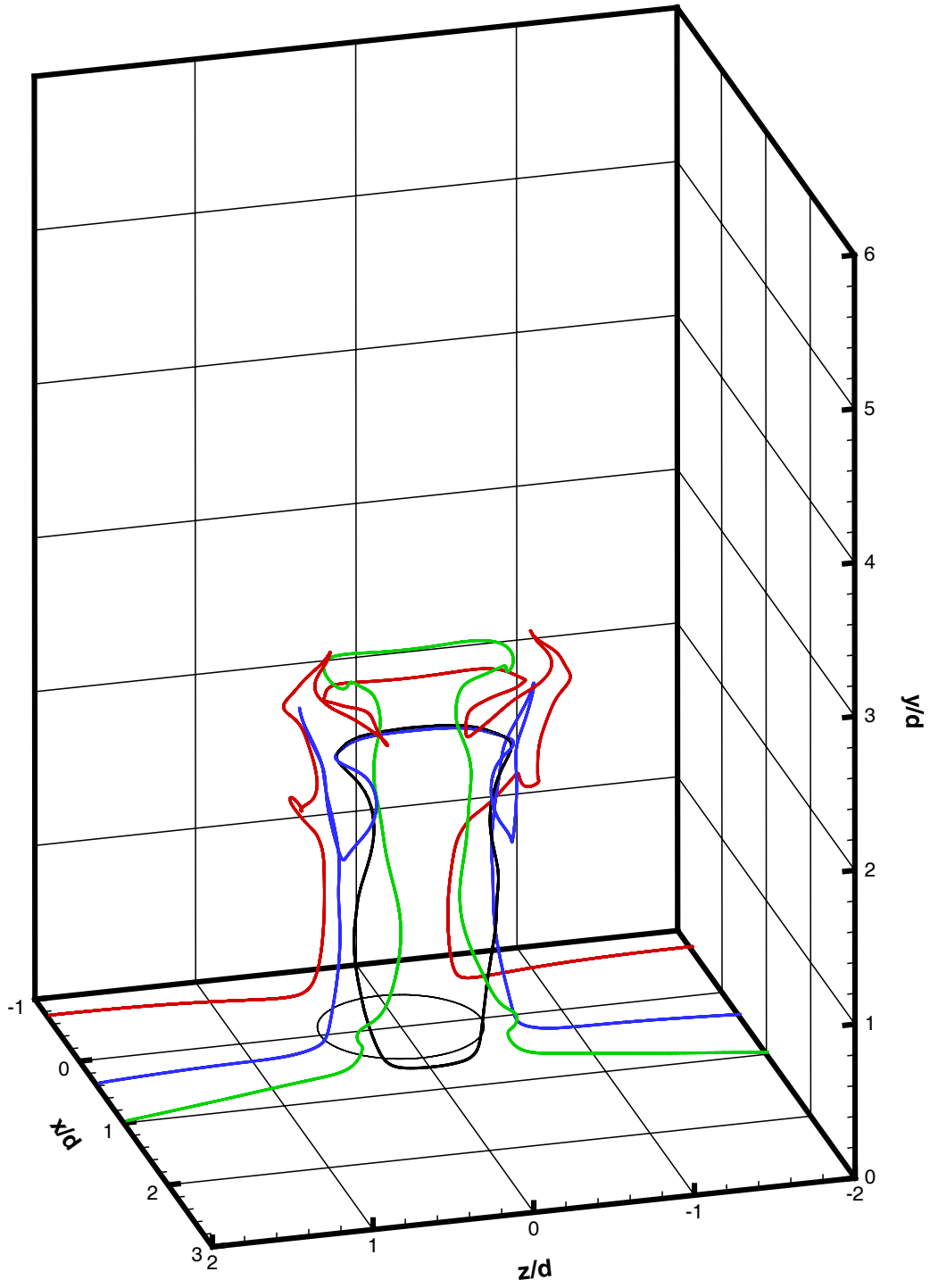

(d) $t = 5.00$

Figure 4-37: Continued from the previous page.

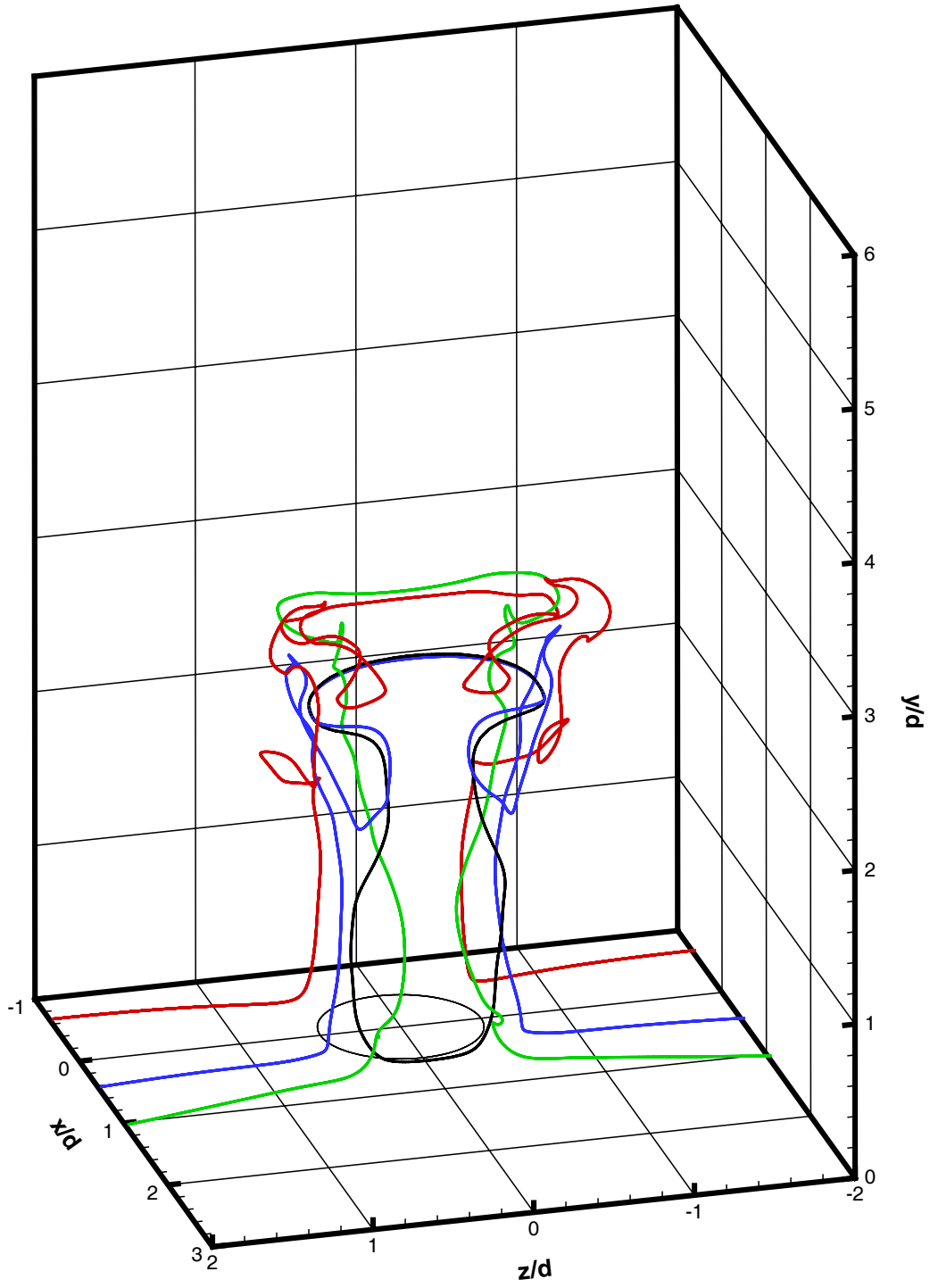

(e) $t = 5.20$

Figure 4-37: Continued from the previous page.

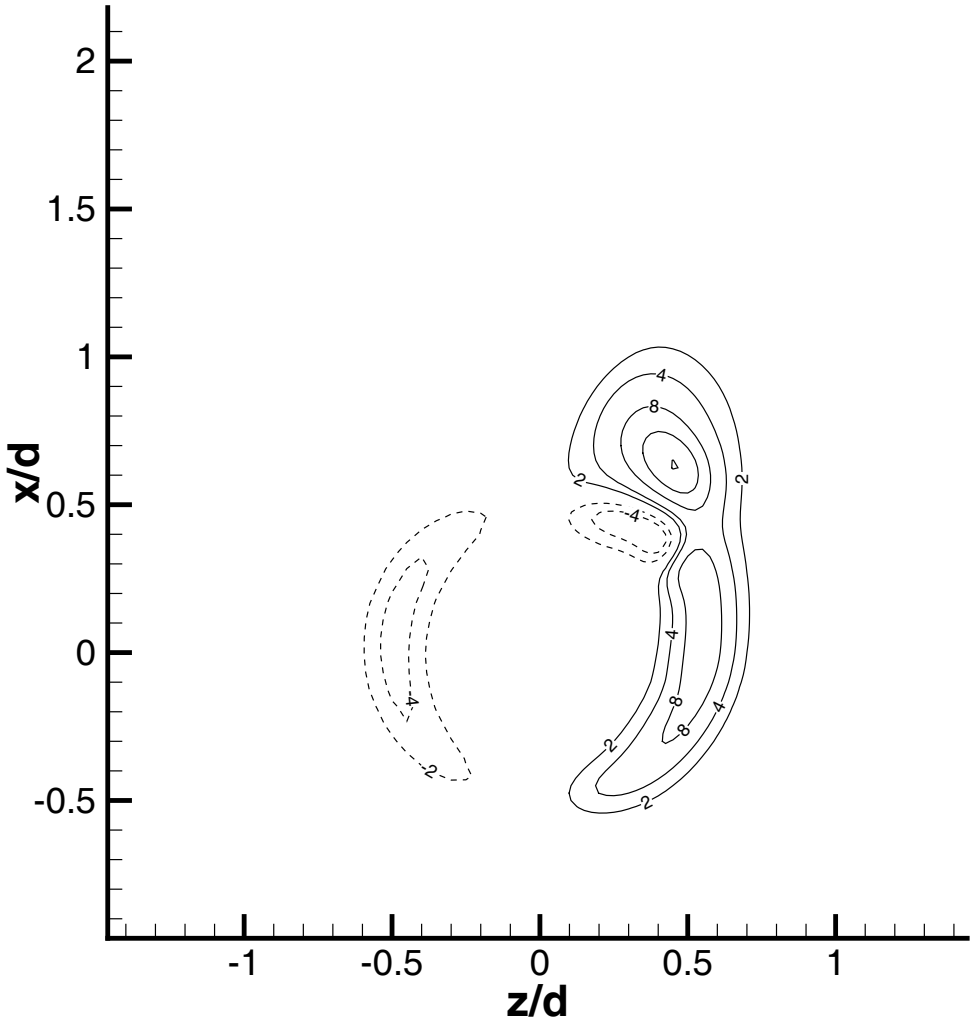

(a) $y/d = 0.2$

Figure 4-38: Contours of ω_y on planes of constant y. Contours at $z > 0$ corresponds to the instantaneous vorticity field of Case III at $t = 4.0$. Contours at $z < 0$ corresponds to the instantaneous vorticity field of Case I at $t = 12.0$. Dashed lines represent negative values.

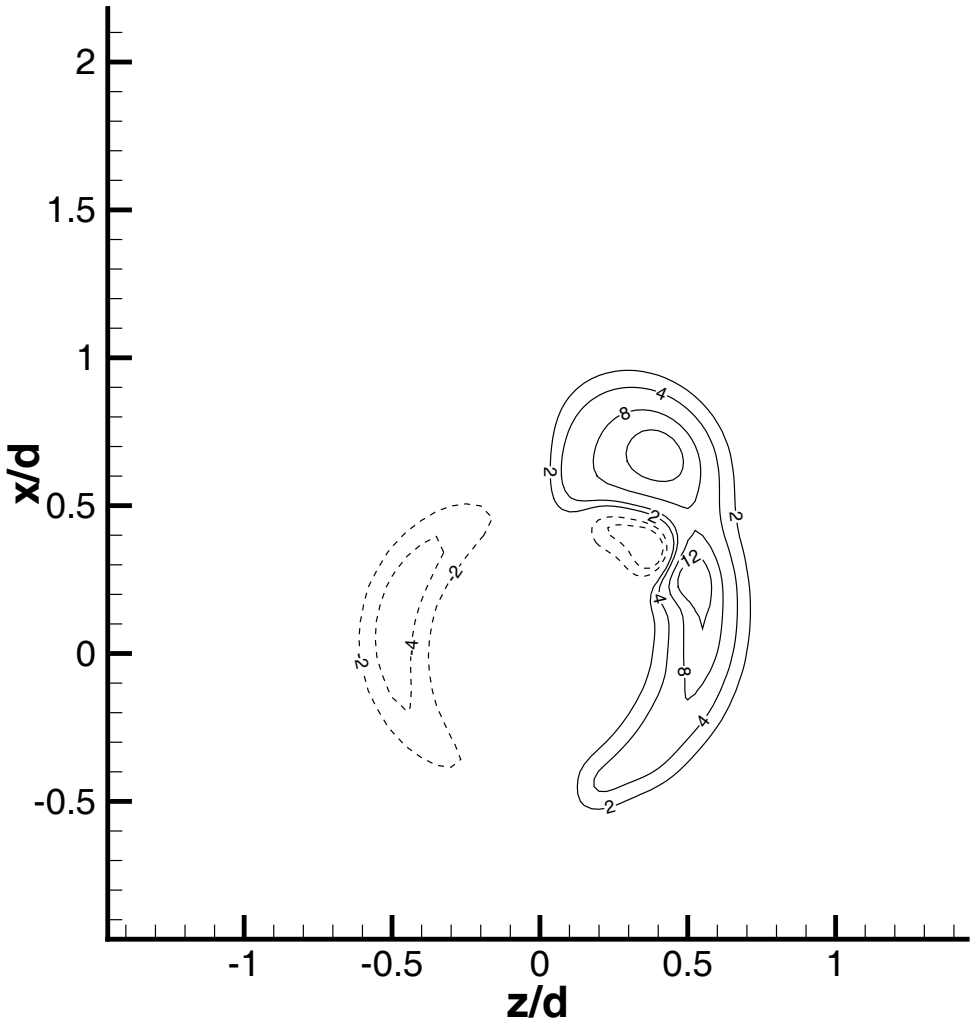

(b) $y/d = 0.4$

Figure 4-38: Continued from the previous page.

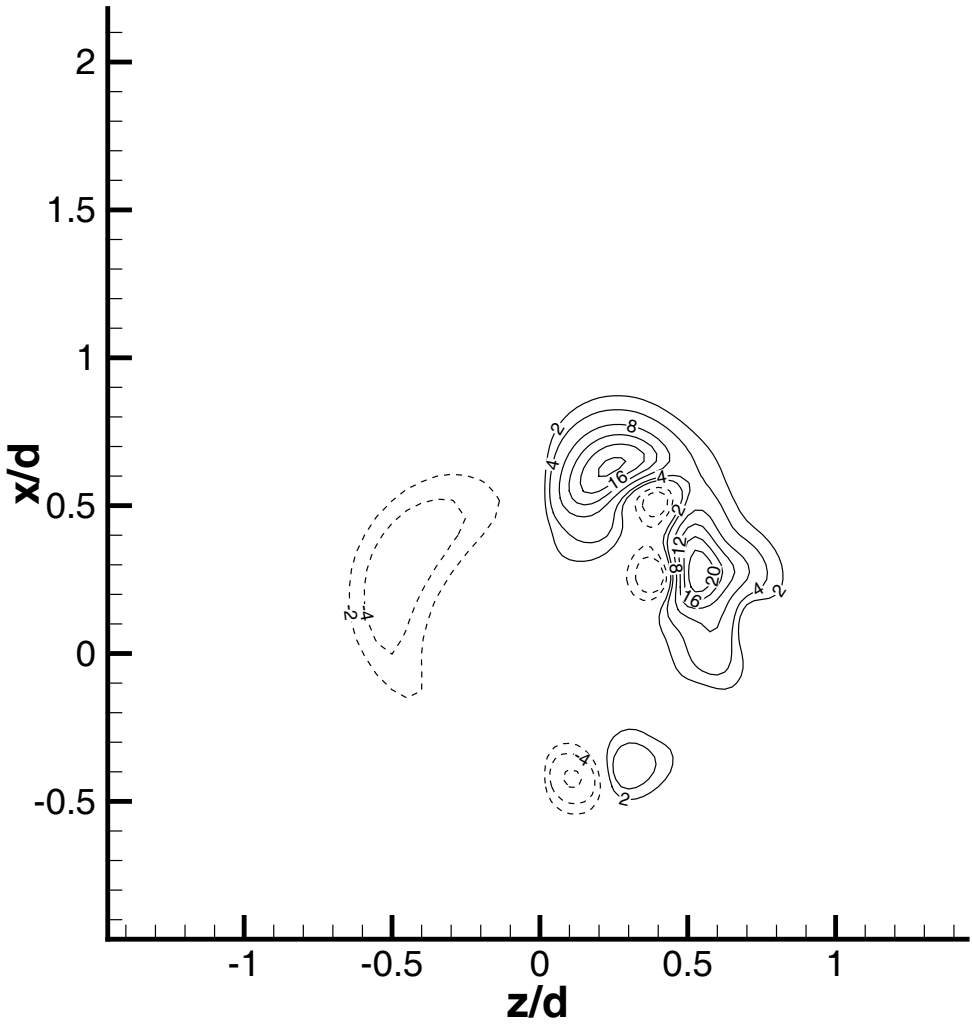

(c) $y/d = 1.0$

Figure 4-38: Continued from the previous page.

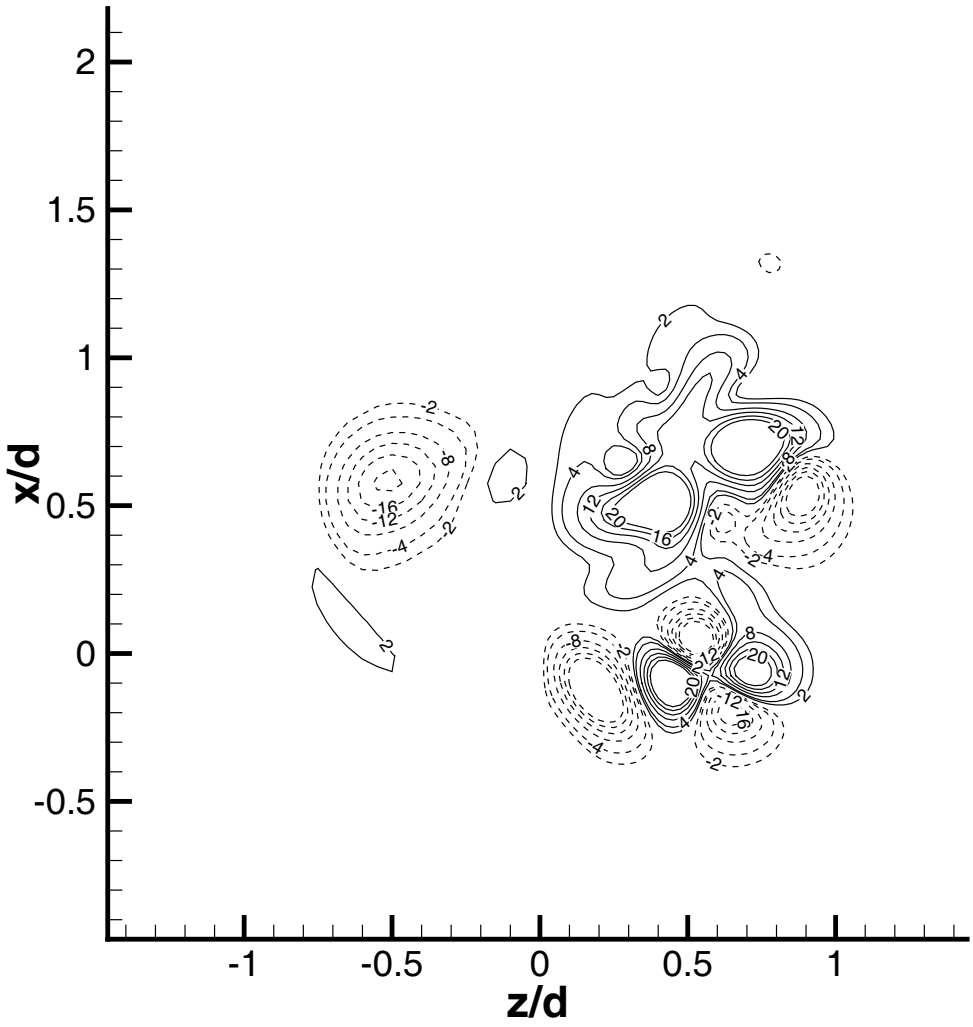

(d) $y/d = 2.0$

Figure 4-38: Continued from the previous page.

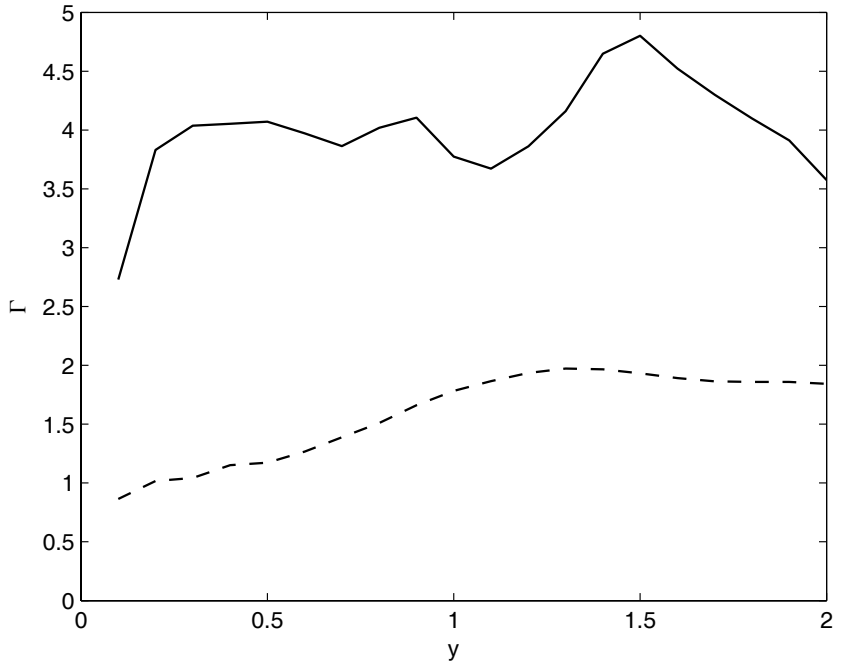

Figure 4-39: Evolution of the wall normal circulation $\Gamma(y) = \int\int_{z>0} \omega_y dz dx$. The solid line represents the results obtained from the flow field of Case III at $t = 4.0$, and the dashed line represents the results obtained from the flow field of Case I at $t = 12.0$.

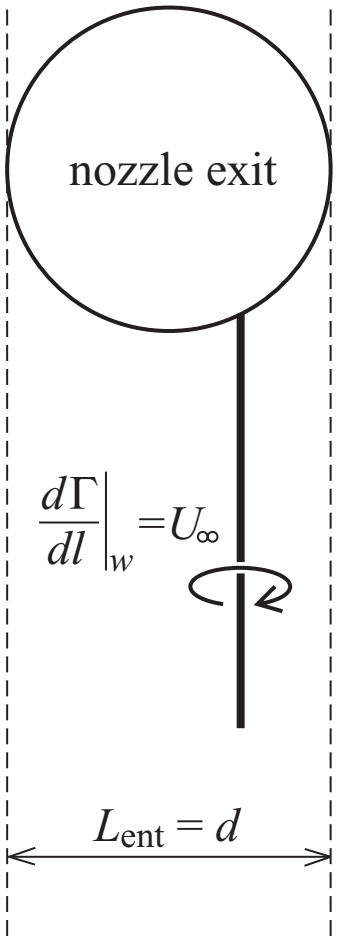

(a) reduced model

Figure 4-40: Comparison of entrainment processes of vorticity from the wall boundary layer into the jet. The reduced vorticity influx model assumes an unperturbed wall vortex sheet that is separated only along the jet nozzle exit. The full no-slip boundary condition fully considers two entrained vortices, one of which is a vortex tube extended to infinity, denoted by ∞, and the other of which is a vortex ring formed in the recirculation zone, denoted by r.

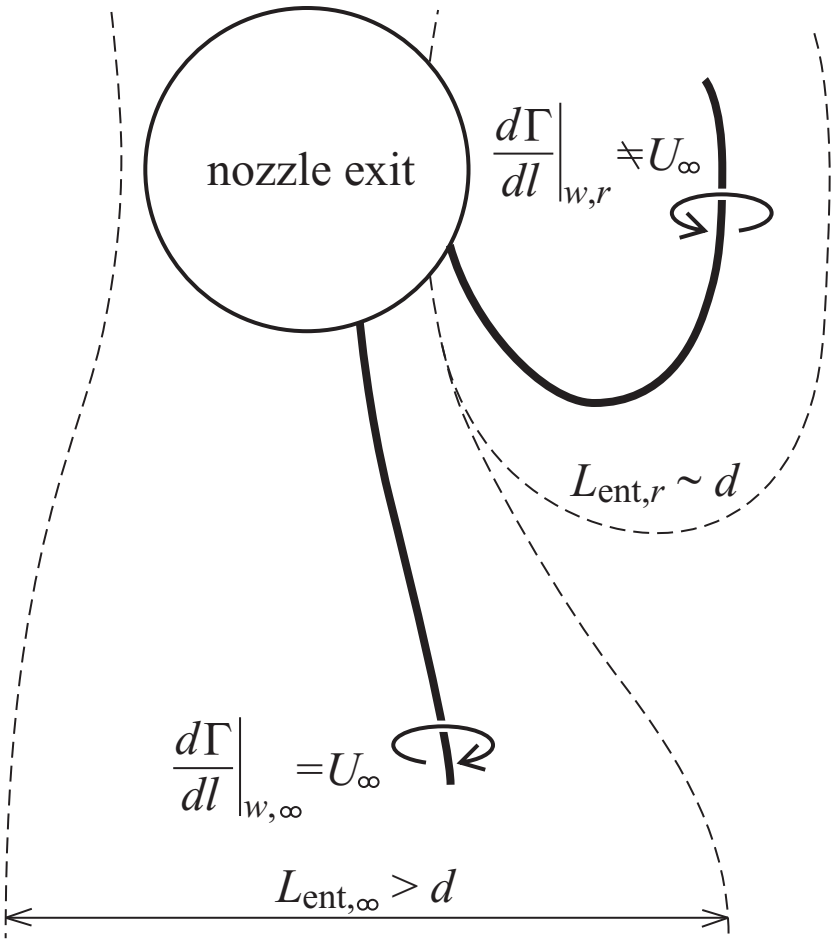

(b) full no-slip boundary condition

Figure 4-40: Continued from the previous page.

Chapter 5

Conclusions

5.1 Physics of transverse jets

Transverse jets find many applications in combustion and other industrial processes. They can be also considered as canonical examples of the cases where large-scale vortical structures dominate flow fields. In this thesis, detailed mechanistic description of vorticity dynamics in transverse jets has been pursued. Primary focus has been placed on strong transverse jets at intermediate Reynolds numbers. Massively parallel three-dimensional vortex simulations have been performed to this end.

Our rigorous modeling of vorticity dynamics in transverse jets, discussed in the thesis, includes the implementation of the full no-slip boundary condition, which results in the complete identification of vorticity introduction mechanisms in transverse jets. With such a rigorous model, we have fully described the interaction between the wall boundary layer and the jet shear layer. The reduced model partially accounting for the interaction between the wall boundary layer and the jet shear layer, which was previously developed in [51] based on heuristic arguments, has been derived with minimal additional assumptions from the full model. These additional assumptions are the neglected feedback from the jet shear layer to the wall boundary layer and the suppressed separation of the wall boundary layer except along the jet nozzle boundary. The comparison between two models has provided an interesting chance to investigate the impact of these neglected effects on the overall jet dynamics.

Especially, near-wall jet-streamwise vortices are created by the separation of the wall boundary layer and its subsequent entrainment into the jet in the case with the full model, while such a structure is not readily identified in the case with the reduced model. It is demonstrated that the separation of the wall boundary layer also contributes to the excess circulation in these jet-streamwise vortices. We has also shown that the existence of such near-wall counter-rotating vortices exerts qualitative and quantitative impacts on the overall jet dynamics.

The formation mechanism of counter-rotating vortices at intermediate Reynolds number does show great similarity to what we have observed in previous inviscid investigations [51]. The stages of the transformation of the cylindrical jet shear layer, emanating from the jet nozzle boundary, are accurately depicted by the technique of material element tracking. The lee side of the jet shear layer is lifted in the jet-streamwise direction, and forms arms of counter-rotating vorticity aligned with the jet trajectory. Periodic roll-up of the jet shear layer accompanies this deformation, creating vortex arcs on the lee and windward sides of the jet, due to a mechanism similar to the Kelvin-Helmholtz instability. The formation mechanism of the counter-rotating vortex pair remains invariant under the effect of viscosity at intermediate Reynolds number.

The mechanism behind the sudden transition from large-scale flow structures into small-scale vortical structures is also proposed. The mechanism involves the interaction between two large-scale vortical structures, i.e., the Kelvin-Helmholtz rings on the windward side and the counter-rotating vortices on the lee side. Vortex filaments from the Kelvin-Helmholtz rings are entrained by the action of the counter-rotating vortices, exhibiting rapid winding up around the counter-rotating vortices. During that process, part of the entrained vortex filaments experiences strong stretching and intensifies its vorticity. Subsequent induction from these vortex filaments onto the counter-rotating vortices gives a rupture to the counter-rotating vortex pair. The broken counter-rotating vortices yield the primary sites for further small-scale development. This induced counter-rotating vortex pair breakdown is demonstrated by presenting the evolution of a material ring and by examining the stretching rate field.

There are still remaining tasks and unanswered questions in transverse jets. Brief outline for some of these tasks and questions, in the context of the present work, is provided in the following:

1. Several flow features found in experiments are not identified in the simulations reported in this thesis. For instance, horseshoe vortices has not been identified in Case III. Discussion on horseshoe vortices is provided in the main text.

   A hovering vortex, which stays right around the jet nozzle boundary, is not captured in our simulations, either. The absence of a hovering vortex is actually expected, since our computational domain excludes in-pipe structures. Hovering vortices are topologically related to the separation of the in-pipe boundary layer [33]. Hence, to resolve this vortical structure, it is essential to include the in-pipe structures during modeling. A careful investigation is essential to achieve such a task.

   Upright wake vortices, which are formed by the separation of the wall boundary layer and are shedding from the jet column, are not expected in the conditions we have investigated in this thesis [33]. Their existence changes the instantaneous flow features in a nontrivial way from what we have observed in this thesis, and the overall jet dynamics can be greatly affected by the difference. For instance, the near-wall counter-rotating vortices or the near-wall jet-streamwise vortices may become weaker than those observed in Case III by constantly shedding their circulation downstream.

   Each of these vortical structures has importance in specific applications, and needs to be studied in a greater extent.

2. Since we have developed a model fully accounting for the interaction of the wall boundary layer and the jet shear layer in this thesis, transverse jets with low r can now be investigated as well. Such a jet has enormous practical importance, for instance, in film cooling processes of turbine blades. Since horseshoe vortices or hovering vortices may contribute to the overall jet dynamics in jets with

low r, it is important to pursue Item 1 simultaneously in order to achieve an appropriate understanding in this case.

3. Our results clearly show that there exist both chance and challenge in active control of transverse jets. The great sensitivity of the overall jet dynamics to the near-nozzle conditions, which has been demonstrated by our comparison between the results with the reduced vorticity influx model and the results with the full no-slip boundary condition, suggests that there exists great chance to affect the flow by imposing relatively small changes around the jet nozzle boundary. On the other hand, such sensitivity requires a very discrete strategy of control to truly achieve what we want from the flow. Especially, since it is clearly demonstrated that not only the jet shear layer but also the wall boundary layer can significantly alter the overall jet dynamics, it may be necessary to actuate both the jet shear layer and the wall boundary layer simultaneously to obtain the best results. Such a concurrent control strategy should be designed from a model fully including the interaction between the jet shear layer and the wall boundary layer, which will be a challenging task. Similar conclusion may be drawn for other flows exhibiting boundary layer separation, e.g., backward facing step flows.

5.2 Distribution-based numerical analysis

An inviscid vortex method provides a canonical example where a partial differential equation is transformed into an integro-differential equation whose solution may be considered as a measure or even as a distribution. In this thesis, a diffusion scheme, i.e., the vorticity redistribution method, has been reformulated in the same spirit. In Appendix A, by invoking the Paley-Wiener-Schwartz theorem [22], we have shown that a distribution can be matched to an analytic function through the Fourier transform. An analytic function may be expanded into a Taylor series, whose coefficients are equivalent to the moments of the corresponding distribution. By going through such a conceptual process, it is demonstrated that how moments may define topology

in a space of distributions. Then, the concept is integrated into the redistribution method to allow an appropriate convergence analysis. Validation has been performed by presenting three-dimensional vortex ring simulations.

There still are several unresolved difficulties in distribution-based computations, while the approach has been successful in our cases. One of the most fundamental limitations is the lack of a universally accepted strategy for nonlinearity. This is due to the fact that multiplication of two distributions is not defined in general. Roughly speaking, multiplication is only defined when the singular supports of the distributions are disjoint, though there exists a method to extend this limit by considering wavefront sets. In any case, unrestricted multiplication between distributions is not allowed, which makes the treatment of nonlinearity a nontrivial problem. In inviscid vortex methods, the problem was effectively addressed by smoothing the velocity field by changing the Biot-Savart kernel into a nonsingular kernel. In Chapter 2, we have shown that a similar strategy is working for a simple nonlinear diffusion problem. However, more theoretical investigation should follow to address the problem in general contexts.

Development of the Lagrangian counterpart of the Eulerian adaptive mesh refinement becomes a task of great importance. As clearly seen in our simulations, effective resolution of a boundary layer is critical in vortex simulations. A thin boundary layer at high Reynolds number may require a spatial length scale beyond the current computational limit if the spatial length scale is uniformly applied to the entire computational domain. Spatial adaptation of the core size and/or of the inter-particle distance will enable us to deal with such difficulty. Our distribution-based approach of matching moments may provide an answer in this context also. When we transform one representation into another, that is, when we refine the current particle distribution into the one with smaller spatial length scale, one may match low-order moments to control the error introduced during such a transformation. More intense research should be devoted onto this subject.

The direction proposed in this thesis can be even generalized beyond the boundary of typical partial differential equations. Much more general classes of operators

can be studied within the context. One obvious extension is the generalization of the methodology into pseudodifferential operators [62]. A differential operator is represented by a multiplication of a polynomial when the Fourier transform is applied. A pseudodifferential operator is represented by a multiplication of an analytic function, instead. Still, the concept of moment evolution can be used in a similar way for the analysis of the pseudodifferential operators.

Finally, the discussion provided in this thesis may even serve as the starting point to ask a more fundamental question on the general condition for a topological space to be appropriate for numerical approximation. In Appendix A, we have mentioned that topology for numerical approximation must be metrizable, but this conclusion is based only on a practical concern. Instead, we may pursue a more fundamental answer for this question by considering the limit of computations. For instance, one trivial answer may be provided right away: topology for numerical approximation should be at least separable [53]. This conclusion may be deduced from the fact that all the current digital computers are actually finite-state approximations of a deterministic Turing machine [6]. Since the possible states of a Turing machine are at most countablely many, there must exist a countable dense set in the space we are making an approximation to achieve convergence in general. However, it is only a necessary condition, and developing a sharper statement can be an interesting challenge for researchers from three distinct fields, i.e., numerical analysis, computer science, and topology.

Appendix A

Consistency of the Redistribution Scheme

A.1 Background

In [64], the convergence of the redistribution method was established for the case of constant diffusivity. The argument used in that work relied heavily on the fact that the fundamental solution in this case is explicitly given by a Gaussian distribution. Since the fundamental solution of (2.1) is not a Gaussian distribution, the argument given in [64] is not directly applicable to the analysis of the redistribution formulae (2.11). In this section, we provide a brief proof for the consistency of these formulae. Once the consistency is established, the convergence follows by having an additional condition on stability.

As we discussed in the main text, the proof of consistency is developed in the distribution sense [22, 68], since the approximation is made up with δ distributions. This actually makes a historical connection to the previous development in [64], since the earlier proof of the redistribution method was implicitly distribution-based. To give some insight, we hereby state the Paley-Wiener-Schwartz theorem [22]:

> The Fourier-Laplace transform of a member of $\mathcal{E}'(\mathbf{R}^d)$ is an analytic function on $\mathbf{C}^d$. Moreover, if $u \in \mathcal{E}'(\mathbf{R}^d)$ and supp $u \in \{|\mathbf{x}| \leq a\}$, where a is a

positive real number, then there are constants C, $N \geq 0$ such that

$$|\hat{u}(\zeta)| \leq C(1+|\zeta|)^N e^{a|\mathrm{Im}\zeta|}, \quad \zeta \in \mathbf{C}^d, \tag{A.1}$$

where $|\zeta| = \sqrt{|\zeta_1|^2 + |\zeta_2|^2 + \cdots + |\zeta_d|^2}$. $\hat{u}$ is the Fourier transform of u.

In its essence, the theorem suggests that distributions of compact support of certain size, i.e, members in $\mathcal{E}'$, is equivalent, under the Fourier-Laplace transform, to analytic functions with certain exponential growth rate at infinity. The later can be expanded into a Taylor series expansion around the origin in the wavenumber space, and each coefficient of the Taylor series expansion is corresponding to a moment of the distribution in the physical space. This roughly explains how matching of a few lowest moments provides an equivalent error control in distribution spaces. Since the proof in [64] was constructed by comparing the Taylor series expansion of the fundamental solution, which was just a Gaussian distribution in the case of constant diffusivity, and that of the redistributed particle distribution after applying the Fourier transform, which implies that the proof was, at least implicitly, constructed in a distribution space. Unfortunately, the idea was never made explicit after on however, though an attempt was made [63].

In the following, we investigate the redistribution method, explicitly in a distribution space, namely, in $\left(C_B^M(\mathbf{R}^d)\right)'$, which is the normed dual space of $C_B^M(\mathbf{R}^d)$. Note that $\left(C_B^M(\mathbf{R}^d)\right)'$ is a much smaller space than the space of distributions of compact support. The reason we choose such a more limited space is that its topology is more amenable for our purposes. In numerical analysis, one needs to discuss convergence in a more or less quantitative way. Since the topologies provided for larger spaces, e.g., $\mathcal{D}'$, $\mathcal{S}'$, or $\mathcal{E}'$ [22], are usually not even metrizable, which makes quantitative assessment of convergence difficult. On the other hand, $\left(C_B^M(\mathbf{R}^d)\right)'$ forms a Banach space with the equipped dual norm [1]. It should be also noted that, unlike the previous proof [64], we do not use the Fourier transform either, for the fundamental solution of a uniformly parabolic differential equation is not conveniently represented by a simple Gaussian distribution under the transform in general [63]. Rather, we

pursue analysis in the physical space directly by carefully estimating various portions of error in the approximation.

A.2 Analysis of consistency

To establish consistency, we use the following estimate for the fundamental solution of a uniformly parabolic linear equation [40]:

$$|D_t^r D_x^s Z(x,\xi,t,\tau)| \le c(t-\tau)^{-\frac{d+2r+s}{2}} \exp\left(-C\frac{|x-\xi|^2}{t-\tau}\right), \tag{A.2}$$

where $2r+s \le 2$. Two consequences of this estimate are exploited in the following discussion. The first is quite straightforward. Let f be a function, which is continuous and globally Lipschitz with a constant K in $\mathbf{R}^d$. Then, we can show that

$$\left| \int_{\mathbf{R}^d} Z(x,\xi,t,t-\Delta t) f(x) dx - f(\xi) \right| \le cK\sqrt{\Delta t} \int_{\mathbf{R}^d} |z| \exp\left(-Cz^2\right) dz, \tag{A.3}$$

which in turn shows that $\left|\int_{\mathbf{R}^d} Z(x,\xi,t,t-\Delta t) f(x) dx - f(\xi)\right| = O(\sqrt{\Delta t})$. The other important consequence is that

$$\begin{aligned}
&\int_{|x-\xi|\ge\left(\sqrt{\Delta t}\right)^{1-\epsilon}} |Z(x,\xi,t,t-\Delta t)|\,|x-\xi|^m\,dx \\
&\qquad \le \int_{|x-\xi|\ge\left(\sqrt{\Delta t}\right)^{1-\epsilon}} c\Delta t^{-d/2} \exp\left(-C\frac{|x-\xi|^2}{\Delta t}\right) |x-\xi|^m\,dx \\
&\qquad \le \int_{|z|\ge\left(\sqrt{\Delta t}\right)^{-\epsilon}} c\exp(-Cz^2) \left|z\sqrt{\Delta t}\right|^m dz = o(\Delta t^q),
\end{aligned} \tag{A.4}$$

for $0<\epsilon<1$, $q>0$ and $m \ge 0$.

With these estimates at hand, we may show the consistency of the redistribution formulae (2.11) in the sense that the new particle distribution truly approximates the fundamental solution. Each source particle is assumed to be redistributed into target particles within a ball of radius R, centered at the location of the source particle. we assume that R scales as $O(h)$, where $h = \sqrt{\Delta t}$.

First, we show that each moment evolves consistently. For the 0th moment,

$G^n_{0,i} = \underline{G}^n_{0,i} = 1$, if f^n_{ij} satisfies (2.11). Thus the moment matching condition is satisfied exactly. For $G^n_{1,i}$, we have

$$\frac{d}{dt}\left(G^n_{1,i} - \underline{G}^n_{1,i}\right) = \int_{\mathbf{R}} Z(x, x_i^{n-1}, t, 0)\frac{d\nu}{dx}dx - \left(\frac{d\nu}{dx}\right)_{x=x_i^{n-1}} = O(\Delta t^{1/2})$$

by the application of (A.3). Thus, $|G^n_{1,i} - \underline{G}^n_{1,i}| = O(\Delta t^{3/2})$. For $G^n_{2,i}$, we separate the integral into two parts.

$$\begin{aligned}\left|\frac{d}{dt}\left(G^n_{2,i} - \underline{G}^n_{2,i}\right)\right| \;\leq\; & \int_{\mathbf{R}} \left|2\nu(x) - 2\nu(x_i^{n-1})\right| Z(x, x_i^{n-1}, t, 0)dx \\ & + \int_{\mathbf{R}} \left|2(x - x_i^{n-1})\frac{d\nu}{dx}\right| Z(x, x_i^{n-1}, t, 0)dx.\end{aligned}$$

The first term is $O(\Delta t^{1/2})$ by the application of (A.3). The second term is estimated as follows.

$$\begin{aligned}&\int_{\mathbf{R}} \left|2(x - x_i^{n-1})\frac{d\nu}{dx}\right| Z(x, x_i^{n-1}, t, 0)dx \\ &\qquad \leq \int_{\Omega} \left|2(x - x_i^{n-1})\frac{d\nu}{dx}\right| Z(x, x_i^{n-1}, t, 0)dx \\ &\qquad\quad + \int_{\Omega^c} \left|2(x - x_i^{n-1})\frac{d\nu}{dx}\right| Z(x, x_i^{n-1}, t, 0)dx.\end{aligned}$$

where $\Omega = \left\{x \in \mathbf{R}, s.t.\ |x - x_i^{n-1}| < R'h\right\}$, where $R' = O(h^{-\epsilon})$. It can be shown that the first term is $O(R'h) = O(\Delta t^{1/2-\epsilon})$, and the second term is $o(h^q)$ for all $q > 0$ from (A.4). Thus, we have $|G^n_{2,i} - \underline{G}^n_{2,i}| = O(\Delta t^{3/2-\epsilon})$.

Therefore, for the ith source particle, the redistribution formulae (2.11) give f^n_{ij} satisfying the following conditions around x_i^{n-1} for $M = 1$, i.e.,

$$\forall\, |k| \leq M+1, \exists\, C_{k,M'},\ s.t.\ \forall\, i,\ n, \left|\underline{G}^n_{k,i} - G^n_{k,i}\right| \leq C_{k,M'}h^{M'}\Delta t, \tag{A.5}$$

for any M' satisfying $M - 1 < M' < M$.

We are finally at the stage where we can estimate the error between the new particle distribution and the fundamental solution using (A.5). From the Taylor

series remainder theorem of a test function ϕ, we get

$$
\begin{aligned}
&\forall \phi \in C_B^{M+2}(\mathbf{R}), \\
&\left| \int_{\mathbf{R}} \left(\sum_{j=1}^{N} f_{ij}^n \delta(x - x_j^n) - Z(x, x_i^{n-1}, \Delta t, 0) \right) \phi(x) dx \right| \\
&\quad \leq \sum_{|k| \leq M+1} \frac{1}{k!} \|\phi\|_{C_B^{M+2}(\mathbf{R})} \\
&\qquad \times \left| \int_{\mathbf{R}} (x - x_i^{n-1})^k \left(\sum_{j=1}^{N} f_{ij}^n \delta(x - x_j^n) - Z(x, x_i^{n-1}, \Delta t, 0) \right) dx \right| \\
&\quad + \sum_{|k|=M+2} \frac{1}{k!} \|\phi\|_{C_B^{M+2}(\mathbf{R})} \\
&\qquad \times \left| \int_{\Omega} (x - x_i^{n-1})^k \left(\sum_{j=1}^{N} f_{ij}^n \delta(x - x_j^n) - Z(x, x_i^{n-1}, \Delta t, 0) \right) dx \right| \\
&\quad + \sum_{|k|=M+2} \frac{1}{k!} \|\phi\|_{C_B^{M+2}(\mathbf{R})} \\
&\qquad \times \left| \int_{\Omega^c} (x - x_i^{n-1})^k Z(x, x_i^{n-1}, \Delta t, 0) dx \right|.
\end{aligned}
\tag{A.6}
$$

The first term in the right hand side is $O(h^{M'}\Delta t)$ by the assumed moment conditions, and the last term is $o(h^q)$ for all $q > 0$ by the estimate (A.4). The second term is $O(R'^{M+2} h^M \Delta t)$, because

$$
\forall x \in \Omega, \left| (x - x_i^{n-1})^{(k)} \right| \leq (R'h)^{M+2} = R'^{M+2} h^M \Delta t.
$$

Since $R = O(h)$, we may take ϵ as small as we want. Therefore, we have the following result for all $M' < M$.

$$
\left\| \sum_{j=1}^{N} f_{ij}^n \delta(x - x_j^n) - Z(x, x_i^{n-1}, \Delta t, 0) \right\|_{\left(C_B^{M+2}(\mathbf{R})\right)'} \leq C h^{M'} \Delta t, \tag{A.7}
$$

Using a standard argument with the additional condition of stability, we can also show that the global truncation error behaves as $O(h^{M'})$, where $M' < M$. This is not as sharp as what we had for the case of constant diffusivity considered in [64], where the global truncation error was $O(h^M)$.

We have shown consistency in the distribution sense [22, 68], i.e., in $\left(C_B^{M+2}(\mathbf{R})\right)'$, not in typical L^p spaces. As discussed earlier, the reason is that the spirit of the method can be more clearly recognized in terms of the approximation of the fundamental solution by δ distributions, which cannot be treated in L^p. However, it is easy to show that the method also generates a convergent sequence in L^p by convolving the particle distribution with a sufficiently regular core function f. For example, given $f \in C_B^{M+2}(\mathbf{R})$, we define $f_\sigma(x) \equiv \frac{1}{\sigma} f(\frac{x}{\sigma})$. Then, for a regular enough solution u,

$$\|u - \underline{u} * f_\sigma\|_\infty \leq \|u - u * f_\sigma\|_\infty + \|(u - \underline{u}) * f_\sigma\|_\infty,$$

where $\underline{u}$ is the approximation made up with a linear superposition of δ distributions, i.e., $\|u - \underline{u}\|_{\left(C_B^{M+2}(\mathbf{R})\right)'} = O(h^{M'})$. It is easy to see that

$$\begin{aligned} \exists m_1, \quad m_2 \ > 0, \quad s.t. \quad \|u - u * f_\sigma\|_\infty &= O(\sigma^{m_1}), \\ \|(u - \underline{u}) * f_\sigma\|_\infty &\leq \sup_{x \in \mathbf{R}} \left| \int_{\mathbf{R}} (u - \underline{u})(y) f_\sigma(x - y) dy \right| \\ &\leq \|(u - \underline{u})\|_{\left(C_B^{M+2}(\mathbf{R})\right)'} \|f_\sigma\|_{C_B^{M+2}(\mathbf{R})} = O(h^{M'}/\sigma^{m_2}). \end{aligned}$$

This shows that the error in L^∞ can be estimated as $O(\sigma^{m_1}) + O(h^{M'}/\sigma^{m_2})$.

Convergence in other distribution spaces can be deduced from the Sobolev imbedding theorem [1]. For instance, it can be shown that the scheme converges in the normed dual space of $W_0^{m,p}(\mathbf{R}^d) = W^{m,p}(\mathbf{R}^d)$, which is denoted as $W^{-m,p'}(\mathbf{R}^d)$, where p' stands for the conjugate power of p, i.e., $1/p + 1/p' = 1$ [1]. Its topology is described by the following norm.

$$\|u\|_{-m,p'} = \sup_{\|\phi\|_{m,p} \leq 1} |\langle u, \phi \rangle| .$$

With this norm, $W^{-m,p'}(\mathbf{R}^d)$ is complete, hence forms a Banach space. For m and p satisfying $(m - M - 2)p > d$, where M is the expected order of accuracy, the Sobolev imbedding theorem guarantees $W^{m,p}(\mathbf{R}^d) \hookrightarrow C_B^{M+2}(\mathbf{R}^d)$. This imbedding is continuous, i.e., $\exists c_1 > 0, s.t. \|\phi\|_{C_B^{M+2}(\mathbf{R}^d)} \leq c_1 \|\phi\|_{m,p}$ for all $\phi \in W^{m,p}(\mathbf{R}^d)$, and thus the convergence in the norm $\|\cdot\|_{\left(C_B^{M+2}(\mathbf{R}^d)\right)'}$ implies the convergence in the norm $\|\cdot\|_{-m,p'}$. Since $W^{-m,p}$ type spaces are the spaces used in [13], this property

effectively provides a connection between the convergence properties of two substeps, i.e., convection and diffusion.

We note that the error estimate given here does not include any detailed consideration on the contribution of the error from initial discretization, and the error scaling as $O(\sigma^{m_1})$ is due to variable diffusivity, and not due to initial discretization. This additional error does not occur when one only deals with the case of constant diffusivity, where one can use convolution to separate the core function from the error estimate, assuming that the core function behaves well. However, in the case of variable diffusivity, the independency of the error estimate from the core function is lost even in the redistribution method.

Appendix B

Tree-code Algorithm for a High-Order Algebraic Kernel

B.1 Background

The evaluation of inter-particle interactions in Lagrangian vortex methods forms a classical N-body problem, whose cost scales as $O(N^2)$ with a naive implementation. This computational cost turns out to be too expensive for large-scale three-dimensional computations. To alleviate this difficulty, fast summation algorithms have been proposed by various researchers [2, 27, 72]. In many of these approaches, particles are divided into a nested set of clusters, and particle-particle interactions are replaced into particle-cluster interactions, which can be efficiently evaluated by using an expansion. Such tree-code algorithms reduce the operation count to $O(N \log N)$ or even to $O(N)$.

Among these tree-code algorithms, we have chosen the algorithm developed by Lindsay and Krasny [45] to perform our simulations in the main text. In this method, particle-cluster interactions are evaluated by use of Taylor series expansion of the Rosenhead-Moore kernel [58, 52], or equivalently the low-order algebraic kernel [74], up to the 8th order, where the Taylor coefficients are computed with a recurrence relation. A parallel version of the code was also developed [50].

The status of the Rosenhead-Moore kernel, however, is somewhat controversial.

From many previous applications of the kernel, it is generally believed that the kernel does provide convergence in all cases of practical interest. However, some researchers, most notably in [74], have claimed that the kernel does not satisfy an inequality required in the classical proof of convergence of vortex methods, and have warned that it may not converge at all. The controversy still lasts, even in today – an anonymous reviewer of [73] criticized the manuscript for using the Rosenhead-Moore kernel, for instance. It is, therefore, worth extending the tree-code algorithm to other kernels, which are less controversial.

In this context, we develop a method to recursively evaluate the Taylor coefficients of a high-order algebraic kernel, which was introduced by Winckelmans and Leonard [74]. Honoring the inventors, we shall refer the kernel as the Winckelmans-Leonard kernel from now on. The kernel was claimed to satisfy all the requirements in the classical convergence analysis of vortex methods and to be more convenient than those kernels involving transcendental functions numerically.

Appendix B is organized as follows: we first briefly describe the adaptive tree-code for the Rosenhead-Moore kernel. In the next section, a recursive method to evaluate the Taylor coefficients of the Winckelmans-Leonard kernel is presented. The new recursive method for the Winckelmans-Leonard kernel bears great similarity to the method used for the Rosenhead-Moore kernel, and hence is easily implemented in the existing tree-code without too much effort. Finally, a numerical example is provided to test its efficiency and accuracy.

The tree-code developed in Appendix B is used in Appendix C to provide additional discussion on the convergence properties of the Rosenhead-Moore kernel and the Winckelmans-Leonard kernel. Note, however, that the Winckelmans-Leonard kernel has not been used for the simulations reported in the main text. For simulations of transverse jets, we have only used the Rosenhead-Moore kernel.

B.2 Adaptive tree-code for the Rosenhead-Moore kernel

The problem can be stated as follows. For each time step during vortex simulations, it is necessary to invert the following equation:

$$\boldsymbol{\omega} = \nabla \times \mathbf{u}. \tag{B.1}$$

That is, knowing the vorticity field $\boldsymbol{\omega}$, we need to calculate the velocity field $\mathbf{u}$. $\boldsymbol{\omega}$ is discretized into Lagrangian computational elements or particles:

$$\boldsymbol{\omega}(\mathbf{x}) \approx \sum_{j=1}^{N} \mathbf{W}_j f_\sigma(\mathbf{x} - \mathbf{y}_j), \tag{B.2}$$

f_σ is a radially symmetric core function of radius σ, given by $f_\sigma(\mathbf{x}) \equiv \sigma^{-3} f(|\mathbf{x}|/\sigma)$. In $\mathbf{R}^3$, the solution of (B.1) is given by the Biot-Savart law.

$$\mathbf{u}(\mathbf{x}) = -\frac{1}{4\pi} \int \frac{\mathbf{x} - \mathbf{y}}{|\mathbf{x} - \mathbf{y}|^3} \times \boldsymbol{\omega}(\mathbf{y}) d\mathbf{y}. \tag{B.3}$$

Equivalently, the following expression can be used:

$$\mathbf{u}(\mathbf{x}) = \sum_{j=1}^{N} \mathbf{K}_\sigma(\mathbf{x}, \mathbf{y}_j) \times \mathbf{W}_j, \tag{B.4}$$

where $\mathbf{K}_\sigma$ is given by

$$\mathbf{K}_\sigma(\mathbf{x}, \mathbf{y}) = -\frac{1}{4\pi} \int \frac{\mathbf{x} - \mathbf{z}}{|\mathbf{x} - \mathbf{z}|^3} f_\sigma(\mathbf{z} - \mathbf{y}) d\mathbf{z}. \tag{B.5}$$

To evaluate (B.4), a tree is constructed. Computational particles are divided into a nested set of clusters by constructing a tree, and particle-particle interactions are replaced by a smaller number of particle-cluster interactions. The tree construction starts with the root cell containing all the particles. The cell on the next level is obtained by bisecting one of the cells at the current level in one of three coordinate

directions. When every terminal cell in the tree contains a number of particles smaller than the predefined leaf size, N_0, which is predefined by the user, the process terminates and returns the tree structure. Once the tree is constructed, (B.4) is rewritten in the following form:

$$\mathbf{u}(\mathbf{x}) = \sum_{c} \sum_{j=1}^{N_c} \mathbf{K}_\sigma(\mathbf{x}, \mathbf{y}_j) \times \mathbf{W}_j, \tag{B.6}$$

where c denotes a cluster containing N_c particles. Each particle-cluster interaction is evaluated either by using Taylor approximation or by direct summation. The procedure uses a complex combination of theoretical error estimates and empirical computational time estimates to determine the best order of the approximation and the best size of the cluster.

To derive the Taylor approximation for a particle-cluster interaction, $\mathbf{K}_\sigma(\mathbf{x}, \mathbf{y})$ in (B.6) is expanded in the Taylor series with respect to $\mathbf{y}$, around the cluster center $\mathbf{y}_c$, such that

$$\sum_{j=1}^{N_c} \mathbf{K}_\sigma(\mathbf{x}, \mathbf{y}_j) \times \mathbf{W}_j = \sum_{\mathbf{k}} \mathbf{a}_\mathbf{k}(\mathbf{x}, \mathbf{y}_c) \times \mathbf{m}_\mathbf{k}(c). \tag{B.7}$$

Here, $\mathbf{a}_\mathbf{k}(\mathbf{x}, \mathbf{y}_c)$ is the $\mathbf{k}$th Taylor coefficient of $\mathbf{K}_\sigma(\mathbf{x}, \mathbf{y})$ at $\mathbf{y}_c$:

$$\mathbf{a}_\mathbf{k}(\mathbf{x}, \mathbf{y}_c) = \frac{1}{\mathbf{k}!} D_\mathbf{y}^\mathbf{k} \mathbf{K}_\sigma(\mathbf{x}, \mathbf{y}), \tag{B.8}$$

and $\mathbf{m}_\mathbf{k}(c)$ is the $\mathbf{k}$th moment of the vortex elements in cluster c about its center $\mathbf{y}_c$:

$$\mathbf{m}_\mathbf{k}(c) = \sum_{j=1}^{N_c} \mathbf{W}_j (\mathbf{y}_j - \mathbf{y}_c)^\mathbf{k}. \tag{B.9}$$

$\mathbf{k} = (k_1, k_2, k_3)$ is an integer multi-index with $k_i \geq 0$, and $\mathbf{k}! = k_1! k_2! k_3!$. For $\mathbf{x} \in \mathbf{R}^3$, $\mathbf{x}^\mathbf{k}$ and $D_\mathbf{y}^\mathbf{n}$ is interpreted in the standard way, i.e., $\mathbf{x}^\mathbf{k} = x_1^{k_1} x_2^{k_2} x_3^{k_3}$ and $D_\mathbf{y}^\mathbf{n} = D_{y_1}^{n_1} D_{y_2}^{n_2} D_{y_3}^{n_3}$, where $D_{y_i} = \frac{\partial}{\partial y_i}$. The infinite series in (B.7) is approximated by a finite sum,

$$\sum_{j=1}^{N_c} \mathbf{K}_\sigma(\mathbf{x}, \mathbf{y}_j) \times \mathbf{W}_j \approx \sum_{|\mathbf{k}|<p} \mathbf{a}_\mathbf{k}(\mathbf{x}, \mathbf{y}_c) \times \mathbf{m}_\mathbf{k}(c), \tag{B.10}$$

where $|\mathbf{k}| = k_1 + k_2 + k_3$. The order of the approximation, p, must be chosen so that

the error due to truncation remains small. To evaluate (B.10), we need the Taylor coefficients, i.e., $\mathbf{a_k}$. We define a scalar potential, ϕ_σ, which yields the kernel, $\mathbf{K}_\sigma$, as its gradient:

$$\mathbf{K}_\sigma(\mathbf{x},\mathbf{y}) = -\nabla_y \phi_\sigma(\mathbf{x},\mathbf{y}). \tag{B.11}$$

We set the $\mathbf{k}$th Taylor coefficient of $\phi_\sigma(\mathbf{x},\mathbf{y})$ at $\mathbf{y} = \mathbf{y}_c$ as

$$T_\mathbf{k}(\mathbf{x},\mathbf{y}_c) = \frac{1}{\mathbf{k}!} D^\mathbf{k}_\mathbf{y} \phi_\sigma(\mathbf{x},\mathbf{y}_c). \tag{B.12}$$

Then, $\mathbf{a_k}$ is related to $T_\mathbf{k}$ as follows:

$$\mathbf{a_k}(\mathbf{x},\mathbf{y}_c) = -\sum_{i=1}^{3} \hat{\mathbf{e}}_i (k_i+1) T_{\mathbf{k}+\hat{\mathbf{e}}_i}(\mathbf{x},\mathbf{y}_c), \tag{B.13}$$

where $\hat{\mathbf{e}}_i$ is the ith Cartesian-basis vector. Therefore, to compute $\mathbf{a_k}$, it is sufficient to obtain $T_\mathbf{k}$. For the Rosenhead-Moore kernel:

$$\mathbf{K}^{RM}_\sigma(\mathbf{x},\mathbf{y}) = -\frac{1}{4\pi} \frac{\mathbf{x}-\mathbf{y}}{(|\mathbf{x}-\mathbf{y}|^2+\sigma^2)^{3/2}}, \tag{B.14}$$

the potential is the Plummer potential:

$$\phi^{RM}_\sigma(\mathbf{x},\mathbf{y}) = \frac{1}{4\pi} \frac{1}{(|\mathbf{x}-\mathbf{y}|^2+\sigma^2)^{1/2}}. \tag{B.15}$$

The calculation of the corresponding $T_\mathbf{k}$ is performed recursively, using the following formula [45].

$$|\mathbf{k}| R^2 T_\mathbf{k} - (2|\mathbf{k}|-1) \sum_{i=1}^{3} (\mathbf{x}-\mathbf{y}) \cdot \hat{\mathbf{e}}_i T_{\mathbf{k}-\hat{\mathbf{e}}_i} + (|\mathbf{k}|-1) \sum_{i=1}^{3} T_{\mathbf{k}-2\hat{\mathbf{e}}_i} = 0, \tag{B.16}$$

for $|\mathbf{k}| \geq 1$, where $T_0(\mathbf{x},\mathbf{y}_c) = \phi_\sigma(\mathbf{x},\mathbf{y}_c)$, $T_\mathbf{k}(\mathbf{x},\mathbf{y}_c) = 0$ if any $k_i < 0$, and $R = \sqrt{|\mathbf{x}-\mathbf{y}_c|^2+\sigma^2}$.

Further details of the tree-code can be found in the work by Lindsay and Krasny [45].

B.3 Extension to the Winckelmans-Leonard kernel

The high-order algebraic kernel, or equivalently the Winckelmans-Leonard kernel, is given as follows [74]:

$$\mathbf{K}_\sigma^{WL}(\mathbf{x},\mathbf{y}) = -\frac{1}{4\pi}\frac{|\mathbf{x}-\mathbf{y}|^2+\frac{5}{2}\sigma^2}{(|\mathbf{x}-\mathbf{y}|^2+\sigma^2)^{5/2}}(\mathbf{x}-\mathbf{y}). \tag{B.17}$$

The corresponding potential is given by:

$$\phi_\sigma^{WL}(\mathbf{x},\mathbf{y}) = \frac{1}{4\pi}\frac{|\mathbf{x}-\mathbf{y}|^2+\frac{3}{2}\sigma^2}{(|\mathbf{x}-\mathbf{y}|^2+\sigma^2)^{3/2}}. \tag{B.18}$$

One way to compute the Taylor coefficients of the Winckelmans-Leonard kernel is to split $\phi_\sigma^{WL}(\mathbf{x},\mathbf{y})$ into two parts and to develop a recurrence relation for each part separately, i.e.

$$\phi_\sigma^{WL}(\mathbf{x},\mathbf{y}) = \frac{\phi_\sigma^1(\mathbf{x},\mathbf{y})}{4\pi} + \frac{\sigma^2\phi_\sigma^3(\mathbf{x},\mathbf{y})}{8\pi}, \tag{B.19}$$

where $\phi_\sigma^\nu(\mathbf{x},\mathbf{y}) = (|\mathbf{x}-\mathbf{y}|^2+\sigma^2)^{-\nu/2}$. Note that $\phi_\sigma^{RM} = \phi_\sigma^1/4\pi$. That is, the potential for the Winckelmans-Leonard kernel can be obtained by adding a correction term to the Plummer potential. The recurrence relation for the Taylor coefficients of ϕ_σ^ν for each ν is already available [20]. Setting

$$T_\mathbf{n}^\nu = T_\mathbf{n}^\nu(\mathbf{x},\mathbf{y}) = \frac{1}{\mathbf{n}!}D_\mathbf{y}^\mathbf{n}\phi_\sigma^\nu(\mathbf{x},\mathbf{y}), \tag{B.20}$$

it has been shown that

$$\begin{aligned} |\mathbf{n}|(|\mathbf{x}-\mathbf{y}|^2+\sigma^2)T_\mathbf{n}^\nu \;&-\; (2|\mathbf{n}|+\nu-2)\sum_{i=1}^{3}(x_i-y_i)T_{\mathbf{n}-\hat{\mathbf{e}}_i}^\nu \\ &+\; (|\mathbf{n}|+\nu-2)\sum_{i=1}^{3}T_{\mathbf{n}-2\hat{\mathbf{e}}_i}^\nu = 0. \end{aligned} \tag{B.21}$$

Once knowing $T^1_{\mathbf{n}}$ and $T^3_{\mathbf{n}}$, the Taylor coefficients of $\phi^{WL}_\sigma(\mathbf{x},\mathbf{y})$, i.e., $T_{\mathbf{n}} = \frac{1}{\mathbf{n}!} D^{\mathbf{n}}_{\mathbf{y}} \phi^{WL}_\sigma(\mathbf{x},\mathbf{y})$, can be obtained by taking the sum.

$$T_{\mathbf{n}} = \frac{T^1_{\mathbf{n}}}{4\pi} + \frac{\sigma^2 T^3_{\mathbf{n}}}{8\pi}. \tag{B.22}$$

Using (B.22), we write

$$\begin{aligned} \sum_{j=1}^{N_c} \phi^{WL}_\sigma(\mathbf{x},\mathbf{y}_c)\mathbf{W}_j &\approx \frac{1}{4\pi} \sum_{|\mathbf{n}|<p} T^1_{\mathbf{n}}(\mathbf{x},\mathbf{y}_c)\mathbf{m}_{\mathbf{n}}(c) \\ &+ \frac{\sigma^2}{8\pi} \sum_{|\mathbf{n}|<p} T^3_{\mathbf{n}}(\mathbf{x},\mathbf{y}_c)\mathbf{m}_{\mathbf{n}}(c). \end{aligned} \tag{B.23}$$

To estimate the error in (B.23), we write the sum of the neglected terms as follows:

$$\begin{aligned} &\frac{1}{4\pi} \sum_{|\mathbf{n}|\geq p} T^1_{\mathbf{n}}(\mathbf{x},\mathbf{y}_c)\mathbf{m}_{\mathbf{n}}(c) + \frac{\sigma^2}{8\pi} \sum_{|\mathbf{n}|\geq p} T^3_{\mathbf{n}}(\mathbf{x},\mathbf{y}_c)\mathbf{m}_{\mathbf{n}}(c) \\ = \;& \frac{1}{4\pi} \sum_{n\geq p} \sum_{j=1}^{N_c} B^1_n(\mathbf{x},\mathbf{y}_c,\mathbf{y}_j)\mathbf{W}_j + \frac{\sigma^2}{8\pi} \sum_{n\geq p} \sum_{j=1}^{N_c} B^3_n(\mathbf{x},\mathbf{y}_c,\mathbf{y}_j)\mathbf{W}_j, \end{aligned} \tag{B.24}$$

where

$$B^\nu_n(\mathbf{x},\mathbf{y}_c,\mathbf{y}_j) = \sum_{|\mathbf{k}|=n} T^\nu_{\mathbf{k}}(\mathbf{x},\mathbf{y}_c)(\mathbf{y}_j - \mathbf{y}_c)^{\mathbf{k}}. \tag{B.25}$$

Multiplying (B.21) by $(\mathbf{y}_j - \mathbf{y}_c)^{\mathbf{n}}$ and summing over all indices $\mathbf{n}$ with $|\mathbf{n}| = n$, we obtain

$$nR^2 B^\nu_n - (2n+\nu-2)\alpha B^\nu_{n-1} + (n+\nu-2)\beta^2 B^\nu_{n-2} = 0, \tag{B.26}$$

where $\alpha = (\mathbf{x}-\mathbf{y}_c)\cdot(\mathbf{y}_j-\mathbf{y}_c)$, and $\beta = |\mathbf{y}_j-\mathbf{y}_c|$ [45]. (B.26) is similar to the recurrence relation of the Gegenbauer polynomials [20]:

$$nC^{(\nu/2)}_n(x) - (2n+\nu-2)xC^{(\nu/2)}_{n-1}(x) + (n+\nu-2)C^{(\nu/2)}_{n-2}(x) = 0. \tag{B.27}$$

Comparing (B.26) and (B.27), we conclude that

$$B^\nu_n(\mathbf{x},\mathbf{y}_c,\mathbf{y}_j) = \frac{1}{R^\nu}\left(\frac{\beta}{R}\right)^n C^{(\nu/2)}_n(\alpha/\beta R). \tag{B.28}$$

Note that $|\alpha/\beta R| \leq 1$, and that

$$\forall |x| \leq 1, |C_n^{(\nu/2)}(x)| \leq \frac{(n+\nu-1)!}{n!(\nu-1)!}. \tag{B.29}$$

Hence,

$$|B_n^1(\mathbf{x}, \mathbf{y}_c, \mathbf{y}_j)| \leq \frac{1}{R}\left(\frac{|\mathbf{y}_j - \mathbf{y}_c|}{R}\right)^n, \tag{B.30}$$

and

$$|B_n^3(\mathbf{x}, \mathbf{y}_c, \mathbf{y}_j)| \leq \frac{(n+2)(n+1)}{2R^3}\left(\frac{|\mathbf{y}_j - \mathbf{y}_c|}{R}\right)^n. \tag{B.31}$$

We take the first term of the series in (B.24) as a heuristic estimate of the error. With (B.30) and (B.31), the estimated error, E_p, becomes

$$E_p = \frac{M_p(c)}{4\pi R^{p+1}}\left(1 + \frac{(p+2)(p+1)}{2}\frac{\sigma^2}{R^2}\right), \tag{B.32}$$

where

$$M_p(c) = \sum_{j=1}^{N_c} |\mathbf{y}_j - \mathbf{y}_c|^p |\mathbf{W}_j|. \tag{B.33}$$

Since $M_p(c) \leq M_0(c) r^p$, where r represents the radius of the cluster c, the asymptotic behavior of the error is given by

$$E_p = O(h^p) + O(p^2 h^p \eta^2), \tag{B.34}$$

where $h = r/R$, and $\eta = \sigma/R$, as $h \to 0$, $\eta \to 0$ and $p \to \infty$.

B.4 Numerical results

The method described in the previous section has been implemented into the tree-code originally developed by Lindsay and Krasny [45]. We compute the velocity field around colliding vortex rings, whose particle distribution is shown in Figure B-1, to test the new tree-code. The rings consist of 163,251 particles, and the velocity field is evaluated on a uniform rectangular grid encompassing the particles. The number

of grid points is 96,000. The total number of particle-particle interactions is roughly 1.57×10^{10}. The number of particles chosen here is slightly higher than that is typically enclosed in one cluster in our parallel simulations reported in the thesis.

Expansion, i.e., (B.10, B.13, B.22) with (B.21), is used to compute the velocity field when the following criterion is met:

$$4\pi E_p = \frac{M_p(c)}{R^{p+1}}\left(1+\frac{(p+2)(p+1)}{2}\frac{\sigma^2}{R^2}\right) \le \epsilon, \tag{B.35}$$

where ϵ is a user-defined parameter. This criterion is derived from (B.32). We set $N_0 = 64$ and $\sigma = 0.1$. The maximum order of expansion is limited to 8. The calculation is performed with double precision on a Pentium 4 workstation. Figure B-2 shows the error in the velocity field verses ϵ. The absolute error is defined as:

$$E_{\text{abs}} = \max|\mathbf{u}_{\text{sum}}(\mathbf{x}) - \mathbf{u}_{\text{app}}(\mathbf{x})|. \tag{B.36}$$

The subscript 'sum' denotes direct summation, while the subscript 'app' denotes tree-code approximation. It is important to distinguish E_{abs} from the error discussed in Appendix B. E_{abs} is just the error induced by tree-code approximation, which does not include the error due to desingularization. We also plot the relative error, which is given by:

$$E_{\text{rel}} = \max\frac{|\mathbf{u}_{\text{sum}}(\mathbf{x}) - \mathbf{u}_{\text{app}}(\mathbf{x})|}{|\mathbf{u}_{\text{sum}}(\mathbf{x})|}. \tag{B.37}$$

The error varies linearly to ϵ, implying that (B.35) provides reasonable error control. The computational time is shown in Figure B-3. t_{sum} represents the computational time for direct summation, which is 1,800 seconds in this case. t_{app} is the computational time for the same job with tree-code approximation. We plot $t_{\text{app}}/t_{\text{sum}}$, since t_{app} may vary significantly from one machine to another. The result shows that we achieve $E_{\text{abs}} \approx 10^{-6}$ with about 10% of the computational time for direct summation, which is comparable performance to the original tree-code for the Rosenhead-Moore kernel [45]. In our experiments, for the same value of E_{abs}, the use of the Winckelmans-Leonard kernel roughly takes only 25% more time than that of the

Rosenhead-Moore kernel. We reiterate that the same value of E_{abs} does not necessarily imply that the error from the exact velocity field is the same for the different kernels, since E_{abs} is estimated from $\mathbf{u}_{\text{sum}}(\mathbf{x})$, which can be very different from the exact velocity field.

B.5 Summary

A recurrence relation for the Taylor coefficients of the high-order algebraic kernel, or equivalently the Winckelmans-Leonard kernel, is presented. An error estimate has been obtained to ensure adaptive error control. The recurrence relation is integrated within a tree-code to evaluate vorticity-induced velocity. Our numerical example shows that the tree-code really provides an accurate and efficient way of evaluating a velocity field.

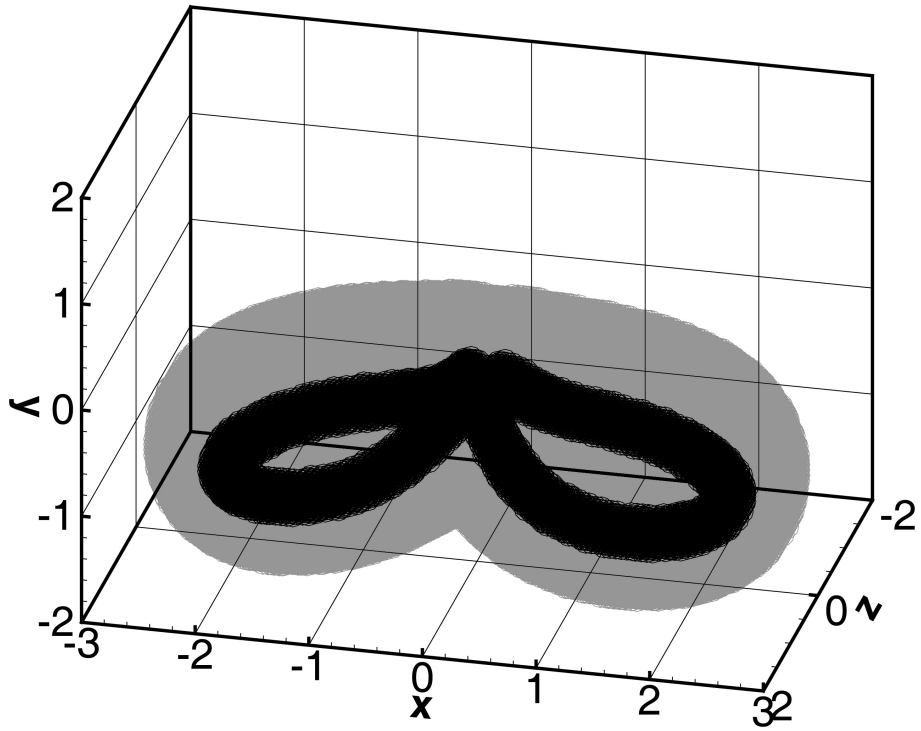

Figure B-1: Particle distribution for the test case: black, particles with $|\mathbf{W}_j| > 0.0005$ and gray, all particles.

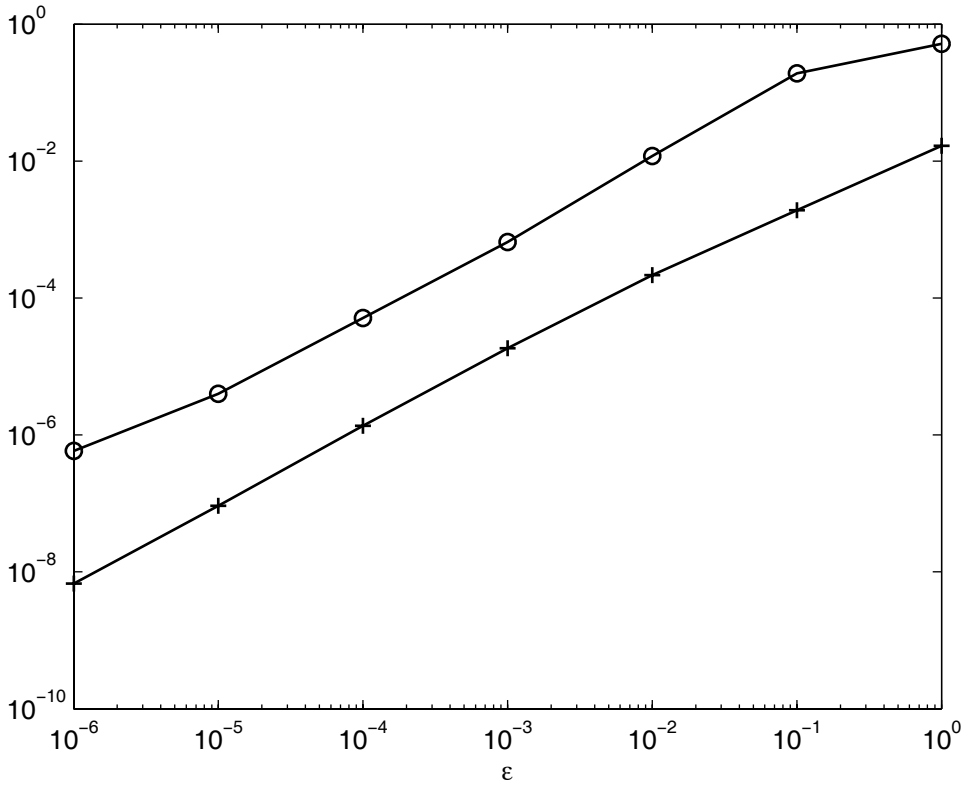

Figure B-2: Error verses ϵ. Crosses represent E_{abs}, and circles represent E_{rel}.

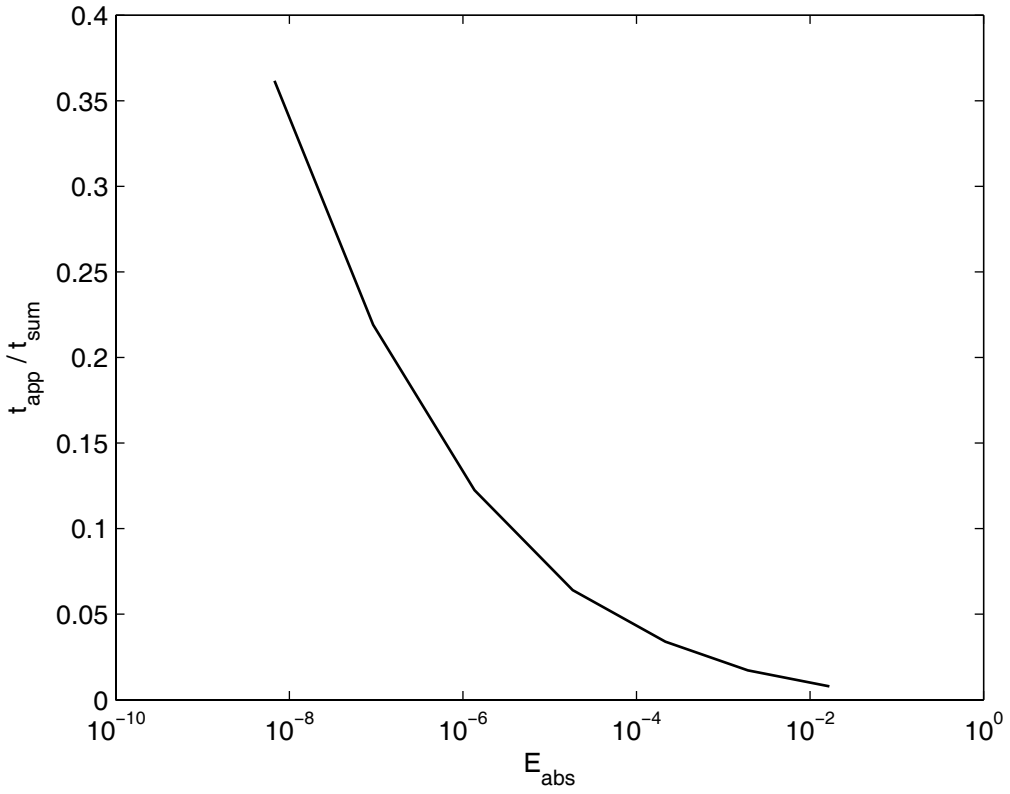

Figure B-3: Computational time verses E_{abs}.

Appendix C

Convergence Characteristics of Two Algebraic Kernels

C.1 Background

The Rosenhead-Moore kernel, used for the study of transverse jets in the main text, does not satisfy the following inequality:

$$\exists d \geq 2, \quad s.t. \quad \int_0^\infty |f(\rho)| \rho^{2+d} d\rho < \infty, \tag{C.1}$$

where f is the radially symmetric core function corresponding to the kernel. Citing the study by Cottet [13], Winckelmans and Leonard [74] have claimed that the Rosenhead-Moore kernel may not lead to convergence due to the lack of this inequality. Although we are fully comfortable with the Rosenhead-Moore kernel, since all our numerical experiments with the kernel show quantitatively accurate results [73], it is of interest to check whether such a danger of non-convergence truly lies.

In this context, we investigate the convergence characteristics of two algebraic kernels, i.e., the Rosenhead-Moore kernel and the Winckelmans-Leonard kernel. First, we check the proof given in [13] carefully to see where the inequality is used and suggest how to modify the part to extend the analysis to the Rosenhead-Moore kernel. Then, we investigate the convergence characteristics of these two algebraic kernels

numerically in a more realistic setting. Based on the observations made, recommendations are given in the final section of this chapter.

C.2 On the convergence analysis of the Rosenhead-Moore kernel

Tracing the proof in [13], it is found that the only major place where the inequality (C.1) matters is Item (iv) in Lemma 5.4, which is restated here:

Assuming that

$$\int f(|\mathbf{x}|)d\mathbf{x} = 1, \tag{C.2}$$

$$\int \mathbf{x}^{\mathbf{k}} f(|\mathbf{x}|)d\mathbf{x} = 0, \qquad 1 \leq |\mathbf{k}| < d-1, \tag{C.3}$$

$$\int |\mathbf{x}|^d |f(|\mathbf{x}|)|d\mathbf{x} < \infty, \tag{C.4}$$

we get

$$||(\mathbf{K} - \mathbf{K}_\sigma)\star\mathbf{T}||_{0,p} \leq C\sigma^d(||\mathbf{T}||_{d,1} + ||\mathbf{T}||_{d,\infty}), \tag{C.5}$$

if $\mathbf{T} \in W^{d,\infty}(\mathbf{R}^3) \cap W^{d,1}(\mathbf{R}^3)$, and

$$||(\mathbf{K} - \mathbf{K}_\sigma)\star\mathbf{T}||_{0,p} \leq C\sigma^d||\mathbf{T}||_{d-1,p}, \tag{C.6}$$

if $\mathbf{T} \in W^{d-1,p}(\mathbf{R}^3)$, $1 < p < \infty$.

Here, the following notation is used:

$$(\mathbf{F}\star\mathbf{G})(\mathbf{x}) \equiv \int_{\mathbf{R}^3} \mathbf{F}(\mathbf{x},\mathbf{y}) \times \mathbf{G}(\mathbf{y})d\mathbf{y}, \tag{C.7}$$

$$\mathbf{K}(\mathbf{x},\mathbf{y}) = -\frac{1}{4\pi}\frac{\mathbf{x}-\mathbf{y}}{|\mathbf{x}-\mathbf{y}|^3}, \tag{C.8}$$

and

$$\mathbf{K}_\sigma(\mathbf{x},\mathbf{y}) = \int_{\mathbf{R}^3} \mathbf{K}(\mathbf{x},\mathbf{z})f_\sigma(\mathbf{z}-\mathbf{y})d\mathbf{z}. \tag{C.9}$$

In particular, (C.4) corresponds to (C.1). This shows two things:

1. The inequality is used to show that the error of desingularization behaves in a consistent way. The other part of the error, i.e., the error of discretization, behaves independent from the inequality.

2. In [13], it is *never* explicitly stated that $d \geq 2$. The condition of $d \geq 2$ turns out necessary, however, for developing (C.6). We shall suggest that the statement can be modified to include the case of $d = 1$. This is of particular importance. If d is chosen to be 1, the Rosenhead-Moore kernel does satisfy all the requirements. It certainly satisfies (C.2) and (C.4), and (C.3) is vacuously true.

In the following, we show how to modify the statement to include the case of $d = 1$. For $d = 1$, given a test function ϕ, we use integration by parts to get:

$$\begin{aligned} & \left| \int (\mathbf{T} - f_\sigma * \mathbf{T})(\mathbf{x})\, \phi(\mathbf{x}) d\mathbf{x} \right| \\ = & \left| \int \left(\int_{t=0}^{1} \int \mathbf{z} \cdot \nabla \mathbf{T}(\mathbf{x} + t\mathbf{z}) f_\sigma(\mathbf{z}) d\mathbf{z}\, dt \right) \phi(\mathbf{x}) d\mathbf{x} \right| \\ \leq & C||\mathbf{T}||_{1,p}\, ||\phi||_{1,p'} \int |\mathbf{z}||f_\sigma(\mathbf{z})| d\mathbf{z} \qquad \text{(C.10)} \\ = & C\sigma||\mathbf{T}||_{1,p}\, ||\phi||_{1,p'} \int |\mathbf{z}||f(|\mathbf{z}|)| d\mathbf{z}. \\ \leq & C\sigma||\mathbf{T}||_{1,p}\, ||\phi||_{1,p'} \end{aligned}$$

where $1/p + 1/p' = 1$. Thus, $||\mathbf{T} - f_\sigma * \mathbf{T}||_{-1,p} \leq C\sigma||\mathbf{T}||_{1,p}$. Once after this distribution estimate is established, (C.6) simply follows from the Calderon's theorem [14]:

$$||\mathbf{K} \star (\mathbf{T} - f_\sigma * \mathbf{T})||_{0,p} \leq C||\mathbf{T} - f_\sigma * \mathbf{T}||_{-1,p} \leq C\sigma||\mathbf{T}||_{1,p}. \qquad \text{(C.11)}$$

With this last inequality, we modify (C.6) as follows:

$$||(\mathbf{K} - \mathbf{K}_\sigma) \star \mathbf{T}||_{0,p} \leq C\sigma^d ||\mathbf{T}||_{d'-1,p}, \qquad \text{(C.12)}$$

if $\mathbf{T} \in W^{d'-1,p}(\mathbf{R}^3)$, $1 < p < \infty$, $d' = \max(d, 2)$. (C.12) is valid for $d \geq 1$.

This new inequality of (C.12) seems enough for the further development of the convergence analysis given in [13]. For instance, Lemma 5.5 in [13] can be proven for the Rosenhead-Moore kernel, if enough regularity for the initial vorticity field $\boldsymbol{\omega}(\cdot, 0)$ is kept to ensure that $\boldsymbol{\omega}(\cdot, t) \in W^{1,p}(\mathbf{R}^3)$ instead of $W^{0,p}(\mathbf{R}^3)$ for all $0 < t < T$. The regularity of $\boldsymbol{\omega}(\cdot, t)$ is obviously related to the existence of a smooth solution for the Euler equation for small time, as mentioned in [13, 14]. It is an independent issue from (C.1). The same story goes on for the smoothed vorticity, i.e., $\boldsymbol{\omega}_\epsilon$ in [13].

Thus, apparently, the point initially missed was that (C.6) did not separately address two truly unrelated issues: the regularity requirement of the vorticity distribution and the consistency of desingularization. Once these two issues are separately addressed as in (C.12), one may show that the Rosenhead-Moore kernel leads to convergence as $\sigma \to 0$, as far as the initial vorticity distribution is regular enough. The error due to desingularization should behave at least as $O(\sigma)$ in this case.

Note that the Winckelmans-Leonard kernel [74] satisfies (C.6) with $d = 2$, and hence its desingularization error should behave at least as $O(\sigma^2)$. Certainly, the Winckelmans-Leonard kernel is superior over the Rosenhead-Moore kernel in theoretical convergence rate by one order, and thus the Winckelmans-Leonard kernel deserves the title of the high-order algebraic kernel in this sense.

C.3 Numerical results

The error discussed in the previous section only includes the error due to desingularization. However, the error due to desingularization becomes a meaningful estimate of the overall error only for the case where the error due to discretization is small. In practice, one performs simulations, keeping the overlap ratio, i.e., $\sigma/\Delta x$, const. In such a case, the apparent convergence rate may be different from that predicted by analysis. As a guide, a numerical example is provided in this section.

Using two algebraic kernels, we compute the velocity field induced by a Gaussian distribution:

$$\mathbf{T}(\mathbf{x}) = \frac{\hat{\mathbf{e}}_2}{(2\pi)^{3/2}} e^{-|\mathbf{x}|^2/2}, \tag{C.13}$$

whose exact solution of the velocity field is given by:

$$\mathbf{u}(\mathbf{x}) = (\mathbf{K}\star\mathbf{T})(\mathbf{x}) = -\frac{\mathbf{x}\times\hat{\mathbf{e}}_2}{4\pi|\mathbf{x}|^3}\left(\mathrm{erf}\left(\frac{|\mathbf{x}|}{2^{1/2}}\right) - \left(\frac{2}{\pi}\right)^{1/2}|\mathbf{x}|e^{-|\mathbf{x}|^2/2}\right). \tag{C.14}$$

Due to the azimuthal symmetry of the distribution, one may just compute the velocity on a plane, e.g., $x_3 = 0$ in this case, to estimate the error in $\mathbf{R}^3$. Since it is apparent that the maximum error should occur along the line of $x_2 = 0$ in this plane, where high velocity occurs, we only compute the velocity on that line. Furthermore, with a few calculations at coarse resolutions, we have found that the maximum error actually occurs near $x_1 = 1$. Thus, we concentrate our computational efforts for the computation of the velocity only on the segment of the line of $x_2 = x_3 = 0$ where $x_1 \in [0, 1.5]$. Among three components of the velocity field, i.e., u_1, u_2, and u_3, only u_3 is nontrivial on the line of $x_2 = x_3 = 0$, and hence only u_3 is reported. Such simplification is essential to realize calculations at a resolution fine enough to get converging behaviors.

The distribution in (C.13) is not of compact support. However, it exponentially decays at infinity, and we may specify a reasonable cutoff distance: our numerical discretization is only made for $-4 \le x_i \le 4$. Within the domain of discretization, we place a uniform grid with specified grid size of Δx, and construct the discretized distribution as follows:

$$\underline{\mathbf{T}}(\mathbf{x}) = \sum_j \mathbf{T}(\mathbf{x}_j)\Delta x^3\delta(\mathbf{x}-\mathbf{x}_j), \tag{C.15}$$

where the index j runs for all the grid point. The discretized velocity field is recovered by taking

$$\underline{\mathbf{u}}^{RM}(\mathbf{x}) = (\mathbf{K}_\sigma^{RM}\star\underline{\mathbf{T}})(\mathbf{x}), \tag{C.16}$$

$$\underline{\mathbf{u}}^{WL}(\mathbf{x}) = (\mathbf{K}_\sigma^{WL}\star\underline{\mathbf{T}})(\mathbf{x}), \tag{C.17}$$

where $\mathbf{K}_\sigma^{RM}$ and $\mathbf{K}_\sigma^{WL}$ are defined in Appendix B. The actual calculation is performed

by the tree-code developed in Appendix B with $\epsilon = 0.0005$ and $N_0 = 64$.

The computation is done as Δx is refined while $\sigma/\Delta x$ is kept as 2. This is a typical overlap ratio reported to be effective previously [41]. Typical velocity profiles are shown in Figure C-1, where the results with $\sigma = 0.2$ and $\Delta x = 0.1$ are plotted. With the same value of σ, the velocity profile obtained from the Rosenhead-Moore kernel is in general less sharp than that obtained from the Winckelmans-Leonard kernel, as expected.

The overall convergence rate is estimated by refining Δx. The result is shown in Figure C-2, where the error is plotted against Δx. The error reported for the Winckelmans-Leonard kernel truly decays faster than that of the Rosenhead-Moore kernel. The rate of convergence for the Rosenhead-Moore kernel is around $O(\sigma^{1.75})$. The rate of convergence for the Winckelmans-Leonard kernel turns out to be $O(\sigma^2)$, which is higher than that of the Rosenhead-Moore kernel, but not higher by one order as expected from the previous discussion. This is not inconsistent to the previous discussion however, since the convergence rate estimated for the Rosenhead-Moore kernel in the previous section is conservative. In any case, the Winckelmans-Leonard kernel generally yields a result better than that of the Rosenhead-Moore kernel when a fixed number of computational elements is specified. For a typical resolution, it seems that switching the Rosenhead-Moore kernel into the Winckelmans-Leonard kernel gives order-of-magnitude reduction of the error, and the difference becomes greater as the resolution increases.

Similar analysis has been performed with different overlap ratios, but the rate of convergence remains almost invariant under the change of the overlap ratio, as far as it ensures smooth enough recovery of the velocity profile.

C.4 Summary

We have discussed the convergence characteristics of two algebraic kernels, i.e., the Rosenhead-Moore kernel and the Winckelmans-Leonard kernel. The following list summarizes what we have found:

1. Both algebraic kernels seem to lead to convergence, in theory and in practice. A potential way to extend the current theoretical convergence analysis to the Rosenhead-Moore kernel is suggested. Constructing a rigorous convergence analysis is left as the subject of further research.

2. For a typical resolution, the error from the Winckelmans-Leonard kernel is order-of-magnitude smaller than that from the Rosenhead-Moore kernel.

3. The Winckelmans-Leonard kernel shows a superior convergence rate than that of the Rosenhead-Moore kernel.

From these observations, since the price of using the Winckelmans-Leonard kernel instead of the Rosenhead-Moore kernel is minimal as discussed in Appendix B, it is recommended to use the Winckelmans-Leonard kernel for high-resolution calculations.

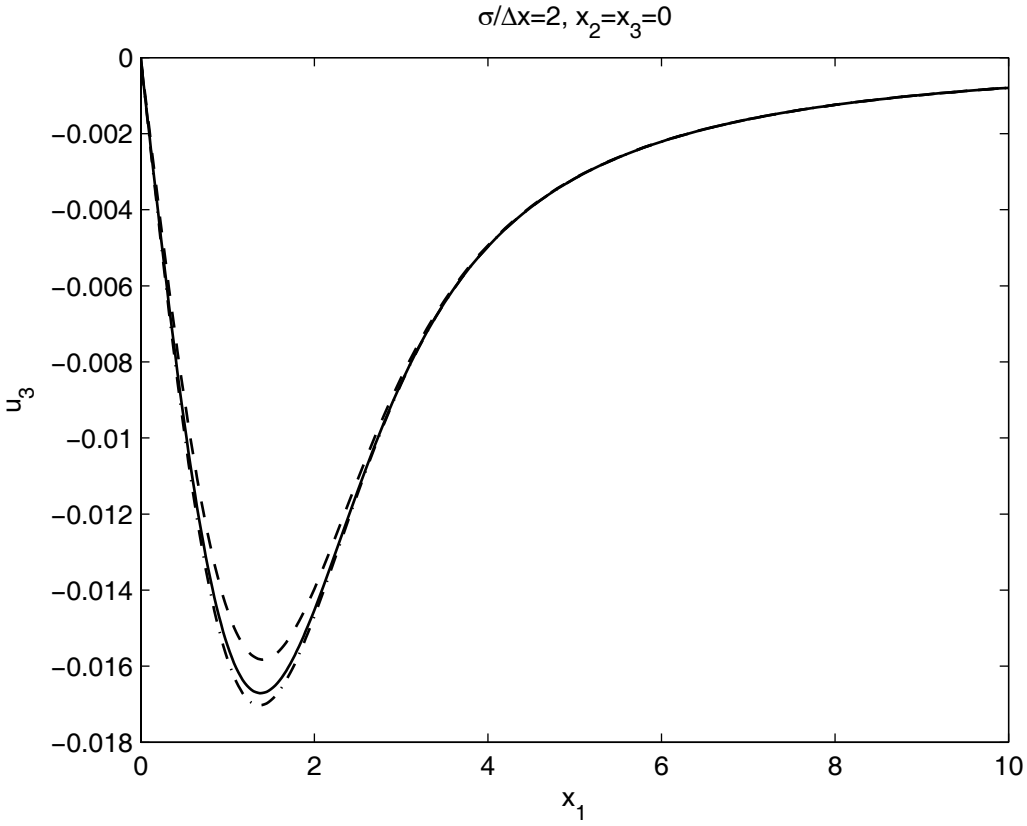

Figure C-1: Typical velocity profiles. u_3 computed with $\sigma = 0.2$ and $\Delta x = 0.1$. The solid curve represents the result by the Winckelmans-Leonard kernel. The dashed curve represents the result by the Rosenhead-Moore kernel. The dash-dot curve is the exact solution given in (C.14).

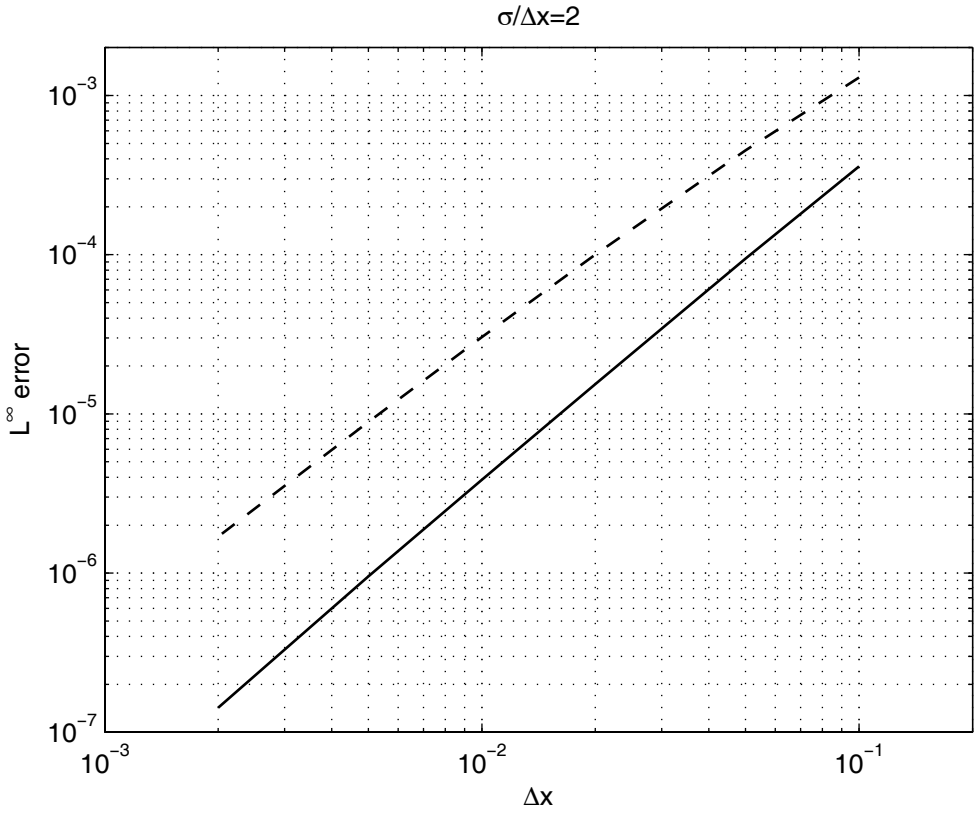

Figure C-2: L^∞ error of u_3 verses Δx. The solid curve represents the result by the Winckelmans-Leonard kernel. The dashed curve represents the result by the Rosenhead-Moore kernel.

Bibliography

[1] R. Adams and J. J. F. Fournier. *Sobolev Spaces*. Elsevier Science, second edition, 2003.

[2] C. R. Anderson. An implementation of the fast multipole method without multipoles. *SIAM Journal on Scientific and Statistical Computing*, 13(4):923–947, 1992.

[3] J. Andreopoulos. On the structure of jets in a cross-flow. *Journal of Fluid Mechanics*, 157:163–197, 1985.

[4] L. A. Barba, A. Leonard, and C. B. Allen. Advances in viscous vortex methods-meshless spatial adaption based on radial basis function interpolation. *International Journal for Numerical Methods in Fluids*, 47:387–421, 2005.

[5] A. I. Barcilon and P. G. Drazin. Dust devil formation. *Geophysical Fluid Dynamics*, 4:147–158, 1972.

[6] D. P. Bovet and P. Crescenzi. *Introduction to the Theory of Complexity*. Prentice Hall, 1994.

[7] J. E. Broadwell and R. E. Breidenthal. Structure and mixing of a transverse jet in incompressible-flow. *Journal of Fluid Mechanics*, 148:405–412, 1984.

[8] S. C. Chapra and R. P. Canale. *Numerical Methods for Engineers*. McGraw-Hill, second edition, 1988.

[9] P. Chatelain and A. Leonard. Face-centred cubic lattices and particle redistribution in vortex methods. *Journal of Turbulence*, 3-046, 2002.

[10] R. C. Y. Chin and G. W. Hedstrom. A dispersive analysis for difference schemes: tables of generalized Airy functions. *Mathematics of Computation*, 32:1163–1170, 1978.

[11] A. J. Chorin. Numerical study of slightly viscous flow. *Journal of Fluid Mechanics*, 57:785–796, 1973.

[12] L. Cortelezzi and A. R. Karagozian. On the formation of the counter-rotating vortex pair in transverse jets. *Journal of Fluid Mechanics*, 446:347–373, 2001.

[13] G.-H. Cottet. A new approach for the analysis of vortex methods in two and three dimensions. *Annales de L'Institut Henri Poincare—Analyse Non Lineaire*, 5(3):227–285, 1988.

[14] G.-H. Cottet and P. D. Koumoutsakos. *Vortex Methods: Theory and Practice*. Cambridge University Press, 2000.

[15] G.-H. Cottet, P. D. Koumoutsakos, and M. L. Ould-Salihi. Vortex methods with spatially varying cores. *Journal of Computational Physics*, 162:164–185, 2000.

[16] G.-H. Cottet and S. Mas-Gallic. A particle method to solve the Navier-Stokes system. *Numerische Mathematik*, 57:805–827, 1990.

[17] P. Degond and S. Masgallic. The weighted particle method for convection-diffusion equations: 1. The case of an isotropic viscosity. *Mathematics of Computation*, 53(188):485–507, 1989.

[18] P. Degond and S. Masgallic. The weighted particle method for convection-diffusion equations: 2. The anisotropic case. *Mathematics of Computation*, 53(188):509–525, 1989.

[19] P. Degond and F.-J. Mustieles. A deterministic approximation of diffusion-equations using particles. *SIAM Journal on Scientific and Statistical Computing*, 11:293–310, 1990.

[20] Z. H. Duan and R. Krasny. An adaptive treecode for computing nonbonded potential energy in classical molecular systems. *Journal of Computational Chemistry*, 22(2):184–195, 2001.

[21] T. F. Fric and A. Roshko. Vortical structure in the wake of a transverse jet. *Journal of Fluid Mechanics*, 279:1–47, 1994.

[22] G. Friedlander and M. Joshi. *Introduction to the Theory of Distributions*. Cambridge University Press, second edition, 1998.

[23] A. Gharakhani. A higher order vorticity redistribution method for 3-D diffusion in free space. *Sandia Report*, SAND2000-2505, 2000.

[24] A. F. Ghoniem, G. Heidarinejad, and A. Krishnan. Numerical simulation of a thermally stratified shear layer using the vortex element method. *Journal of Computational Physics*, 79:135–166, 1988.

[25] M. N. Glauser and W. K. George. An orthogonal decomposition of the axisymmetric jet mixing layer utilizing cross wire measurements. In *Proc. Sixth Symp. Turbulent Shear Flows, Toulouse, France*, number 10.1.1, 1987.

[26] N. Goren-Inbar, N. Alperson, M. E. Kislev, O. Simchoni, Y. Melamed, A. Ben-Nun, and E. Werker. Evidence of hominin control of fire at Gesher Benot Ya'aqov, Israel. *Science*, 304:725–727, 2004.

[27] L. Greengard and V. Rokhlin. A fast algorithm for particle simulations. *Journal of Computational Physics*, 73:325–348, 1997.

[28] E. F. Hasselbrink and M. G. Mungal. Transverse jets and jet flames. Part 1: Scaling laws for strong transverse jets. *Journal of Fluid Mechanics*, 443:1–25, 2001.

[29] J. Huizinga. *Homo Ludens: A Study of the Play-Element in Culture*. Beacon Press, first Beacon paperback edition, 1955.

[30] Y. Kamotani and I. Greber. Experiments on a turbulent jet in a cross flow. *AIAA Journal*, 10:1425–1429, 1972.

[31] A. R. Karagozian. An analytical model for the vorticity associated with a transverse jet. *AIAA Journal*, 24:429–436, 1986.

[32] J. F. Keffer and W. D. Baines. The round turbulent jet in a cross-wind. *Journal of Fluid Mechanics*, Vol. 15:481–496, 1962.

[33] R. M. Kelso, T. T. Lim, and A. E. Perry. An experimental study of round jets in cross-flow. *Journal of Fluid Mechanics*, 306:111–144, 1996.

[34] R. M. Kelso and A. J. Smits. Horseshoe vortex systems resulting from the interaction between a laminar boundary-layer and a transverse jet. *Physics of Fluids*, 7(1):153–158, 1995.

[35] S. Kida, M. Takaoka, and F. Hussain. Collision of two vortex rings. *Journal of Fluid Mechanics*, 230:583–646, 1991.

[36] O. M. Knio and A. F. Ghoniem. Numerical study of a three-dimensional vortex method. *Journal of Computational Physics*, 86:75–106, 1990.

[37] O. M. Knio and A. F. Ghoniem. Three-dimensional vortex simulation of rollup and entrainment in a shear layer. *Journal of Computational Physics*, 97:172–223, 1991.

[38] P. D. Koumoutsakos. Inviscid axisymmetrization of an elliptical vortex. *Journal of Computational Physics*, 138:821–857, 1997.

[39] P. D. Koumoutsakos, A. Leonard, and F. Pepin. Boundary conditions for viscous vortex methods. *Journal of Computational Physics*, 113:52–56, 1994.

[40] O. A. Ladyženskaja, V. A. Solonnikov, and N. N. Ural'ceva. *Linear and Quasilinear Equations of Parabolic Type*. American Mathematical Society, first edition, 1968.

[41] I. Lakkis and A. F. Ghoniem. Axisymmetric vortex method for low-Mach number, diffusion-controlled combustion. *Journal of Computational Physics*, 184(2):435–475, 2003.

[42] A. Leonard. Computing three-dimensional incompressible flows with vortex elements. *Annual Review of Fluid Mechanics*, 17:523–559, 1985.

[43] R. J. LeVeque. *Numerical Methods for Conservation Laws*. Birkhäuser Verlag, second edition, 1992.

[44] T. T. Lim, T. H. New, and S. C. Luo. On the development of large-scale structures of a jet normal to a cross flow. *Physics of Fluids*, 13(3):770–775, 2001.

[45] K. Lindsay and R. Krasny. A particle method and adaptive treecode for vortex sheet motion in three-dimensional flow. *Journal of Computational Physics*, 172(2):879–907, 2001.

[46] Z. Y. Lu and T. J. Ross. Diffusing-vortex numerical scheme for solving incompressible Navier-Stokes equations. *Journal of Computational Physics*, 95:400–435, 1991.

[47] O. Lucca-Negro and T. O'Doherty. Vortex breakdown: a review. *Progress in Energy and Combustion Science*, 27:431–481, 2001.

[48] A. Majda and A. L. Bertozzi. *Vorticity and incompressible flow*. Cambridge University Press, Cambridge; New York, 2002.

[49] R. J. Margason. The path of a jet directed at large angles to a subsonic free stream. *NASA Technical Note*, NASA TN D-4919, 1968.

[50] Y. M. Marzouk and A. F. Ghoniem. k-means clustering for optimal partitioning and dynamic load balancing of parallel hierarchical N-body simulations. *Journal of Computational Physics*, 207:493–528, 2005.

[51] Y. M. Marzouk and A. F. Ghoniem. Vorticity structure and evolution in a transverse jet. *Journal of Fluid Mechanics*, 575:267–305, 2007.

[52] D. W. Moore. Finite amplitude waves on aircraft trailing vortices. *Aeronautical Quarterly*, 23:307–314, 1972.

[53] J. R. Munkres. *Topology: a First Course*. Prentice Hall, first edition, 1975.

[54] S. Muppidi and K. Mahesh. Study of trajectories of jets in crossflow using direct numerical simulations. *Journal of Fluid Mechanics*, 530:81–100, 2005.

[55] U.S. Department of Energy. *International Energy Outlook 2006*. DOE/EIA-0484(2006), 2006.

[56] P. Ploumhans, G. S. Winckelmans, J. K. Salmon, A. Leonard, and M. S. Warren. Vortex methods for direct numerical simulation of three-dimensional bluff body flows: Application to the sphere at Re = 300, 500, and 1000. *Journal of Computational Physics*, 178(2):427–463, 2002.

[57] G. Rosen. Nonlinear heat conduction in solid H_2. *Physical Review B*, 19:2398–2399, 1979.

[58] L. Rosenhead. The formation of vortices from a surface of discontinuity. *Proc. Royal Society A*, 134:170–192, 1931.

[59] L. F. Rossi. Resurrecting core spreading vortex methods: a new scheme that is both deterministic and convergent. *SIAM Journal of Scientific Computing*, 17:370–397, 1996.

[60] N. Rott and B. J. Cantwell. Vortex drift. I: dynamic interpretation. *Physics of Fluids A*, 5:1443–1450, 1993.

[61] G. Russo. A deterministic vortex method for the Navier-Stokes equations. *Journal of Computational Physics*, 108:84–94, 1992.

[62] X. Saint Raymond. *Elementary Introduction to the Theory of Pseudodifferential Operators*. CRC Press, 1991.

[63] S. Shankar. Grid-free redistribution methods for axisymmetric and anisotropic diffusion. *Internal Report, Reacting Gas Dynamics Laboratory, Massachusetts Institute of Technology*, 1999.

[64] S. Shankar and L. van Dommelen. A new diffusion procedure for vortex methods. *Journal of Computational Physics*, 127(1):88–109, 1996.

[65] K. Shariff and A. Leonard. Vortex rings. *Annual Review of Fluid Mechanics*, 24:235–279, 1992.

[66] S. K. Stanaway, B. J. Cantwell, and P. R. Spalart. Navier-Stokes simulations of axisymmetric vortex rings. *AIAA Technical Paper*, AIAA-88-0318, 1988.

[67] S. K. Stanaway, B. J. Cantwell, and P. R. Spalart. A numerical study of viscous vortex rings using a spectral method. *NASA Technical Memorandum*, NASA TM 101041, 1988.

[68] R. S. Strichartz. *A Guide to Distribution Theory and Fourier Transforms*. World Scientific Publishing, first edition, 1994.

[69] J. C. Strikwerda. *Finite Difference Schemes and Partial Differential Equations*. Wadsworth & Brooks/Cole, first edition, 1989.

[70] F. Thirifay and G. S. Winckelmans. Development of a Lagrangian method for combustion and application to the planar methane air jet diffusion flame. *Journal of Turbulence*, 3-059, 2002.

[71] H. Trac and U. Pen. A primer on Eulerian computational fluid dynamics for astrophysics. *Publications of the Astronomical Society of the Pacific*, 115:303–321, 2003.

[72] L. van Dommelen and E. A. Rundensteiner. Fast, adaptive summation of point forces in the two-dimensional poisson equation. *Journal of Computational Physics*, 83(1):126–147, 1989.

[73] D. Wee and A. F. Ghoniem. Modified interpolation kernels for diffusion and remeshing in vortex methods. *Journal of Computational Physics*, 213:239–263, 2006.

[74] G. S. Winckelmans and A. Leonard. Contributions to vortex particle methods for the computation of three-dimensional incompressible unsteady flows. *Journal of Computational Physics*, 109(2):247–273, 1993.

[75] G. S. Winckelmans, J. K. Salmon, M. S. Warren, A. Leonard, and B. Jodoin. Application of fast parallel and sequential tree codes to computing three-dimensional flows with the vortex element and boundary element methods. *ESAIM Proceedings: Vortex Flows and Related Numerical Methods II*, 1:225–240, 1996.

[76] L. L. Yuan, R. L. Street, and J. H. Ferziger. Large-eddy simulations of a round jet in crossflow. *Journal of Fluid Mechanics*, 379:71–104, 1999.